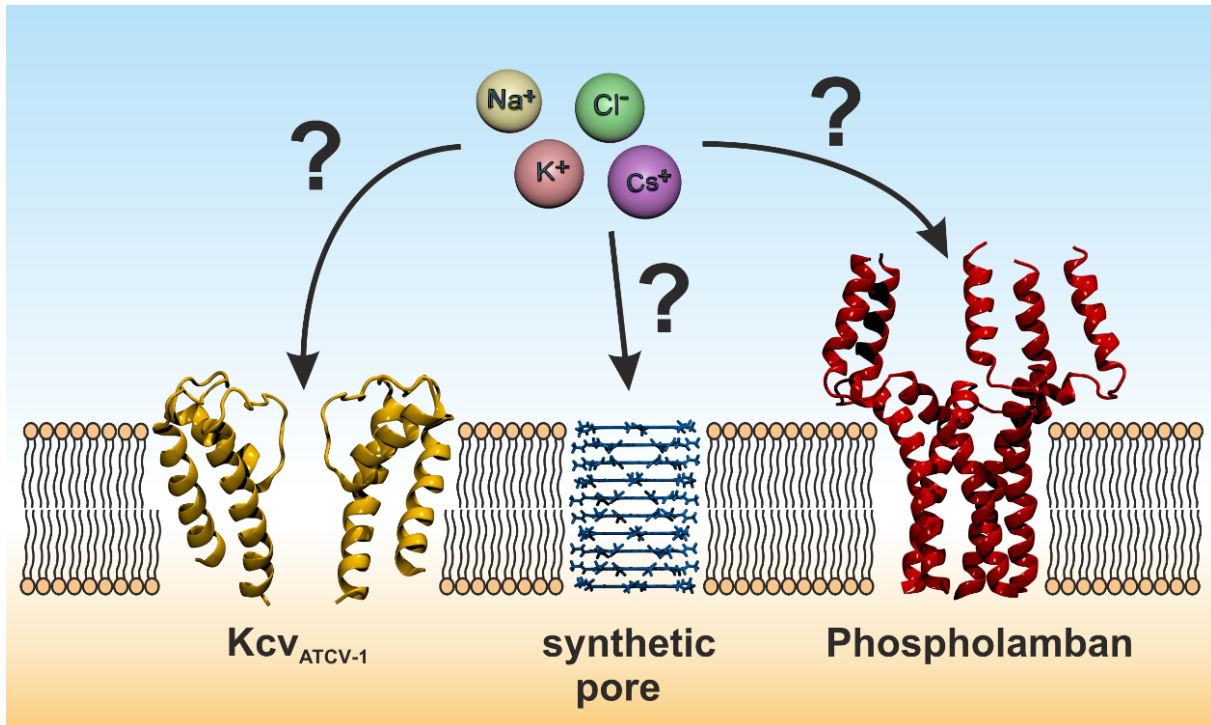# Investigation of ion-selective nanopores by a multi-level approach



Dissertation
zur Erlangung des Doktorgrads

vorgelegt von

## Dipl.-Biol. Leonhard M. Henkes

Erster Gutachter:    Prof. Dr. Stefan M. Kast
Zweiter Gutachter:  Prof. Dr. Gerhard Thiel

# Table of contents

4

# Contributions to this work

The here presented work was performed by the author except,

the basic version of the radial integration, which was provided by **Thomas Kloss**, IPhT, L'Orme des Merisiers, CEA-Saclay, France,

calculations and results with the hard cylinder pore (HCP) were permitted by **Martin Urban**, Technische Universität Dortmund, Dortmund, Fakultät Chemie und chemische Biologie, Germany,

homology models of the $Kcv_{PBCV-1}$ channel and corresponding scripts for the creation of their symmetric, average structure were provided by **Sascha Tayefeh**, Software AG, Switzerland,

**patch-clamp experiments** regarding the pentameric ion channel phospholamban, which were measured and analyzed by Serena Smeazzetto, University of Florence, Florence, Dipartimento di Chimica. Italy.

# Danksagung

An dieser Stelle möchte ich mich bei allen Menschen bedanken, die zur Entstehung dieser Arbeit beigetragen haben. Mein besonderer Dank gilt

Herr Professor **Stefan M. Kast** für die Ausgabe spannender Aufgabenstellungen, für die stetige und geduldige Betreuung und nicht zu Letzt für eine immer offene Tür in allen Lagen,

Herrn Professor **Gerhard Thiel** für die Betreuung und Unterstützung in allen biologischen und experimentellen Fragestellungen und für die Begleitung meiner gesamten biologischen Laufbahn,

meiner **gesamten AG** inklusive Herrn Professor **Alfons Geiger** und **Sandra Frach** für die lustige Zeit und die heiteren Mittagessen,

allen Freunden und Kooperationspartnern aus der Pflanzenphysiologie Darmstadt,

meinen Kollegen **Florian Mrugalla** und **Roland Frach**, für ihre Unterstützung und Freundschaft,

meinem Bruder **Benedikt** und meinen **Eltern** für die Ihre Hilfe in allen Lebenslagen,

mein größter Dank gilt meinen Kindern **Julia** und **Tristan**, sowie meiner Frau **Catharina**, die mich in allen Hoch- und Tiefphasen der gesamten Zeit mit Ihrer Liebe unterstützt haben.

# Eidesstattliche Versicherung (Affidavit)

Henkes, Leonhard

**Name, Vorname**
(Surname, first name)

147086

**Matrikel-Nr.**
(Enrolment number)

| Belehrung: | Official notification: |
|---|---|
| Wer vorsätzlich gegen eine die Täuschung über Prüfungsleistungen betreffende Regelung einer Hochschulprüfungsordnung verstößt, handelt ordnungswidrig. Die Ordnungswidrigkeit kann mit einer Geldbuße von bis zu 50.000,00 € geahndet werden. Zuständige Verwaltungsbehörde für die Verfolgung und Ahndung von Ordnungswidrigkeiten ist der Kanzler/die Kanzlerin der Technischen Universität Dortmund. Im Falle eines mehrfachen oder sonstigen schwerwiegenden Täuschungsversuches kann der Prüfling zudem exmatrikuliert werden, § 63 Abs. 5 Hochschulgesetz NRW. | Any person who intentionally breaches any regulation of university examination regulations relating to deception in examination performance is acting improperly. This offence can be punished with a fine of up to EUR 50,000.00. The competent administrative authority for the pursuit and prosecution of offences of this type is the chancellor of the TU Dortmund University. In the case of multiple or other serious attempts at deception, the candidate can also be unenrolled, Section 63, paragraph 5 of the Universities Act of North Rhine-Westphalia. |
| Die Abgabe einer falschen Versicherung an Eides statt ist strafbar. | The submission of a false affidavit is punishable. |
| Wer vorsätzlich eine falsche Versicherung an Eides statt abgibt, kann mit einer Freiheitsstrafe bis zu drei Jahren oder mit Geldstrafe bestraft werden, § 156 StGB. Die fahrlässige Abgabe einer falschen Versicherung an Eides statt kann mit einer Freiheitsstrafe bis zu einem Jahr oder Geldstrafe bestraft werden, § 161 StGB. | Any person who intentionally submits a false affidavit can be punished with a prison sentence of up to three years or a fine, Section 156 of the Criminal Code. The negligent submission of a false affidavit can be punished with a prison sentence of up to one year or a fine, Section 161 of the Criminal Code. |
| Die oben stehende Belehrung habe ich zur Kenntnis genommen: | I have taken note of the above official notification. |

**Ort, Datum**
(Place, date)

**Unterschrift**
(Signature)

**Titel der Dissertation:**
(Title of the thesis):

Investigation of ion-selective nanopores by a multi-level approach

| Ich versichere hiermit an Eides statt, dass ich die vorliegende Dissertation mit dem Titel selbstständig und ohne unzulässige fremde Hilfe angefertigt habe. Ich habe keine anderen als die angegebenen Quellen und Hilfsmittel benutzt sowie wörtliche und sinngemäße Zitate kenntlich gemacht. Die Arbeit hat in gegenwärtiger oder in einer anderen Fassung weder der TU Dortmund noch einer anderen Hochschule im Zusammenhang mit einer staatlichen oder akademischen Prüfung vorgelegen. | I hereby swear that I have completed the present dissertation independently and without inadmissible external support. I have not used any sources or tools other than those indicated and have identified literal and analogous quotations. The thesis in its current version or another version has not been presented to the TU Dortmund University or another university in connection with a state or academic examination.* |

*Please be aware that solely the German version of the affidavit ("Eidesstattliche Versicherung") for the PhD thesis is the official and legally binding version.

**Ort, Datum**
(Place, date)

**Unterschrift**
(Signature)

# 1 Abstracts

## 1.1 Zusammenfassung

Der selektive Transport von Ionen durch Membranen ist eine bekannte Eigenschaft von biologischen sowie synthetischen Poren, die bis heute trotz einer Vielzahl an existierenden theoretischen und praktischen Studien an verschiedensten Porensystemen nicht vollständig aufgeklärt wurde.[1–3] Ein tieferes Verständnis von Ionenselektivität würde die Behandlung von damit verbunden Krankheitsbildern erleichtern und wäre in den technischen Bereichen der Wasseraufbereitung, Biosensorik und im Bereich des Proteindesigns von großem Nutzen. Aus diesen Gründen steht die theoretische Erforschung der thermodynamischen und kinetischen Ionenselektivität von biologischen tetrameren und pentameren sowie synthetischen Kanalsystemen im Fokus dieser Arbeit. Hierzu wurde in einem ersten Ansatz ein Homologiemodell des kleinen viralen tertrameren Ionenkanals $Kcv_{ATCV-1}$ erstellt und in Molekulardynamik-Simulationen mit verschiedenen Ionenlösungen untersucht.[4] Anhand simulationsbasierter symmetrischer Strukturen dieses biologischen Kanals wurde eine thermodynamische Analysemethodik in Kombination mit einer Integralgleichungstheorie etabliert und verifiziert. Um die kinetischen Aspekte der Ionenselektivität zu untersuchen wurden theoretische Leitfähigkeiten auf Basis von Molekulardynamik-Simulationen sowie Ergebnissen von Integralgleichungsberechnungen unter Verwendung der Vorarbeiten von Hummer et al.[5] berechnet. Für diese vergleichenden Arbeiten wurde ein geeignetes hydrophobes synthetisches Porensystem von Gong et al. ausgewählt, welches die Annahmen von Referenz 5 erfüllen.[5–7] Das Ergebnis dieser Untersuchung zeigte eine qualitative Übereinstimmung der Leitfähigkeiten zwischen beiden Methoden, welche im Fall dieser Pore eine starke Anionen-Selektivität nachwiesen. Auf Grund seiner hydrophoben und gleichzeitig biologischen Eigenschaften wurde die etablierte Analysemethodik abschließend auf den putativen pentameren Ionenkanal Phospholamban angewandt. Hierbei konnte eine mit experimentellen Ergebnissen von Smeazzetto et al. übereinstimmende Kationen-über-Anionen Selektivität nachgewiesen werden, welche zusätzlich die richtige Inter-Kationen-Leitfähigkeiten reproduzierte. Durch die thermodynamische Analyse wurde eine hydrophobe Engstelle als mögliches Selektivitätselement identifiziert. Durch die Formulierung eines thermodynamischen Kreisprozess wurden der lokale und globale Einfluss von Solvatationsbeiträgen im Hinblick auf Ihren Einfluss auf die Kationen-über-Anionen-Selektivität und Inter-Kationen-Selektivität

untersucht. Diese Studien zeigten eine große Abhängigkeit beider Selektivitäten von Solvatationseffekten. Zusammengefasst konnte in dieser Arbeit der Einfluss des Solvens auf die thermodynamische und kinetische Selektivität von polaren und hydrophoben Ionenkanälen gezeigt werden.

## 1.2 Abstract

The selective transport of ions through membranes is a known feature of biological and synthetic pores, which remains still not fully understood despite a variety of existing experimental and theoretical investigations with different pore systems.[1–3] A deeper understanding of ion selectivity would be desirable for the treatment of related diseases and would have an application in the technical fields of water purification, biosensoric and protein design. For this reason a focus was laid on the theoretical basis of the thermodynamic and kinetic ion selectivity of tetrameric and pentameric ion channels as well as on synthetic channel systems. In a first approach a homology model system for the small viral potassium channel $Kcv_{ATCV-1}$ was created and investigated in molecular dynamics simulations with various ion solutions.[4] Averaged channel structures, obtained from these simulations, were used to establish and verify a new thermodynamic analysis approach in combination with an integral equation theory. To tackle the kinetic aspects of ion selectivity, theoretical conductances were obtained from molecular dynamics simulations and also calculated from integral equation theory, by making use of previous work of Hummer et al.[5] A synthetic hydrophobic pore system of Gong et al.[6] was supposed to be appropriate for this investigation, as it fulfilled the assumptions made by Hummer et al.[5] The calculated conductances from the independent methods showed a qualitative agreement between them and revealed an anion selectivity of this pore system. The established thermodynamic and kinetic analysis techniques were also used to shed light on the putative pentameric ion channel phospholamban, as it is a biological membrane protein with a hydrophobic character. Compared to experimentally measured conductances by Smeazzetto et al. the calculated conductances could reproduce the observed cation over anion selectivity as well as the inter-cationic selectivity order. In the course of this investigation a hydrophobic restriction was identified to play a significant role for the ion selectivity as identified by the thermodynamic analysis of phospholamban. Formulation of a thermodynamic cycle permitted the investigation of single solvation free energy contributions to the cation over anion selectivity and the inter-cationic selectivity. This investigations identified strong global and local solvation effects to control the observed selectivity. In this work, the

influence of the solvent on thermodynamic and kinetic selectivity in polar and hydrophobic ion channels has been revealed.

# 2 Introduction

## 2.1 Biological background on ion channels

Ion channels are transmembrane proteins, fulfilling the selective transport of ion species through a lipid bilayer with turnover rates of ($10^8$ s$^{-1}$) which is near their diffusion limit in the bulk.[1–3] Eukaryotic and prokaryotic cells use this functionality to establish a membrane potential by distinct regulation of the inner and outer ion concentrations. Besides their important functionality in maintaining the cell homeostasis, ion channels are key regulators for the action potential firing, intercellular signaling and hormone release,.[8,9] In consequence of their universality, malfunctions and aberrations of ion channels cause many disease patterns for example the long and short QT syndrome as well as epilepsy.[10–12] In the historical context the electrophysiological experiments on huge squid axons of Hodgkin and Huxley in 1952 were an important step for the field of ion channel research. Their measurements showed different currents, which was related correctly to signals of permeating potassium (K$^+$) and sodium (Na$^+$) ions transported over the membran.[13–15] Furthermore they identified the propagation of electric potentials in a membrane, finally describing the process nowaday well known as the neuronal action potential.[16] By subsequent tracer experiments with radioactive potassium ions in 1955 Hodgkin and Keynes were capable to observe ion transitions in squid axons, leading to the first postulation for the existence of "channels".[17] This theory was supported by supplementing ion size experiments of Hille, identifying the minimum radius for permeation through the supposed channels.[18–21] Revelation of channel type specific blockers like the small tetraethylammonium (TEA) ion, the puffer fish toxin tertrodotoxin (TTX) and even the divalent ion Ba$^{2+}$ became supplemental tools for the identification of ion channel functionality by prohibiting the ion permeation.[16,22–25] By application of TEA in a series of electrophysiological experiments an internal (cytosolic) and external (extra cellular) blocking site were identified by Armstrong et al.[23] These blocking studies confirmed the existence of separate channels for each ion species and were further used to relate the ion species to measured current profiles.[2] Altogether these results gave reason to define ion selectivity as the passive transport of specific ion species along their electrochemical activity gradient through biological pores.[2] In this context the existence

of a biochemical selectivity element was implicitly given. At this point this hypothesis remained experimentally uncorroborated.

Further advancements in the field of electrophysiology led to the development of the important gigaseal patch and whole-cell techniques by Bert Sackmann and Erwin Neher in 1975, which allow for measurements of currents of a whole cell as well as those of single ion channels with high resolution.[14] These methods improved the search and characterization of new potassium, sodium, chloride and calcium ion channels until today.[2] Measured current profiles showed alternating periods of impermeability and conductivity, which were related to the process that is today known as gating. A detailed view showed that the channel can exhibit "open", "closed" or "inactivated" states. The latter is distinguished from a closed state by a fast transition from conductive into a non-conductive state.[2] Trying to explain the phenomenon of gating, cytosolic protease experiments with voltage sensitive potassium channels by Armstrong et al. related the process of inactivation to a ball like structure attached to the cytosolic N-terminus, often referred to as the "ball and chain" model.[26]

High permeation rates of $> 10^6$ ions per seconds became a striking criterion to distinguish ion selective pores from slower and stoichiometrically controlled transporter systems like the $Na^+/K^+$-Pump.[2] Besides the clarity in the reviewed results of Armstrong, Hille, Huxley and Hodgkin, their results identified a voltage, concentration and temperature dependency of the measured currents, which emphasized and foreshadowed the complexity of a potential structure-selectivity relation in channels. Trying to explain this structure-selectivity relation became even more difficult considering its tight assignment with the gating functionality. Nonetheless their outstanding results and techniques improved the understanding of selectivity and lifted the whole field of ion channel research to the next level.

A focus is laid in the following discussion on potassium ion channels, due to their importance in the field of ion channel research. Progress in molecular biology and the development of genetic techniques, like the invention of the site-directed mutagenesis and improved sequencing techniques, helped to rapidly identify new channels from eukaryotic and prokaryotic organisms as well as from viruses.[16,27–29] In benefit of these inventions a common mutation in *drosophila spec.*, described by a strong "shaking" phenotype, could be related to a mutation in gene encoding of a potassium channel of the family Kv1, also known as the "Shaker" family. The amino acid sequence

of the Shaker type potassium channel was the first to be revealed completely, allowing speculations about its exhibited spatial structure in the context of the existing gating and selectivity hypothesis.[27,30–33] Constant growth of available ion channel sequences gave access to comparative gene alignments, which led to the confirmation of a highly conserved consensus sequence, comprised of the amino acids Thr-X-Gly-Phe-Gly (one letter: TXGYG). Because of its global presence in known as well as designated ion channels, this "signature sequence" was assumed to be of functional importance, which led to the proposal of a selectivity "filter" domain by Heginbotham et al. in 1994.[34]

The prokaryotic, tetrameric potassium ($K^+$) ion channel KcsA was the first structure to be revealed completely by X-ray experiments of Doyle et al.[35] In accordance with the measured densities the previously identified signal sequence formed a narrow structural funnel domain with four potential ion binding sites, which are occupied by $K^+$ ions with a probability of 1/2.[35–37] For this reason, the ion channel was assumed to be populated by two $K^+$ ions in average. This discovery indicated the existence of a structural selectivity element. Revelation of the KcsA structure motivated the first ion selectivity hypothesis based on the rigid filter geometry. It assumed the carbonyl oxygens to function as a surrogate for the water molecules of an ions hydration shell.[8] According to the KcsA structure, the filter provided an ideal distance for the coordination of $K^+$ with an ion radius of 1.3 Å, whereas the same geometry would be less favorable for the coordination of the smaller $Na^+$ with the radius of 0.9 Å.[8,35,38] In agreement with these investigations the $K^+$ over $Na^+$ selectivity could be explained by the "snug fit" of potassium ions inside the binding sites. In consequence, selectivity was linked to the provided filter geometry only. In spite of the flexible nature of proteins, the "snug fit" theory required necessarily a precise positioning of the filter backbone carbonyl groups on a sub-Ångström level, which could be provided by a rigid structure only.

Due to the known spatial conformation of KcsA, computational methods and analysis became of more importance, as they can characterize experimentally mostly inaccessible energetic details. Computational experiments allowed to tackle the thermodynamic and kinetic contributions to ion selectivity seperatly.[39] A feasible technique is the molecular dynamics (MD) simulation, which allows to study the motions of channels on nano- to microsecond time scales.[40–42] By accessing the free energies for the ion transfer from bulk into the filter with  MD simulations, Roux et al. identified a preference for $K^+$ over $Na^+$ inside a flexible filter structure of KcsA on a thermodynamic

basis, which could be inverted by artificially turning off the electrostatic carbonyl-carbonyl interactions.[38] However the repelling effect of the carbonyl-carbonyl interactions had only little effect on the overall filter structure in comparison with the ion-carbonyl interaction energies of $K^+$ (150 kcal mol$^{-1}$) and $Na^+$ (170 kcal mol$^{-1}$). These results indicated carbonyl-carbonyl interactions to establish a pure "thermodynamic selectivity", while the average filter structure was controlled by the ion-carbonyl interaction. Roux et al. concluded that selectivity would not necessarily demand distinct topology on Ångström-scale in the filter as required by the "snug fit" model. Instead a flexible filter model was assumed to be more appropriate, considering the constant thermal fluctuations happening in proteins.[38,43–52] This flexible filter and selectivity model was supported by further MD simulations with different ion channels. However investigations of the KcsA filter and reduced structure models by Kast and Kloss revealed a strong competition between in plane $Na^+$ with $K^+$ ions in binding sites to be necessary for ion selectivity.[53] This result argues for the importance of kinetic influences on the selectivity, due to the contribution of multiple ions. The identified ion selectivity in fixed structures by the calculations of Kast and Kloss do also query the necessity for an flexible filter as a requirement for selectivity.[53]

The possibilities of computational methods and the new view on ion selectivity led to the creation of reduced "toy system" by Noskov and Roux to investigate it in greater detail.[38] Thus free energy simulations were used to characterize model systems comprised of isolated binding sites as well as experiments using *N*-methylacetamide (NMA) as an peptide mimetic to study ion coordination in comparison to their situation in the filter.[38] Their results support the thermodynamic selectivity of the filter and revealed eight carbonyls to be mandatory for a $K^+$ over $Na^+$ selectivity.[38] However intensive theoretical studies of the thermodynamic $K^+$ over $Na^+$ selectivity in the cyclic depsipeptid Valinomycin by Rempe et al. revealed an intercationic selectivity optimum in this ionophore, establishing ion coordination by six carbonyl atoms.[54] Additionally provided coordination partners like water molecules had a destabilizing effect on the coordination and diminished thereby the selectivity.[54]

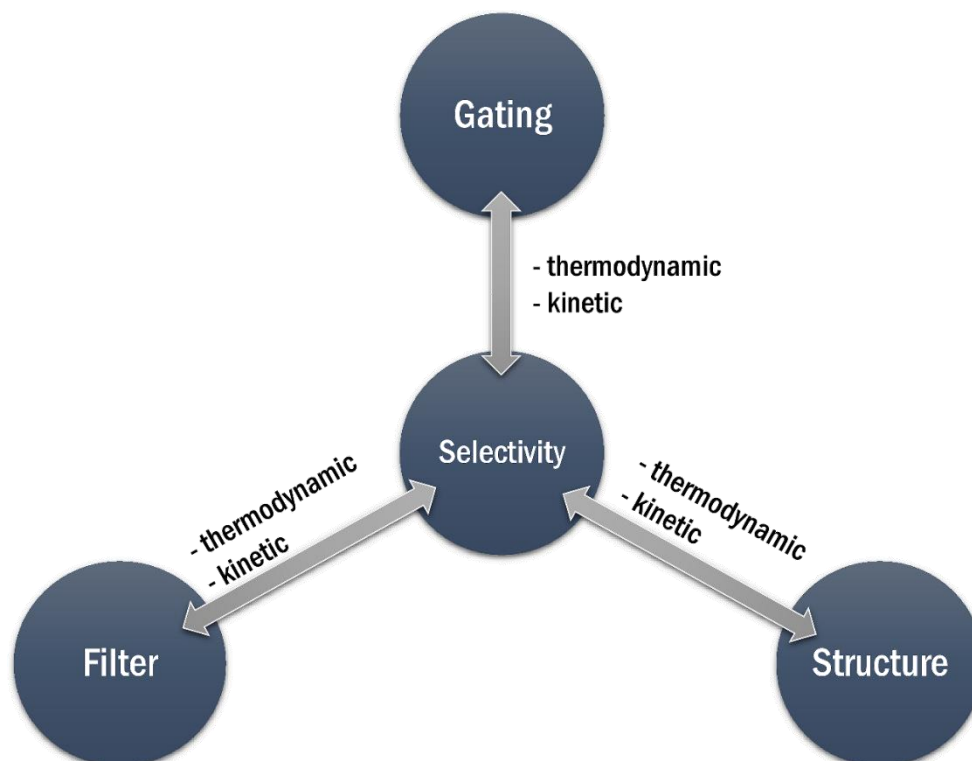Connected to the selectivity, the ion permeation process through the filter by estimation of the free energy, became also a focus of research in addition to further exploration of structure-selectivity relations. Investigation of the energy barriers between separate filter binding sites of KcsA revealed only insignificant barriers, which in principle allow for smooth transitions of ions between

them.[43,55,56] This picture of ion transfer was comprehensible considering the requirement to stabilize ions inside the channel at binding sites and at the same time permit a further propagation.[43] However computational investigations revealed suitable binding sites also for $Na^+$ in between the carbonyl cages.[53,57] Propagation of ions through the filter was assumed to occur in "single file", based on observations in early electrophysiological experiments and the confirmation of the KcsA filter population itself.[15,20,35,53] This process could finally be observed directly in MD simulations.[56,58–60] Particularly the filter was occupied only by two $K^+$ ions at the time, which were alternated by water molecules. A third ion entering the filter initiated the single file transfer of the two residing ions inside the filter. This mechanism was termed the "smooth knock on" and was widely accepted. Results of DeGroot et al. questioned this water-ion single filing mechanism by identification of direct ion-ion interactions that propagate the ion permeation.[61] However a "hard knock on" mechanism, assuming a filter structure populated with 3 $K^+$ ions pushed by a fourth, is recently under discussion.[62]

Notably free energy calculations for single ions did deliberately neglect the kinetic aspects occurring inside the filter.[43,57,63] In consequence, investigations of the free energy surfaces of multiple ions were conducted to estimate the influence of kinetic aspects.[56,57,64,65] This results showed that kinetic contributions play also a role in ion selectivity in addition to the previously described thermodynamic aspects.[57]

To gain a deeper understanding of ion selectivity and the gating process non-biological pores, like single walled carbon nanotubes (SWCNT), synthetic pores or technically created etched polyethylene terephthalate (PET) pores were scrutinized as mimetics for biological pores.[66,67] These differ from their biological analogues, as they can provide ion selectivity without having filter elements. Computational investigations by Corry et al. showed that water and ion selectivity is an intrinsic and radius dependent feature of SWCNT (see chapter 2.3 and 5.0 for details).[68] In addition, synthetic hydrophobic PET pores with a radius of 20 Å permitted the conduction of $K^+$ ions.[69] The measured ion currents where thereby depending on the applied pH value, emphasizing the complexity of ion selectivity in hydrophobic pores. Efforts in the field of synthetic chemistry have fruitfully established a portfolio of nanoscale molecules with ion channel properties. Amongst these is a recently synthesized self-assembling, cation selective, hydrophobic pore, which is investigated in detail in chapter 5 of this work.[6,70] The feature of hydrophobic cation or anion

selectivity can also be found in biological ligand gated ion channels (pLGIC).[71] Members of this family were investigated in respect to their gating properties. From these investigations originated the concept of "hydrophobic gating".[71–73] This concept assumes water to vaporize in narrow parts of the pore and create thereby energetic barriers due to "dewetting". However the origin of this effect is not fully understood and remains experimentally inaccessible as well as its occurrence in other channels is not fully clarified yet.[72]



**Figure 2.1.1**: Influences on selectivity. The scheme illustrates the dependency of ion selectivity on thermodynamic and kinetic aspects, which are connected to the process of gating, to structural changes and the ion filter itself.

Still computational and experimental studies of ion channel features pointed out the complexity of ion selectivity, ion permeation and gating mechanisms, by showing their dependency on each other. An example was given by the gating mechanism of the KcsA channel, called C-terminal gating, where changes in the filter geometry are supposed to happen due to conformational changes at the distant C-terminus.[63] In addition this example emphasizes the difficulty of an isolated view of the gating and selectivity process, as those might be coupled (Fig. 2.1.1). Furthermore protein-lipid interactions in the bacterial inward rectifier channel KirBac1.1 were revealed to perform conformational changes, which influence the gating and ion permeation process.[74] This emphasizes the importance of the often neglected membrane environment. Varying in their total size and

architecture, ion channels might have developed different mechanisms for gating, which makes the derivation of a general gating principle an unsolved task.[75] This is exemplified by the existing models of C-terminal, N-terminal gating as well as the occurring "bundle crossing" in members of the KirBac family.[76] Yet none of these known gating mechanisms is fully understood, especially in respect to their transitions between open, closed and inactive states.

Furthermore small viral potassium channels (Kcv) were revealed to perform full gating and selectivity functionality with a minimalistic set of amino acids, ruled out that gating, selectivity and structural interaction are coupled, even without the existence of huge cytosolic domains. [28,29,77–81]Amongst the members of the Kcv family, variability in even the highly conserved TVGYG filter sequence occurred with preserved potassium selectivity.[29]

Taken together, experimental and computational investigations were capable to establish models of ion selectivity, permeation and gating mechanisms in polar as well as hydrophobic biological, synthetic and artificial toy systems.[45,55,62,68,75,82–96] However after years of intense experimental and theoretical research of the structural, conformational and chemical natures of ion channels, no principles or patterns could be derived with global generality, explaining the remarkable ion selectivity features or the process of gating. In this work a selection of different channel types including (i) small viral potassium channels, (ii) hydrophobic synthetic pores and (iii) pentameric ligand gated ion channels (pLGIC) will be examined by MD simulations and the reference interaction site model (RISM) integral equation theory, to shed new light onto the dynamic, thermodynamic and kinetic aspects. The background of these channels and pore systems will be introduced in the following subchapters.

## 2.2 Tetrameric potassium ion channels

The basic structure of tetrameric $K^+$ channels is the canonical 2TM/P architecture, which is described by two transmembrane domains (TM) connected by a pore loop (P) (fig. 2.2.1).[8] This pore loop carries the amino acids forming the conserved signature sequence TXGXG (X = variable amino acid) of the essential selectivity filter.[35] Demonstrated in the $K^+$ inward rectifier KirBac1.1, potassium channels can possess proteinogenic receptor domains at their cytosolic termini.[97] An example for a 2TM/P architecture is the bacterial KcsA channel.[35] Modifications of this channel blueprint lead to three further classes, denoted as 6TM/P, 4TM/2P, 8TM/2P.[8] The predominant

6TM/P class is characterized by six preceding TM domains, enabling the channel to respond to changes in the membrane potential, leading to a voltage dependent gating, which is exemplified in the Shaker type channels.[31,32,96,98,99]
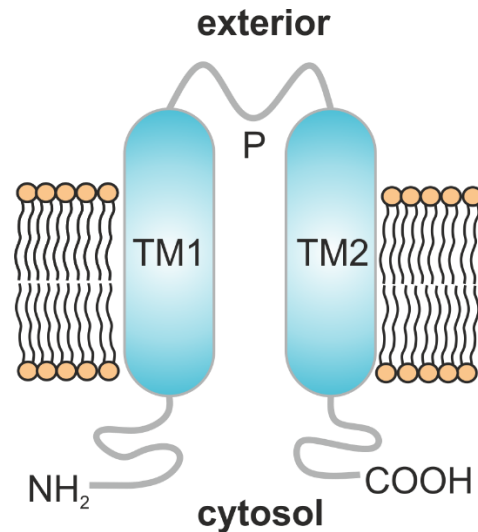


**Figure 2.2.1**: Illustration of the 2TM/P potassium channel architecture. A single monomer of a 2TM/P class K^{+} ion channels is represented, showing the two TM segments TM1 and TM2 connected by the pore loop P, which inherits the filter sequence motive. The monomer is embedded in a lipid bilayer (orange sphere with black tails) with its termini reaching into the cytosol. The graphic was adapted from Choe et al.[8]

The association into a fully functional tetrameric complex creates new elements besides the described secondary structure features. Complexation leads to the precise positioning of pore loop elements, finally creating the selectivity filter, which is characterized by distinct spatial conformation of the backbone oxygen atoms (Fig. 2.2.2).[8] Besides the filter, a water filled void is created by oligomerisation, the so called cavity that extends to the mouth region. According to the previous discussion, the mouth region undergoes conformational changes, which are supposed to be related to the context of gating.[75,76] Despite their known core architecture and their sequence homology, K^{+} channels exhibit a huge variety in their total size and in their realization of functional features.[1,8,77,80,100,101] The latter retards the understanding of their structure-function relation until today.

Double stranded DNA plant viruses (*Phycoviridae*), were identified to express small K^{+} channels comprised of 94 amino acids or even less.[1,28,29,77] Exhibiting full channel functionality while their structure is reduced to the maximum established them as model systems for experimental and theoretical investigations.[28,53,59,78–81,102,103]

17
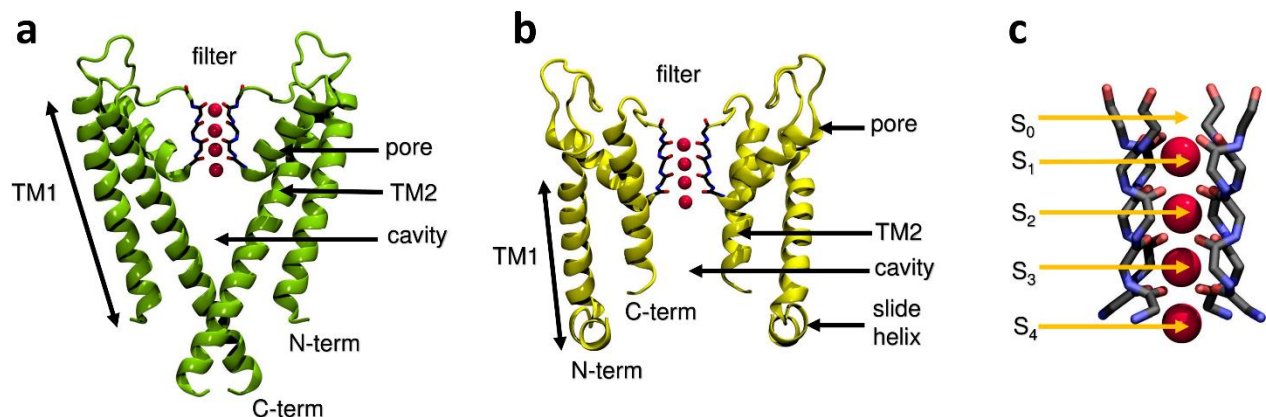
**Figure 2.2.2**: Tetrameric potassium channels. Cartoon representation of the bacterial $K^+$ channel KcsA (PDB code: 1K4C) (**a**) and the viral $K^+$ channel $Kcv_{PBCV-1}$ (**b**). For clarification only two of the four monomers are shown. The filter motive is illustrated as ball and sticks without hydrogen atoms. The backbone elements oxygen, nitrogen and carbon are colored in red, blue and black. A detailed excerpt of the filter structure is given in **c**. Populating potassium ions (dark red) are placed at the filter positions $S_1$-$S_4$ to exemplify possible population modes. The structure of $Kcv_{PBCV-1}$ (**b**) is based on a homology model of Tayefeh et al.[59]

In the biological context, *Phycoviridae* transfer these channels to the membrane of their primary host, which are different species of the salt and fresh water algae *Chlorella*, to disturb the local membrane potential and inject the virus DNA accompanied by its associated transcription machinery.[77,101,104] Amongst the exhibited variety of $K^+$ channels observed in the family of *Phycoviridae*, the $Kcv_{PBCV-1}$and its near relative $Kcv_{ATCV-1}$ are prominent examples, as their remarkably compact 2TM/P structure still endows aspects of gating and ion selectivity. While the $Kcv_{PBCV-1}$ channel was subject to intense experimental and theoretical studies, only little is known from the theoretical point of view about the later identified $Kcv_{ATCV-1}$. The $Kcv_{ATCV-1}$ channel, with a total of 82 amino acids per monomer is significantly reduced by 8 amino acids in comparison to the already small $Kcv_{PBCV-1}$ (94 amino acids). Furthermore the research on $Kcv_{PBCV-1}$ has already pointed out differences in its realization of gating and ion selectivity when compared to other bacterial channels, like the prominent KcsA channel.[83,102,103] Those aspects further encourages the research in the field of small potassium channels from plant viruses.[53,80] Therefore the $Kcv_{ATCV-1}$ channel was suggested as a valuable target for theoretical studies, characterizing its structure and thermodynamic aspects. The details of these studies are given in chapter 4.

Still it would be desirable to fully understand the structural and chemical details of the ion selectivity and the entangled process of gating, to enable the rational design of proteins with distinct

properties. These could find direct application in biosensors, water purification and in advance help to find new treatments for related illnesses.

In the presented work a focus was laid on two aspects, which were emphasized equally: (**i**) homology model creation for the closed state Kcv$_{\text{ATCV-1}}$ followed by an opening attempt of the ion channel; (**ii**) establishment of new thermodynamic tools and their application to tetrameric ion channels. Thereby a conceivable way to transfer a closed state modeled structure of the Kcv$_{\text{ATCV-1}}$ ion channel by combination of homology modelling (HM), molecular dynamics (MD) simulations, Gaussian network model (GNM) analysis and anisotropic network modelling (ANM) into an potentially open state, was demonstrated. Furthermore investigation with the reference interaction site model (RISM) as an application of the classical density functional theory results in a thorough thermodynamic analysis of the ion channel structure under physiological equilibrium conditions, characterizing the possible open and closed states.

## 2.3 Synthetic pores

The controlled creation of biological pores with distinct selectivity features on a sub-nanometer scale was a main goal for several technical as well as chemical approaches.[66,67,105–111] State of the art techniques like electron-beam lithography and etching approaches can produce pores with sizes of 1 or 2 nm.[85,110,112–116] An experimentally well characterized example for an etched pore is provided by the polyethylene terephthalate (PET) pores of Siwy et al., which are cation selective and pH sensitive.[113,117,118] However currently reached scales are just scratching the sub nanometer range, which is at most relevant for the modulation of ion selectivity.[6,115] A related problem occurs when it comes to controlled shapes.[114] On bigger scales, various controlled shapes could be realized, but on the sub nanometer scale this challenge remains unobtainable. Also most of the technical approaches work only with non-biological materials.

The domain of synthetic chemistry and biology tryies to create and design pores with distinct features, as they can modify already existing biological modules or use the wide spectrum of chemistry to design completely new scaffolds.[66,67] Successful mutation and modification of biological channels has already created pores which adapted a photo controlled gating mechanism.[119] Also exchange of sensing domains between existing channels and the formation of chimeras, by e.g. the assembly of tetrameric ion channels with unequal monomers, were successful

19

in exhibiting new ion channel characteristics.[66,67] While most of the biological approaches are primarily focused on modification of currently existing channels, chemically synthesized pores are not restricted to these scaffolds. In the last years, several chemical structures with cation or anion ion selectivity were revealed. Single walled carbon nanotubes (SWNT) are an example for such a promising target. SWNTs have been studied intensively by theoretical approaches, revealing their capability for selective water and ion transport as a function of artificial charges and SWNT radii.[68,85,87–91,111,115,120–127] Besides these successes of *in silico* SWNT studies, the spectrum for possible experimental modifications is still restricted and limits the use of SWNT as a suitable model system.[128,129] Their results will be discussed in further detail in chapter 3. In addition to the before mentioned approaches, a variety of computational models and methods were established for the description and scrutinizing of nanopore systems.[128–131] The diversity of these methods reaches from explicit coarse grained pore models up to completely implicit pores, defined by potentials only.[132–142]

Still a noteworthy accomplishment was reached by the group of Gong et al., which realized the synthesis of a chemical ring structure that self organizes into a multimeric, ion selective pore which adopts distinct open and closed states in electrophysiological experiments.[6,67] These pores are of great interest as they self-assemble into biological membranes *in vitro* and even more so create ion selectivity without any obvious selectivity domains, in contrast to the usually needed filter motif of tetrameric channels.[143] The key feature of selective ion permeation remains yet unsolved for rather simple pores as well as for more complex mulitmeric channels. For those reasons, this new pore is the main subject of theoretical investigations in chapter 5.

## 2.4  Pentameric ion channels

This chapter is subdivided into subsections explaining the biological and structural background of the pentameric membrane protein phospholamban (PLN) and the pentameric ligand gated ion channels (pLGIC). This shall provide an introduction to the class of biological hydrophobic ion channels, as a designated ion channel functionality will be the focus of chapters 6 and 7.

### 2.4.1 Phospholamban

Phospholamban is a small integral membrane protein, which is involved in the contractility of cardiac muscles by regulating the sarco/endoplasmic CaATPase (SERCA).[144] In its biological

context, the primary regulatory function of PLN is the inhibition of the calcium $Ca^{2+}$ transport of SERCA, which is modulated by a phosphorylation/dephosphorylated process of PLN at its N-terminal domains. SERCA inhibition is released by phosphorylation of PLN allowing for the pumping activity of $Ca^{2+}$.[144] The protein structure of PLN exists in an equilibrium between a monomeric (6KDa) and a pentameric form (30KDa).[145] Two common structure models of PLN namely *pinwheel* (PDB code: 1XNU) and *bellflower* (PDB code: 1ZLL) are known to form stable mono pentameric complexes in membranes (fig. 2.4.1).[146–148] While 1XNU is a multi-structure model from various sources, 1ZLL was originated by NMR experiments



**a**          **b**

*pinwheel*          *bellflower*
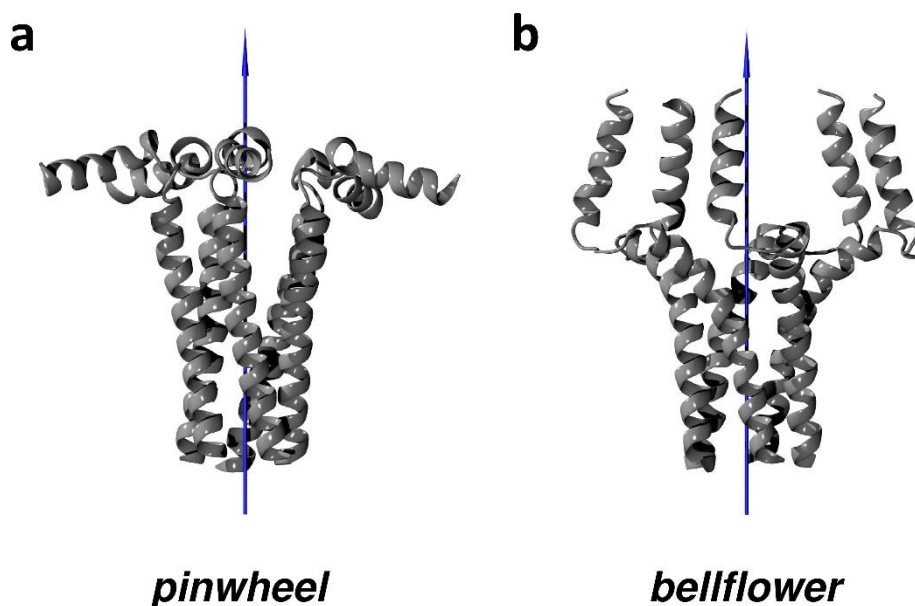
**Figure 2.4.1**: Different conformations of PLN. Cartoon representation of the pentameric complex of PLN in the *pinwheel* (PDB code: 1XNU) (**a**) and the *bellflower* (PDB code: 1ZLL) (**b**) conformation. The principle axis is indicated by a blue arrow.

In addition to its identified regulatory role as a monomer, the physiological role of the pentameric complex is still under discussion. One hypothesis suggests that the complex is a simple storage form for the monomers and thereby a possible control mechanism for the free PLN monomer concentration level. Also the PLN pentamer could be acting as an ion channel in order to keep the electro-neutrality of the sarcoplasmic reticulum (SR) intact.[147,149] The ion channel hypothesis is supported by previous experimental results and corresponding studies.[147,150–154] In addition a present hydrophobic ring motive inside the transmembrane segment (TM) of PLN could be an ion selective element as known from the similar pentameric ligand gated ion channels (pLGICs) (see following chapter).[73,94,155] However recent findings revealed phosphorylated PLN can adopt an

21

overall *pinwheel* like structure in lipid membranes, which is supposed to be incapable of any ion channel functionality.[156–158] Still PLN was object to several MD simulations, revealing a high flexibility of the cytosolic domain, which would finally allow a transition between the *bellflower* and the *pinwheel* structure.[159] It has been shown by MD simulations at pH 7 in 0.3 M KCl that this flexibility is even preserved in phosphorylated monomeric and pentameric PLN structures as well.[160] To shed light on the designated ion channel functionality of PLN, this channel is scrutinized in chapter 6 in comparison with the pLGICs, which are introduced in the following subchapter 2.4.2.

## 2.4.2 Pentameric ligand gated ion channels (pLGICs)

The super family of pLGICs is comprised of pentameric receptor ion channels which play a role in the regulation of excitatory signaling. All members have a huge cylindrical extracellular receptor domain as well as four transmembrane helices (M1-M4) per monomer, creating a pore lining inside the membrane.[161] The pLGIC family includes members with known cationic selective channel function like the nicotinic acetylcholin receptor (nAChR), the *Gloebacter violaceus* LIC (GLIC), the *Erwinia chysanthemi* LIC (ELIC) and the serotonin receptor channel 5-hydroxytryptamine type 3 (5-HT$_3$R), as well as the anion conductive pLGICs like glutamin-gated chloride channel α (GluCl), and the γ-aminobutyric acid receptor (GABA$_A$).[162–165] The focus in the following discussion is laid on 5-HT$_3$R and GluCl due to their influence on this work (chapter 6). The increase of recently revealed high resolution structures of pLGICs in their open and closed states allow a detailed reinvestigation of their pore structure.[161,162] In this context, negative charged rings formed by glutamic acid residues were identified in all cation selective channels (nAChR, GLIC, ELIC and 5-HT$_3$R), localized at the intra and extra cellular channel entrances (M2).[166] Flanking the pore entrances, these residues are supposed to discriminate anions over cations and also regulate the ion permeation in 5-HT$_3$R.[5,92,161] This was reasoned by an ion selectivity inversion experiment with 5-HT$_3$R by Gunthorpe.[167] Thereby an inversion of the cation selectivity in the 5-HT$_3$R channel could be realized by two mutations E1A, V13T and introduction of a new prolin residue adjacent to the E1A mutation, analog to previous experiments of Keramidas et al. with nAChR.[167,168] The core of the 5-HT$_3$R pentamer funnel is lined by uncharged amino acids, forming a restriction of 4.6 Å diameter at the position of Leu9, which exhibits a proposed ion selectivity function.[92,161] This restriction formed by Leu9 was called the hydrophobic girdle by White and Cohen and is also reasoned to be involved in the cation selectivity of nAChR.[169] The influence of restrictions on ion

selectivity was identified by a diminished cation selectivity in the E1A mutant of the GLIC channel, which is related to a restriction formed at the intra cellular mouth.[165] The influence of a negative charge at positon E1 in GLIC channels was revealed to play a role in ion selectivity, as Brownian dynamics (BD) simulations of Corry et al. observed an anion selectivity in calculations without charges for the residue E1.[170] In addition to its assumed functionality in the control of ion selectivity, BD and MD simulations estimated the influence of the hydrophobic girdle on the mechanism of gating.[171–173] These studies revealed a major influence of the hydrophobic girdle on the gating functionality.[71,172,174,175]

The glutamic acid residues present in cation selective pores at both entrances are substituted by positively charged residue like arginine at the equivalent positions.[92] In case of anion selective pLGICs an hydrophobic restriction, equivalent to the "girdle", was identified at the pore center and described to be an control element of selectivity and ion permeation.[162,176] In comparison to their cation selective relatives, significant differences arise in the pore radius before and after this hydrophobic restriction, as these regions are much wider in anion selective pLGICs like GluCl and GABA$_A$ in accordance to the currently available structures.[164,176] Experimental as well as *in silico* mutation of alanine residues against negatively charged glutamic acid residues in the hydrophobic restriction of GlyR inverted its anion selectivity, emphasizing its relation to ion selectivity.[168,171] The influence of the hydrophobic girdle as well as charge are investigated in the context of PLN in chapter 6.

# 3 Methods

## 3.1 Molecular dynamics (MD) simulations

MD simulations allow to calculate the time resolved progression of a system by sampling the phase space at distinct points.[177,178] The set of obtained configurations at distinct phase space points comprise the so called trajectory, which is the primary result of an MD simulation. Particles are typically treated in a classical way and parametrized by empirical force fields (FF), neglecting quantum mechanical electronic effects.[179,180]

In today's MD simulation codes the intermolecular potential $V_{\text{inter}}$ is a sum over all dispersion and electrostatic interactions, which are often described by the Lennard-Jones- ($V_{\text{LJ}}$) and Coulomb-potential ($V_{\text{elec}}$). $V_{\text{LJ}}$ is described by

$$V_{\text{LJ}}(\mathbf{r}_{ij}) = 4\varepsilon_{ij}\left(\left(\frac{\sigma_{ij}}{|\mathbf{r}_{ij}|}\right)^6 - \left(\frac{\sigma_{ij}}{|\mathbf{r}_{ij}|}\right)^{12}\right),$$

[3.1.1]

with the well depth $\varepsilon_{ij}$, the distance $|\mathbf{r}_{ij}|$ and the parameter $\sigma_{ij}$, which is connected to the minimum distance $\mathbf{r}_{ij,\text{min}}$ by $2^{1/6}\sigma_{ij} = \mathbf{r}_{ij,\text{min}}$. The Coulomb potential has the form of

$$V_{\text{elec}}(\mathbf{r}_{ij}) = \frac{1}{4\pi\varepsilon_0\varepsilon_r}\frac{q_i q_j}{|\mathbf{r}_{ij}|},$$

[3.1.2]

with the vacuum permittivity $\varepsilon_0$, the relative dielectric constant $\varepsilon_r$ (usually set to 1), the charges $q_i$ and $q_j$ the distance $|\mathbf{r}_{ij}|$ of particles $i$ and $j$. Electrostatic interactions are treated by the particle mesh Ewald method, a numerical implementation for the computation of the Ewald sum, which is a possible way to treat the long range nature of electrostatics efficiently.[181,182]

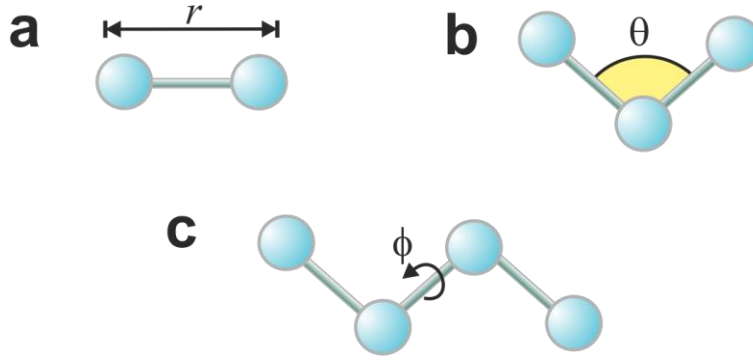The parameters $\sigma_{ij}$ and $\varepsilon_{ij}$ are calculated by using mixing rules of Lorentz-Berthelot

$$\sigma_{ij} = \frac{1}{2}(\sigma_{ii} + \sigma_{jj}),$$

[3.1.3]

$$\varepsilon_{ij} = \sqrt{(\varepsilon_{ii} + \varepsilon_{jj})}.$$

[3.1.4]

In accordance to both potentials $V_{\text{LJ}}$ and $V_{\text{elec}}$, the particles are commonly represented as penetrable spheres with a single point charge.

**Figure 3.1.1**: Illustration of force field potentials. Schematic depiction of an atomic bond (**a**), a corresponding bond angle (**b**) between three atoms and a dihedral angle (**c**) composed of four interaction sites. Atomic elements are symbolized by blue spheres, connected by bonds (gray sticks). The characteristic bond length $r$, the bond angle in $\theta$ and the dihedral angle $\phi$ are indicated.Graphic was adopted from Phillips et al.[183]

Molecular features of bending, stretching and kinking are described by formulation of intramolecular harmonic potentials (fig. 3.1.1) for bonds, angles and dihedrals, leading to an internal potential $V_{\text{intra}}$ comprised of $V_{\text{bond}}$, $V_{\text{angle}}$ and $V_{\text{dihedral}}$ of the form[183]

$$V_{\text{bond}} = \sum_{\text{bonds} b} \frac{1}{2} k_b^{\text{bonds}} (r_b^{\text{bonds}} - r_{0,b})^2 \,, \qquad [3.1.5]$$

$$V_{\text{angle}} = \sum_{\text{angle } a} \frac{1}{2} k_a^{\text{angle}} (\theta_a^{\text{angle}} - \theta_{0a})^2 \,, \qquad [3.1.6]$$

$$V_{\text{dihedral}} = \sum_{\text{dihedral } d} \begin{cases} k_d^{\text{dihedral}} [1 + \cos(n_d \phi_d - \kappa_d)], n \neq 0 \\ k_d^{\text{dihedral}} (0_d - \kappa_d)^2, n = 0 \end{cases} \,. \qquad [3.1.7]$$

The spring constant for a single bond $b$ with bond length $r_b$ or an bond angle $a$ with angle $\theta_a$ is denoted by $k_a$. For each dihedral $d$ the multiplicity is described by $n_d$, the current angle is given by $\phi_d$ and the corresponding equilibrium angle is denoted as $\kappa_d$.

The full potential $V(\mathbf{r}_i)$ permits the calculation of the force vector $\mathbf{F}_i$ for each particle $i$ using

$$\mathbf{F}_i = -\nabla V(\mathbf{r}_i)\,. \qquad [3.1.8]$$

25

With $\mathbf{F}_i$ the acceleration $\mathbf{a}_i$ estimated by Newton's second law of motion

$$\mathbf{a}_i = \frac{\mathbf{F}_i}{m_i} .$$

[3.1.9]

For the integration over time the configurations are stepwise approximated by the so called integrator algorithms. The Verlet integrator

$$\mathbf{r}_i(t + \delta t) = 2\mathbf{r}_i(t) + \mathbf{a}_i(t)\delta t^2 - \mathbf{r}_i(t - \delta t) ,$$

[3.1.10]

as one of the most widely used integrators, is based on a Taylor expansion around the current position $\mathbf{r}_i(t)$ obtaining an expression for the advancing step $\mathbf{r}_i(t+\delta t)$ and a step in the past $\mathbf{r}_i(t-\delta t)$

$$\mathbf{r}_i(t + \delta t) = \mathbf{r}_i(t) + \delta t \mathbf{v}_i(t) + \frac{1}{2}\mathbf{a}_i(t)\delta t^2 + \ldots$$

[3.1.11]

and

$$\mathbf{r}_i(t - \delta t) = \mathbf{r}_i(t) - \delta t \mathbf{v}_i(t) + \frac{1}{2}\mathbf{a}_i(t)\delta t^2 - \ldots .$$

[3.1.12]

Addition of equation 3.1.11 and 3.1.12 leads to the described Verlet algorithm 3.1.10. The velocities cancel in this approximation due to the opposite signs in eq. 3.1.11 and 3.1.12. The obtained Verlet algorithm (eq. 3.1.10) allows the approximation of the new position $\mathbf{r}_i(t+\delta t)$ by using information about the acceleration $\mathbf{a}_i$ , the old position $\mathbf{r}_i(t-\delta t)$ and the current position $\mathbf{r}_i(t)$. The acceleration $\mathbf{a}_i$ is derived from the potential $V(\mathrm{r}_i)$, which depends on several parameters (eq. 3.1.1-3.1.7). The required numerical parameters (see eq. 3.1.1-3.1.7) for the calculation of $V(\mathrm{r}_i)$ are stored in so called force fields (FF), which are parametrized by various approximations.

Besides the advantages of MD simulations, some limitations should be pointed out. Initially defined bonds, angles and dihedrals are immutable in the here presented form of MD simulations, due to the choice of a harmonic description of their potentials. In association charges are neither polarizable nor a function of the sphere surface, in the here presented approximations. Features of polarization and bond breaking are desirable, in particular for chemical reactions, but likewise, they are computationally time consuming and yet nonstandard in the field of protein simulations.

Another issue regards the parametrization of the peptide $\varphi$, $\psi$ angles, which is already difficult for simple poly-alanin-helices.[184] Force fields like CHARMM22* apply corrections, known as the cmap extension (indicated by the asterisk), to tackle these problems.[184–186] In addition to the correct description of the solute, respectively the protein, the parameters and models applied for the solvent are of importance, as most simulation settings consist of just a few solutes and many more solvent particles. Amongst the available explicit water models, TIP3P, TIP4P and "extended single point charge" (SPC/E) are currently the most prominent and commonly used.[187,188] While TIP3P and SPC/E models are described by three charge interaction sites, an additional fourth charge center is defined in TIP4P models. The corresponding force field parameters were adjusted to reproduce experimental densities, radial distribution functions (rdf), phase transitions and many more. But, comparison to experiments revealed that none of the mentioned models is capable to reflect all macroscopic properties of liquid water. While the SPC/E water model reproduces the dielectric constant and diffusion coefficient of water appropriately, oxygen-oxygen rdf functions are very well described by TIP4P, properly matching the first and second shoulder. Free energy simulations of TIP4P obtained a value of -6.1 $\pm$ 0.3 kcal mol$^{-1}$ for the solvation of a water molecule in water, which reproduces the experimental value of -6.3 kcal mol$^{-1}$.[184,189] The TIP3P model has not the quality of the TIP4P or SPC/E models, but it is still widely used due to its performance with protein force fields. As we used the TIP3P model in this work, complementary ion parameters of Beglov and Roux were chosen, due to their optimization for the CHARMM22* and CHARMM27 force fields (see *Appendix*).[190,191]

## 3.2 Global mode Analysis

The ability to describe and predict biological functionality on a structural basis is the most striking feature of NMA, which explains the increasing relevance over the last decade, especially in combination with coarse graining (CG) techniques. In the process of coarse graining, chemical details of the structure are neglected in consequence and reformulated into a mass-spring-network, where the network nodes are connected by springs, in analogy to harmonic potential functions. The validity of this so called elastic network model (ENM) approach was verified by many examples, demonstrating the insensitivity of global modes to chemical detail.[192–196] ENM takes advantage of the CG network representation (fig. 3.2.1), but neglects the detail of a full molecular potential, which accelerates the calculations in comparison to a full atomistic NMA model. Two prominent applications for the realization of ENM calculations are the Gaussian network model (GNM) and the anisotropic network model (ANM). According to its name GNM expects structural fluctuations to be distributed in a Gaussian shape around an equilibrium situation, while ANM analysis assumes harmonic fluctuation. In opposite to NMA techniques, GNM and ANM analysis define the given structure to be in a local minimum. The methodological details of GNM and ANM are presented following the publications of Bahar et al. and Karimi et al.[192,197–201] Both methods are used during the opening process of the KCV$_{ATCV-1}$ described in chapter 4.

## 3.2.1 GNM

Assuming the investigation of a protein structure, the nodes forming the network for the GNM analysis are commonly defined by the C$\alpha$ backbone positons. To consider the influence of non-boned interactions on the protein fluctuations, all interaction sites within a cutoff radius $r_c$ around a specific node position $\mathbf{R}_i$ are connected with it by harmonic springs. A schematic illustration of the network is given in figure 3.2.1. The connections between the total numbers of nodes $N$ are organized in an $N$ x $N$ Kirchhoff matrix of the form

$$\mathbf{\Gamma}_{ij} = \begin{cases} -1 \text{ if } \mathbf{s}_{ij} \leq r_c \\ 0 \text{ if } \mathbf{s}_{ij} > r_c \\ -\sum_{i \neq j}^{N} \mathbf{\Gamma}_{ij} \text{ if } \mathbf{\Gamma}_{ii} \end{cases}, \qquad \textbf{[3.2.1]}$$

with the nodes $i$, $j$ and the separation vectors $\mathbf{s}_{ij}$ between the instantaneous node positions $\mathbf{R}_i$ and $\mathbf{R}_j$. By the definition of 3.1.2 , the diagonal element $\Gamma_{ii}$ corresponds to the sum of contacts for node $\mathbf{R}_{ii}$, while the off-diagonal entries reflect the sole contacts contributing to $\Gamma_{ii}$.
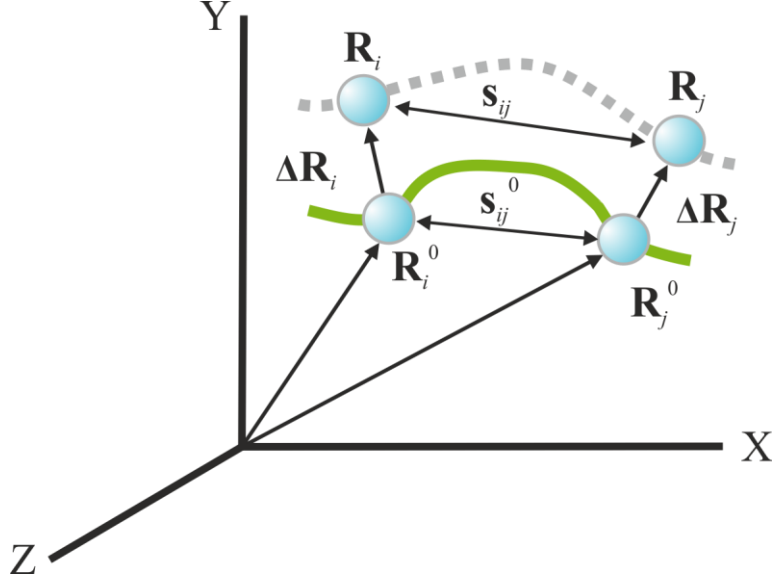


**Figure 3.2.1**: Schematic illustration of the structural changes. The displacement for two particles (blue spheres) with equilibrium positions $\mathbf{R}_i^0$ and $\mathbf{R}_j^0$ are described by the vectors $\Delta\mathbf{R}_i$ and $\Delta\mathbf{R}_j$, leading to the new positions $\mathbf{R}_i$ and $\mathbf{R}_j$. The connections $\mathbf{s}_{ij}^0$ (green, solid line) and $\mathbf{s}_{ij}$ (gray, dashed line) between the two particles represents the structural details. The graphic is reproduced from Bahar et al.[192]

The potential of the whole conformation can be defined as

$$V = \frac{\gamma}{2}\Delta\mathbf{R}^{\mathrm{T}}\Gamma\Delta\mathbf{R} \qquad\qquad \textbf{[3.2.2]}$$

with the $N$-dimensional vector $\Delta\mathbf{R}$ consisting of the single fluctuation vectors $\Delta\mathbf{R}_i$ and the force constant $\gamma$, which is usually the same for all springs in GNM. Equation 3.2.2 connects the configurational partition function $Z$ by random Gaussian network models to [202,203]

$$Z = K\int \exp(-\Delta\mathbf{R}^{\mathrm{T}}\Gamma\Delta\mathbf{R}), \qquad\qquad \textbf{[3.2.3]}$$

where $K$ is a constant. The mean correlation between two fluctuation vectors $\mathbf{R}_i$ and $\mathbf{R}_j$ for the nodes $i$ and $j$ can be derived from the configurational partition function by

$$\left\langle \Delta \mathbf{R}_i \cdot \Delta \mathbf{R}_j \right\rangle = \frac{1}{Z} \int \left( \Delta \mathbf{R}_i \cdot \Delta \mathbf{R}_j \right) \exp(-V / k_{\mathrm{B}} T) \, \mathrm{d}\Delta \mathbf{R}$$

$$= (3k_B T / \gamma_{ij}) \left[ \mathbf{\Gamma}^{-1} \right]_{ij}$$

[3.2.4]

with the temperature $T$, the Boltzmann constant $k_{\mathrm{B}}$, the force constant $\gamma_{ij}$ and the $ij$th element of the inverse Kirchhoff matrix $[\mathbf{\Gamma}^{-1}]_{ij}$. The mean fluctuation correlation $\langle \Delta \mathbf{R}_i \cdot \Delta \mathbf{R}_j \rangle$ for a single atom follows the form

$$\left\langle \Delta \mathbf{R}_i \cdot \Delta \mathbf{R}_j \right\rangle = \left\langle (\Delta R_i)^2 \right\rangle = (3k_B T / \gamma_i) \left[ \mathbf{\Gamma}^{-1} \right]_{ii}.$$

[3.2.5]

The mean fluctuation $\langle \Delta \mathbf{R}_i \cdot \Delta \mathbf{R}_j \rangle$ results from contributions of $N$-1 modes $k$ and can thereby be formulated as

$$\left\langle \Delta \mathbf{R}_i \cdot \Delta \mathbf{R}_j \right\rangle = \sum_{k=1}^{N-1} \left[ \Delta \mathbf{R}_i \cdot \Delta \mathbf{R}_j \right]_k.$$

[3.2.6]

The modes $k$ and its corresponding eigenvectors $\mathbf{u}_k$ and eigenvalues $\lambda_k$ can be accessed by decomposition of the invers Kirchhoff matrix

$$\mathbf{\Gamma}^{-1} = \sum_{k=2}^{N} \lambda_k^{-1} \mathbf{u}_k \mathbf{u}_k^{\mathrm{T}}.$$

[3.2.7]

The sum over $k$ starts at 2 as the first eigenvalue equals zero. As the eigenvalue $\lambda_k$ is related to the frequency and the eigenvector $\mathbf{u}_k$ describes the mode as a function of the residue fluctuation, equation 3.2.7 obtains the variability of each investigated residue without providing spatial information. This gap is closed by ANM analysis, which permits the derivation of directional information of the fluctuations.

## 3.2.2 ANM

In analogy to GNM, molecular structures are also coarse grained in ANM, formulating a network of nodes, which are interconnected by harmonic spring potentials of the form

$$V = \frac{\gamma_{ij}}{2} (s_{ij} - s_{ij}^0)^2 = \frac{\gamma_{ij}}{2} \left\{ \left[ (x_j - x_i)^2 + (y_j - y_i)^2 + (z_j - z_i)^2 \right]^{1/2} - s_{ij}^0 \right\}^2,$$

[3.2.8]

with the force constant $\gamma_{ij}$, the instantaneous and equilibrium distances $s_{ij}$ and $s_{ij}^0$ for the nodes $i$ and $j$ and their spatial distance components $x_j$-$x_i$, $y_j$-$y_i$ and $z_j$-$z_i$. For the first and second derivative of $V$ in dependency of the $x$ direction follows

$$\frac{\partial V}{\partial x_i} = -\frac{\partial V}{\partial x_j}$$
$$= -\gamma(x_j - x_i)(1 - s_{ij}0/s_{ij})$$
$$\frac{\partial^2 V}{\partial x_i^2} = \frac{\partial^2 V}{\partial x_j^2}$$
$$= \gamma\left(1 + s_{ij}^0(x_j - x_i)^2 / s_{ij}^3 - s_{ij}^0 / s_{ij}\right).$$

[**3.2.9**]

Defining the molecular structure as an equilibrium, expressed by $s_{ij} = s_{ij}^0$, equation 3.2.9 simplifies to

$$\frac{\partial V}{\partial x_i} = 0$$
$$\frac{\partial^2 V}{\partial x_i^2} = \gamma\left((x_j - x_i)^2 / s_{ij}^2\right).$$

[**3.2.10**]

For the second cross-derivation follows

$$\frac{\partial^2 V}{\partial x_i \partial y_j} = -\gamma\left((x_j - x_i)(y_j - y_i)/ s_{ij}^2\right).$$

[**3.2.11**]

The equivalent to the Kirchhoff matrix in GNM Analysis is the $N$ x $N$ Hessian matrix $\mathbf{H}$ in ANM analyses, taking the form of

$$\mathbf{H} = \begin{bmatrix} \mathbf{H}_{11} & \mathbf{H}_{12} & \cdots & \mathbf{H}_{1N} \\ \mathbf{H}_{21} & \mathbf{H}_{22} & & \vdots \\ \vdots & & \ddots & \\ \mathbf{H}_{N1} & \cdots & & \mathbf{H}_{NN} \end{bmatrix}.$$

[**3.2.12**]

The single elements $\mathbf{H}_{ij}$ are $3N$ x $3N$

$$\mathbf{H}_{ij} = \begin{bmatrix} \dfrac{\partial^2 V}{\partial x_i \partial x_j} & \dfrac{\partial^2 V}{\partial x_i \partial y_j} & \dfrac{\partial^2 V}{\partial x_i \partial z_j} \\[2ex] \dfrac{\partial^2 V}{\partial y_i \partial x_j} & \dfrac{\partial^2 V}{\partial y_i \partial y_j} & \dfrac{\partial^2 V}{\partial y_i \partial z_j} \\[2ex] \dfrac{\partial^2 V}{\partial z_i \partial x_j} & \dfrac{\partial^2 V}{\partial z_i \partial y_j} & \dfrac{\partial^2 V}{\partial z_i \partial z_j} \end{bmatrix}. \qquad \text{[3.2.13]}$$

The information about the frequencies and shapes of the superimposed modes are accessible by decomposition of $\mathbf{H}$

$$\mathbf{H} = \mathbf{U}\boldsymbol{\Lambda}\mathbf{U}^T. \qquad \text{[3.2.14]}$$

where $\boldsymbol{\Lambda}$ is an diagonal matrix containing the eigenvalues $\lambda_i$ and $\mathbf{U}$ is an orthogonal matrix whose columns are the eigenvectors $\mathbf{u}_i$. A total of $3N$ -6 non-zero eigenvalues and $3N$-6 eigenvectors can thereby be obtained, accessing the vibrational direction and amplitude of the different ANM modes.

In a concluding comparison GNM and ANM depend both on the quality of the initial structure, as an energetic minimum is assumed. The use of a uniform global spring constant $\gamma_{ij}$ might be questioned. Still the invariance between an individual $\gamma_{ij}$ and a single global $\gamma$ was verified by Tirion et al.[204] This result was confirmed by studies proofing that the protein shape controls predominantly the global modes.[193,205,206] Furthermore environmental effects, e.g. explicitly placed water molecules, were revealed to play a minor role for the ENM results.[192]

## 3.3 Reference interaction site model (RISM)

In contrast to full atomistic and explicit solvent models, RISM describes the solvent implicitly and with refined granularity via distribution functions. Thereby RISM calculations access the local density of aqueous solutions around a given solute (e.g. protein)

$$\rho_i(\mathbf{r}) = \rho_{i,\infty} g_i(\mathbf{r}), \qquad \text{[3.3.1]}$$

where $\rho_{i,\infty}$ is the density of the bulk phase and $g_i(\mathbf{r})$ represents the pair distribution function in three dimensional form. $g_i(\mathbf{r})$ is connected to the so-called total correlation function $h_i(\mathbf{r})$ by

$h_i(\mathbf{r}) = g_i(\mathbf{r}) - 1$. The total correlation function $h(\mathbf{r})$ is the key quantity obtained by solving the RISM equation in its three dimensional form (3D RISM)

$$\rho_i h_i(\mathbf{r}) = \sum_j c_j * \chi_{ij}(\mathbf{r}), \qquad [3.3.2]$$

with the solvent density $\rho$, the direct correlation function $c$ and the solvent susceptibility $\chi_{ij}$ for the interaction sites $i$ and all other interaction sites $j$ (also including $i$). Equation 3.3.3 can be solved by using a further relation between $c$ and $h$, which is provided in the form of the so-called closure

$$h_i(\mathbf{r}) = \exp\left(h_i(\mathbf{r}) - c_i(\mathbf{r}) - \beta u_i(\mathbf{r}) - B(\mathbf{r})\right) - 1, \qquad [3.3.3]$$

which connects the information of the local densities 3.3.1 with the solvent-solute interaction potential $u_i$ . The closure 3.3.3 includes also the bridge function, which is set to zero for the hypernetted chain closure (HNC) approximation

$$h_i(\mathbf{r}) = \exp\left(h_i(\mathbf{r}) - c_i(\mathbf{r}) - \beta u_i(\mathbf{r})\right) - 1. \qquad [3.3.4]$$

A Taylor series expansion of the HNC closure leads to the partial series expansion (PSE-$k$)[207]

$$h_i(\mathbf{r}) = \begin{cases} \exp\left(h_i(\mathbf{r}) - c_i(\mathbf{r}) - \beta u_i(\mathbf{r})\right) - 1 & \Leftrightarrow \quad h_i(\mathbf{r}) - c_i(\mathbf{r}) - \beta u_i(\mathbf{r}) \leq 0 \\ \sum_{a=0}^{k} \dfrac{\left(h_i(\mathbf{r}) - c_i(\mathbf{r}) - \beta u_i(\mathbf{r})\right)^a}{a!} & \Leftrightarrow \quad h_i(\mathbf{r}) - c_i(\mathbf{r}) - \beta u_i(\mathbf{r}) > 0 \end{cases} \qquad [3.3.5]$$

where $k$ defines the order of the expansion. The established system of equations is solved iteratively and gains thereby access to $g(\mathbf{r})$, which is related to the potential of mean force $w(\mathbf{r})$ by the reversible work theorem

$$g(\mathbf{r}) = \exp(-\beta w(\mathbf{r})). \qquad [3.3.6]$$

The quantity of $w(\mathbf{r})$ is the reversible work needed for moving one particle from infinity to a given distance. Using a constant particle number ($N$), temperature ($T$) and volume ($V$), $w(\mathbf{r})$ describes the Helmholtz free energy for the mentioned process.[208,209]

Chandler and Anderson introduced the intramolecular distribution function[210]

$$\omega(r_{\alpha\gamma}) = \frac{\delta(|r - l_{\alpha\gamma}|)}{4\pi l_{\alpha\gamma}^2} \qquad\qquad\text{[3.3.7]}$$

which describes a molecule by its internal distances $l_{\alpha\gamma}$ between the interaction sites $\alpha$ and $\gamma$, the distance $r$ and the Dirac delta function $\delta(x)$. The resulting functions of eq. 3.3.7 are organized in a matrix $\omega^v$. This formulation was used to describe the molecular geometry in the 1D reference interaction site model (1D RISM). Assuming the solute to be a part of the solvent, which is referred as the Percus trick, leads to the definition of the pure solvent total correlation function in 1D RISM-$vv$

$$\mathbf{h}^{vv} = \boldsymbol{\omega}^v * \mathbf{c}^{vv} * \boldsymbol{\omega}^v + \boldsymbol{\omega}^v * \mathbf{c}^{vv} * \boldsymbol{\rho}^v \mathbf{h}^{vv}, \qquad\qquad\text{[3.3.8]}$$

where * indicates a convolution. Eq. 3.3.8 can be solved iteratively in combination with a closure function, which further demands calculation of the potential $u_i$. Values for the solvent density $\boldsymbol{\rho}^v = (\rho_\gamma)^v$, the permittivity and the temperature must also be provided. To include further solutes e.g ions to the solvent, equation 3.3.8 can be extended to

$$\mathbf{h}^{uv} = \boldsymbol{\omega}^u * \mathbf{c}^{uv} * \boldsymbol{\omega}^v + \boldsymbol{\omega}^u * \mathbf{c}^{uv} * \boldsymbol{\rho}^v \mathbf{h}^{uv}, \qquad\qquad\text{[3.3.9]}$$

assuming an infinite dilution of the solute in the solvent. The solvent susceptibility matrix $\boldsymbol{\chi}$ for the solution of the 3D RISM equation 3.3.2 can be derived by

$$\boldsymbol{\chi}^{vv} = \boldsymbol{\omega}^v (1 + \boldsymbol{\rho}^v \mathbf{h}^{vv}). \qquad\qquad\text{[3.3.10]}$$

In case of an ion consisting solution the DRISM correction from Pettit and Perkyns must be applied for dielectric consistence.[211]

The applicability of RISM in the field of ion channel research was confirmed by examples of Kast et al. and Hirata et al., which scrutinized complete channel structures as well as toy systems with 3D RISM.[53,80,102,212,213] In spite of these examples it shall be pointed out, that the application of 3D RISM in combination with ion solutions are still non-standard today and not always successful. Ion

containing solutions were used in all parts of this work. As RISM calculations consider internal interactions of the solvent, possible cooperative effects can be observed. Concentration dependent changes can also be reflected in 3D RISM by calculation of corresponding solvent susceptibilities with 1D-*vv* RISM, which will play a role during the investigation of the synthetic pore in chapter 5.

## 3.4 Computation of thermodynamic quantities

Parts of the following approach are based on the previous work of Kloss et al.[214] Distribution functions $g(\mathbf{r})$, obtained from 3D RISM-*uv* calculations, contain the information about the distribution for a particle $i$ and thereby allow the formulation of the mass action law in form of

$$K_{c,i} = \frac{c_{\text{ch},i}}{c_{\text{bulk}i}} = \frac{N_{\text{ch},i}}{V_{\text{ch}}\rho_i} = V_{\text{ch}}^{-1} \int_{V_{\text{Ch}}} g_i^{uv}(\mathbf{r})\, d\mathbf{r} \qquad \text{[3.3.11]}$$

by integration over the spatial coordinates $\mathbf{r}$, the channel Volume $V_{\text{Ch}}$, the particle density $\rho_i$ and the concentrations in bulk $c_{\text{bulk}}$ and inside a channel $c_{\text{ch}}$. The particle number $N_{\text{ch},i}$ can be obtained by

$$N_{\text{ch},i} = \rho_i \int_{V_{\text{ch}}} g_i^{uv}(\mathbf{r})\, d\mathbf{r}\,. \qquad \text{[3.3.12]}$$

Assuming the activities as the values for the concentrations, $K_c$ corresponds to the partition coefficient.

$$\int_{V_{\text{ch}}} g_i^{uv}(\mathbf{r})\, d\mathbf{r} \approx \Delta x \Delta y \Delta z \sum_{z \in [z_{\min}, z_{\max}]} \sum \sum_{x,y \in Q(z)} g_i^{uv}(x, y, z) \qquad \text{[3.3.13]}$$

describes the evaluation of the integral, which is computed on a grid from the position $Z_{\min}$ to $Z_{\max}$. The accessible volume $V_{\text{Ch}}$ and the corresponding inner radius for each position $z$ is gained by sampling with the program HOLE. [215] The area corresponding to a given $z$ position is denoted as $Q(z)$ and is thereby connected to the free channel volume by

$$V_{\text{ch}} = \int_{z_{\min}}^{z_{\max}} dz \iint_{Q(z)} dx\, dy \approx \sum_{z \in [z_{\min}, z_{\max}]} \sum \sum_{x,y \in Q(z)} \Delta x \Delta y \Delta z\,. \qquad \text{[3.3.14]}$$

A local concentration $c_i(z)$ is connected to the partition coefficient $K_c$ by

$$K_{c,i} = (c_{\text{bulk}i} V_{\text{ch}})^{-1} \int_{z_{\text{min}}}^{z_{\text{max}}} c_i(z) Q(z) \, dz = V_{\text{ch}}^{-1} \int_{z_{\text{min}}}^{z_{\text{max}}} dz \iint_{Q(z)} dx \, dy \, g_i^{uv}(x,y,z) \,, \quad \textbf{[3.3.15]}$$

and can be evaluated as

$$c_i(z)/c_{\text{bulk}i} \approx Q^{-1}(z) \Delta x \Delta y \sum \sum_{x,y \in A(z)} g_i^{uv}(x,y,z) \,. \quad \textbf{[3.3.16]}$$

The pmf as a key quantity for estimating ion permeabilities to first order can be defined in various ways based on 3D RISM calculations. According to Hummer et al.[216] we compute the one-dimensional probability density along the $z$ axis by

$$p_i^{(1)}(z) = N_A c_i(z) Q(z) \quad \textbf{[3.3.17]}$$

and the corresponding pmf $w(z)$ normalized to a reference area at $z_0$ from

$$\exp[-\beta w_i(z)] = \frac{p_i^{(1)}(z)}{p_i^{(1)}(z_0)} \,, \quad \textbf{[3.3.18]}$$

where $\beta = 1/k_B T$ with the Boltzmann constant $k_B$ and temperature $T$,

$$w_i(z) = -\beta^{-1} \ln \frac{c_i(z)}{c_i(z_0)} - \beta^{-1} \ln \frac{Q(z)}{Q(z_0)} \,. \quad \textbf{[3.3.19]}$$

Equation 3.3.19 reflects a one dimensional pmf $w_i(z)$, which can be used to characterize energetic barriers exhibited during an ion transfer through a pore. Due to its origin from multi ionic calculation's, the pmf includes inter-ionic contributions which influence the exhibited energies. $w_i(z)$ was obtained by stepwise integration of the $g_i(\mathbf{r})$ function inside small cylindrical elements along a predefined path. In case of nanopore systems, this path was defined by sampling of the accessible surface area by the software HOLE.[215] Assuming an idealized cylindrical form the reference area $Q(z_0)$ was computed by $Q(z_0) = \pi \cdot r(z_0)^2$. This normalization is conversely discussed by others.[217] The normalization of $g_i(z)$ is necessary to be independent of the chosen total system volume, while $g(\mathbf{r})$ would elsewise not reach zero in the bulk phase in the limit of an infinite box.[5]

## 3.5 Conductance calculation

As the selectivity of ion channels can be characterized by their conductance values, a theoretical approach for calculation of those was established based on the mean field approach of Hummer et al.[5] According to them a conductance $\gamma_i$ for an ion species $i$ can be estimated by

$$\gamma = \frac{q_i^2 \rho_i Q(z_0)}{\int_{z1}^{z2} \exp w_i(z)/k_B T]/D_i(z)\,dz} , \qquad\qquad [\textbf{3.3.20}]$$

with the ion specific diffusion coefficient $D(z)$, the bulk density $\rho$ the ionic charge $q$, temperature $T$, the reference area $Q(z_0)$ at the cartesian position $z$ and the Boltzmann constant $k_B$.[5] Equation 3.3.20 therefore allows the theoretical calculation of ion transport through pores with certain properties. The calculated ion conductances correspond to an external potential of zero and are interpreted as a first order perturbation, due to the derivation of eq. 3.3.20 from linear response theory. A requirement for the correct calculation of conductances with equation 3.3.20 is therefore, that ion transitions occur independent from others. Considering the "single file" mechanism in tetrameric potassium channels, eq. 3.3.20 could not be applied to them. For those reasons eq. 3.3.20 will be used in this work to investigate hydrophobic pore systems. A constant $D(z)$ value was used for the theoretical calculation of ion conductances, as changes in $D(z)$ remain experimentally inaccessible (see chapter 5 and 6).[218] To quantify the effect of an confined environment on $D(z)$, control calculations with spatial dependent diffusion coefficients are performed in chapter 6, by a Fick-Jacobs related approach of Rubi and Reguera.[219]

# 4   The plant virus potassium ion channel Kcv$_{ATCV-1}$

## 4.1  Introduction

To shed light onto the functionality of hydrophilic ion channels, potassium channels comprised only of a minimalistic aa set are exclusively investigated. These were identified and studied in dsDNA plant viruses of the family *Phycodnaviridae* of the genus *Chlorovirus*.[101] Hence those viruses infect different species of the fresh and salt water green algea *Chlorella* living predominantly symbiotic as *Zoochlorella*.[101] Among the smallest and most prominent K$^+$ channels with only 94 or rather 82 aa are those expressed by the *Paramecium bursaria* chlorella virus (Kcv$_{PBCV-1}$) or chlorella virus (Kcv$_{ATCV-1}$).[4,28,29] Reduced to the minimum, their ion selectivity and gating functionality was verified in various electrophysiological experiments.[28] In spite of their small size the Kcv$_{ATCV-1}$ differentiates not only by its vast open probability of 90 % from Kcv$_{PBCV-1}$ but also structurally by absence of a N-terminal slide helix.[28] Notably this slide helix modulates crucial conformational changes related in the gating process due to formation of salt bridges in Kcv$_{PBCV-1}$.[102] So this difference is a demonstration for the variety realized in topology and functionality quiet in spite of their genetic similarity and their strong reduction. This statement still emphasizes the difficulty of understanding structure related ion selectivity. Yet this matter is still not finally clarified and thereby evokes the need for additional investigations and thus new analysis methods to gain further insights.

The huge structural diversity in the family of potassium ion channels exhibits a broad variety of architectures mediating the fulfillment of various tasks.[77] Still the above mentioned studies helped to identify common structural domains (see chapter 2.2), which comprise the potassium ion channels. Due to its minimalist nature, the Kcv$_{ATCV-1}$ channel is supposed to carry only essential domains to achieve its purpose.[80] In detail one monomer of this viral, hydrophilic channel is comprised of two transmembrane (TM) domains linked by a loop which is intersected by the filter domain with the amino acid consensus motive TVGTGD and a short pore helix (p-helix) in between (fig. 4.1a-c). While the outer TM domain (TM1) mediates mostly the anchoring by hydrophilic interactions, the water filled inner cavity region is formed by the topology of the inner TM helix (TM2).[80] The linking loop region allows the distinct formation of the carbonyl groups of the filter

amino acids, to create the filter positions $S_0$ - $S_4$ (fig. 4.1c), which was proven to be at most important for the selectivity functionality in previous work.[53]
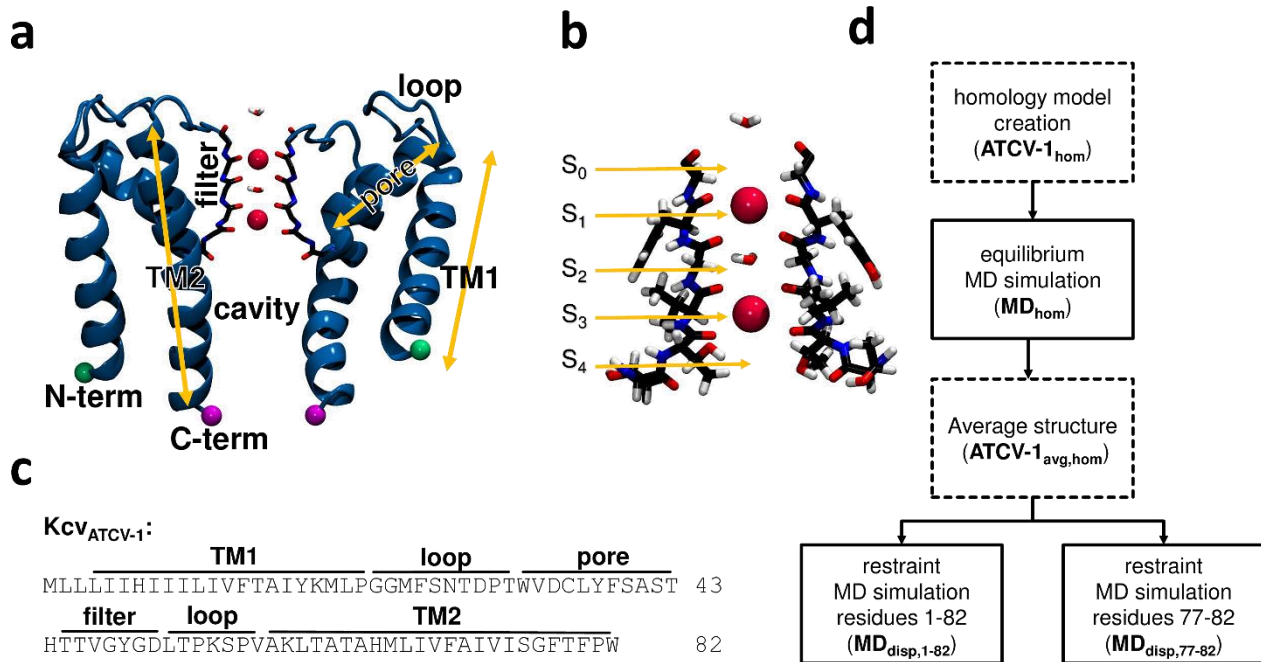


**Figure 4.1**: $Kcv_{ATCV-1}$ features and simulation overview diagram. Cartoon representation of the $Kcv_{ATCV-1}$ homology model structure (**a**). Only two monomers are shown for clarification. Different domains of TM1, TM2, filter, pore helix, cavity, loops as well as the N- (green) and C-termini (pink) are labeled. $K^+$ ions (red) are shown as spheres, while water is represented as licorice. The corresponding one letter sequence was marked alike (**b**). For clear assignment of the filter positions $S_0$-$S_4$ a detailed representation is given (**c**). An overview off the complete process is shown as a diagram (**d**). Subsequent stages are connected by arrows. MD simulation steps are distinguished from others by solid box lines. Structures are visualized with VMD-1.9.1.[220]

In case of the $Kcv_{ATCV-1}$ channel no experimental spatial structure is currently available. To overcome this hurdle, creation of homology models is a feasible approach. The applicability of homology models in combination with small viral potassium channels was confirmed by the work of Kast and Tayefeh, which created a model of the $KCV_{PBCV-1}$ channel on basis of the KirBac1.1 channel.[59,103] Following their approach the three dimensional (3D) structure for the $Kcv_{ATCV-1}$ channel was also created on basis of this bacterial inward rectifier. The created structure was used as the initial basis for investigation by MD simulations. Therefore a simulation system was created comprised of the tetrameric ion channel model embedded in a 1,2-dimyristoyl-*sn*-glycero-3-phosphocholine (DMPC) lipid double layer, dissolved in a 100 mM KCl solution in analogue to physiological conditions. Afterwards an averaged structure was derived based on this equilibrium simulation results and its properties were further scrutinized by GNM and ANM analysis alike to

previous work by others.[103,199,221] Identification of an possible corresponding opening ANM mode, enabled the formulation of appropriate restrains for MD simulations, leading to an most likely open state of the Kcv$_{ATCV-1}$. However the accessible time scales of MD simulations are limited. To close this gap and investigate thermodynamic properties under equilibrium conditions, we inspected averaged structures from the here conducted MD simulations with a classical density functional method, namely the reference interaction site model (RISM) in its three dimensional form (3D RISM), according to the chapters 3.3 to 3.5.[222]

A possible way to obtain a complementary characterization of thermodynamic properties is presented by application of the described 3D RISM methodology to MD based average structures. The advantage of this novel combination permits access to scrutinize ion channels under equilibrium conditions.

Application to our new homology model verifies the asset of this method as well as the possibility to obtain open averaged structures of the Kcv$_{ATCV-1}$ resulting from MD simulations. To verify the generality of this approach a representative selection of four tetrameric potassium channels is processed identically.

## 4.2  Methods

### 4.2.1 Homology model

As a required template structure the closed KirBac1.1 (pdb code: 1P7B) was chosen and processed in analogy to model creation of the Kcv$_{PBCV-1}$ by Tayefeh et al.[3] Deletion of the huge cytosolic domain resulted in a truncated KirBac1.1 tertiary structure sharing the same total amount of 82 aa as the Kcv$_{ATCV-1}$. The full KirBac1.1 tetramer was reconstructed based on one monomer by using VMD in version 1.9.1 and the rotation information included the PDB file.[220] In addition to the structural preparations, an amino acid alignment between the truncated template structure (neglecting the huge cytosolic domains) and the known Kcv$_{ATCV-1}$ sequence was prepared with CLUSTAL (version 2.1).[223] The sequence alignment between the Kcv$_{ATCV-1}$ and the ion channel part of the KirBac1.1 structure

```
KirBac    MDLYYWALKVSWPVFFASLAALFVVNNTLFALLYQLGDAPIANQSPPGFVGAFFFSVETL        60
ATCV-1    -------------MLLLIIHIIILI---VFTAIYKMLPGGMFSNTDPTWVDCLYFSASTH        44
                   :::   :  ::::   :*: :*::  . : .:: * :*...::**..*

KirBac               ATVGYGDMHPQTVYAHAIATLEIFVG----MSGIALST        94
ATCV-1               TTVGYGDLTPKSPVAKLTATAHMLIVFAIVISGFTFPW        82
                     :******: *:: *: ** .:::    :**:::.
```

obtained a total score of 21.95 %. This result was transformed into a required input alignment for the homology software (see *Appendix*). All homology models were created using the software MODELLER in version 9.10 with default optimization cycles.[224,225] Occurring huge gaps in the alignment introduced unreasoned helix breaks. To circumvent this issue, the residues 10 - 15 (aa sequence: SWPVF) and 75 - 82 (aa sequence ISGFTFPW) were restrained to an alpha helical structure during the model creation. The energetically most favored model out of ten was identified by DOPE score and post processed.[225] By addition of hydrogen atoms with CHARMM HBUILD all titrable residues remained in their standard protonation state equivalent to *p*H 7. C-terminal residues remained deprotonated while the N-terminus was protonated. Histidine residues were protonated at their delta nitrogen. The model was minimized in awareness of two ions and two water molecules, which were introduced into the filter positions of the model by modification of the available information from the KirBac1.1 structure.[59] As there are four potassium ions available inside the filter of the KirBac1.1 structure 1P7B, the two potassium ions at the $S_1$ and $S_3$ binding site were exchanged against water molecules therefore. To evaluate the created homology model PROCHECK was utilized in its online version (http://www.ebi.ac.uk/pdbsum/).[226] Hydrogen atoms were neglected to gain a meaningful result.

## 4.2.2 Equilibration MD simulation

The KirBac1.1 based homology model of the ATCV-1$_{hom}$ was introduced into a pre-equilibrated double bilayer membrane of DMPC utilizing the CHARMM-GUI tools.[227] Protein embedding was realized by formation of a superposition followed by deletion of colliding lipids with any protein residues within a sharp radius of 0.5 Å of the protein. The membrane was comprised of 192 lipids in total, distributed into 90 lipids inside the upper and 102 in the lower layer. Asymmetric distribution was forced by the overall conic geometry of the protein. A total of 16726 water molecules (TIP3P model) were added to solvate the system. Misplaced water inside the membrane was deleted. By random exchange of 60 water molecules 31 $Cl^-$ and 29 $K^+$ ions were introduced into the bulk solution creating a concentration of 100 mM KCl. However two potassium ions were already located inside the filter structure of ATCV-1$_{hom}$, sustaining the electro neutrality of the

whole system. The system dimensions reached 90 Å x 90 Å x 115 Å for the *x, y* and *z* dimensions of the core box. Periodic boundary conditions were used. Long electrostatics were treated with the particle mesh ewald algorithm on a grid of size 90 x 90 x 120 points using a spacing of 0.1 Å between grid points. The temperature was set to 320 K for production runs, controlled by a Langevin thermostat with a dumping coefficient of 1 ps$^{-1}$. A pressure of 1.01325 bar was controlled by a Langevin-Piston Nose-Hoover barostat. The CHARMM22* force field for proteins and CHARMM27 for lipids were used throughout the simulations (see *Appendix*) .[186,190] NAMD was used for all simulation.[183,228–230]

## 4.2.3 GNM/ANM analysis and correlation

The created average structure model ATCV-1$_{avg,hom}$ was superimposed by its filter backbone positions with the last frame of the MD simulation of the closed structure for later applicability. The structure was scrutinized in a GNM analysis using the Webserver of Bahar et al. with a cutoff of 10 Å.[194,199,231,232] Inspection of the calculated mean square fluctuation profiles revealed a possible opening transition due to significant hinge around Gly77 in mode 8, which was present in each monomer. The neglected spatial information of the GNM mode was completed by a subsequent ANM analysis.[194,199,231,232] Computation of the Euclidian norm

$$R_{k,\mathrm{ANM}} = \sqrt{u_k^x(i)^2 + u_k^y(i)^2 + u_k^z(i)^2} \qquad \textbf{[4.1]}$$

was conducted for the Eigenvectors *u*, where *k* describes the mode, *i* the residues and the *x,y* and *z* the coordinate dimension. The 20 ANM eigenvectors with the lowest frequency were evaluated and finally compared to the corresponding GNM norm of the selected leading mode

$$R_{k,\mathrm{GNM}} = \sqrt{u_k(i)^2} \qquad \textbf{[4.2]}$$

by calculation of the scalar product

$$\cos(\varphi) = \frac{R_{k,\mathrm{GNM}} \cdot R_{k,\mathrm{ANM}}}{\left|R_{k,\mathrm{GNM}}\right| \cdot \left|R_{k,\mathrm{ANM}}\right|} . \qquad \textbf{[4.3]}$$

The computed cosine of the angle $\varphi$ between the two vectors has possible values in the range of 0 and 1, where the latter was associated with a perfect match of the GNM and ANM vectors. Through

this correlation procedure a single ANM vector with an agreement of 90.75 % was identified (mode 4), describing the spatial transition process into a designated open state. This allowed the extraction of putative open state coordinates. Those positions were used in subsequent MD simulations to successively transfer the closed into the open state (see open mode MD simulation).

## 4.2.4 Restrained MD simulations

Initial starting point was the last frame of the previous equilibrium simulation. Cα positions of and identified opening mode structure ATCV-1$_{ANM}$ were used as target coordinates for opening attempt simulations. The restraints were applied by additional harmonic potentials with spring constants of 1 kcal mol$^{-1}$ to all concerned Cα atoms. In MD$_{disp,77-82}$ only Cα atoms of residues 77-82 were restrained, whereas all 82 residues were restrained in MD$_{disp,1-82}$. The following simulation steps were carried out alike in simulations with the restrained homology model, denoted by the subscript "disp" for displacement. A minimization of 1000 steps was followed by simulations with constant pressure, particle number and temperature (*NpT*) using the described additional restraining potentials for 181 ns in case of MD$_{disp,77-82}$ and 51 ns for MD$_{disp,1-82}$ (fig. 4.12). To enable the adaptation to conformational changes inside the filter, the two K$^+$ ions and their coordinated water were flexible. After this equilibration phase, unrestrained production runs for 80 ns were conducted for both approaches. Continuing from the last conformation of the unrestrained homology model simulation MD$_{hom}$ the system volume, temperature and pressure in MD$_{disp,77-82}$ and MD$_{disp,1-82}$ were kept identical to those of MD$_{hom}$.

## 4.2.5 MD Analysis

By post processing of the calculated trajectories, all systems were moved to the system origin by the geometric center of the protein. To avoid artifacts due to periodic boundary condition effects, displaced protein monomers were also moved back. The root mean square deviation (RMSD) was calculated with VMD-1.9.1 using only the backbone atoms for the initial alignment with a reference structure.[220] The first structure of the trajectory was thereby used as the reference. The STRIDE algorithm was applied in its implemented form in VMD-1.9.1 to estimate the degree of helicity of the ion channel.[220] *Z* positions over time are given in respect to the membrane position to avoid artificial drift translation effects. Therefore the *z* position of the membrane's geometric center was subtracted from the corresponding center position of the ion channel. Evaluation of the mouth radius occurred each 1 ns. The therefore extracted snapshots were superimposed with the filter

backbone atoms to a reference structure. Information about the radius were calculated by sampling with HOLE.[215] The minimum radius of ATCV-1$_{avg,hom}$ was identified at $z$ position -10.5 Å. Investigation of the current mouth radius were conducted accordingly at this reference position. For calculation of water molecules inside the cavity the trajectory was processed in 1 ns steps. All conformations were aligned by their filter motive. The water density was assessed in a volume of 18 x 18 x 16 Å$^3$ which considers the distance between the last filter residue THR45 and the C-terminal TRP82. An illustration of it is provided in the attachment (fig. A4.1)

## 4.2.6 3D RISM

*Structure preparation*

The protein structures of the potassium ion channels KcsA (PDB code 1K4C) and NaK (PDB code 2AHZ) were completed to symmetric tetrameric structures based on the information provided in the corresponding PDB file.[36,233] In case of KB-Kcv and Kcv$_{PBCV-1}$ refined homology models were used.[29,103] According to Tayefeh et al. the KB-KcV represents a truncated Kcv$_{PBCV-1}$ model on basis of the bacterial inward rectifier channel KirBac1.1.[59] Each structure was minimized in the presence of two potassium ions and water molecules using MODELLER V9.10.[224,225] Ions and water were deleted afterwards. All structures remained their titratable residues in the standard ionization state. Structures were aligned by their filter sequence with VMD V1.9.1.[220] For creation of corresponding protein structure files (PSF), the CHARMM22* force field for proteins and CHARMM27 for lipids were used (parameters are listed in *Appendix*).[186,190]

*Computational details for RISM*

To yield the solvent susceptibility $\chi$ individual 1D RISM calculations were carried out on a grid ranging from 5.98·10$^{-3}$ Å to 164.02 Å with a total of 512 points. Temperature was set to 298.15 K. The HNC approximation was used for the closure. Implicit solvents were calculated for 0.1 M KCl, NaCl and CsCl using the densities 0.0333295 Å$^{-3}$ (pure water), 0.033236 Å$^{-3}$ (KCl), 0.033270 Å$^{-3}$ (NaCl), 0.033236 Å$^{-3}$ (CsCl) according to a pressure of 1 bar. For water, NaCl and KCl solutions a permittivity of 78.4 was applied, while a permittivity of 75.8 was chosen for CsCl. 3D RISM calculations were done on a 160 x 160 x 160 grid for ATCV-1$_{Avg,Closed}$, ATCV-1$_{Avg,1-82}$ and ATCV-1$_{Avg,77-82}$ (table 4.1), while the bigger channels of KcsA, KB-Kcv, NaK and Kcv$_{PBCV-1}$ were computed on 200 x 200 x 200 grid points (table 4.1). A grid point distance of 0.6 Å was chosen throughout all calculations. The partial series expansion (PSE) of order 4 was applied for all

3D RISM calculations. Atom parameters were taken from the CHARMM22* force field (see *Appendix*).[186,190]

**Table 4.1**: System and analysis overview for 3D RISM calculations

| Ion channel | grid dimension $(x,y,z)$ | grid space $(x,y,z)$ | closure | lower border | upper border | $V_{Ch}$ Å³ |
|---|---|---|---|---|---|---|
| ATCV-1$_{Avg,Closed}$ | 160 x 160 x 160 | 0.6 Å | PSE-4 | -26.7 | 27.9 | 4165.4 |
| ATCV-1$_{Avg,1-82}$ | 160 x 160 x 160 | 0.6 Å | PSE-4 | -24.3 | 27.9 | 3493.5 |
| ATCV-1$_{Avg,77-82}$ | 160 x 160 x 160 | 0.6 Å | PSE-4 | -26.7 | 27.9 | 3147.5 |
| NaK | 200 x 200 x 200 | 0.6 Å | PSE-4 | -21.3 | 28.5 | 1622.8 |
| KcsA | 200 x 200 x 200 | 0.6 Å | PSE-4 | -33.9 | 25.5 | 1789.4 |
| KB-KcV | 200 x 200 x 200 | 0.6 Å | PSE-4 | -29.7 | 24.9 | 3051.7 |
| KcV | 200 x 200 x 200 | 0.6 Å | PSE-4 | -29.1 | 29.7 | 6872.0 |

$x,y,z$ identifies spatial grid coordinates.
lower and upper border designate the $z$ position used for the calculation of $K_c$ and $Q_0(z)$.
The accessible volume between the lower and upper border is denoted by $V_{Ch}$.

## 4.3  Results

## 4.3.1 Model creation

Due to the absence of an available three dimensional configuration for the Kcv$_{ATCV-1}$ structure, a homology model was created using the satisfaction of spatial restraints method implemented in the software MODELLER (see *methods*).[224,225] However the creation of a homology model requires a template structure of known configuration. Yet neither crystal nor NMR structures of comparable viral potassium ion channel proteins are available. In case of the Kcv$_{ATCV-1}$ homologue Kcv$_{PBCV-1}$ the closed structure of the KirBac1.1 channel was a suitable template for the successful model creation.[59] Therefore KirBac1.1 was considered as a possible template for the Kcv$_{ATCV-1}$. Calculation of a local sequence alignment with *Blastp* between the KirBac1.1 and the Kcv$_{ATCV-1}$ revealed a total of 17 identical residues (see *Appendix*).[234] The overall agreement was estimated to be 54 %, which was considered to be appropriate enough for a homology template. While the KirBac1.1 was available in its closed state the gained model for the Kcv$_{ATCV-1}$ was considered to be initially in a closed state. The calculated homology model will be denoted as ATCV-1$_{hom}$ in the following.

## 4.3.2 Structure evaluation

Protein configurations created by homology modelling need to be reviewed appropriately. For this reason a variety of tools already exists.[225,226,235] However most of these programs are intended to be used in the context of soluble proteins. So their computed score is most likely obtained as a combination of results from different methods, including for e.g. hydrophobic surface criteria, which are not necessarily directly applicable to the here investigated transmembrane proteins. Nevertheless the accurate configuration of amino acid residues in transmembrane segments can be used as an indicator for a correct structure, especially those of the alpha helices. For this reason investigation by a Ramachandran plot (fig. 4.2) was selected as the most meaningful descriptor to assess the residue localization in the context of their secondary and tertiary structure. Investigation of the full tetramer revealed the reliability of the model by placing 321 of the 328 residues in the most favored and allowed regions. However in several monomers misplacement of LEU21, THR32 and VAL58 occurred. Still all of these three residues are placed at a helix-loop or loop-helix change. Nonetheless the correct placement of 321 residues supported the applicability of the here created model.
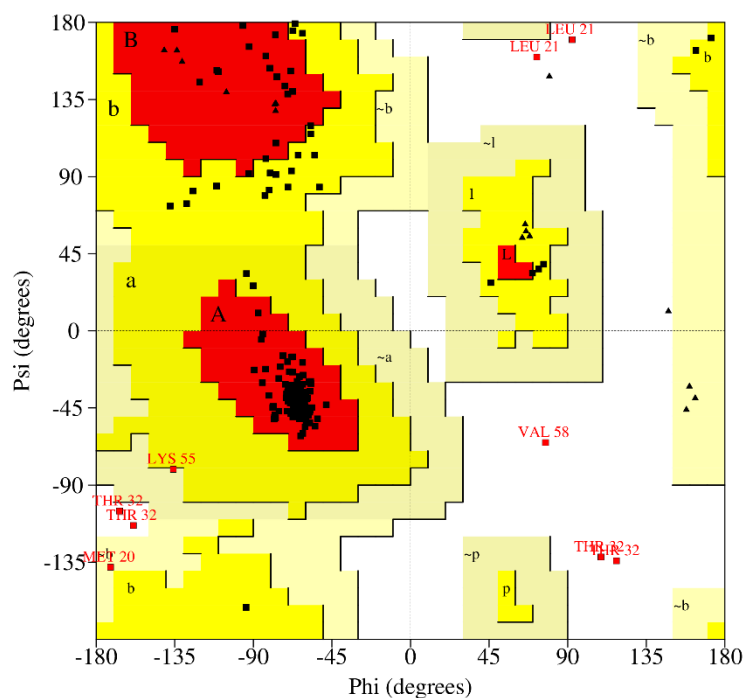


**Figure 4.2**: Ramachandran diagram of ATCV-1$_{hom.}$ Depiction of the $\psi$ and $\varphi$ angles of the backbone. Values are shown as black dots. Residue $\psi$ and $\varphi$ angles are labeled by black squares. Red and yellow colored areas mark regions of commonly found protein structure $\psi$ and $\varphi$ angle combinations, while white areas identify unusual ones. The latter are additionally highlighted by red font and red squares.

## 4.3.3 Simulation of the ATCV-1$_{hom}$ model

The homology model of ATCV-1$_{hom}$ was used as the basis for the assembly of the MD simulation system. The structure was embedded directly into a DMPC membrane, which was solvated with explicit water molecules and ions in a subsequent step, equivalent to a concentration of 100 mM KCl in total (see methods for details).[81,236]

For the MD simulation (MD$_{hom}$) of this system, established simulation schemes were adapted and realized stepwise.[40,42,237,238] To avoid initial clashes and misplaced geometries a minimization was performed for a total of 1000 steps. All residues corresponding to the filter (HTTVGTGD) as well as the associated ions and water molecules inside the filter were excluded from the minimization steps. Despite the fact that the here used bilayer of DMPC was already pre-equilibrated the insertion of the protein as well as the process of solvation in an ion solution introduces a huge disturbance. To diminish these effects, a simulation over 0.2 ns was conducted with constrained phospholipid head groups, protein backbone, complete filter structure (including the water and ions) and the solvent, to allow only the lipid tails and the protein residues to adapt to the temperature and to each other. A pressure of 1.01325 bar was introduced to the system at this point. To permit a slow adaptation, additional harmonic potentials were applied to all backbone atoms, which were stepwise slowly released over 0.2 ns. The filter motive as well as the corresponding water molecules and ions were highly restrained (10 kcal mol$^{-1}$ Å$^{-2}$) during this process, allowing only slight adaptions. The *NpT* simulation with a now fully unconstrained protein backbone of the ATCV-1$_{hom}$ was continued after these 0.2 ns for further 5.6 ns to allow additional adjustment. In the next 5 ns the complete filter with both water molecules and ions was set free. This completely flexible system was simulated for 74.63 ns, leading to a complete simulation time of 85.43 ns.
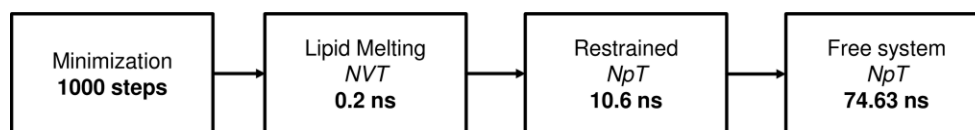


**Figure 4.3**: Equilibration simulation overview. Diagram of the homology model equilibrium simulation MD$_{hom.}$ The individual simulation steps are shown in rectangles. Related stages are connected by arrows, pointing in the following direction. Volume, temperature and pressure details are provided in the method section.

By visual control of the simulation results (fig. 4.4), the ion channel seems to tighten up around the mouth region, leading to an interrupted exchange between the bulk phase and the water enclosed

in the cavity. Interruption of the cavity-bulk transition foreshadows a nonconductive state of the structure.

## 25 ns                               85 ns
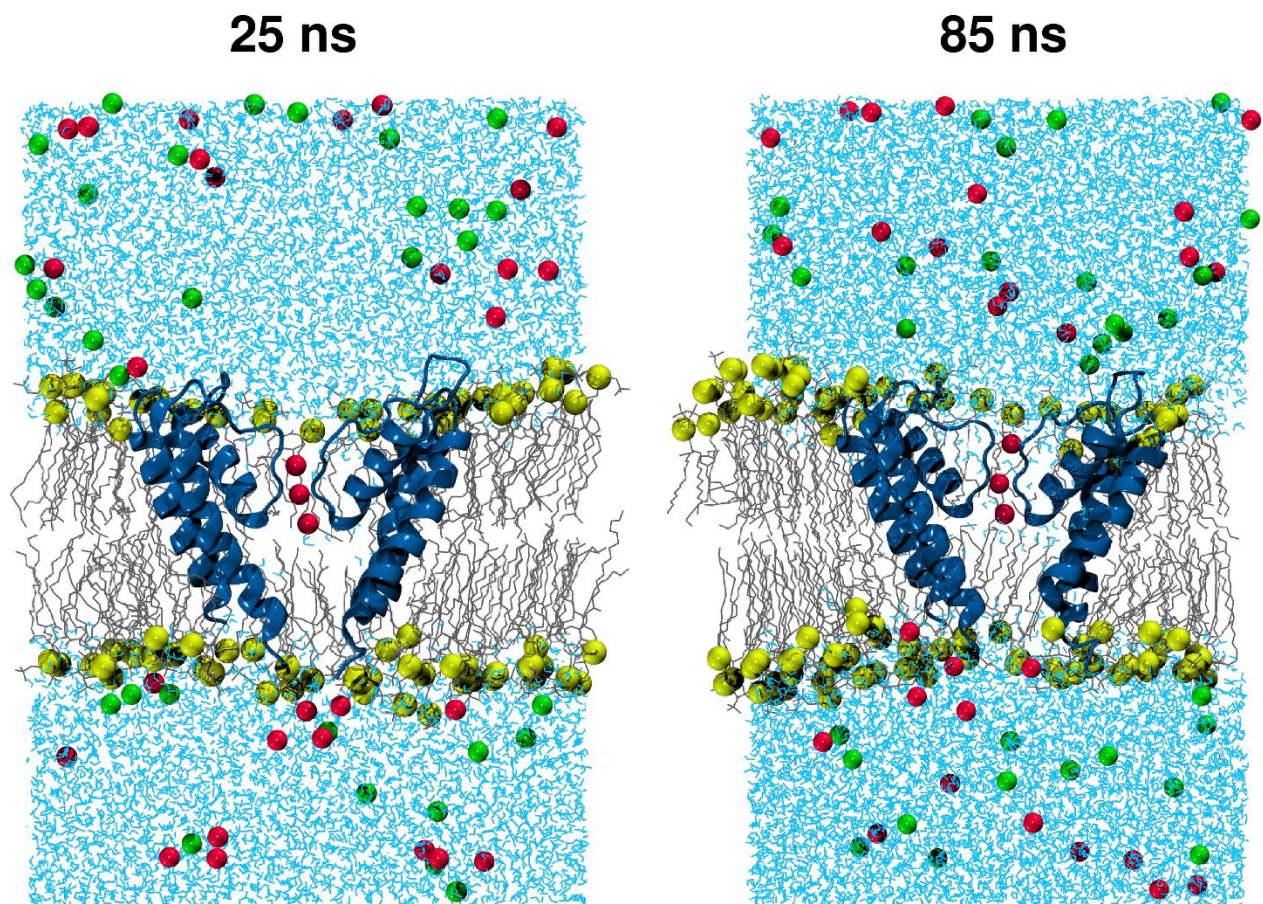


**Figure 4.4**: Illustration of MD$_{hom}$. Visualization of the difference between the MD$_{hom}$ simulation after 25 ns and 85 ns. The protein is shown in blue as cartoon, while the lipids are drawn as gray lines whitout hydrogen atoms. The phosphate of their headgroups is represented by yellow spheres. Water is illustrated as a blue lines, while potassium (red) and chloride (green) ions are drawn as spheres. Two monomers and several lipids are hidden for clarification.

The unrestrained simulation parts (74.63 ns) were scrutinized for the characterization of the ion channel behavior. As descriptor for the simulation stability the root mean square deviation (RMSD) was estimated over the last 74.63 ns (fig. 4.5). A first period of equilibration over the first 30 ns is revealed and characterized by soft and steady increase of the RMSD. All values fluctuate at a normal extent with no significant deviations. A plateau is reached after these first 30 ns indicating a stable conformation of the ion channel. Detailed investigation of the filter motive (aa 44-50), the inner pore helix (aa 33-43) and the transmembrane helices TM1 (aa 4-22) and TM2 (aa 59-82) revealed noteworthy changes in only one monomer. While the outer TM1, the filter region and the pore helix show a nearly indistinguishable progress of the RMSD for all four monomers, this single

monomer deviates after 20 ns significantly in its TM2 helix. The reason is a slight distortion of a single TM2 domain into the pore cavity (fig 4.5f). The mouth region area around the C-terminus is effected and tightened during this process. This conformational change is comprehensibly induced by the initially closed template structure of KirBac1.1 channel. However the individual movement of a single monomer was rather unpredicted.

Known opening mechanisms are usually described by a concerted movement of two or four monomers fulfilling similar bending, swivel or kinking motions. Such is the case for the bundle crossing in KirBac1.1 or the bending of the TM2 domain in KcsA.[83,238,239] Of course the here observed individual movement of a single monomer in ATCV-1$_{hom}$ might exclude an opening mechanism analogue to those of KcsA or KirBac1.1 for the here investigated ATCV-1$_{hom}$, but in contrast these mechanisms are possibly specific for their channel families and cannot be directly assigned to the Kcv$_{ATCV-1}$ channel family. Furthermore the concerted movement of four monomers has yet not been observed and is unlikely in comparison to the individual movement of a single monomer. Considering the strong diversity between the two close relatives Kcv$_{ATCV-1}$ and Kcv$_{PBCV-1}$ involvement of a novel and specific opening or gating mechanism should not be disregarded.

A further characterization of the protein stability was performed by the analysis of the helical fraction (fig. 4.6), obtaining a quantity for the characterization of the secondary structure stability of proteins in MD simulations.[59] In this context a rigid topology is described by a predominantly constant value. Such is the case for each of the here analyzed monomers of the ATCV-1$_{hom}$ model during the MD$_{hom}$, also corroborating their individual and structural stability.
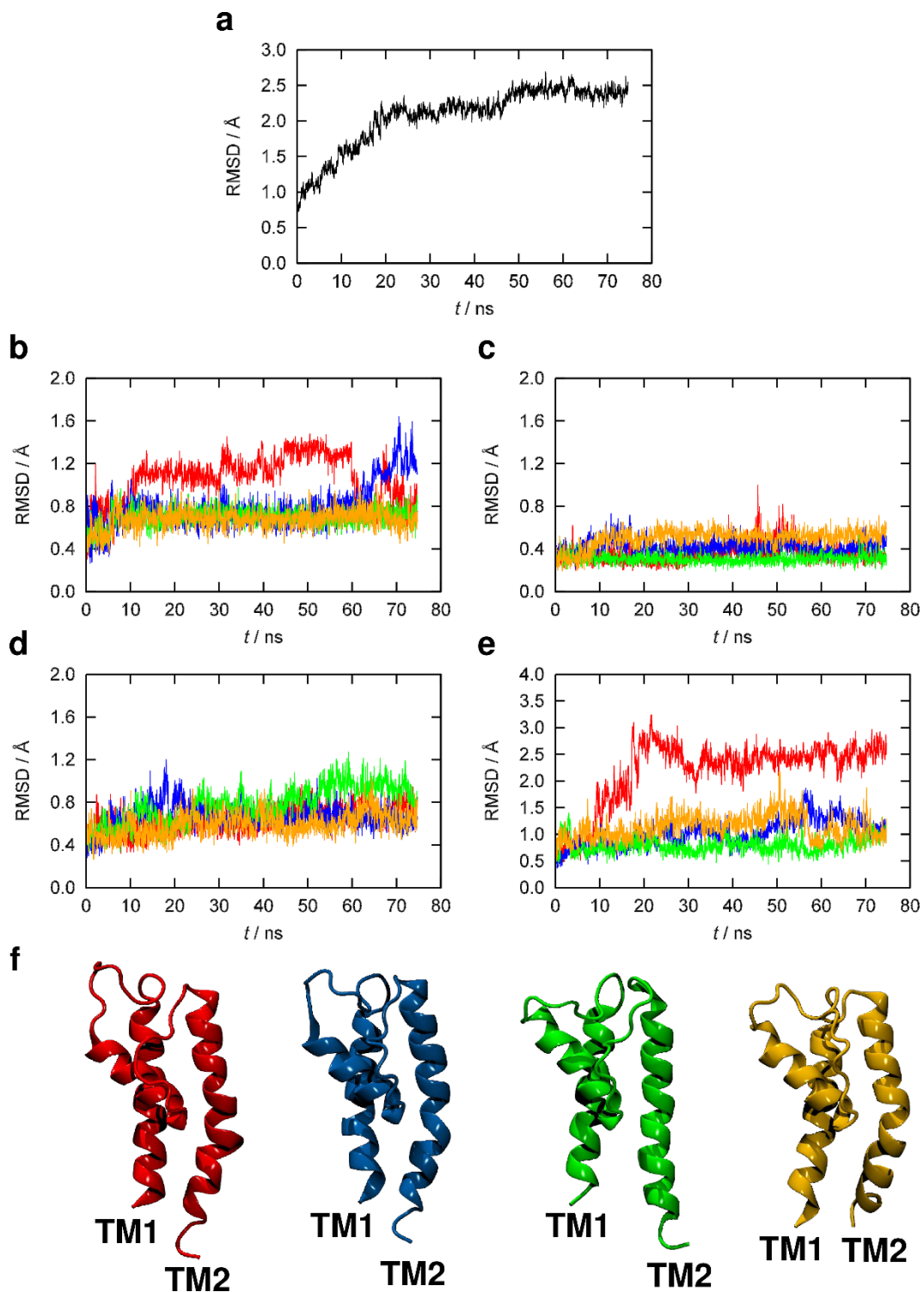
**Figure 4.5**: Representation of the computed RMSD. The RMSD value is shown for the complete tetramer (**a**). The RMSD values for the filter (**b**), the pore helix (**c**), TM1 (**d**), TM2 (**e**) of ATCV-1$_{hom}$ are shown for each individual monomer (monomer 1-4: blue, orange, brown, red). A cartoon representation of the ATCV-1$_{hom}$ monomer configurations after 25 ns are shown (**f**). Monomers colors are in correspondence with to those of the RMSD plots.

50
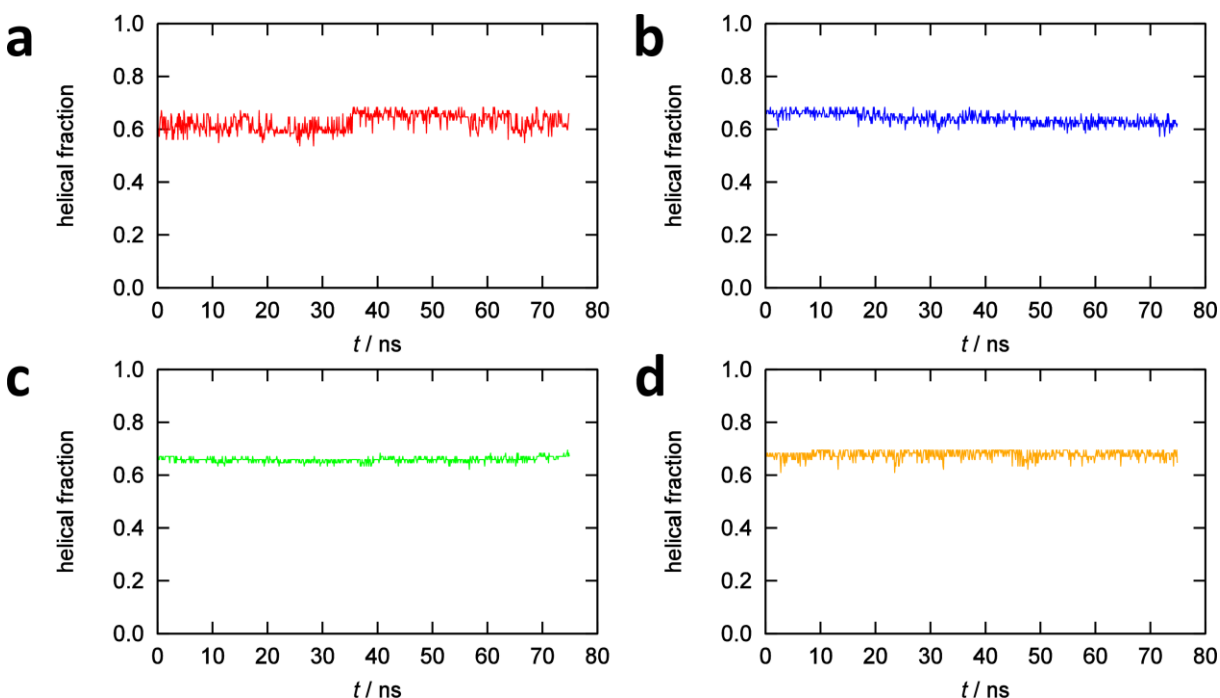
**Figure 4.6**: Helical fraction of ATCV-1$_{hom}$ in MD$_{hom}$. The time resolved progression of the total helical fraction is represented for each monomer independent. The four monomers are colored (first to last) by the colors red, blue, green and orange. Only data from free runs were scrutinized.

As stability of a transmembrane protein is directly connected to its membrane environment, a suitable incorporation and steady anchoring can be confirmed by its movement behavior along the membrane normal vector. To describe the vertical movement of the ATCV-1$_{hom}$ channel inside the DMPC membrane, the $z$ position of the protein was normalized to the geometric center of the membrane (see methods). In this context the results of the analysis corroborate a stable incorporation of the tetrameric complex as shown by small movements of the center inside the membrane (fig. 4.7a), whereas instability would be correlated with rapid fluctuations. The steady global behavior is elicited in detail by the associated stability of the four individual monomers as shown in fig. 4.7b. The entire results indicate a suitable incorporation of the ATCV-1$_{hom}$ model inside the DMPC membrane.
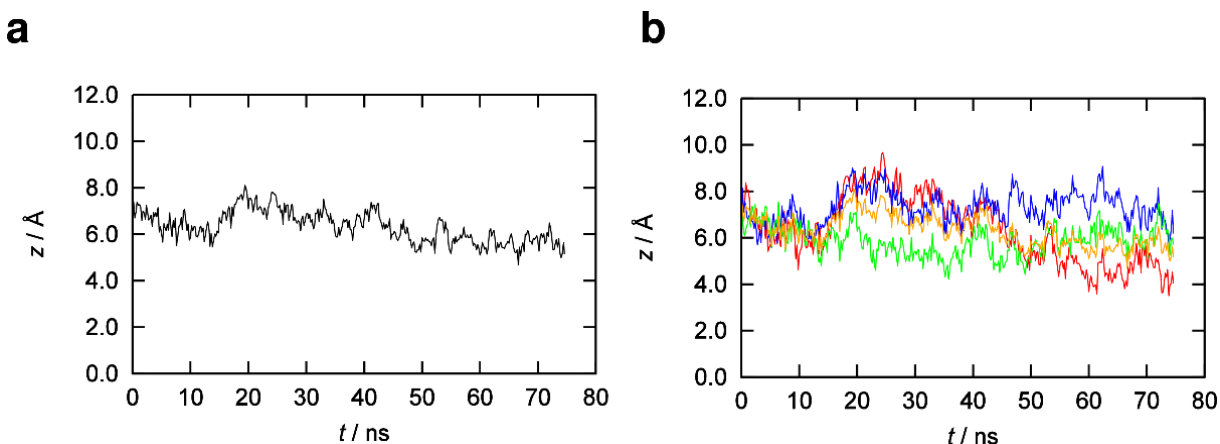
**Figure 4.7**: $z$ coordinate of the geometric center of the complete ATCV-1$_{hom}$ tetramer (**a**) and the depiction of the separate four monomers (**b**). Color code from monomer 1 to 4: red, blue, green, orange.

## 4.3.4 Creation of the average structure from MD simulation

The conducted MD simulation offered the opportunity to calculate an average structure model for the ATCV-1$_{hom}$ which in return creates a reliable mean over the dynamic. The creation of mean structures of homology model based simulations (last 74. 64 ns) seemed beneficial and was verified by previous work as well as by others.[59,240] To distinguish the averaged ATCV-1$_{hom}$ structure clearly from the initial homology model an additional subscript was added denoting the average model as ATCV-1$_{avg,hom}$. The creation of the average ATCV-1$_{avg,hom}$ structure utilized the already applied schedule for the Kcv$_{PBCV-1}$ and published by Tayefeh.[59] This method computes the mean distance of all heavy atoms over the simulation time and sets harmonic restraints for all Cα pair distances as well as for all other heavy atoms within a cutoff radius of 11 Å. For direct Cα - Cα interactions restraints of 10 kcal mol$^{-1}$ Å$^{-2}$ were applied, while a force constant of 0.1 kcal mol$^{-1}$ Å$^{-2}$ was used for all others. The estimated mean distances are used to reweight the initial harmonic restraints to consider the individual fluctuations occurring during the simulation. Refinement of the structure is achieved by a series of 100 steps steepest descent and 50 steps of adopted-basis Newton-Raphson minimizations and simulated annealing. Symmetrizing annealing procedures are used to find a local minimum of the structure.[103] By this process a rotationally symmetric, tetrameric ion channel structure was obtained, including the influence of its interactions with the environment. Also the thereby gained model is far from being a simple geometric mean. It also abolishes probable local disturbances in single monomers that exist only on a short timescale and vanish by this procedure.

## 4.3.5 Evaluation of the mean structure ATCV-1$_{avg,hom}$

An influential feature for the characteristics of ion transport and the channel state is the radius profile along its central axis. Radius profiles allow to identify steric impermeabilities and passable gates in dependency of a given structure. To analyze these features in the average structure ATCV-1$_{avg,hom}$ radius profiles were calculated (fig. 4.8a) as well as a Ramachandran plot (fig. 4.8a). The averaging process diminished the number of unfavorably residue confirmations, according to the results of the Ramachandran plot, with only THR32 as an significant outlier (fig. 4.8b). Regarding the open state, the radius around the mouth region is crucial for the ion exchange between cavity and bulk solution. Unsurprisingly the region around the filter residues is one of the most constricted parts localized between 2 to 15 Å (aa 64-50; TVGTGD) in the case of ATCV-1$_{avg,hom}$. Examination of the radius revealed a wider structure in comparison to the analogue KB-Kcv and Kcv$_{PBCV-1}$ channel (fig. 4.8a). Extending into the direction of the C-terminus the radius becomes wider forming the water filled cavity volume. The mouth region at a $z$ position of -20 Å (relative to the filter S$_4$ position) was identified with a mean radius of 4-5 Å, which is not highly constricted and still permeable for ions and water. By their influence on the local ion concentrations, exhibited constrictions influence the channel permittivity through formation of steric barriers.

To investigate these aspects in greater detail, 3D RISM calculations with 100 mM NaCl, KCl and CsCl in presence of ATCV-1$_{avg,hom}$ were conducted. Subsequent analysis yields the concentration distributions $c(z)$ at equilibrium (fig. 4.9). All concentrations were normalized to their bulk concentration $c_0$. An important point concerns the calculation of the concentration, which occurred only at positions of accessible channel volume generated by HOLE.[215] The algorithm was stopped if a radius greater than 15 Å was reached. Usually the concentrations at these points were still slightly different from the pure bulk phase due to their adjacency to the protein. This explains bulk values deviating from 1.0 at the borders. Inspection of the concentration profiles revealed an overall enrichment of all three cations Na$^+$, K$^+$ and Cs$^+$ while the anion Cl$^-$ was nearly completely depleted. In accordance to these 3D RISM results, the ATCV-1$_{avg,hom}$ structure is capable to select cations from anions. Among the intra cation concentration an enrichment order of Na$^+$ over K$^+$ to Cs$^+$ was obtained ranging from the mouth region up to the S$_4$ filter side.
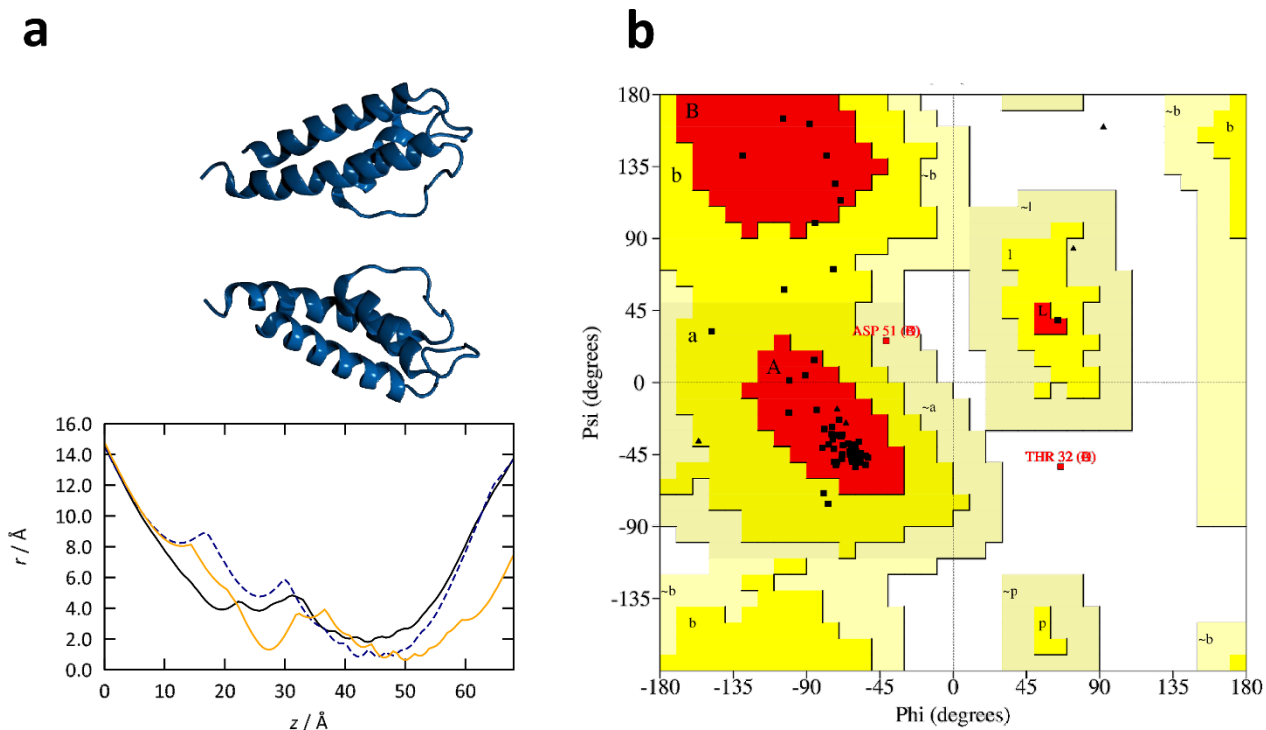
**Figure 4.8**: Radius profile and Ramachandran plot of ATCV-1$_{avg,hom}$. The radius profile (**a**) was calculated along the accessible central channel axis of the ATCV-1$_{avg,hom}$ (black line) as well as for related Kcv$_{PBCV-1}$ and the KB-Kcv (see next subchapter for details). An cartoon representation of ATCV-1$_{avg,hom}$ was aligned to the radius profile for structural assignment. The radius information was generated by HOLE.[215] The Ramachandran plot (**b**) for ATCV-1$_{avg,hom}$ was obtained in accordance to Figure 4.2.

Scrutinizing the concentration profile at the filter region reveals a tight but very distinct pattern, which can be related to the different binding positions created by the backbone. Further clear peaks in dependency of the ion species are recognized representing the individual binding affinities. The binding positions are formed by carbonyl and oxygen atoms of the backbone. Complexation of ions can occur in between the eight oxygen atoms or alternatively "in plane" with four oxygen atoms. Looking at the binding positions of $K^+$ and $Cs^+$ they populate the filter positons $S_1$ to $S_4$ in accordance with their corresponding enriched concentrations. The concentration peaks of $Cs^+$ and $K^+$ are localized at the same positions in ATCV-1$_{avg,hom}$, with a finally higher population of $K^+$ than $Cs^+$ at the binding site positions. This implicates a $Cs^+$ over $K^+$ selectivity which is also found in electrophysiological experiments. In contrast to $K^+$ and $Cs^+$ the cation with the smallest radius $Na^+$ populates the transitions, predominantly the positions in between $S_2$ and $S_3$. Such a behavior was already studied and described for a reduced filter motive of the tetratmeric potassium ion channel KcsA by Kloss and Kast.[53] At this point it should be noted, that in addition to the four filter binding sites a fifth concentration hotspot was revealed at the transition from $S_4$ to cavity at $z = 0$ Å. Beside

the strong accumulations inside the filter, an anticipated enrichment of the positively charged cations at the negatively charged C-terminus was identified at $z = -23$ Å. Besides the situation in the filter, $Cs^+$ is the most abundant ion in terms of concentrations, particularly in the cavity region. To investigate the ion selectivity in greater detail, the calculated concentration information were integrated to compute partition coefficients $K_c$. This procedure anticipates selectivity as an accumulation of ion concentrations. Thus a significant criteria for selectivity of an ion channel can be achieved by integration along the principle axis and weighting by the passed through volume. Referring to the structure of ATCV-$1_{avg,hom}$ $K_c$ values of 3.32, 3.75 and 3.78 were identified for $Na^+$, $K^+$ and $Cs^+$ instating a cation selectivity series identical with the previous concentration order. By this examination the meaning of $K_c$ as a quantity for selectivity was further verified. It further demonstrates the direct influence of the concentration distribution to the selectivity. In contrast to the cations, ATCV-$1_{avg,hom}$ was recognized to be nearly impermeable for the anion $Cl^-$ as shown by $K_c$ values of 0.67, 0.59, 0.57 for $Cl_{Na}$, $Cl_K$ and $Cl_{Cs}$ (corresponding cation as subscript). In addition these results reveal a slight counter ion dependency of the $Cl^-$ selectivity, further demonstrating that all interactions of solvent partners are considered. This is one of the advantages of the here applied 3D-RISM solvent model.
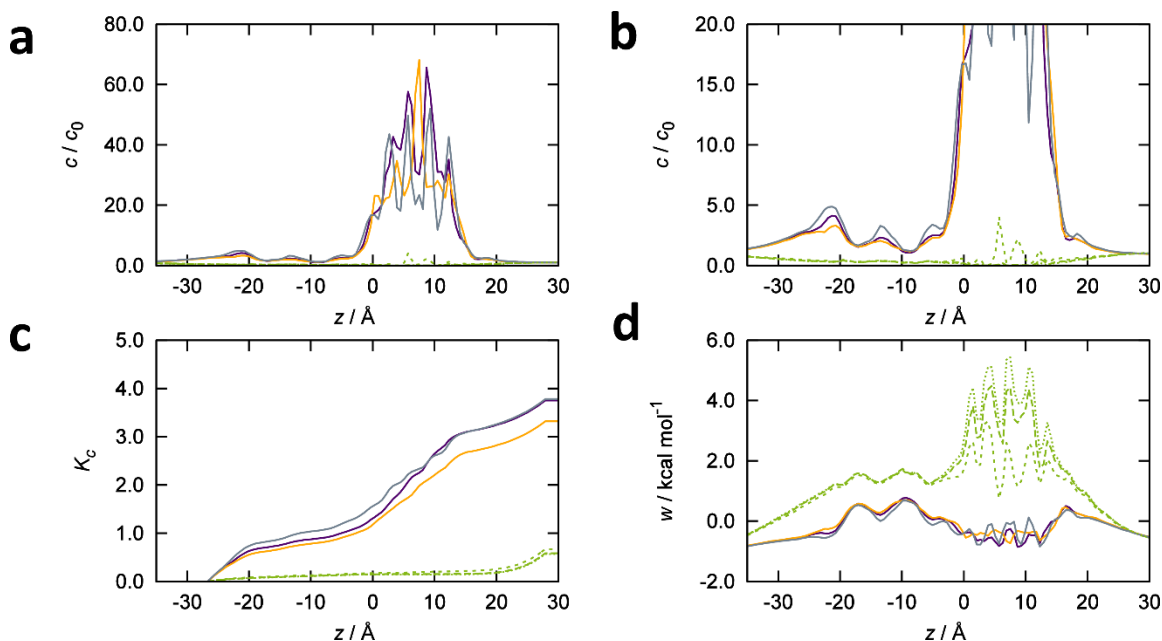


**Figure 4.9:** Depiction of analysis results for ATCV-$1_{avg,hom}$. The concentration profile is shown in full extent (**a**) and as an excerpt (**b**) for greater detail. Also the corresponding $K_c$ profile (**c**) and pmf (**d**) are presented. The pmf was normalized to a reference area $Q(z_0)$. Cations are shown in orange ($Na^+$), purple ($K^+$) and gray ($Cs^+$) while anions are green ($Cl^-$). Dashed lines distinguish the different anions. All profiles were calculated along the central axis of the tetrameric ATCV-$1_{avg,hom}$ channel structure.

To explore the previously stated ion selectivity of ATCV-1$_{avg,hom}$ the free energy profile was examined through calculation of the pmf along the central axis. The calculation along a predestined 1D path can be interpreted as a reaction coordinate, identifying low barriers as well as regions of energetic preference. Since the one dimensional pmf was calculated from information of the three dimensional pair distribution, interactions between all solvent components are still considered. Barriers are defined as the energy change of $w(z)$ between two $z$ positions. Investigation of the pmf profile (fig. 4.9) revealed high barriers for the anion $Cl^-$. Expectedly the highest barriers are localized at the filter positons exhibiting energies of 4 kcal mol$^{-1}$ and higher. Interestingly these barriers support a strong influence of the counter cation. In case of $Na^+$ the barriers for $Cl^-$ are significantly lower than in the case of $K^+$ or $Cs^+$. Nonetheless based on the presented pmf results the anion permeability would be nearly excluded at room temperature. In opposite the cations are energetically favored as indicated by pmf values below zero especially at the filter positions. As previously stated the energetically most favored region for the small cation $Na^+$ was found between the $S_2$ and $S_3$. Remarkably the pmf results are also consistent with the previously observed concentration profiles, drawing a reliable picture of a cation selective channel in combination with the $K_c$ information.

## 4.3.6 Proof of principle: Tetrameric ion channels

To validate the general applicability of the here presented method in combination with potassium ion channels, an additional selection of comparable ion channels was treated alike. 3D RISM was therefore applied to a set of tetrameric ion channels including the potassium ion channel KcsA, the potassium/sodium selective channel NaK, a homology model of Kcv$_{PBCV-1}$ as well as a truncated structure of the KirBac1.1 channel KB-Kcv.[36,59,103,233] The results for solutions of 0.1 M KCl, NaCl and CsCl are depicted in fig. 4.10. In general, potassium ion channels are known to have increased concentrations of $K^+$ inside their inner cavity region as well as in their selectivity filter. As a result of these 3D RISM calculations, high $K^+$ concentrations in the selectivity filter could be observed for each of the four ion channels. Focusing on the anion, $Cl^-$ is strongly excluded from the inner core of the protein and accumulates most likely at the positively charged, accessible residues on the outside, e.g. the N-terminal regions. In the case of NaK, KB-Kcv and Kcv$_{PBCV-1}$ even the inner cavity $K^+$ concentration is significantly higher in respect to the bulk phase. In addition a strong cation over anion selectivity (fig. 4.10) was found in all four channels by investigation of the $K_c$. Investigation of the pmf profiles reveal barriers (Fig 4.10c) for cations as well as anions of over 20

kcal mol$^{-1}$ at the mouth regions and inside the cavity of the KB-Kcv, NaK and KcsA channel. These barriers are caused by strong concentration depletions (Fig 4.10a) and are assumed to permit the ion permeation in these configuration. A comparison between the ATCV-1$_{avg,hom}$ pmf (fig. 4.9) and the here investigated channels revealed significantly lower barriers for all ions in the filter, cavity and mouth region of the ATCV-1. This observation could possibly contribute to the experimentally confirmed high open probability of the KCV$_{ATCV-1}$. In sum these results support the applicability of 3D RISM calculations tetrameric potassium ion channels.
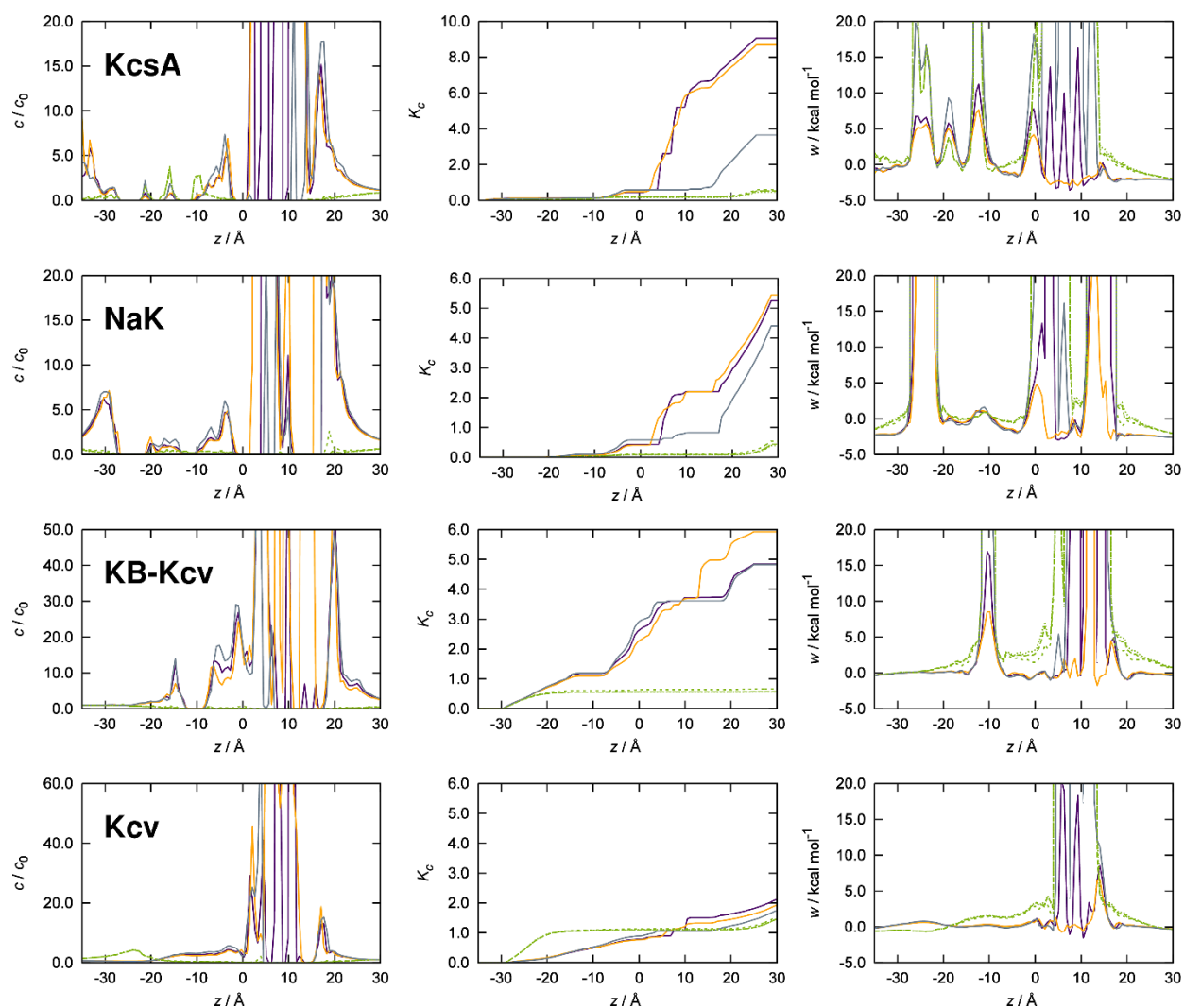


**Figure 4.10**: Thermodynmic anylsis of the tetrameric ion channel set. Depiction of the concentration (left row), $K_c$ (middle) and pmf profile (right row) for the tetrameric ion channels KcsA, NaK, KB-Kcv, Kcv$_{PBCV-1}$. Abbreviations indicate the investigated channel. The partition coefficient $K_c$ values are normalized to the individual, accessible channel volume. Cations are color coded in orange (Na$^+$), purple (K$^+$) and gray (Cs$^+$) while anions are represented in green (Cl$^-$). Dashed lines distinguish the different anions. All profiles were calculated along the corresponding central axis. Concentration and pmf profiles are restricted for clarification.

## 4.3.7 GNM/ANM opening strategy

Until today no standard approach for transferring a closed state channel into its open structure is established. This circumstance is related to the lack of experimentally available structures as well as on the fact that different channel types realize their open to close transition with individual solutions. The latter explains the ongoing research issue of finding a general pattern that suits to all ion channels at the same time. Still for the structure of KirBac3.1 an opening strategy was created by combination of experiments and theoretical studies, successfully gaining a designated open structure by bundle crossing.[83] Characterization of the open state was defined via the radius profile, originated from a crystalized S129 mutant, with experimentally higher activity. In case of KcsA Sansom et al. created an open state model by stepwise increasing a van der Waals sphere inside the mouth region during an MD simulation.[239] The combined effects of increased amounts of cavity water and significantly wider radius at the mouth after conducted relaxing simulations were considered as criteria for an open state. However this outstanding examples presented specific solutions for the KirBac3.1 and KcsA channel cases.[83,239] To overcome the time intensive and often unsuitable way of searching for individual opening strategies, Bahar et al. targeted this problem in a more general and exclusively theoretical way by utilization of network models. By application of this coarse graining method a transition between two states was calculated for a selection of tetrameric ion channels, gaining a suggested transition mode and also yielding the final coordinates for the new state. We adapted the overall principle to calculate an open-state structure for ATCV-1$_{avg,hom}$. First a Gaussian network model (GNM) analysis was carried out, returning different modes on basis of the averaged structure input. GNM models calculated in such a way characterize the global fluctuation on the basis of all Cα atoms inherited in the protein, but neglect the 3D information of the structure movement. Due to a focus on global protein motions, the slowest modes were of greatest interest. Among these a mode with a significant fluctuation around glycine residue (aa 77) was identified. This is remarkable, because the crucial function of glycine 77 was previously revealed by mutation experiments in KCV$_{ATCV-1}$.[28] Furthermore an analogue bending motion induced by a flexible glycine has been confirmed to open the prominent potassium channel KcsA (Gly-99) and KirBac1.1 (Gly-134).[238,239,241] Still the selected GNM mode contains primarily the fluctuation information and neglects the spatial movement. To obtain the required 3D transition an anisotropic network model (ANM) analysis was also conducted with the same structure. Correlation of the twenty slowest ANM modes with the previously selected GNM was

used to identify the best match. Until this point the here presented strategy followed the successfully verified and established work of Bahar et al.. Now a new potentially open structure further denoted as ATCV-1$_{\text{ANM}}$ (fig. 4.11) could be derived, due to the availability of a complementary ANM mode and its Eigenvectors. The thereby gained C$\alpha$ atom coordinates of ATCV-1$_{\text{ANM}}$ were used in subsequent MD simulations to open the closed state ATCV-1$_{\text{hom}}$ stepwise by application of harmonic potential. Visual control of ATCV-1$_{\text{ANM}}$ revealed the positive displacement direction of the eigenvector as feasible, due to widening of the mouth region. This was quantified by the calculation of the displacement $|\Delta\mathbf{r}|$ between the C$\alpha$ positions of residue 82 of ATCV-1$_{\text{avg,hom}}$ and ATCV-1$_{\text{ANM}}$. The displacement was estimated to be 5.5 Å.

**ATCV-1$_{\text{hom}}$**　　　　　**ATCV-1$_{\text{avg,hom}}$**　　　　　**ATCV-1$_{\text{ANM}}$**
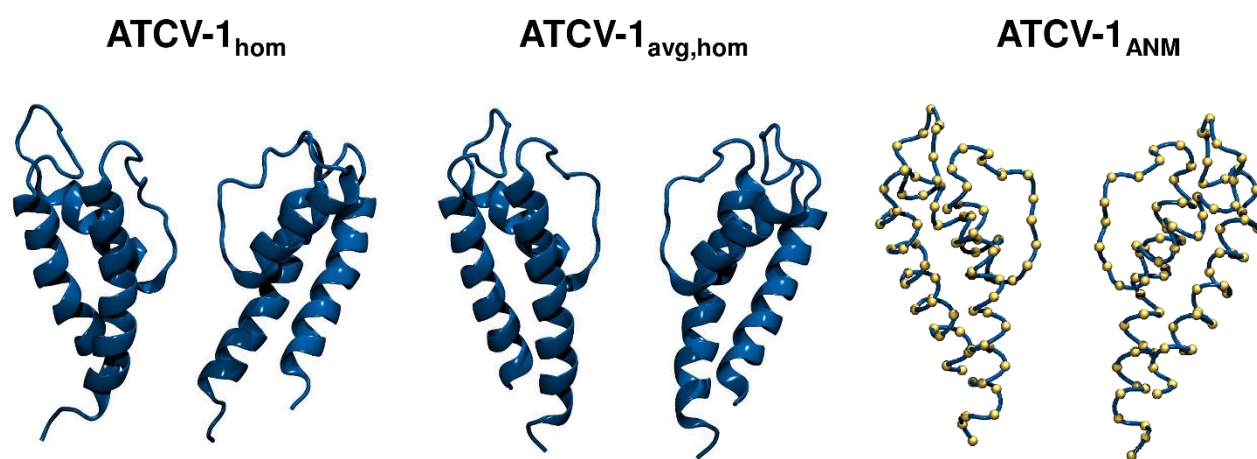


**Figure 4.11**: Representation of the ATCV-1$_{\text{hom}}$, ATCV-1$_{\text{avg,hom}}$ and the ANM based ATCV-1$_{\text{ANM}}$ structure. A cartoon representation was chosen for the presented structures of ATCV-1$_{\text{hom}}$ (left) and ATCV-1$_{\text{avg,hom}}$ (middle), while a tube depiction was chosen ATCV-1$_{\text{ANM}}$ structure. C$\alpha$ position are shown for clarification in ATCV-1$_{\text{ANM}}$ as yellow spheres. Only two oposing monomers are shown.

The extracted coordinates from the identified open ANM mode allowed the conduction of opening attempts by subsequent MD simulations. For this purpose additional harmonic potentials were applied to transfer the ATCV-1$_{\text{hom}}$ into a designated open state. As a consequence, force constants were defined to pull the corresponding backbone C-$\alpha$ atoms towards their new position. Structural disruption was avoided by slow increase of those harmonic restraints. Thus the ATCV-1$_{\text{hom}}$ structure was transferred gradually into an open configuration (see methods for simulation details). Two different opening strategies were done in parallel, which are presented in the following. The first attempt translates only the channel residues 77 to 82 along the open mode leaving the rest of the protein completely free. In the second approach all residues were slowly transferred into the derived open configuration, generating the ANM derived equivalent. To clearly distinguish

between these simulations, the first will be denoted as $MD_{disp,77-82}$ and the second approach as $MD_{disp,1-82}$ in accordance to the restrained residues and their displacement during the simulation. The reason for a dual opening strategy shall be reasoned in more detail. Considering the results of the identified GNM and ANM mode, the channel was supposed to adopt a conductive topology due to a bending movement at position Gly77. To introduce the least global disturbance by execution of this transition $MD_{disp,77-82}$ was the most promising approach. However even starting with a well equilibrated structure and carefully introducing the opening motion, the finally adopted displaced topology could possibly have introduced disturbance in the residues 1-76. A consequence might be an adopted stable, but nonconductive tetramer complex. Due to these possible issues $MD_{disp,1-82}$ was carried out transferring all residues of the equilibrated closed channel conformation slowly into the corresponding open positions. Another difference between both approaches regards the lipid membrane. While most of the ATCV-$1_{hom}$ domains can adapt completely free and individually per monomer in $MD_{disp,77-82}$ the related changes in the DMPC membrane as well as vice versa influence can lead to a different result, than it is the case for $MD_{disp,1-82}$.
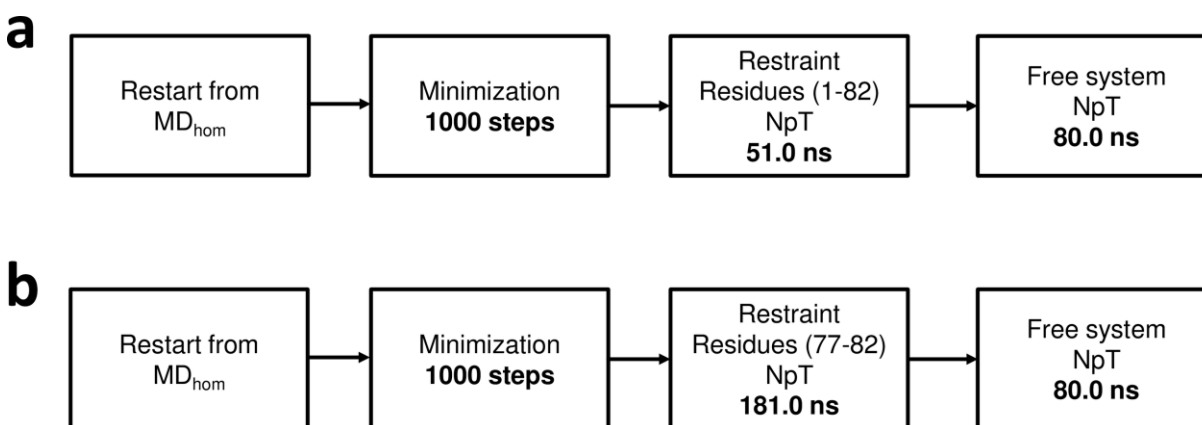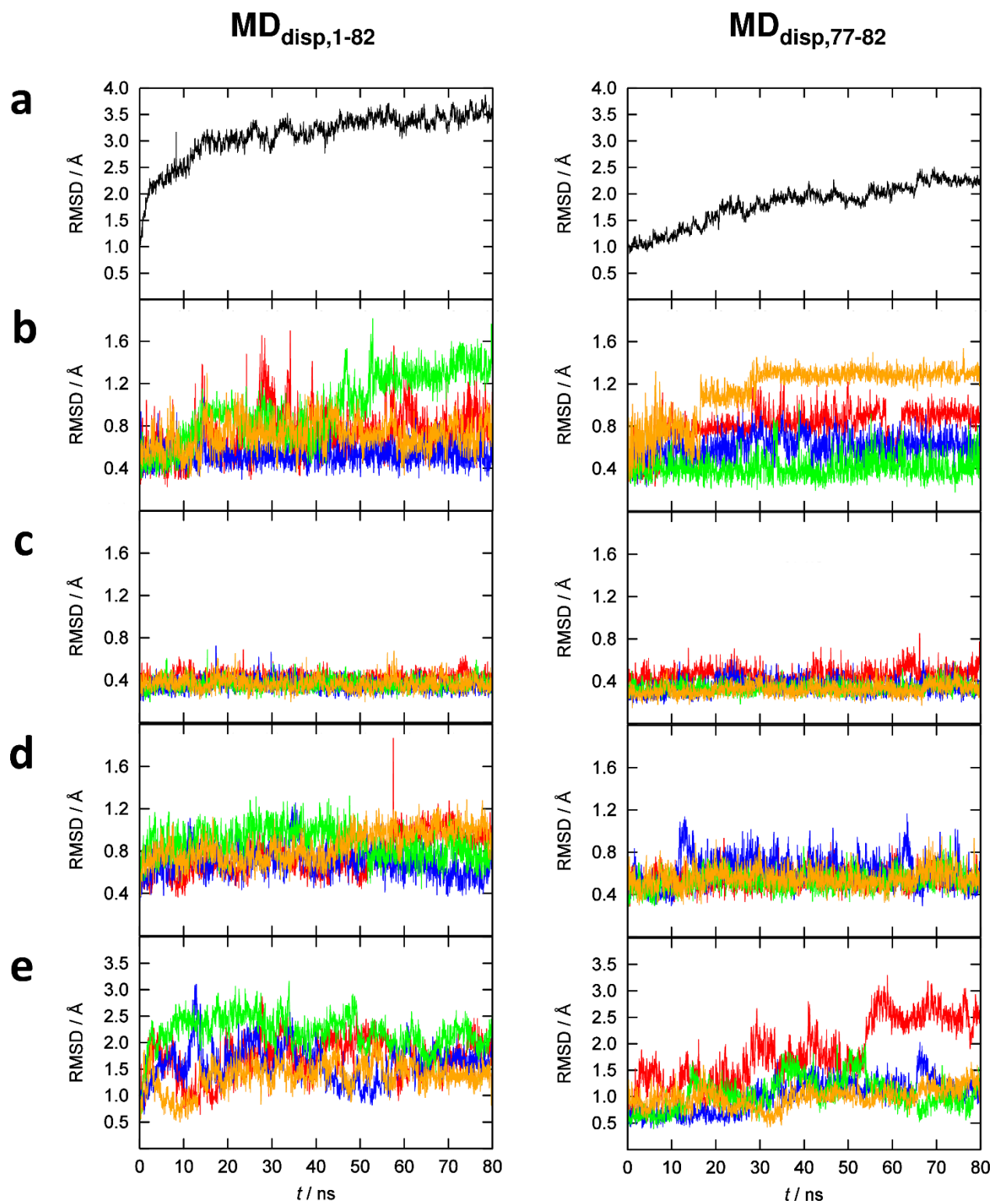


**Figure 4.12:** Restrained simulation overview. Diagram of the restrained simulations $MD_{disp,1-82}$ (**a**) and $MD_{disp,77-82}$ (**b**). The individual simulation steps are shown in rounded rectangles. Subsequent stages are connected by arrows. Volume, temperature and pressure details are provided in the method section.

In accordance with the analysis of $MD_{hom}$ the $z$ coordinate, RMSD and the helicity were also scrutinized for $MD_{disp,1-82}$ and $MD_{disp,77-82}$. Again the RMSD and the helicity values are observables for the overall stability of the protein, whereas the $z$ coordinate describes the positioning and movement in respect to the DMPC membrane. The analysis only the last 80 ns run results were used (fig. 4.12). As a descriptor for the stability, the here presented RMSD values support for a robust configuration of the protein over the free simulation time of 80 ns (fig. 4.13a). Both systems are considered to be equilibrated already after 20 ns due to the plateau of the RMSD. In detail the

protein domains TM1 and the pore helix occupy a very stable topology in respect to the RMSD, while the filter region is only steady in three out of the four monomers (fig. 4.14b). But significant fluctuations caused by a deviating monomer are limited to the first nanoseconds, before a stable topology is found. These filter fluctuations are found in both approaches, but with different monomers involved. Still for $MD_{disp,77-82}$ all major transitions of the fluctuating filter monomer end after 30 ns. In the case of $MD_{disp,1-82}$ a stable state of the filter configuration is settled after 70 ns. Independently of the simulation system TM2 performs huge changes in its TM2 domain, which can be explained in referring to changes introduced to the system.

Independent of the chosen opening approach, analysis of the helical fraction confirmed the structural stability of the simulated $Kcv_{ATCV-1}$ (fig. 4.13) structure. The successful outcome of this analysis does additionally support the applicability of both approaches.

**Figure 4.13**: RMSD results of the restrained simulations $MD_{disp,1\text{-}82}$ and $MD_{disp,77\text{-}82}$. Illustration of the complete (**a**) RMSD and the domain specific RMSD for the filter (**b**), pore helix (**c**), TM1 (**d**) and TM2 (**e**). Monomers are colorized in red, blue, green and orange in accordance to $MD_{hom}$.
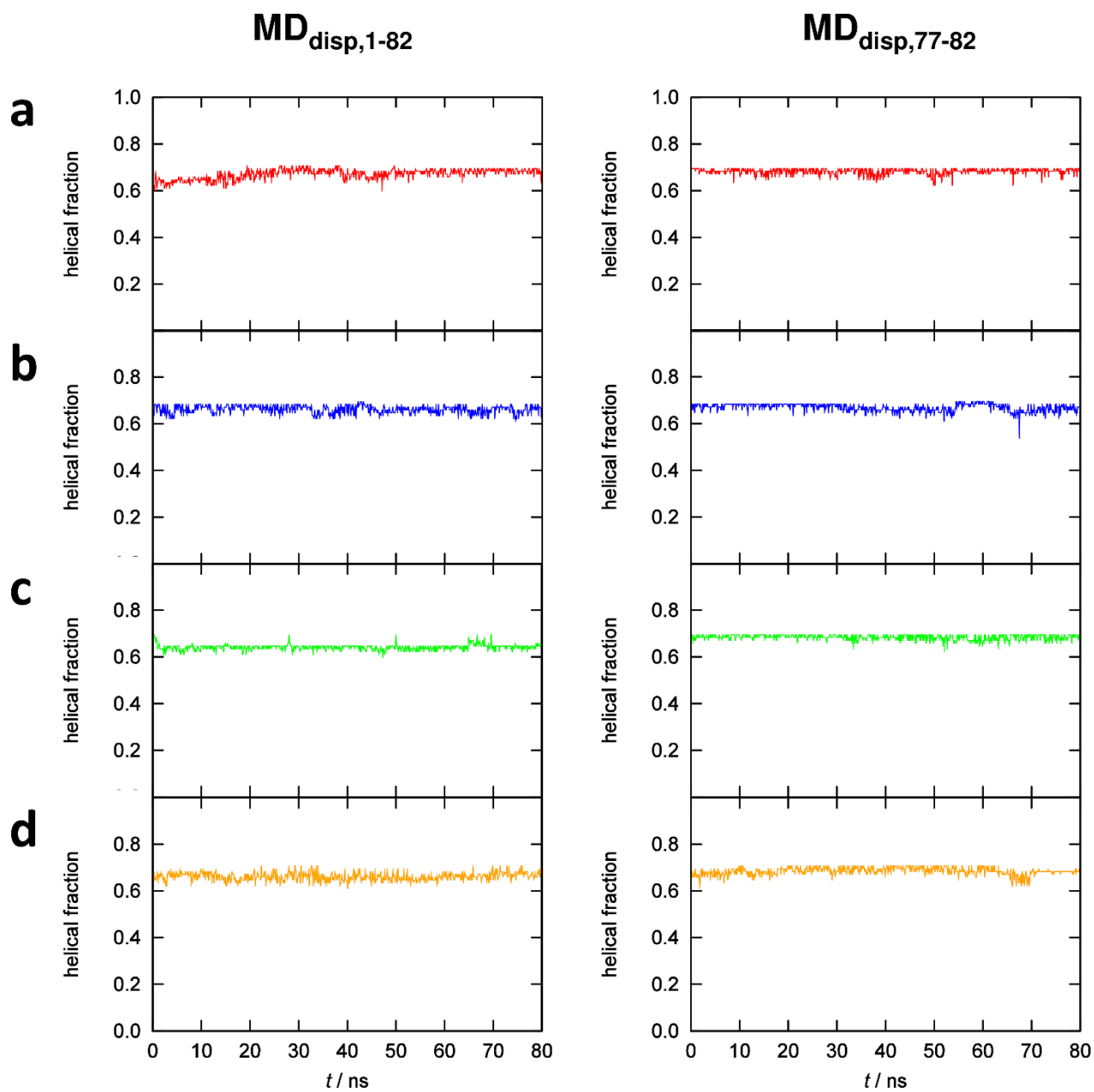
**Figure 4.14**: Helical fraction of KcvATCV-1. Time resolved total helical fraction in simulations MD$_{disp,1-82}$ and MD$_{disp,77-82}$. The helical fraction is represented for each monomer independently. The four monomers are colored (first to last) by the colors red, blue, green and orange.

## 4.3.8 Filter ions

To describe the dynamic situation of the filter ions during the conducted equilibrium and opening attempt simulations, their movements along the $z$-axis were investigated (fig. 4.16). The geometric center of the filter, defined by the residues TTVGYGD (residues 45 to 51), was subtracted from the ion current ions position for normalization.
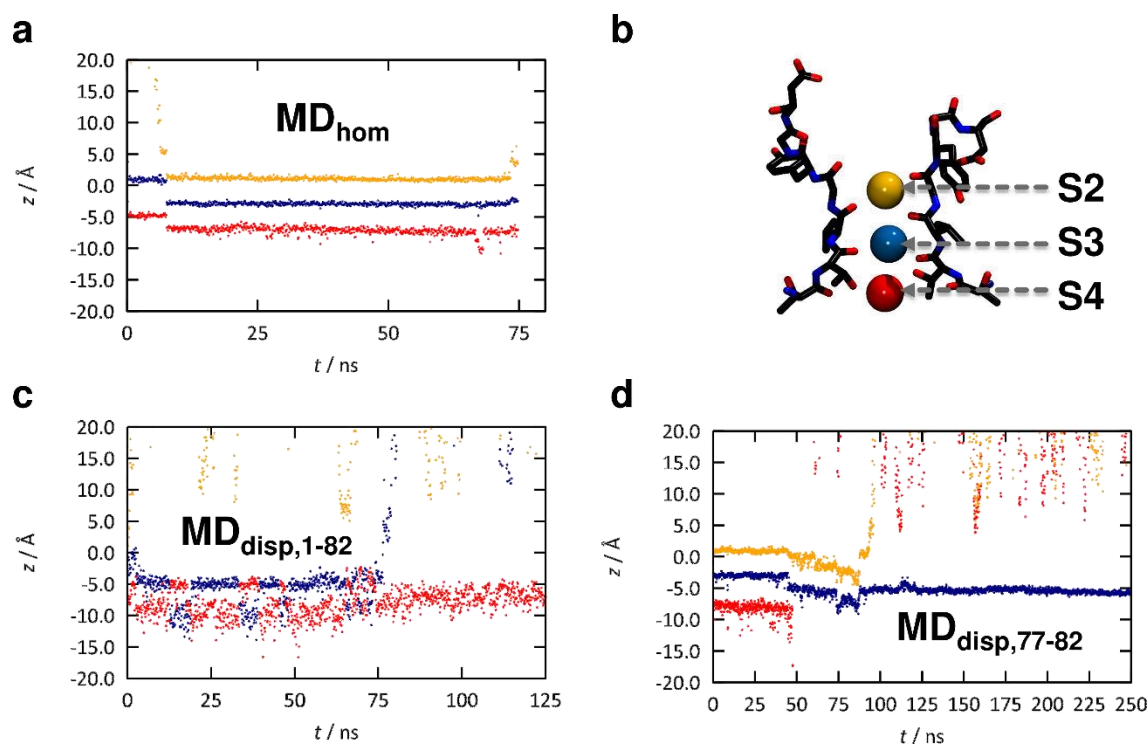
**Figure 4.16**: Filter ion dynamics. The permeation of potassium filter ions (orange, blue and red), described by their change in $z$ position, are represetend for $MD_{hom}$ (**a**), $MD_{disp,1-82}$ (**c**) and $MD_{disp,77-82}$ (**d**). An illsutration of the final state (**b**) of $MD_{hom}$ shows the coordination inside the filter.

At the beginning of the flexible $MD_{hom}$ simulation, two potassium ions were coordinated inside the filter. After 7.6 ns, a third ion entered the filter from the exterior site of the filter (Fig 4.16a), inducing a single file event. The three ions are stabilized over a total simulation time of 74.63 ns, occupying the S2, S3 and cytosolic binding site S4 in their final configuration (fig. 4.16b). In the following opening attempt simulations $MD_{disp,1-82}$ and $MD_{disp,77-82}$ the filter got depleted (fig. 4.16c,d). In case of $MD_{1-82}$ the $K^+$ of at the S2 binding site left the filter in the first ns, whereas the remaining ions began to switch places at the cavity until the end of the simulation. In $MD_{disp,77-82}$ the $K^+$ coordinated at the S4 site exited through the cavity after 48.0 ns, followed by a permeation of the S2 occupying $K^+$ into the exterior. The remaining $K^+$ ion lasted inside the whole simulation time

## 4.3.9 Open or closed?

Beyond doubt the transition of ions through a channel is the clearest evidence for a conductive ion channel structure. Throughout the here conducted MD opening approaches no ion transition or even single file events occurred. According to the experimental open probabilities for $Kcv_{ATCV-1}$ ion transition should occur each 1 ns. However the adopted conformations are stable for over

64

80.0 ns in unrestrained production runs. Perhaps these nonconductive conformations might correspond to an open but impermeable topology thus representing a resting or intermediate state. Possible reasons for the adoption of such states can be water depletion as well as steric restraints around the mouth region. To quantify these hypotheses an analysis of the radius around the mouth region as well as the total number of cavity water was conducted (see methods). Both descriptors were investigated by their progress over time. Beginning with the radius the restrained simulation of $MD_{disp,1-82}$ presents a wider mouth region, when compared with the initial $MD_{hom}$ results (fig. 4.15). Further the unrestrained parts of $MD_{disp,1-82}$ are affected by fast radii changes in the range from 0.5 Å (closed) to 2.0 Å (potentially open). The fast fluctuations might explain the missing ion transitions in the $MD_{disp,1-82}$ simulation. Tracking the same radius development in $MD_{disp,77-82}$ revealed a nearly linear convergence against a tight radius of 0.5 Å comparable to those found in the closed $MD_{hom}$, thereby proposing an impermeable and rather closed than open configuration of $Kcv_{ATCV-1}$ in $MD_{disp,77-82}$. Besides the mechanical restraining through residues at the mouth region, also the amount of water kept in the cavity controls the ion permeability of an ion channel and can also prohibit the exchange between cavity and bulk completely. For those reasons the amount of water molecules inside the cavity were observed and compared with the closed state situation in $MD_{hom}$ (see *Appendix*). For the closed structure of $MD_{hom}$ a fast influx of water molecules into the cavity was observed gaining a stable population of at least 25 water molecules through the complete 91 ns. Branching from this point the restraint simulations of $MD_{disp,1-82}$ and $MD_{disp,77-82}$ exhibit a further water influx due to their potentially opened structure. However lifting the restraints in the production runs causes a constant water depletion in both opening simulations. Finally the total local water density in the cavity drops two times below bulk water concentration (fig. 4.15b,c; green line). In context of water depletion it is worth noting that radii below 1.4 are considered as impermeable for water molecules.[242] Under this criteria an exchange between bulk phase and cavity water molecules would only be possible for the ATCV-1 channel in $MD_{disp,1-82}$, but are affected due to the fluctuations. Considering the amount of water inside the cavity as an indicator to decide between closed and open states, $MD_{hom}$ might be already in an open state, in which case the further displacement of this geometry ($MD_{1-82}$, $MD_{77-82}$) might have introduced intolerable disturbances. From this point of view, no clear decision could be made whether the channels are in an open or in a closed state. In spite of its high stability and nearly stable population of cavity waters, $MD_{hom}$ is the most suitable and putatively open configuration.

65
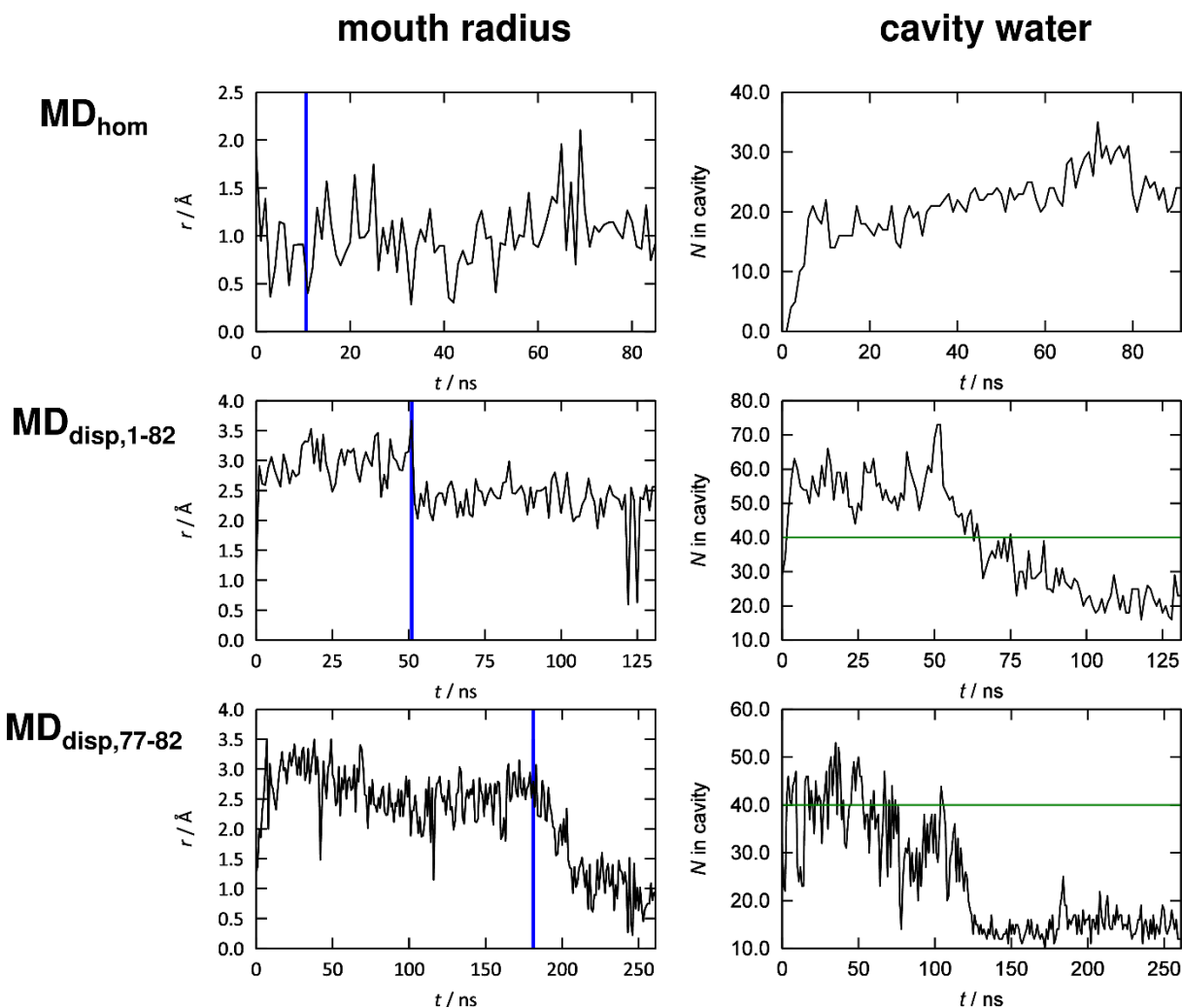
**Figure 4.15**: Mouth radius and water density. Depiction of the radius (left row) at z = -10.5 Å over time for the initial equilibrium simulation $MD_{hom}$ and the subsequently conducted opening approaches $MD_{disp,1-82}$ and $MD_{disp,77-82}$. The positon of -10.5 Å corresponds to the minimum radius of ATCV-$1_{avg,hom}$. The radius was sampled with Hole. The water density in the cavity is plotted as a function of time. Bulk water density for the given volume is shown as the green line. A blue line indicates the moment of full flexebility in the simulation. Data points were assessed in 1 ns steps.

### 4.3.10 3D RISM results of the average structures from the MDdisp,77-82 and MDdisp,1-82

On the basis of these simulation results, two new average structures were calculated (fig. 4.16), further denoted as ATCV-$1_{avg,1-82}$ and ATCV$_{avg,77-82}$ to investigate their thermodynamic properties in comparison to the closed ATCV-$1_{avg,hom}$. The new structures were thermodynamically inspected by 3D RISM computations with solutions of NaCl, KCl and CsCl in concentrations of 100 mM.

66

**ATCV-1$_{avg,1-82}$**  **ATCV-1$_{avg,77-88}$**  **Superposition**
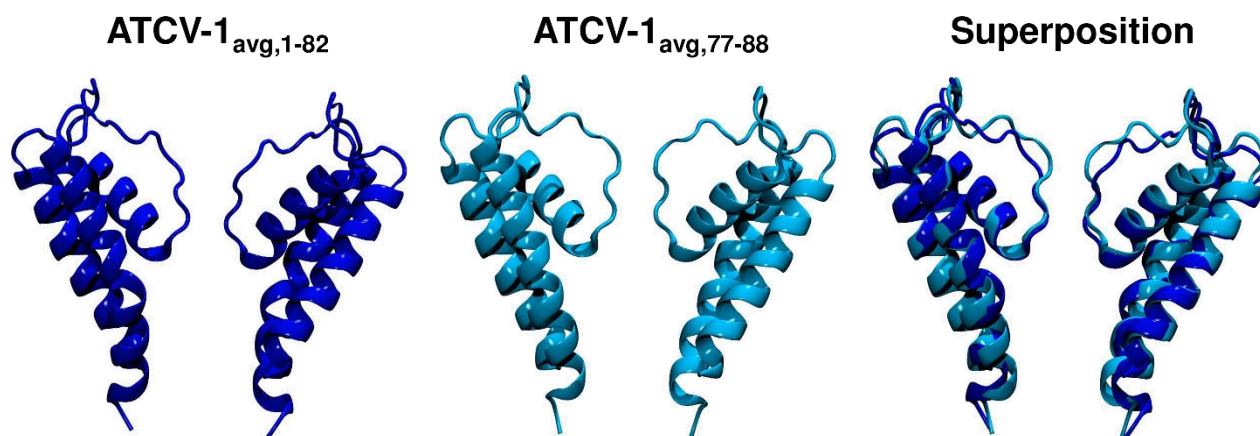


**Figure 4.17**: Comparison of average structures. Cartoon representation of the mean structures ATCV-1$_{avg,1-82}$ (turquoise) and ATCV-1$_{avg,77-82}$ (dark blue), as well as an superposition overlay. Two monomers are shown for clarification.

From the $c(z)$ profiles an enriched concentration for all cations can be stated in the filter region while the concentration in the cavity reflected the situation in bulk. Still the anion $Cl^-$ is completely discriminated or depleted. In difference to ATCV-1$_{avg,77-82}$ the filter positions $S_0$-$S_4$ are clearly defined due to stronger depletion and enrichment alternations in the profile between the transitions in ATCV-1$_{avg,1-82}$. The partition coefficient profiles are stating a clear cation over anion selectivity for both averaged channel structures. In detail only a small deviation in selectivity is observed for $Na^+$, while $Cs^+$ and $K^+$ are nearly undistinguishable. However the selectivity for $K^+$ and $Na^+$ arises at the beginning of the filter positions $S_4$. Focusing on the total selectivity for both averaged structures, the greatest deviation in selectivity occurs in the case of $Na^+$, represented by the ratio $K^+/Na^+$ of 1.17 for ATCV-1$_{avg,77-82}$ and 1.08 forATCV-1$_{avg,1-82}$. Notably the $S_0$ and $S_1$ filter positions are distorted in ATCV-1$_{avg,77-82}$ in comparison to ATCV-1$_{avg,1-82}$ (fig. 4.18), which had an influence on the concentration profile and might therefore also have an influence on the partition coefficient. Besides the mentioned common features in their selectivity the comparison of the corresponding pmf profiles reveals some differences. Speaking of cations the ATCV-1$_{avg,1-82}$ free energy profile is characterized by a smoothly increasing barrier beginning at the mouth region and reaching its maximum inside the cavity around $z$ position -8 Å, which is then followed by a long decrease. For ATCV-1$_{avg,77-82}$ the same progression is observed, but with a much longer and higher extend, forming a barrier of about 2 kcal mol$^{-1}$ at the internal filter position $S_4$. Exhibited barriers at the mouth interface are in accordance with the described constant radius decrease, which influences also the calculated mean structures. However both structures are suggested to be cation selective and in principle ion conductive according to the surmountable barriers.
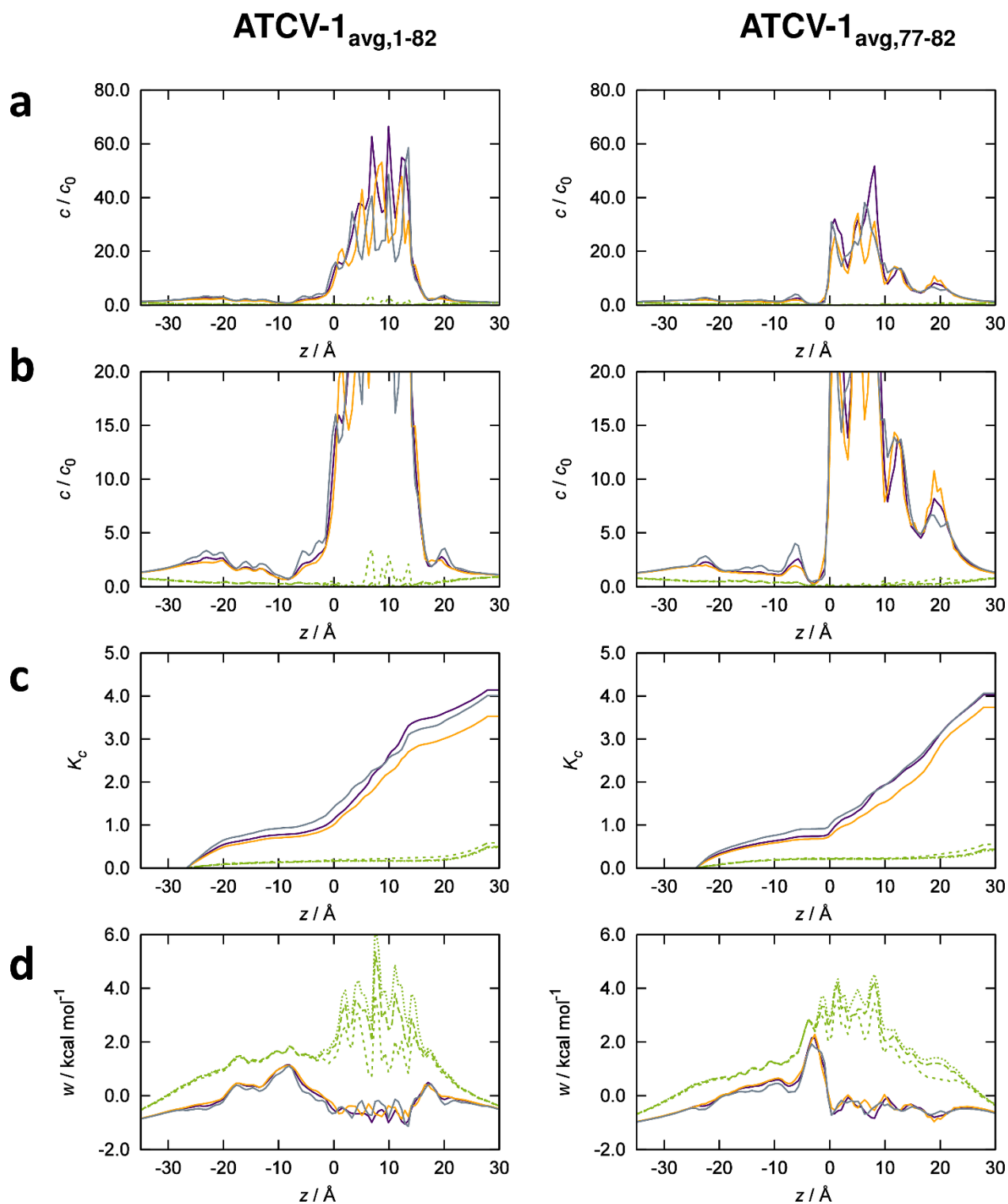
**Figure 4.18**: Analysis of the 3D RISM results for ATCV-$1_{avg,1-82}$ and ATCV-$1_{avg,77-82}$. Depiction of the full (**a**) concentration and partition coefficient profiles (**c**), as well as the illustration of the pmf (**d**) normalized to a reference area $Q(z_0)$. Concentration profile excerpts are provided for detailed resolution in (**b**). Color code: K$^+$ (purple), Na$^+$ (orange), Cs$^+$ (gray) and Cl$^-$ (green).

## 4.4 Conclusion

Supported by the here exhibited results and analysis, the homology modelling approach of Kcv$_{ATCV-1}$ on the basis of KirBac1.1 was proved to be reasonable and successful. The created model was demonstrated to form a stable closed structure in MD simulations. Considering the chosen DMPC membrane the investigated ion channel models were well suited inside the membrane environment which is in agreement with laboratory experiments.[28] The adopted tight geometries of the displaced channels MD$_{disp,1-82}$ and M$_{disp,77-82}$ were identified to be rigid in respect to their monomeric aspects as well as in their tetrameric structures. Both structures adopt a very stable unrestrained conformation with a rigid filter structures over a significant simulation time. Their capability to coordinate free ions and water molecules over long time scales confirms a reasonable filter conformation with inherited potential to conduct ions. Analysis of their unrestrained MD simulations revealed a water depletion and radius tightening of the ion channels prohibiting the essential $K^+$ transfer. So the observed ion channel conformations might be in a resting or intermediate state, which is also considered as a reasonable result for a homology model based approach. Still the thermodynamic characterization of the mean channel structures by 3D RISM confirmed an existing low energy path for an ion transition through the given average structure by the evaluation of pmf. Also the partition coefficient analysis of the 3D RISM outcomes reproduce the a cation selectivity order of $K^+ > Cs^+ > Na^+$ measured in electrophysiological experiments.[28] However all of the yielded structures from the here presented opening attempts are compromised with slight issues. No single file events, which are suggested to be the clearest criteria for a conductive state, occurred neither in MD$_{disp,1-82}$ nor in M$_{disp,77-82}$.

In general a complete workflow created from scratch for the structure and system creation of the potassium ion channel Kcv$_{ATCV-1}$ was presented in this work. Furthermore the applied analysis strategy demonstrated the complementary character of the here applied different computational techniques as well as their extent. In particular the combination of new 3D RISM analysis features in combination with MD simulations gained novel insights into the ion channel free energy landscape in equilibrium state, which is inaccessible on the short time scales by MD simulations. This also accentuates the synergetic strength of 3D RISM in combination with MD simulations.

# 5 A synthetic ion transporter

## 5.1 Introduction

The field of synthetic chemistry targets the challenge to design and realize synthetic pore equivalents for biological ion channels, by using etching techniques and electron-beam lithography.[85,110,112–115] Those methods allow for the creation of pores with a controlled size $\geq$ 5-10 nm.[243] Nonetheless the creation of nanopores with a diameter scale below 2 nm is still a challenging task.[6,115] Unfortunately these small scales exhibit the most interesting features and are thus of most interest. Furthermore, the abiotic nature of such created pores prohibits their direct application in cellular systems.

Continuous progress in the field of synthetic ion channels has achieved the realization of pores with distinct features.[66,67,244] A novel, simple monomeric ring structure (fig. 5.1, left) based on *m*-oligophenylethynyl (OPE) forming stable pores in membrane "bilayers" with a diameter of 8 Å was recently revealed by the group of Gong et al.[6,7] The fully functional pore of Gong et al. is achieved by the self-assembly of 10 monomers in total (fig. 5.1, middle, right), stabilized via π-π interactions, providing a distinct and controlled hydrophobic topology along its central axis. In contrast to other π-stacking synthetic ion channels like the guanosine based G-quartet, the OPE framework used by Gong et al. facilitates a high rigidity through π-π interactions.[6,67,245] Its stability was also verified in molecular dynamics simulations (MD).[6] However the atoms of the pore had no charges during their simulations, according to their provided system data. Investigations with 4 M concentrations of KCl in large unilamelar vesicles (LUV) and electrophysiological experiments revealed a cation selectivity with a small conductance of 5.8 pS observed for $K^+$ in conjunction with distinct open and closed states.[6] Still concentrations of 4 M are far from the physiological *in vivo* concentrations of plants or animals. Furthermore the currents were not observed directly In opposite no conductance was found for the anion $Cl^-$. Such behavior indicates the capability of this outstanding pore to be an ion channel.
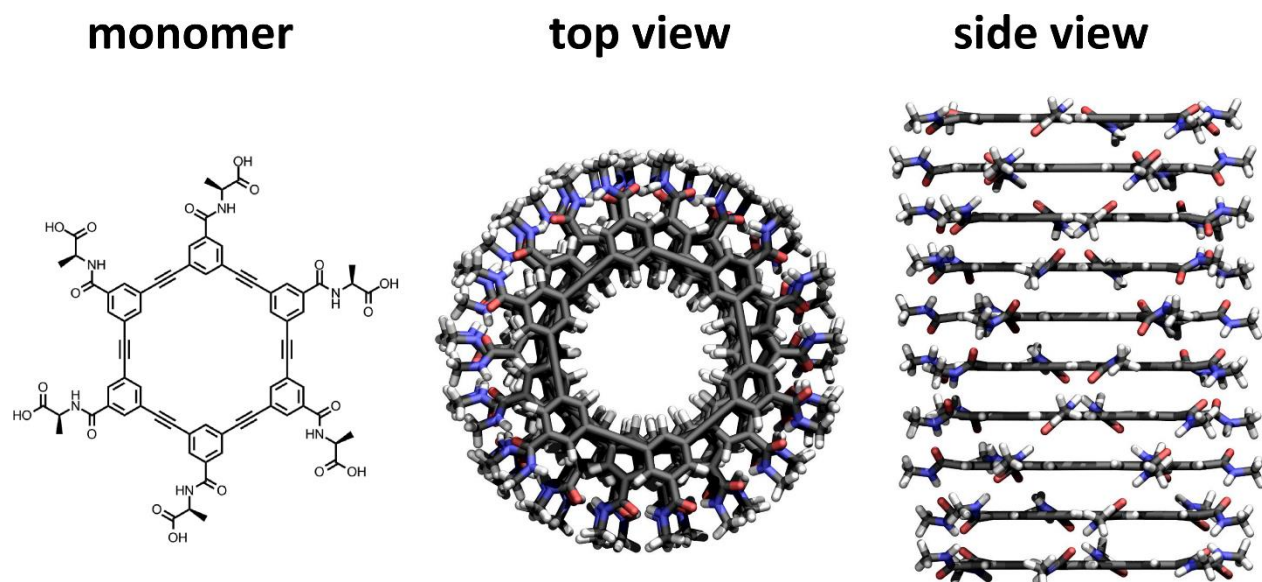
**Figure 5.1**: Illustration of the synthetic pore of Gong et al.[6] The chemical nature of the monomer (left) allows for the adaption of a stacked conformation (middle, right) forming a self-assembling pore with a total of 10 monomers (right) in accordance to analysis of the Hill coefficient.[6] A stick representation is given from a top (middle) and side (right) viewpoint. Color code for the chemical elements: C (black); H (white); O (red); and N (blue).

Considering the small size of the complete pore with its co-occurring ion selectivity and gating properties, the pore is supposed to be a valuable target for ion channel studies. Therefore we investigated the synthetic channel with MD simulations and supplemented the gained results by a thermodynamic analysis using RISM. At first, the pore will be investigated with a restrained pore conformation (fig. 5.1) allowing the calculation of the concentration profile $c(z)$, the partition coefficient $K_c$ and the potential of mean force (pmf) $w(z)$ for each solvent species, which are used to study the hydrophobic pore in greater detail. In addition ion conductances were obtained for both methods, MD and RISM, in dependency of concentrations.

In the second part the influence of motion is emphasized by prolonging the existing MD simulations without restraints. These trajectories allow the extraction of time resolved pore geometries which are investigated by RISM. This complementary approach helps to overcome the non-equilibrium situation in MD simulations and vice versa allows studying changes due to dynamic aspects in RISM.

## 5.2  Methods

## 5.2.1 Structure preparations

In accordance to the Hill slope results in the supporting information of Gong et al. the *in vitro* pore is comprised by a stack of 10 monomers.[6] A corresponding pore with 10 monomers provided by the authors was used throughout all MD simulations and RISM calculations. Charges for the pore were added, as the provided system carried no charges for the pore. An internal net uncharged pore was guaranteed by calculation of counter charges, distributed over corresponding residues, using the group concept of CHARMM force fields.[246] The charges were calculated using the AM1-BCC method. Parameters for a single monomer are provided in the *Appendix* (table A5.1). The provided system from the authors had an unequal distribution of lipids between the two monolayers. The difference of 6 lipids was preserved in the here simulated work for reasons of comparability with results of Gong et al (for details see following section MD simulation) .[6]

Average structures were generated by calculation of the mean geometric positons using 30 snapshots (1 per nanosecond), extracted from unrestrained MD simulation runs with KCl concentrations of 1 M and external potentials of 1 V and 0.1 V. The computation of the direct geometric mean was feasible in case of the pore system of Gong, as the only small structural derivations occurred during the unrestrained MD simulations. To avoid misinterpretation, the here performed calculation of a geometric average structure must clearly be distinguished from the previously applied averaging process used for the $Kcv_{ATCV-1}$ ion channel. VMD in version 1.9.1 was used for all structure preparations.[220]

## 5.2.2 1D and 3D RISM computational details

Solvent susceptibilities $\chi_{ij}$ for KCl solutions for concentrations of 0.1 M, 1 M, 2 M and 4 M were gained by conducted 1D RISM calculations with the adapted permittivity and densities listed in table 5.1.[247,248] The solvent permittivity for pure water was set to 78.4, while the corresponding density was set to 0.0333295 $Å^{-3}$. The values for water and in table 5.1 are equivalent to a pressure of 1 bar. The closure function was approximated by the hyper netted chain (HNC) relation. The temperature was set to 298.15 K.

**Table 5.1** KCl 1D RISM parameter

| $c$ / mol L$^{-1}$ | $\rho$ / Å$^3$ | $\varepsilon$ |
|---|---|---|
| 0.1 M | 0.0332356 | 78.4 |
| 1 M | 0.0323666 | 68.5 |
| 2 M | 0.0313470 | 58.5 |
| 4 M | 0.0291598 | 45.7 |

$c$ designates the KCl concentration

$\varepsilon$ describes the permittivity, $\rho$ represents the density

Integral equations were solved in subsequent 3D RISM calculations on a 120 x 120 x 120 Å³ grid with a mesh spacing of 0.6 Å. The partial series expansion (PSE) of fourth order was applied as the closure approximation. Calculations were accomplished with in house codes and scripts. Atom parameters were taken from CHARMM22* and CHARMM27 (see *Appendix*).[186,190] Calculations of the restrained pore embedded in a membrane extended the system dimension to 160³ Å³.

## 5.2.3 Conductance calculation from MD simulation and RISM calculation

A series of 30 structures was extracted from MD simulations with an unrestrained pore under conditions of 1 M KCl solution and applied external fields of 0.1 V and 1 V. The geometric mean was calculated by implemented functions in VMD in version 1.9.1 and investigated by 3D RISM calculations, obtaining a single conductance value $\gamma_{avg}$ for each of the two structures.[220] 3D RISM calculations were carried out for each of the 30 structures extracted from unrestrained MD simulations. The resulting mean conductance $\gamma_{mean}$ was realized by the calculation of the arithmetic mean over all single $\gamma$ values.

As the conductance corresponds to the amount of transferred elementary charges over time, it can be calculated on the basis of MD simulations by

$$\gamma_{MD} = \frac{n_i \cdot V_{Field} \cdot e}{t_{MD}}$$

[**5.1**]

with the amount of occurring ion transition $n$ for the ion species $i$, the external field strength $V_{field}$, the elementary charge $e$ and the simulation time $t_{MD}$. Ions passing the distance between z -20.0 Å to 20.0 Å were counted as a full transition. As an exception, an entering Cl⁻ ion was counted as an partial transition after the visual control of the unrestrained MD simulation with 1 M KCl and external potential of 0.1 V.

## 5.2.4 MD Simulations

The simulated MD system consists of 44789 atoms with dimensions of 75.03 x 92.26 x 91.243 Å$^3$. The pore was embedded inside a membrane bilayer consisting of 137 lipids, distributed unequally into 66 lipids in the upper leaflet and 71 for the lower leaflet, due to the original setup provided by Gong et al.[6] The solvated system inherited a total of 8209 water molecules. Introduction of 83, 166 or 332 cations and anion occurred randomly in exchange against water molecules to gain final concentrations of 1 M (83), 2 M (166) and 4 M (332). Each system was minimized for 1000 steps and equilibrated by simulation in the *NpT* ensemble for more than 10 ns at 1 bar and 310 K. Temperatures near body temperature provide a higher membrane fluidity and were successfully used in simulations with a restraint McsL channel of Elmore and Doughtery.[249] A mean volume was calculated using the last 5 ns. The least deviating system geometry in accordance to this mean volume of the *NpT* ensemble was thereby identified and used as the restart geometry for subsequently performed simulations with constant volume (*NVT*). For simulations with an electrical field of 1 V or 100 mV, external fields of 0.2562283 V· Å$^{-1}$ or 0.02562283 V· Å$^{-1}$ were applied in the *z*-dimension. All simulations were realized with the combination of VMD (system creation and manipulation) and NAMD.[183,220] The minimized structure was used in simulation runs with restrained topologies. The subscript "free" and "fix" will be used in the following to distinguish simulations with restraints ("fix") from those without ("free").

Extraction of the RMSD and *z* positions for the pore were done with VMD in version 1.9.1. Minimized structures were used as reference for the RMSD calculation.[220] The complete pore, including all hydrogen atoms, were considered for the RMSD calculation. The *z* position was obtained by extraction of the current spatial *z* coordinate of the pore's geometric center. To exclude movement, induced by the membrane translation, the geometric center of the membrane was calculated and subtracted. The membrane center was defined by its phosphate atoms inherited in the lipid head groups.

## 5.2.5 Validation of the reference area $Q(z_0)$

All conductances in this work were normalized to a reference area $Q(z_0)$ in accordance to equation 3.3.20. The change of $\gamma$ in dependency of the chosen $Q(z_0)$ was previously estimated and is shown in table 5.2. In case of the synthetic pore, the default radius for the lower border was estimated to be 15.9 Å. The average structure obtained from simulations of 1 M concentrations of KCl and an external potential of 1 V was chosen as the test system. The results represent an insignificant influence.

**Table 5.2** Variation of the reference area $Q(z_0)$

|  | $z$ position | $K^+$ | $Cl^-$ |
|---|---|---|---|
| $\gamma_{avg,struct}$ / pS | 15.3 | 101.1 | 356.1 |
| $\gamma_{avg,struct}$ / pS | 15.9 | 99.4 | 351.8 |
| $\gamma_{avg,struct}$ / pS | 16.5 | 97.2 | 345.5 |

$\gamma_{avg,struct}$ denotes the conductance value of the average structure

## 5.2.6 Membrane influence

To exhibit the effect of a membrane to the calculated ion conductances, 3D RISM calculations with a POPC membrane were performed, using the restrained pore applied to concentrations of 0.1 $M_{fix}$ and 1 $M_{fix}$ KCl. The addition of the membrane was accompanied by small changes in the conductances for the $Cl^-$ and $K^+$ ions. Still the observed effects are rather insignificant, not interfering with the major anion over cation selectivity (table 5.3).

**Table 5.3** Membrane influence

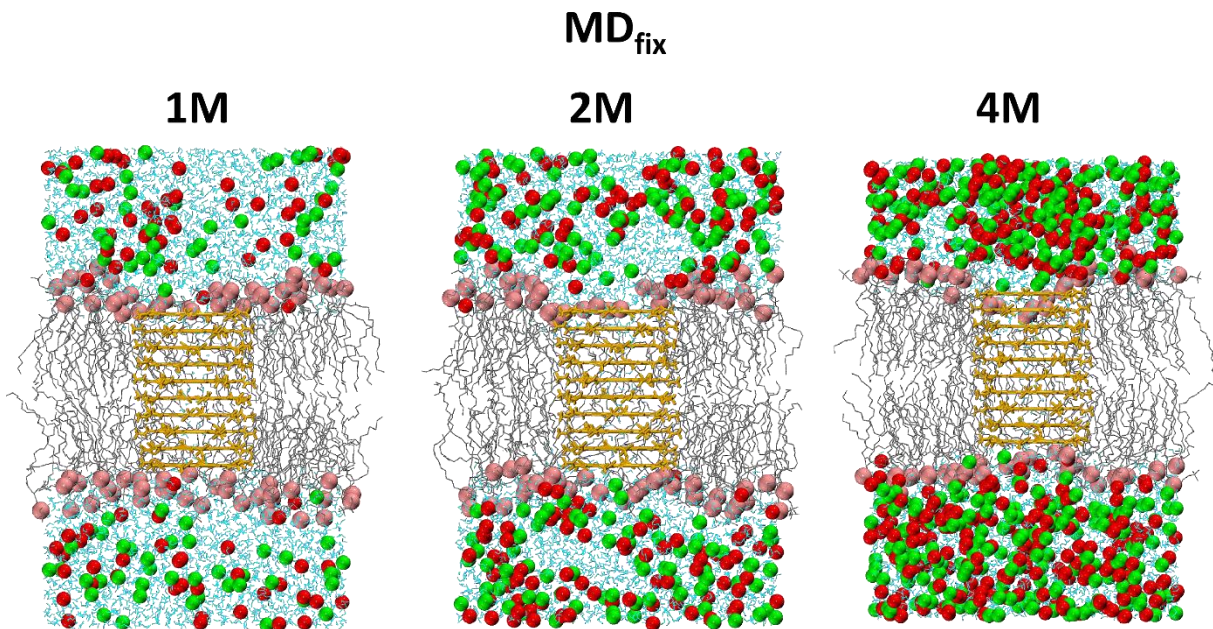|  | Concentration | system | $K^+$ | $Cl^-$ |
|---|---|---|---|---|
| $\gamma$ / pS | 0.1 M KCl | pore | 18.39 | 74.12 |
|  |  | pore + POPC | 23.31 | 55.81 |
|  | 1 M KCl | pore | 171.92 | 440.07 |
|  |  | pore + POPC | 183.67 | 405.04 |

## 5.3 Results

### 5.3.1 Studies of the synthetic pore geometry by MD$_{fix}$ simulations and 3D RISM

To study the properties of this new pore created by Gong et al. MD simulations in varying concentrations of KCl solutions (fig. 5.2 and fig. 5.3) were conducted. In accordance to descriptions in the work of Gong et al. an initial concentration of 4 M KCl was chosen (fig. 5.2 and fig. 5.3). The created system was minimized for 1000 steps and simulated at 1 bar and 310 K for 20 ns with a restrained pore structure (fig. 5.2). Simulations in the *NVT* ensemble were branched from the results of this simulation using a mean volume that corresponds to the *NpT* pressure (Fig 5.2).
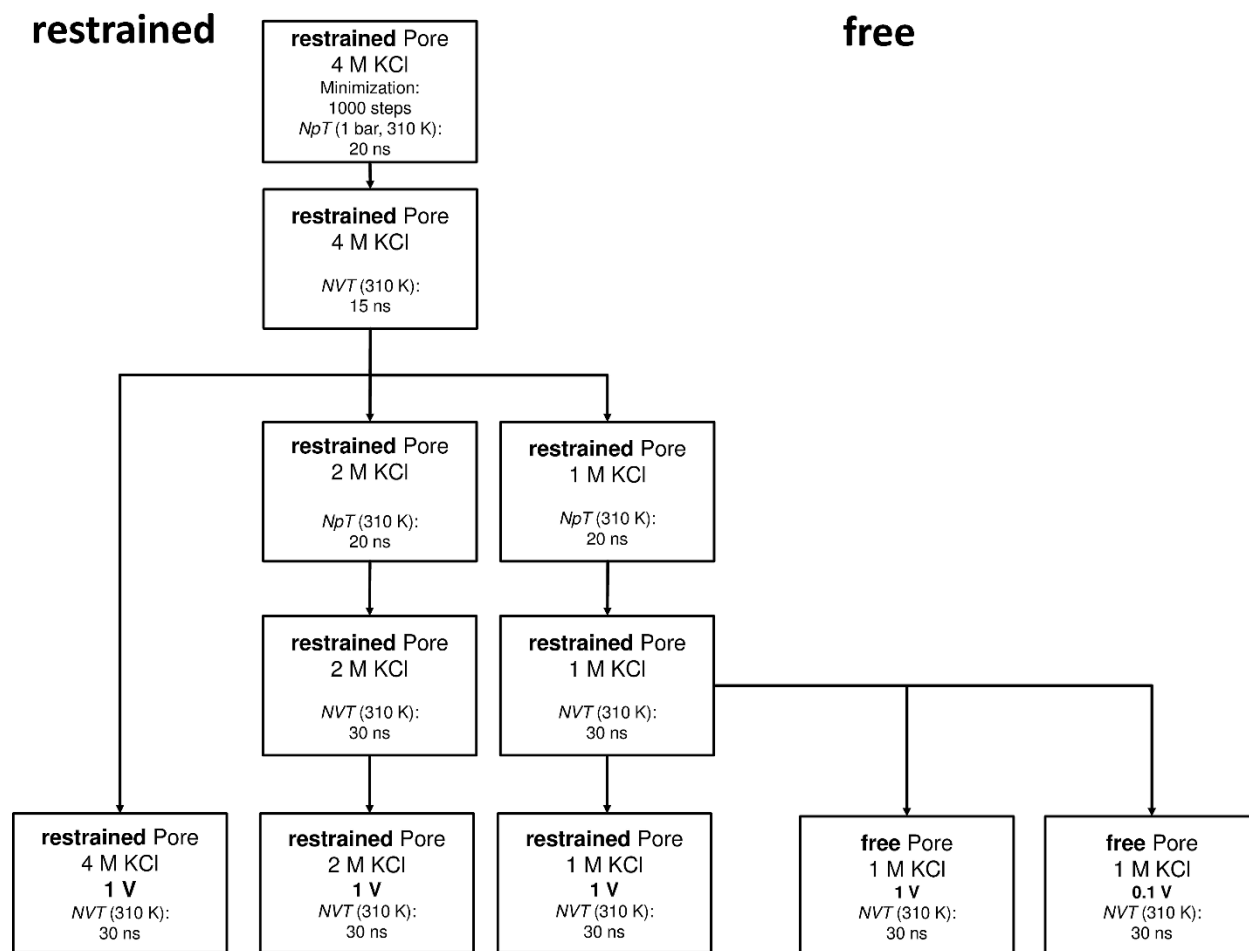


**Figure 5.2**: Diagram for MD simulations with the pore of Gong et al.[6] Depiction of the deductive MD simulation process. Each box represents a single MD simulation. The calculated mean volume according to the pressure (1 bar) of the prior *NpT* simulation was used for the *NVT* simulations.

In these subsequent simulations the influence of the restrained and unrestrained pore geometries were examined as well as the changes to an applied external field. Still concentrations of 4 M KCl are barely physiological and nearly inaccessible in the laboratory. In addition solutions for 4 M KCl concentrations could not be accessed by 1D RISM, due to convergence problems. Thus MD simulations with lower concentrations of 1 M and 2 M were conducted in addition (fig. 5.2 and fig. 5.3). The setup for simulations with 1 M and 2 M concentrations of KCl were branched from the 4 M simulations in the *NVT* ensemble (fig. 5.2). Again, for these simulations the influence of dynamics and an applied external potential was studied. To assure clarification for the reader the results of the restrained pore will be discussed first, followed by the according discussion of the dynamic systems.



**MD$_{fix}$**

**1M**       **2M**       **4M**

**Figure 5.3:** Restrained pore MD$_{fix}$ simulation systems. Representation of the hydrophobic pore (golden) embedded in the lipid POPC bilayer (black) for the KCl concentrations 1 M (left), 2 M (middle), 4 M (right). Ions are shown as red (K$^+$) and green (Cl$^-$) spheres, water as transparent blue ball and sticks. Only one half of the system is shown for clarification.

Insights regarding the ion selectivity were derived by the analysis of MD simulations with a restrained pore topology. Ion transitions did not occur in any of the restrained simulations without an additional external field.
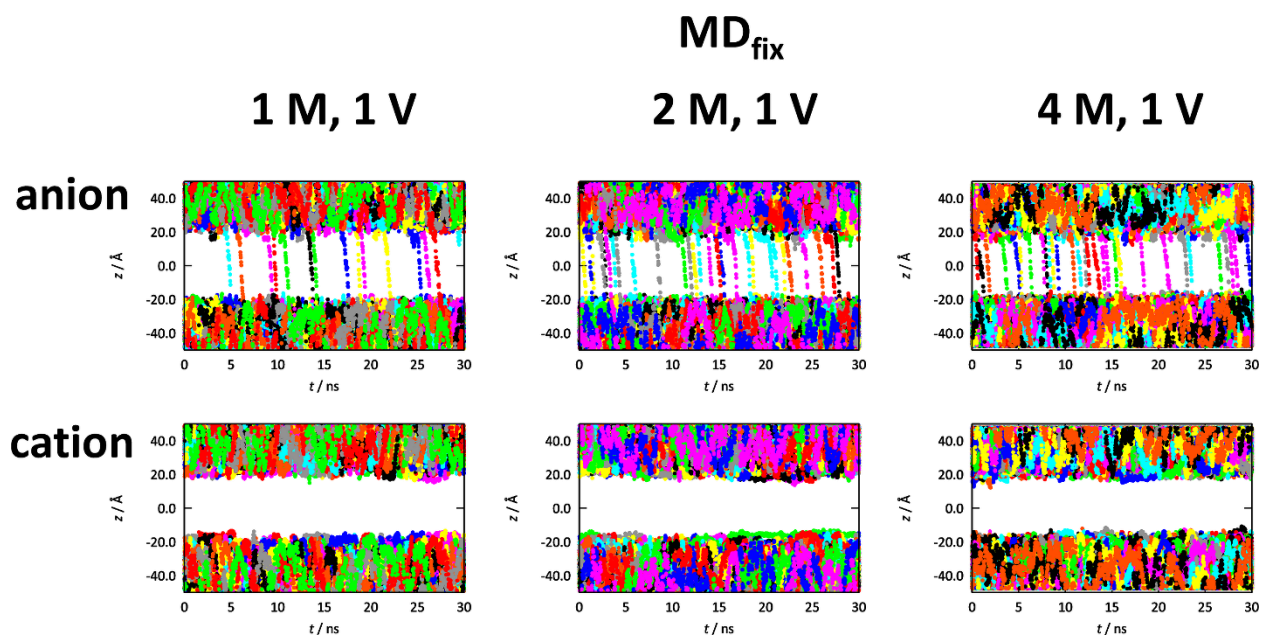
**Figure 5.4:** Illustration of the external field induced ion transfer in restrained $MD_{fix}$ simulations. Depiction of all anions (upper line) and cations (lower line) is shown for $MD_{fix}$ simulations with 1 M (left), 2 M (middle), 4 M (right). The $z$ position of each ion is shown as a single point. The unfilled middle belongs to the membrane slab. Occurring dotted lines are interpreted as transitions through the pore (table 5.3).

In contrast, charge transfer events through the perfectly arranged pore could be observed after addition of an external field with a potential corresponding to 1 V (fig. 5.4). Surprisingly not a single $K^+$ transition event was recognized in simulations with concentrations of 1 M, 2 M and 4 M (fig. 5.4a). In contrast, ascending with higher concentrations 14, 23 and 29 $Cl^-$ transitions through the same pore occurred (fig. 5.4b). The unexpectedly high frequency of ion transitions lead to theoretical conductance values of 74.8 pS, 122.8 pS, and 154.9 pS (table 5.4). As those values are based on counting of complete single ion transitions, its absolute value increases in distinct steps. Illustrating this relation, a single ion transition occurring within a simulation time of 30 ns changes the conductance by 5.3 pS, assuming an external potential of 1 V in this instance. This example demonstrates the sensitivity of the conductance to ion transitions. Higher concentrations are considered in the conductance calculation indirectly by an increased chance for occurring ion events. The cation channel activity observed by Gong et al. is in contrast to the here calculated high $Cl^-$ conductances.[6]

A summary of all obtained conductances in this chapter is provided in table 5.4.

**Table 5.4** Conductance result for MD and 3D RISM.

| System | pore | $\gamma_{MD}$ /pS | | $\gamma_{RISM}$ /pS | | $\gamma_{avg,struct}$ /pS | | $\langle\gamma\rangle$ /pS | |
|---|---|---|---|---|---|---|---|---|---|
| | | K$^+$ | Cl$^-$ | K$^+$ | Cl$^-$ | K$^+$ | Cl$^-$ | K$^+$ | Cl$^-$ |
| 0.1 M | fix | - | - | 18.4 | 74.1 | - | - | - | - |
| 1 M | fix | - | - | 171.9 | 440.1 | - | - | - | - |
| 1 M, 1 V | fix | 0.0 | 74.8 | - | - | - | - | - | - |
| 1 M, 0.1 V | free | 0.0 | 2.7 | - | - | 101.4 | 349.1 | 105.3 | 331.6 |
| 1 M, 1 V | free | 0.0 | 21.4 | - | - | 99.4 | 351.8 | 106.3 | 336.6 |
| 2 M | fix | - | - | 252.9 | 596.2 | - | - | - | - |
| 2 M, 1 V | fix | 0.0 | 122.8 | - | - | - | - | - | - |
| 4 M | fix | - | - | - | - | - | - | - | - |
| 4 M, 1 V | fix | 0.0 | 154.9 | - | - | - | - | - | - |

$\gamma_{MD}$ the conductance from MD simulation.
$\gamma_{RISM}$ describes the conductance values obtained from 3D RISM results.
$\gamma_{avg,struct}$ denotes the conductance based on a single average structure.
$\langle\gamma\rangle$ describes the mean over 30 single structure conductances.(see section mean conductance)
Results obtained with restraint pores are indicated by "fix" in opposite to "free".

## 5.3.2 Thermodynamic analysis of the restrained pore geometry

To conduct 3D RISM calculations with the hydrophobic pore, solvent files for the concentrations of 1 M and 2 M KCl were obtained for direct comparison with the MD simulation results, as well as an additional 0.1 M concentration, due to its physiological relevance. Solvent susceptibilities of higher concentrations could not be achieved due to convergence issues. Each of the described KCl concentrations (0.1 M, 1 M, 2 M) was applied to the restrained hydrophobic pore in individual 3D RISM calculations. The thermodynamic properties were characterized by calculation of their $c(z)$ profile, $K_c$ profile and $w(z)$ profile (fig. 5.5).
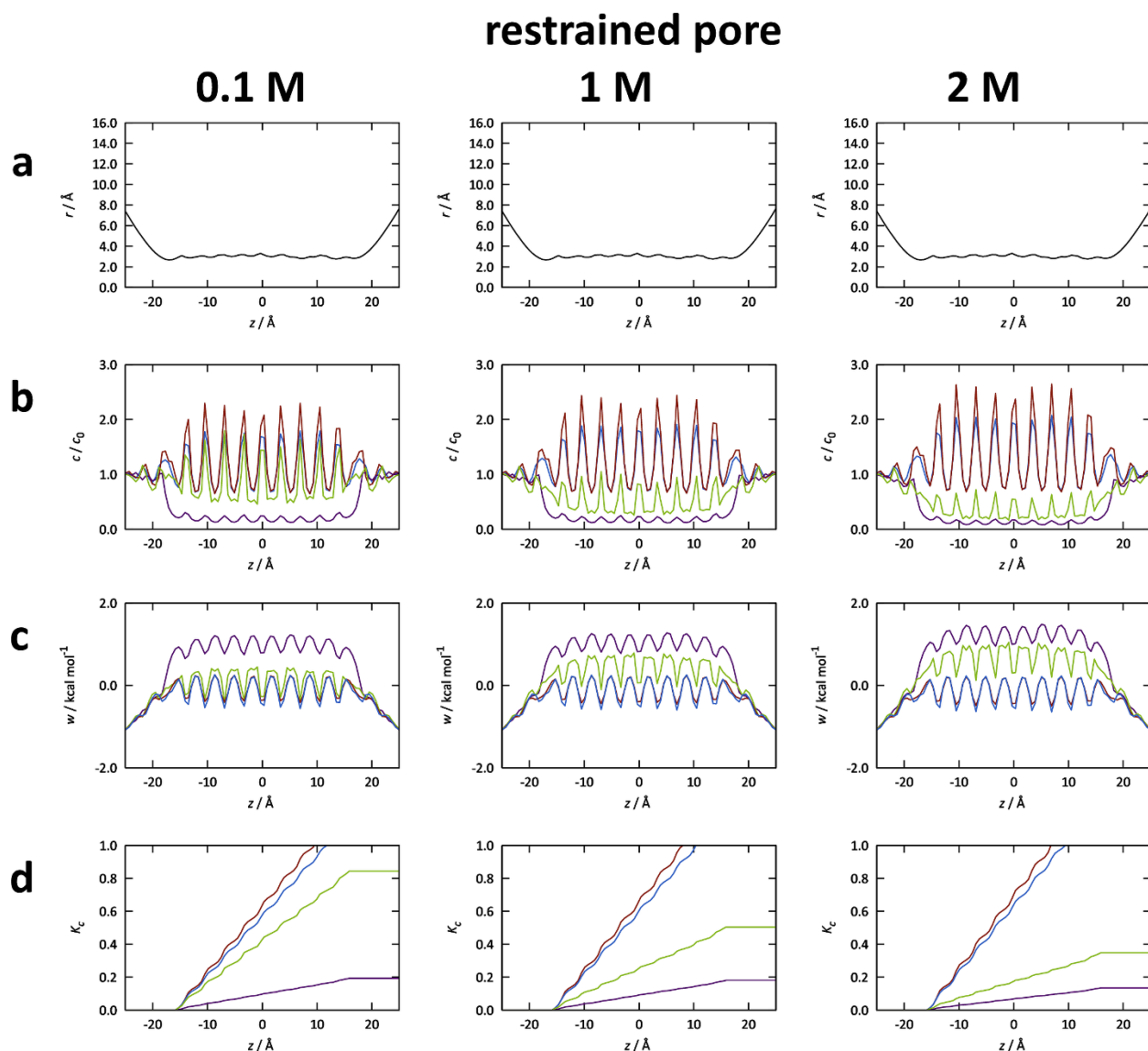
**Figure 5.5**: Thermodynamic profiles obtained by 3D RISM analyis with the restrained pore. Representation of the radius profile $r(z)$ **a** and the $c(z)$ **b**, $w(z)$ **c**, $K_c$ **d** profiles for the restrained pore in concentrations of 0.1 M, 1 M and 2 M KCl. The ions are represented in purple ($K^+$) und green ($Cl^-$). Water (oxygen: red; hydrogen: blue) is shown only in the $c(z)$ and $K_c$.

Inspection of these results reveals also an anion selectivity in accordance to the here observed enrichment of $Cl^-$ over $K^+$ represented in the $c(z)$ (fig. 5.5b). This result is consistently established in all studied concentrations. Still an effect of higher concentrations is characterized by gradually stronger depletion of ion species, while water is further enriched over the complete pore. The observed lower $K^+$ and $Cl^-$ peaks in the $c(z)$ for 1 M and 2 M KCl solutions are explained by their higher bulk concentration. But the detected concentration shrinking describes the effect of a beginning saturation, which is plausible at concentrations of 1 M and 2 M. The $c(z)$ profiles reveal

a super positioning for $K^+$ and $Cl^-$ as well as water, with an enrichment predominantly occurring between two monomers, while positions inside monomers are evaded. This can be inspected in comparison to the radius profile $r(z)$ (fig. 5.5a) and by illustration of the solvent distribution functions (fig. 5.6). Also the $c(z)$ profiles show a huge increase of water inside the pore for all concentration values. Thus the hydrophobic pore is suggested to possess a predominant permittivity for water, as corroborated by the vesicular experiments of Gong et al.[6] Examination of the free energy profile for ion transitions through the pore by $w(z)$ reveals only insignificant barriers with energies below 2 kcal mol$^{-1}$ (fig. 5.5c), which allow for ion conductance and ion flow through the pore in principle. Notably $w(z)$ implies an eased permeation for the anion due to the lower barriers for $Cl^-$. In comparison to the $r(z)$ the occurring barriers can be related to the restriction when passing through a monomer (fig. 5.5a). As the partition coefficients $K_c$ are calculated by integration of the $c(z)$ profiles, their final value represent the accumulated amount of a solvent species along the accessible volume of the pore. Thus the overall high concentration of $Cl^-$ and the discrimination of $K^+$ is represented by the higher final values found in all investigated concentrations (fig. 5.5d), while in analogy the corresponding values for water confirm its broad enrichment. The final $K_c$ $Cl^-/K^+$ ratios of 4.37, 2.80 and 2.57 for the concentrations of 0.1 M, 1 M and 2 M quantify the decreasing $Cl^-$ selectivity of the pore at higher concentrations. Finally the combination of surmountable barriers identified in the $w(z)$ profile, the small restrictions in the $r(z)$ profile and the concentration enrichment agreement between $c(z)$ and $K_c$ give reasons to propose an anion over cation selectivity for the investigated pore. The identified anion over cation selectivity of the hydrophobic pore is further supplemented by the independently gained MD results for the restrained pore. The anion selectivity of the restrained pore geometry is further supported, as they were obtained from independent techniques with a different theoretical background.

## 5.3.3 Restrained pore conductance

Combination of the calculated $w(z)$ and the equation 3.3.20 of Hummer et al. enables the calculation of conductance rates.[5] Conductance values of 18.4 pS (0.1 M), 171.9 pS (1 M) and 252.9 pS (2 M) were calculated by the application of equation 5.2 to the presented 3D RISM results (table 5.2). Corresponding values of 74.1 pS (0.1 M), 440.1 pS (1 M), and 596.2 pS (2 M) were stated for $Cl^-$ (table 5.4). A subscript notation was introduced to properly distinguish between the conductances $\gamma_{MD}$ and $\gamma_{RISM}$ obtained from MD and 3D RISM respectively.

As foreshadowed by the analysis of the 3D RISM results, the calculated $\gamma_{RISM}$ confirms the anion over cation selectivity of the fixed pore topology. In addition $\gamma_{RISM}$ increases with the concentration. This trend is also stated by the results of the MD simulations with an applied external potential of 1 V. Comparison of $\gamma_{RISM}$ and $\gamma_{MD}$ reveals significantly higher values for conductances based on the 3D RISM results. The disparity between $\gamma_{MD}$ and $\gamma_{RISM}$ results could be related by artifacts of the 3D RISM calculations. A visualization of the solvent distribution is provided by fig. 5.6 to illustrate the 3D density function $g(\mathbf{r})$.
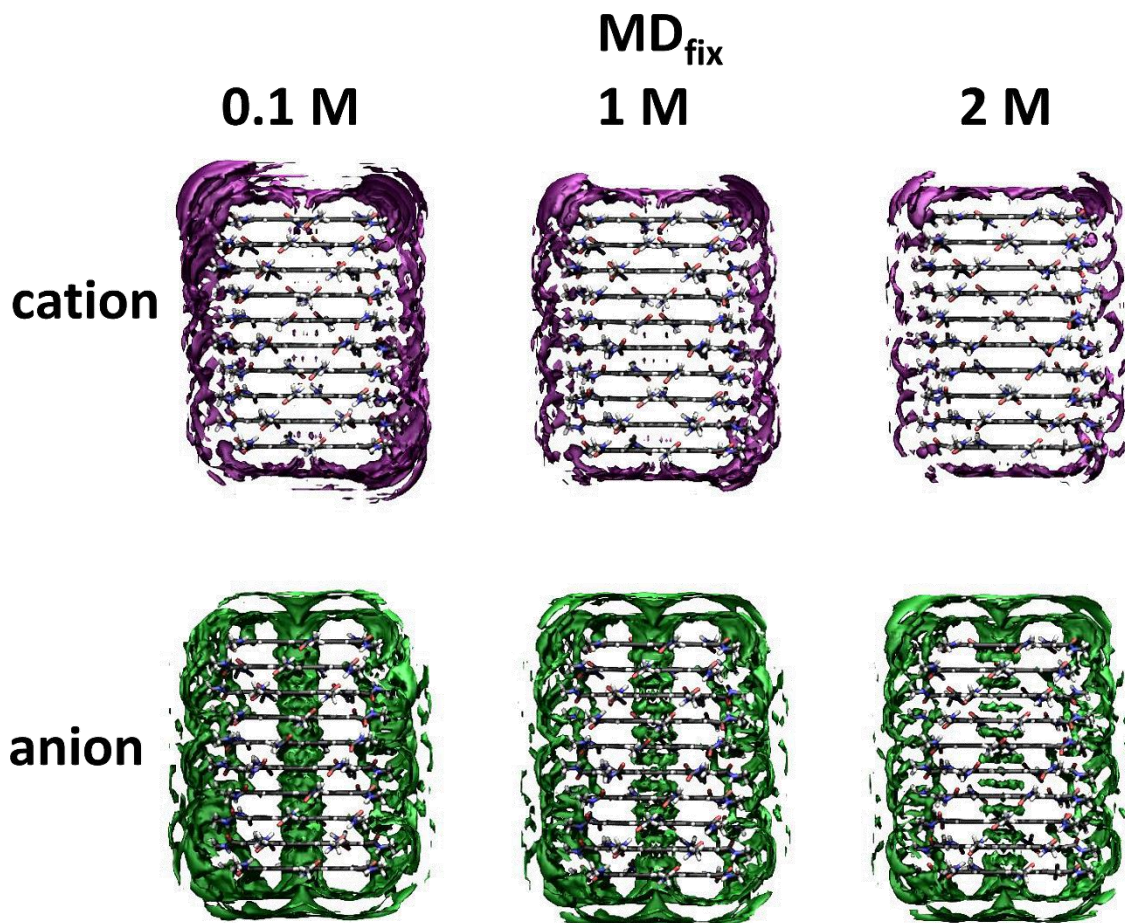


**Figure 5.6**: Density profiles for KCl in the restrained pore case. Representation of the $g(\mathbf{r})$ function around the fixed structure of the pore for concentrations of 0.1 M, 1 M and 2 M KCl. The densities are shown for $K^+$ (purple) and $Cl^-$ (green) separately in subpanels **a** and **b** at an isovalue of 1.15. Clipping planes were used to truncate the densities in the fore- and background, gaining a focus on the concentrations around and inside the pore.

Artificial effects due to the absence of a membrane for the presented 3D RISM results were excluded by test calculations performed with a POPC membrane (see methods). Their results revealed that $\gamma_{RISM}$ is invariant with regard to the use of a membrane (table 5.3). Furthermore equation 3.3.20 assumes ion transition without disturbing or auxiliary influences of other ions,

which is only guaranteed by low ion concentrations. The constant value for the diffusion coefficient $D(z)$, as used in equation 3.3.20 of Hummer et al., might also be criticized, as this quantity changes in association with local restrictions (see next chapter for detailed discussion).[5] However both methods, 3D RISM and MD simulation, are in agreement about the anion selectivity of the here investigated hydrophobic pore.

## 5.3.4 Dynamic pore studies

To investigate the results observed in the restrained case, further studies focused on the dynamic aspects onto the pore. Thus additional $MD_{free}$ simulations were conducted with flexible pore monomers. A focus was laid on KCl solutions of 1 M concentration as those was the most physiological important one with observed ion transitions. External fields were again applied during these $MD_{free}$ simulations, as permeation occurred only with an external field in the restrained case. Fields with a strength corresponding to 1 V Å$^{-1}$ and 0.1 V Å$^{-1}$ were chosen. These were applied to estimate the dynamics under physiological conditions (0.1 V Å$^{-1}$) as well as to gain a result directly comparable to the restrained case (1 V Å$^{-1}$).
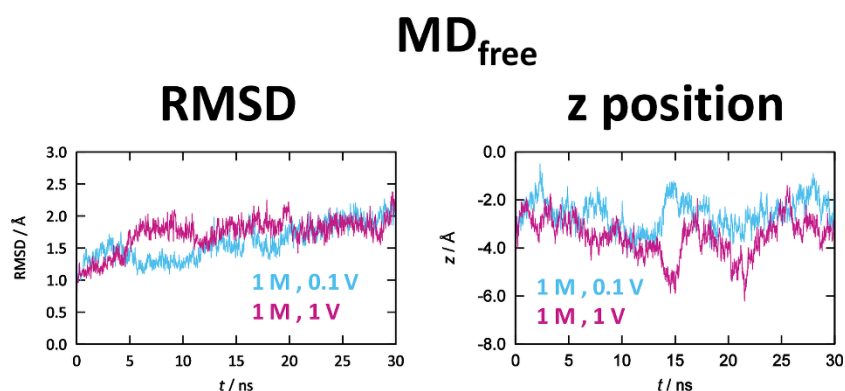


**Figure 5.7**: RMSD and $z$ position of the unrestrained pore. Representation of the RMSD (left) for the $MD_{free}$ simulations in 1 M KCl with a free pore geometry under external field conditions of 1 V Å$^{-1}$ (purple) and 0.1 V Å$^{-1}$ (light blue). The movement of the geometric center along the $z$ position is also shown (right) for both conditions with the same color code. $z$ positions were normalized in respect to the membranes geometric center.

The stability of the synthetic pore was quantified by its root mean square deviation (RMSD) and the movement of its geometric center in $z$ direction (fig. 5.7). The smooth progression of the RMSD (fig. 5.7, left) supports the stability of the simulation. Still in the first nanoseconds of the simulation an adaption of the system to the applied voltage can be observed. As the $z$ positions are normalized to the geometric center of the membrane, the RMSD analysis points out translational movements

of the pore inside the membrane. Nonetheless the pore is suitably incorporated in the membrane in accordance to the shifts of $\pm 3$ Å in $z$.

In accordance to the restrained case, ion transitions were investigated for the conducted $MD_{free}$ simulations of 0.1 V and 1 V (fig. 5.8) in KCl concentrations of 1 M. In analogy to the restrained case, only transitions of anions were observed, while cation transitions did not appear. In addition the anion transitions occurred with a much lesser frequency in comparison to the restrained case (table 5.4). A total of 4 Cl$^-$ transitions happen with a field of the 1 V Å$^{-1}$. With an even lower field of 0.1 V Å$^{-1}$ only two Cl$^-$ ions were found to enter the pore after 20-27 ns. As the latter of both entering Cl$^-$ ions crosses half of the pore before it returned back into the bulk phase, this event was counted as a transition with a value of 0.5. The deduced conductances calculated on the basis of 4 and 0.5 Cl$^-$ correspond to values of 21.4 pS and 2.7 pS. Conductances for K$^+$ are again 0.0 pS in both simulations, as no cation transitions occurred (fig. 5.8, b). A flexibility of the synthetic pore is accompanied by a diminished transition rate, expressed via reduction from 74.8 pS to 21.4 pS (table 5.4), in the restrained simulation at 1 M and 1 V.
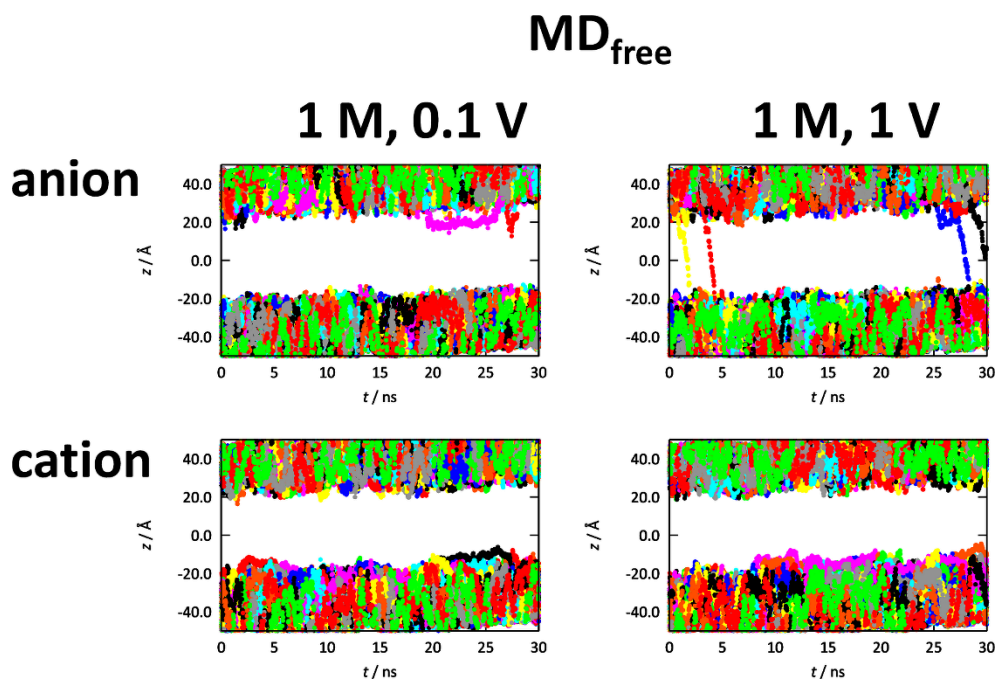


**Figure 5.8**: Illustration of ion transfer under dynamic conditions. A depiction of all anions (**a**) and cations (**b**) is shown for MD simulations with 1 M concentrations of KCl and an external field of 0.1 V Å$^{-1}$ (left) or 1 V Å$^{-1}$ (right). The $z$ position of each ion is shown as a point. The unfilled middle belongs to the membrane slab. Occurring dotted lines (**a**) are interpreted as transitions through the pore. Each ion is colored individually.

An illustration of adopted structures induced by changes happening during the unrestrained simulations in the presence of 0.1 V $Å^{-1}$ and 1 V $Å^{-1}$ external fields is given in Fig 5.9. For this purpose pore structures were extracted in a step size of 1 ns. Thereby a representative set of 30 different structures was created. The collection of snapshots clarifies the stability of the synthetic pore, as corroborated by the always connected monomers due to their π-π stacking interaction.[6] Sill individual monomers are shifted in the *x*, *y* plane slightly, leading to a narrowing of the inner radius. This observation might be related to a possible gating mechanism revealed by the measurements of Gong et al.[6]
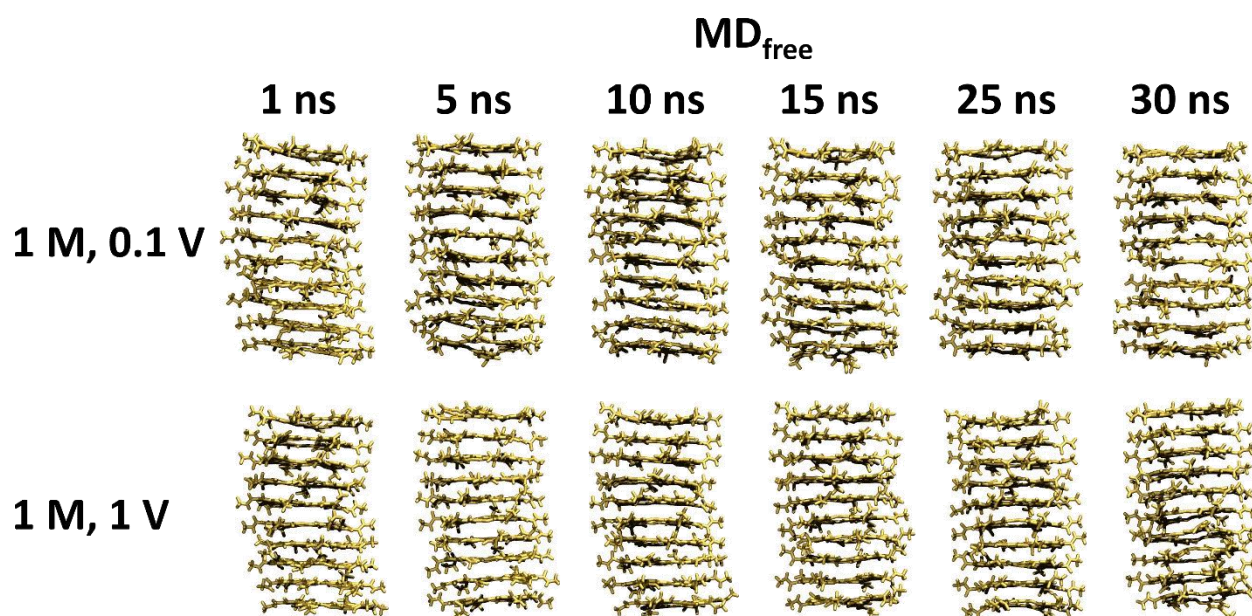


**Figure 5.9:** Pore structures of the unrestrained simulations MD$_{free}$. Visualization of the synthetic pore extracted from the 1M, 1V and 1 M, 0.1 V trajectories. The pore configurations are shown as licorice models for the times steps of 1 ns, 5 ns, 10 ns, 15 ns, 20 ns, 25 ns and 30 ns (left to right).

## 5.3.5 Investigation of the geometric average structure

To condense the information of all snapshots in a single structure, an geometric average structure was calculated for each of the MD$_{free}$ simulations with different external fields (fig. 5.10). The average structures are based on 30 structures taken from simulations of 1 M, 1 V or 1 M and 0.1 V. The obtained structures will be denoted as MD$_{free,avg}$ for clarification. As discussed in the methods section, the here conducted averaging process distinguishes from the calculated average structure of the Kcv$_{ATCV-1}$, due to its calculation of a simple geometric mean. Nevertheless calculation of a direct mean is only possible, if the structure is stable and vice versa does not deviate to much from

its origin. This is the case for the pore of Gong et al., as confirmed by the obtained RMSD values for the corresponding $MD_{free}$ simulations (fig. 5.7 and fig. 5.9). Comparison of the original structure with the calculated average structures by calculation of the RMSD between them, showed values of 1.34 Å for the 0.1 M, 1 V case and 1.40 Å for 1 M, 1 V. Besides their similarities small differences are recognized by the inspection of the accessible volume and the associated radius profile (fig. 5.10). The pore volume inside the restrained pore can be described as an approximated cylinder, whereas bending and wiggling motions occur at the lower parts (negative $z$ position) for the here investigated average structures.
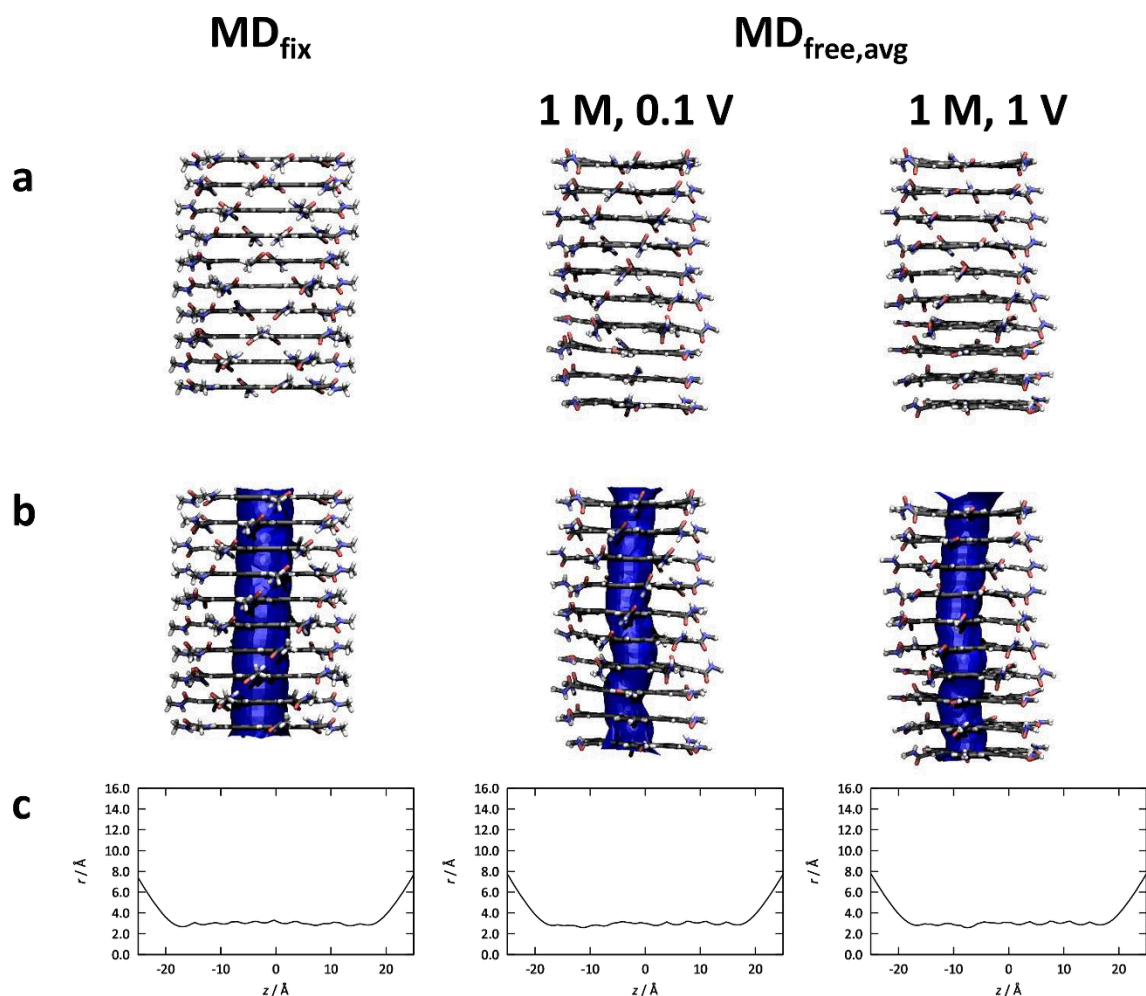


**Figure 5.10**: Comparison of the average structures. Licorice representation of the restrained pore (left column) and the generated average structures from unrestrained 1 M KCl MD simulations with external potentials of 0.1 V (middle) and 1 V (right). Overlay with the accessible volume (blue) is shown in row **b**. Corresponding radius profiles are shown in **c**.

The generated average structures allow for additional investigations with 3D RISM to get a complemental thermodynamic characterization for both structures (fig. 5.11). Thus both structures

were analyzed with 3D RISM calculations using a solvent concentration of 1 M. Investigation of the results state again an anion over cation selectivity, confirmed by the Cl$^-$ over K$^+$ enrichment, described by the corresponding $K_c$ and $c(z)$ profiles (fig. 5.11) as well as by their calculated conductances $\gamma_{avg}$ of 101.4 pS and 349.1 pS for K$^+$ and Cl$^-$ in the case of 0.1 V and 99.4 pS and 351.8 pS for the average structure originated at 1 V (table 5.4). However K$^+$ and Cl$^-$ are depleted over wide parts of the pore while water is still enriched. So considering the influence of motion due to averaging over structures obtained from unrestrained MD$_{free}$ simulations still confirms the anion over cation selectivity with also a high permittivity for water. In comparison with the rigid pore results (fig. 5.6) differences can be recognized for the profiles for $c(z)$, $K_c$ and $w(z)$ (fig. 5.11) localized at $z$ positions below -5 Å. These can be explained in respect to the previously described wiggling and bending motions found in the accessible volume (fig. 5.10).
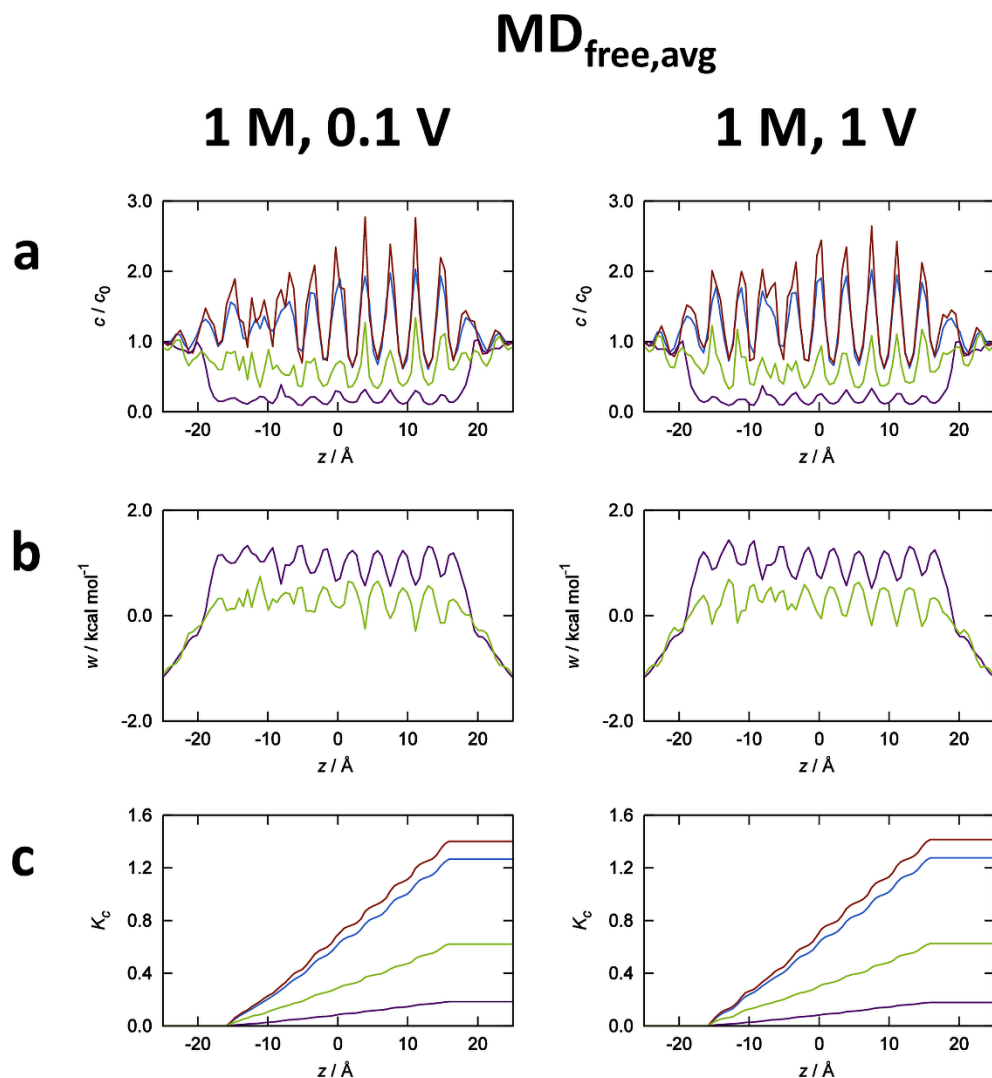
**Figure 5.11**: Thermodynamic investigation of the average structures. Representation of the $c(z)$ (**a**), $w(z)$ (**b**), $K_c$ (**c**) profiles for the average structures from unrestrained 1 M KCl MD$_{free}$ simulations with external potentials of 0.1 V (left) and 1 V (right). The ions are represented in purple (K$^+$) und green (Cl$^-$). Water (oxygen: red; hydrogen: blue) is shown in the $c(z)$, $K_c$ plots only.
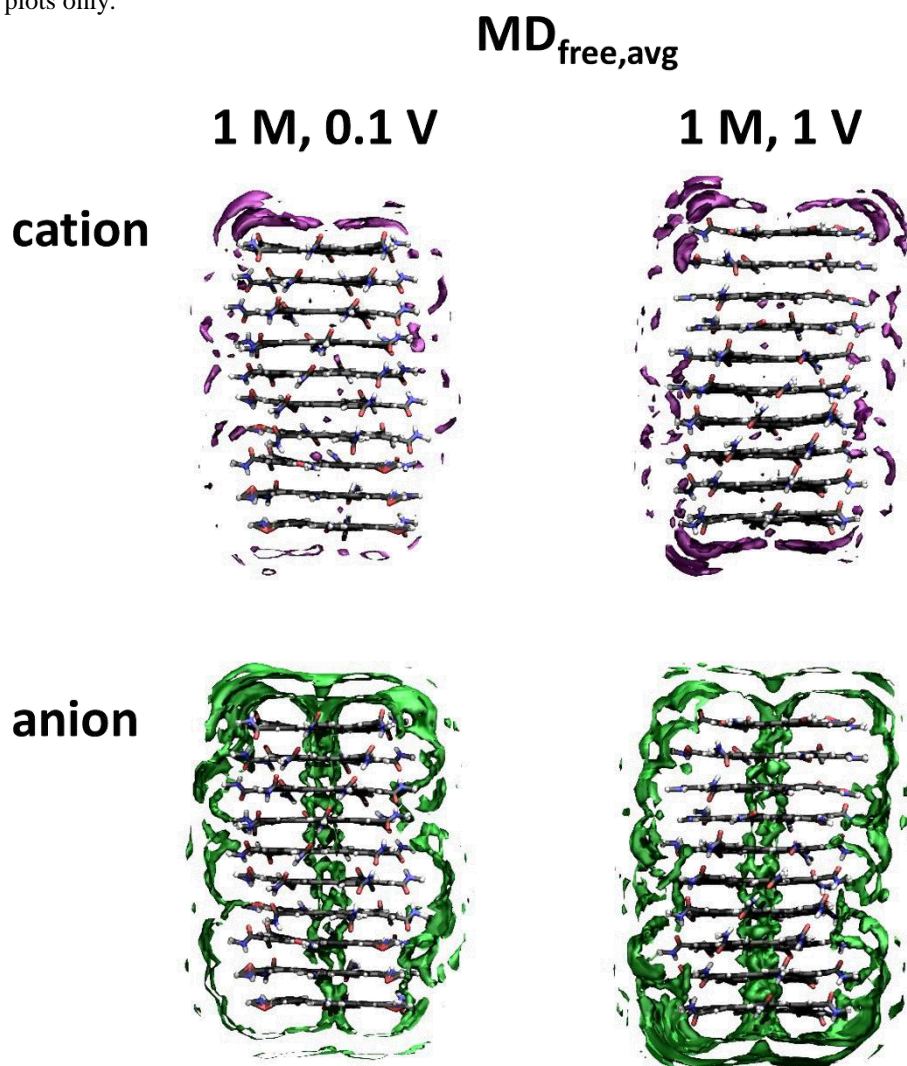


**Figure 5.12**: Ion density profiles. Visualization of the $g(\mathbf{r})$ of K$^+$ (purple) (**a**) and Cl$^-$ (green) (**b**) at an isovalue of 1.15. The concentration around the dynamic pore is illustrated for the average structures gained from simulations with external fields of 0.1 V and 1 V. Clipping planes were used to truncate the densities in the fore- and background, providing an illustraion of the concentrations around and inside the pore. VMD-1.9.1 was used for this procedure.[220]

## 5.3.6 Mean conductance

In addition to the analyzed average structures a simple mean conductance was calculated as further verification of the approach. The 30 topologies used for the calculation of the geometric mean were investigated by individual 3D RISM calculations, with a corresponding solvent concentrations of 1 M KCl. Thereby a total of 30 conductance values were created for each investigated MD$_{free}$

simulation (1 M, 0.1 V and 1 M, 1 V). The calculated single conductances was average to a mean conductance $\langle\gamma\rangle$, exhibiting values of 105.3 pS and 331.6 pS for $K^+$ and $Cl^-$ in the 1 M, 0.1 V case and values of 106.3 pS and 336.6 pS for the corresponding $K^+$ and $Cl^-$ calculations at 1 V (table 5.4). Due to the agreement of these conductances (table 5.4) with those of the earlier described averaged structures, the accuracy of the approach is further secured. However a difference between the RISM based conductances and those obtained from MD simulations still exists.

## 5.4 Conclusion

By the conducted investigations of the synthetic, hydrophobic pore with the presented dual approach of MD simulation and 3D RISM, a significant anion over cation permeability could be identified. This result is different from the cation selectivity reported by the authors Gong et al.[6] Notably the here presented anion selectivity was observed in an MD simulation system corresponding to those of Gong et al., with exception for the pore charges. The here presented results revealed an anion selectivity in restrained as well as unrestrained MD simulations with concentrations of 1 M, 2 M and 4 M KCl. An effect of the bulk concentrations on the ion selectivity could be identified, as increasing concentrations diminished the anion over cation selectivity ratio of the pore. This was also identified by thermodynamic analysis of 3D RISM calculations with ion solutions. An accompanied effect of saturation was also represented by the corresponding partition coefficient and concentration profiles. Derivation of the pmf with 3D RISM allowed the calculation of conductances in accordance to the theory of Hummer et al.[5] In comparison with MD simulations, pmf based conductances were significantly higher, but at the same time supported the anion selectivity of pore in all investigated geometries. The differences in the absolute values of $\gamma_{RISM}$ and $\gamma_{MD}$ could be related to artifacts in 3D RISM or due to the limitations of the eq. 3.3.20 of Hummer, as those assumes ion transitions to occur independent.[5] Such might not be the case at high concentration. Also high concentrations are known to affect the diffusion coefficient, which was not considered by the here applied constant $D(z)$ in eq. 3.3.20. Influences of the neglected membrane in the 3D RISM calculations could be excluded. Dynamic influences, investigated by unrestraint $MD_{free}$ simulations with applied fields and characterization of the corresponding average structures in 3D RISM, were revealed to diminish the ion conductance, confirmed by both methods.

Our results are in agreement with *in silico* observations for carbon nanotubes (CNT) by the group of Aluru et al., which also observed a $Cl^-$ over $K^+$ selectivity at an equivalent CNT radius.[91] Ion

permeation studies in the β barrel like pore protein VDAC32 confirm the here observed concentration effects and obtain also a $Cl^-$ over $K^+$ selectivity.

Still the here presented results and investigations confirmed the complemental character between MD simulations and 3D RISM. While MD simulations allow access to time scales that are often far from equilibrium, RISM allows to pass this shortcoming by sustaining the same ion selectivity. Notably the here presented generation of averages presented an application procedure for studying dynamic influences by 3D RISM in combination with the equations of Hummer.[5]

# 6 The putative ion channel phospholamban

## 6.1 Introduction

Recent experimental data of Smeazetto et al. (unpublished; private communication) reveal a cation selectivity for PLN, which is still under debate.[150,151,157,158] To shed light on the designated ion channel functionality of PLN, the structures 1ZLL and 1XNU were therefore thermodynamically and kinetically investigated by computational studies. The previously used parameter sets of Joung and Cheatham (JC) was applied for comparison with the parameter set from the CHARMM force field (CHA) for the investigation of PLN.[190,250] In the context of hydrophobic selectivity, two truncated versions of 1ZLL were also studied to evaluate the influence of the N-terminal cytosolic domain. As common representatives of the super family of pLGICs the cation selective receptor channel 5-HT$_3$R and the anionic selective GluCl channel were also tackled by 3D RISM for comparison with the results for PLN.[161,164] The influence of charge effects was scrutinized in all channels by artificial removing of charges, leading to pure hydrophobic pores.

## 6.2 Methods

## 6.2.1 Model preparation and numerical calculations

The protein structures 1ZLL, 1XNU, GluCl (pdb code: 4TWN) and 5-HT$_3$R (pdb code: 4PIR) were obtained from the protein data bank (PDB).[161,164] Only the M2 domain forming residues (given in brackets) were considered during the 3D RISM calculations of GluCl (aa 241-268) and 5-HT$_3$R (aa 247-271), as those form the core pore inside the membrane. Missing protons were added for GluCl and 5-HT$_3$R by PSFGEN in combination with the CHARMM force field.[190] All systems were aligned along the $z$ axis by VMD-1.9.1 and remained their titratable residues in the standard ionization state.[220]

## 6.2.2 Computational details for RISM

To obtain solvent susceptibilities the 1D RISM equations were solved on a logarithmic grid ranging from $5.98 \cdot 10^{-3}$ Å to 164.02 Å with a total of 512 points, using a modified inversion of iterative subspace (MDIIS)[251] and a temperature of 298.15 K.[211] Densities were chosen according to the 1D RISM parameters of chapter 4. [247,252] In contrast to chapter 5, a permittivity of 78.4 was used for all ion solutions as well as pure water. While using the parameters of the CHARMM force field

we applied the HNC closure, whereas the PSE closure in order 4 was applied in case of the Cheatham & Joung parameter set during the 1D RISM calculations.[190,250]

3D RISM equations were solved using the MDIIS to a tolerance of $10^{-4}$ on a grid of 130x130x180 points with a distance of 0.6 Å. A larger grid was chosen in case of 5-HT$_3$R and GluCl 3D RISM with dimensions of 160 x 160 x 160 and a point spacing of 0.6 Å. A PSE closure of order 3 was used during the 3D RISM calculations for 5-HT$_3$R and order 4 for GluCl. A benchmark of the closure relations is provided in the *Appendix* (fig. A9.2, A9.3). Electrostatics were computed using Ewald summation under conducting boundary conditions.[253] Net-charged systems were treated with a special renormalization procedure.[207] All accessible internal volumes were sampled by HOLE.[215] Integration of the distribution functions $g_i(\mathbf{r})$ within this corresponding HOLE volumes was used to compute 1D concentration profiles along the channel axis according to chapter 3.4.[53] Equilibrium constants were obtained by integration of concentration profiles and normalization to the core volume (table 6.1). One-dimensional pmfs $w(r)$ were obtained according to equation 3.3.20 on basis of the calculated $c(z)$ profiles.

**Table 6.1**: System and analysis overview for 3D RISM calculations

| Ion channel | grid dimension $(x,y,z)$ | grid space $(x,y,z)$ | closure | lower border | upper border | volume Å³ | $q_{\text{sys}}$ / $q_{\text{no}}$ /e |
|---|---|---|---|---|---|---|---|
| 1ZLL | 130 x 130x 180 | 0.6 Å | PSE-4 | -33.3 | 31.5 | 1066.17 | 20/0 |
| 1XNU | 130 x 130x 180 | 0.6 Å | PSE-4 | -35.1 | 24.9 | 700.90 | 15/0 |
| 1ZLL$_{\Delta 1-27}$ | 130 x 130x 180 | 0.6 Å | PSE-4 | -33.3 | 9.9 | 1066.17 | -5/0 |
| 1ZLL$_{\Delta 1-23}$ | 130 x 130x 180 | 0.6 Å | PSE-4 | -33.3 | 5.1 | 1066.17 | 5/0 |
| 5-HT$_3$R | 200 x 200 x 200 | 0.6 Å | PSE-3 | -23.1 | 20.7 | 2038.4 | -5/0 |
| GluCl | 200 x 200 x 200 | 0.6 Å | PSE-4 | 22.5 | -23.7 | 3283.0 | 5/0 |

$q_{\text{sys}}$ describes the total charge of the protein.
$q_{\text{sys}}$ denotes the total charge of the protein the uncharged case.
The given volume was used for the $K_c$ normalization.
Upper and lower border values were used for the later calculation of the conductance $\gamma$.

## 6.3 Results

### 6.3.1 Experimental conductance

To investigate the designated ion channel functionality of PLN, electrophysiological measurements were carried out by Serena Smeazzetto, provided in private communication, using an established two chamber system.[254] The PLN pentamers were therefore reconstructed in planar lipid bilayers of diphytanoylphosphatidylcholine (DPhPC) allowing *in vitro* measurements for solutions of NaCl, KCl, and CsCl in symmetric concentrations of 0.1 M. A linear fit model with zero intercept was used to obtain the experimental conductances, leading to the final models of $I/pA = 0,0091 (\pm 0.0002) \cdot x/mV$ , $I/pA = 0.0164 (\pm 0.0001) \cdot x/mV$ and $I/pA = 0.0371 (\pm 0.0004) \cdot x/mV$ for the laboratory results of NaCl, KCl and CsCl. The intercept was restrained to the origin in all regressions. The results reveal a clear cation conductance with a selectivity order of $Cs^+ > K^+ > Na^+$ (fig 6.1) according to their conductances in table 6.2. Considering the bigger ion radius it is unusual for $Cs^+$ to be favored over the smaller cations $Na^+$ and $K^+$. During the single channel recordings effects of opening and closing events occurred (fig 6.1, bottom insert), indicating a gating-like functionality. The observation of gating processes supports the ion channel hypothesis as well as it excludes membrane defects as possible errors. Further control experiments with TRIS-P and TRIS/Cl were carried out by Smeazzetto (fig 6.1, left inset), eliminating anionic influences on the measured cation conductances. Despite the obtained cation selectivity no significant conductance for $Cl^-$ was stated. Based on the experimental results of Smeazzetto, PLN pentamers are suggested to form cation selective hydrophobic pores.

**a**
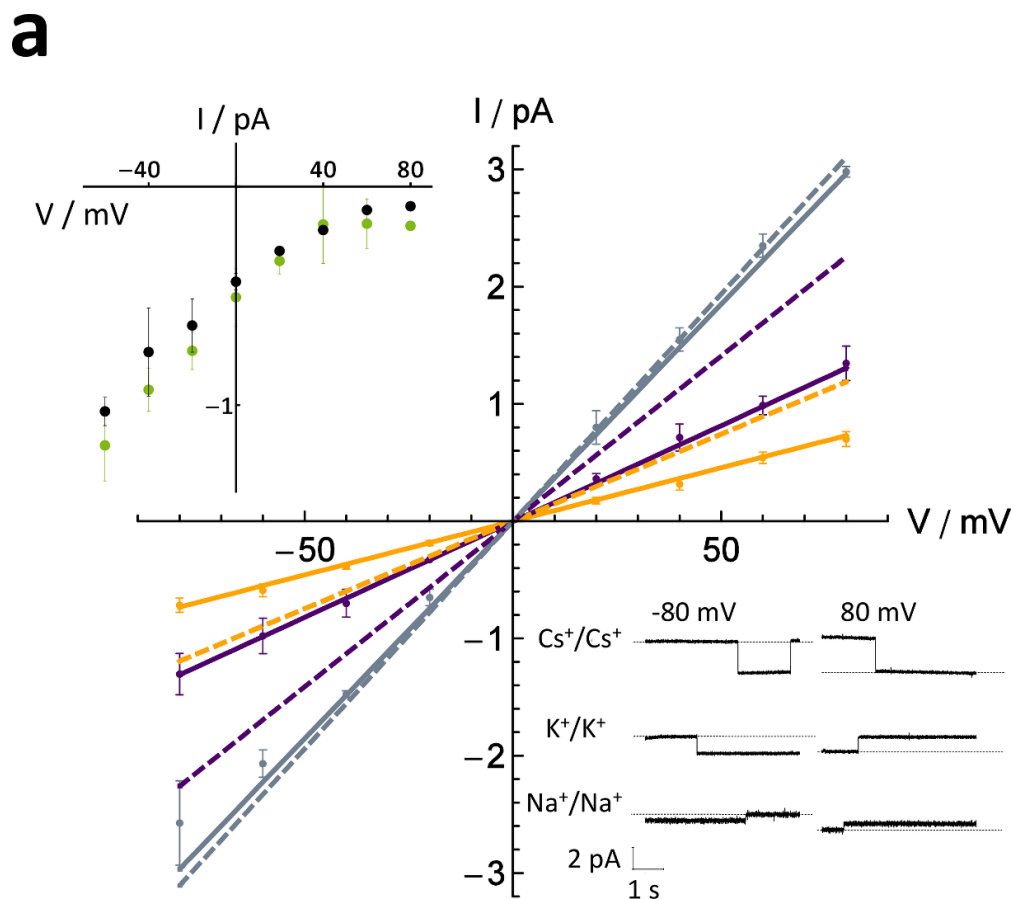


**Figure 6.1:** Experimental and theoretical conductances. Electrophysiological results of Na$^+$ (orange), K$^+$ (purple), and Cs$^+$ (Gray) with corresponding standard errors. Solid lines correspond to the experimental fit. Theoretical conductances are shown in dashed lines. Corresponding single channel currents are shown in the lower right inset, while conductance results in TRIS-P (black) and TRIS/Cl (green) with corresponding standard error bars are shown in the upper left inset.

## 6.3.2 Structure analysis of PLN

The observed ion channel functionality of pentameric PLN raised the question about the origin of a general cation over anion selectivity and the inter-cationic order. This was addressed by combination of theoretical approaches starting with an investigation of 1ZLL and 1XNU.[146–148] Both structures are comprised of 52 amino acids (aa) providing a charge of +3 for 1XNU and +4 in 1ZLL per monomer (table 6.1).

**1ZLL**: MEKVQYLTRSAIRRASTIEMPQQARQ**K**LQNLFINFCLILICLLLICIIVMLL
**1XNU**: MEKVQYLTRSAIRRASTIEMPQQARQ**N**LQNLFINFCLILICLLLICIIVMLL

**Figure 6.2**: One letter sequences of 1ZLL and 1XNU. Differences are shown in bold format.

The charge difference is explained by a difference in residue 27 (fig. 6.2), which is a Lysine in 1ZLL and an Asparagine in 1XNU. By accumulation of the positive charges in the N-terminal

94

amphiphylic helices a strong dipol moment is created. The stability of the pentameric complex is provided by an isoleucin/leucin (aa Ile33 – Leu51) zipper motive inside their transmembrane (TM) helices ranging from -33,3 Å to -0.3 Å for 1ZLL and -35.1 Å to -0.3 Å for 1XNU.[146] Through the nonpolar nature of this TM residues a hydrophobic funnel is created containing restrictions with radius 1.30 Å for *pinwheel* (1XNU) and 2.00 Å for the *bellflower* (1ZLL) at their narrowest points. Experimental quantification by Smeazzetto et al. identified a radius of 2.2 Å for the restriction of PLN, which is in agreement with the structure of 1ZLL.[151] Such restrictions are commonly identified to exhibit unsurmountable entropic barriers.[73,158] Nonetheless MD simulations of anionic single walled carbo nanotubes (ANT) with radii $< 2$ Å were permeable to water, according to the results of Sumikama et al.[120] Aspects of the restriction in context of entropic barriers are investigated in chapter 7 in detail. The accessible inner core volume was estimated ranging from the C-terminus up to the beginning of the cytosolic domains (Fig 6.3 arrows) yielding 1066.17 Å$^3$ for the *bellflower* configuration. The significant lower volume of 700.90 Å$^3$ in the *pinwheel* structure is related to its much tighter tertiary TM structure caused by its flattened cytosolic helices perpendicular to the membrane normal. In contrast, the conformation of the outer cytosolic helices in *bellflower* induces a stronger bent in its TM helices leading to a constant broadening of the funnel radius from the restriction up to the cytosolic N-terminus (fig 6.3).

## 6.3.3 Thermodynamic properties of PLN

3D RISM *uv* results permit the observation of local equilibriums concentrations $c(z)$ along the pores $z$-axis, describing depletion and enrichment in comparison to the bulk concentration $c_0$ (chapter 3.3). By subsequently integration over $c(z)$ (table 6.1) and normalization to the channel volume $V_{Ch}$, partition constants $K_c$ are derived, which are an criteria for the quantification of thermodynamic ion selectivity. Energetic barriers are characterized by the one dimensional pmf $w(z)$, which is acquired by stepwise integration of the $g(\mathbf{r})$ function inside small cylindrical elements and normalization to reference area. This pmf permits access to the calculation of theoretical conductances in accordance to Hummer et al. and allows to study kinetic influences on the process of ion selectivity.[5]
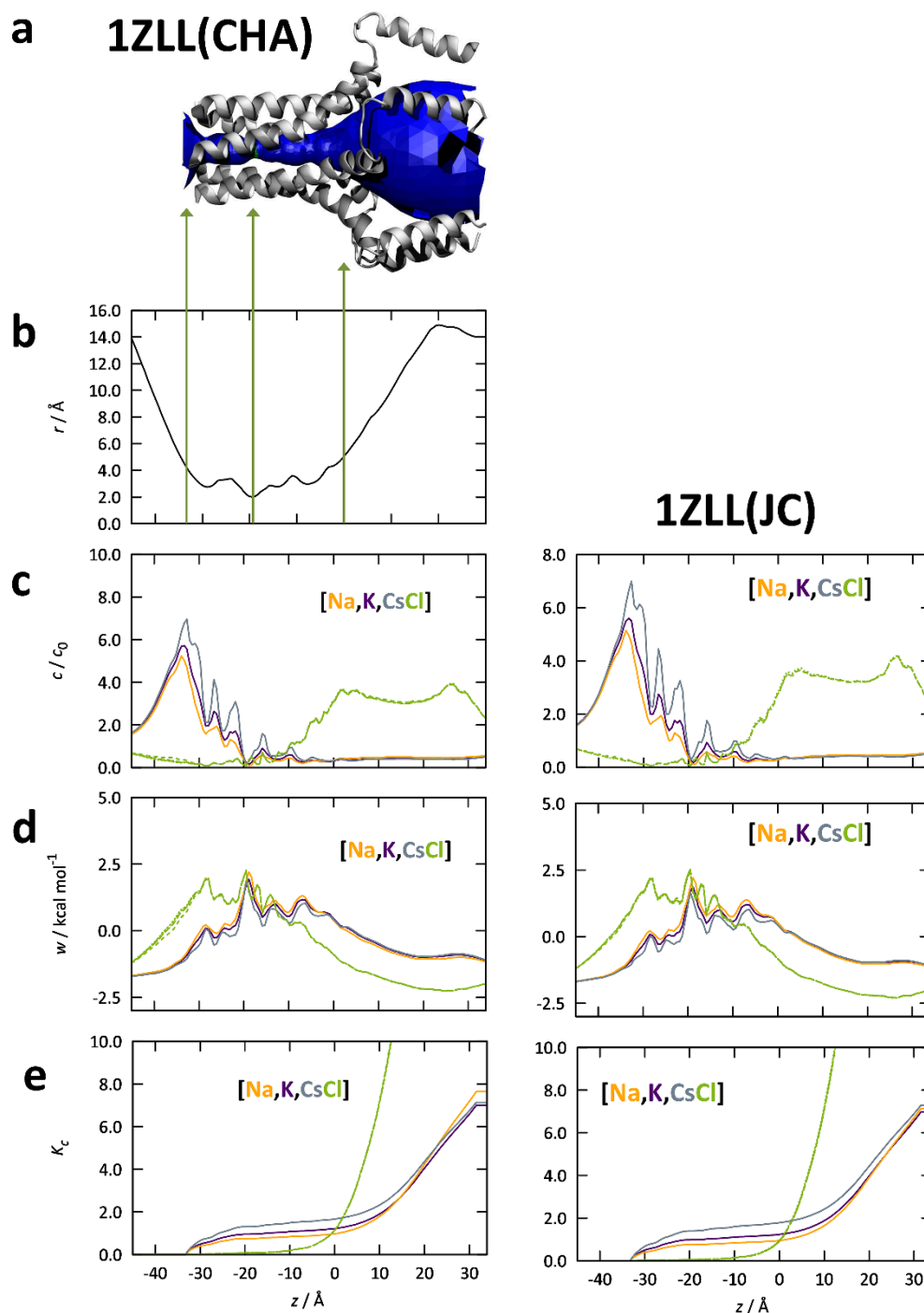
**Figure 6.3**: Selectivity profiles of 1ZLL(CHA) and 1ZLL(JC). **a** Cartoon depiction of the 1ZLL structure overlayed with its accessible core volume (blue). The resulting radius profile is shown in **b**. Outer arrows frame borders of the core volume. Subfigures **c**, **d** and **e** depict the concentration profile, the partition coefficient profile and the pmf for 1ZLL(CHA) (left) and 1ZLL(JC) (left). The arrow points at the constriction position. The volume was sampled by HOLE. Results for the cations $Na^+$ (orange), $K^+$ (purple), and $Cs^+$ (gray) are depicted. Their corresponding $Cl^-$ data are shown as dotted (CsCl), long dashed (NaCl) and short dashed lines (KCl).

96

Results from 3D RISM calculations with concentrations of 0.1 M NaCl, KCl and CsCl using the ion parameters of the CHARMM22 force field or Joung and Cheatham reveal charge driven accumulations of cations at the C-termini and corresponding Cl$^-$ accumulated at the N-termini (fig 6.3).[190,250] Regarding the two different parameter sets, no significant differences between the concentration profiles of 1ZLL(JC) and 1ZLL could be identified (fig. 6.3), further supporting the equivalence of both sets. The evaluated cations show no significant influence on the Cl$^-$ concentration (fig 6.3). Contrary to the ions, water is distinctly distributed inside 1ZLL(JC) and 1ZLL, characterized by alternated depletion and increase over the whole funnel (fig. 6.3).

A single $K_c$ value at a given $z$ position reflects the accumulated concentration till then. In case of 1ZLL and 1XNU, the hydrophobic funnel extends from a lower border (table 6.1) to the exterior transition, localized at $z = -0.3$ Å. Interpretation of the calculated $K_c$ values at this position show a distinct cation selectivity of order Cs$^+$ > K$^+$ > Na$^+$ for the *bellflower* (fig 6.3) as well as for the *pinwheel* (fig. 6.4), reflecting the same order as the conductance measurements of Smeazzetto (table 6.2). In spite of that, both parameter sets have the same cation selectivity order, the experimentally predominant selectivity for Cs$^+$ is slightly better reproduced in 1ZLL(JC) than in 1ZLL (table 6.3). In comparison the partition coefficient in 1ZLL is characterized by a smooth progression (fig. 6.3), while a stepwise increase of the selectivity can be observed in 1XNU (fig. 6.4). In 1ZLL the ion selectivity is already exhibited slightly before the geometric constriction and is than preserved over the complete hydrophobic volume of the TM pore (fig 6.3d). Selectivity elements like the common filter motive of tetrameric ion channels are absent in these channels, elsewise sudden changes would occur in the $K_c$ profile. Focusing on the anion, Cl$^-$ reveals a similar selectivity in comparison to Na$^+$ as indicated by their partition coefficients at $z$ position -0.3 Å. Still, the experiments of Smeazzetto et al. excluded a permittivity of Cl$^-$ (fig. 6.1) in PLN. As $K_c$ values reflect accumulated concentrations, the calculated Cl$^-$ selectivity can be explained by the increasing anion concentrations at the exterior mouth, which is partially included due to chosen $z$ position of -0.3 Å (fig. 6.3). This demonstrates the dependency of the $K_c$ value on the chosen $z$ position and might hereby have a limited significance as a selectivity predictor.

In addition to the thermodynamic investigation of the full 1ZLL and 1XNU structures, two deletion mutants were generated on the basis of 1ZLL by removing the first 23 (1ZLL$_{\Delta 23}$) or 27 (1ZLL$_{\Delta 27}$) amino acids. Truncation of the N-terminus results in a lower total charge of the proteins (table 6.1).

In consequence the strong dipole of the wild type is diminished in these toy systems, while the funnel forming transmembrane helices are still present. The previously observed accumulation of Cl⁻ at the N-terminus of the wildtype 1ZLL is nearly absent in both truncated structures, according to their $c(z)$ profiles. As the truncated mutants still consist of the membrane embedded pore, the $K_c$ transition According to the obtained $K_c$ values for $1ZLL_{\Delta23}$ and $1ZLL_{\Delta27}$ the wildtype ion selectivity order $Cs^+ > K^+ > Na^+$ is maintained in both deletion mutants.

**Table 6.2** Thermodynamic and kinetic data

| | Ion | | $Na/Cl_{NaCl}$ | $K/Cl_{KCl}$ | $Cs/Cl_{CsCl}$ |
|---|---|---|---|---|---|
| $\gamma_{exp}$ [pS] | PLN | | $9.1 \pm 0.0002$/n.a | $16.4 \pm 0.0001$/n.a. | $37.0 \pm 0.0004$/n.a. |
| | 1ZLL | CHA | 14.88/16.70 | 28.23/16.08 | 38.81/16.40 |
| | 1ZLL | CHA,uncharged | 16.05/22.93 | 36.35/22.93 | 57.48/22.93 |
| | 1ZLL | JC | 13.95/10.79 | 28.25/10.81 | 42.80/11.79 |
| | 1ZLL | JC,uncharged | 16.6/13.92 | 39.38/14.69 | 67.22/16.46 |
| | $1ZLL_{\Delta27}$ | CHA | 20.92/13.67 | 40.70/13.31 | 56.56/13.68 |
| | $1ZLL_{\Delta27}$ | CHA,uncharged | 16.57/23.26 | 36.88/24.50 | 59.37/26.07 |
| $\gamma_{theo}$ [pS] | $1ZLL_{\Delta23}$ | CHA | 15.64/16.53 | 30.13/15.94 | 42.21/16.24 |
| | $1ZLL_{\Delta23}$ | CHA,uncharged | 16.61/23.28 | 36.97/24.51 | 59.44/26.12 |
| | 1XNU | CHA | 0.68/0.00 | 0.60/0.00 | 0.00/0.00 |
| | 1XNU | CHA,uncharged | 0.91/0.00 | 1.19/0.00 | 0.00/0.00 |
| | $5HT_3R$ | CHA | 41.74/17.99 | 56.06/10.59 | 7.77/6.64 |
| | $5HT_3R$ | CHA,uncharged | 16.61/27.19 | 34.53/28.63 | 55.66/30.07 |
| | GluCl | CHA | 15.41/69.54 | 25.27/63.68 | 34.67/61.67 |
| | GluCl | CHA,uncharged | 28.12/51.25 | 52.10/53.22 | 80.27/57.41 |
| $\gamma_{theo,FJ}$ [pS] | 1ZLL | CHA,FJ | 15.26/17.11 | 28.91/16.48 | 39.63/16.54 |
| | 1ZLL | CHA,charged | 0.97/1.07 | 1.21/1.07 | 1.66/1.09 |
| | 1ZLL | CHA,uncharged | 0.04/0.05 | 0.05/0.04 | 0.08/0.04 |
| | 1ZLL | JC,charged | 0.94/0.85 | 1.23/0.85 | 1.77/0.89 |
| | 1ZLL | JC,uncharged | 0.04/0.03 | 0.06/0.03 | 0.09/0.03 |
| | $1ZLL_{\Delta27}$ | CHA,charged | 0.99/0.99 | 1.23/1.00 | 1.69/1.02 |
| | $1ZLL_{\Delta27}$ | CHA,uncharged | 0.23/0.23 | 0.29/0.24 | 0.43/0.25 |
| $K_c$ (-0.3 Å) | $1ZLL_{\Delta23}$ | CHA,charged | 1.16/0.64 | 1.44/0.65 | 1.96/0.67 |
| | $1ZLL_{\Delta23}$ | CHA,uncharged | 0.23/0.23 | 0.29/0.24 | 0.43/0.25 |
| | 1XNU | CHA,charged | 1.97/0.82 | 2.35/0.82 | 3.30/0.84 |
| | 1XNU | CHA,uncharged | 0.12/0.10 | 0.10/0.09 | 0.24/0.10 |
| | $5HT_3R$ | CHA,charged | 1.96/0.35 | 1.77/0.40 | 1.58/0.56 |
| | $5HT_3R$ | CHA,uncharged | 0.38/0.39 | 0.40/0.37 | 0.56/0.42 |
| | GluCl | CHA,charged | 0.11/1.64 | 0.09/1.67 | 0.10/1.70 |
| | GluCl | CHA,uncharged | 0.26/0.28 | 0.29/0.29 | 0.40/0.31 |
| $D(z)$ [m² s⁻¹] | | | $1.33 \cdot 10^{-9}$ /$2.30 \cdot 10^{-9}$ | $1.96 \cdot 10^{-9}$ /$2.30 \cdot 10^{-9}$ | $2.05 \cdot 10^{-9}$ /$2.30 \cdot 10^{-9}$ |

$K_c$ (-0.3 Å) denotes the $K_c$ value obtained at position $z = -0.3$ Å.
$\gamma_{exp}$ identifies the experimental values provided by Smeazzetto et al.
$\gamma_{theo}$ is the calculated conductance.
CHA and JC assign the parameter set of CHARMM or Joung & Cheatham.
"charged" and "uncharged" indicate the polarization status of the protein.
1ZLL and 1XNU assign the PLN structures.
$\Delta27$ and $\Delta23$ describe truncated mutants.
5-$HT_3R$ and GluCl designate abbreviations for Cys-Loop channels.
$D(z)$ denotes the diffusion constant.[218]
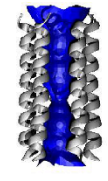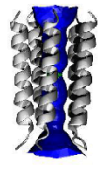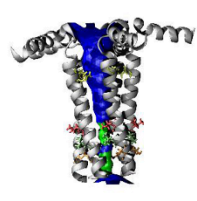$\gamma_{theo,FJ}$ denotes the a calculated conductance with a varied local $D(z)$.[219]
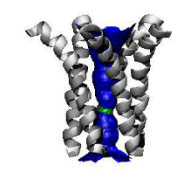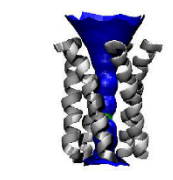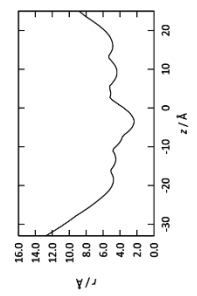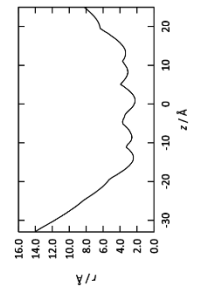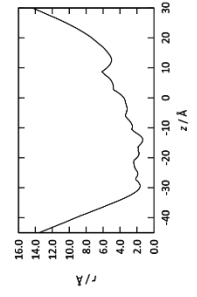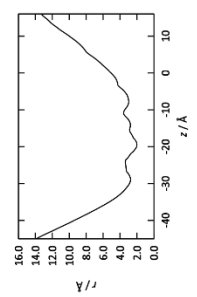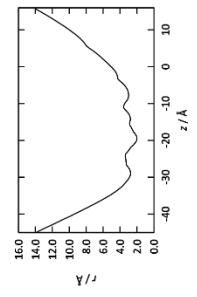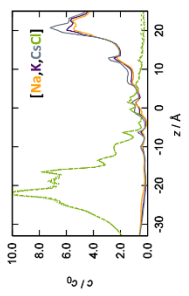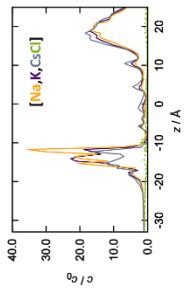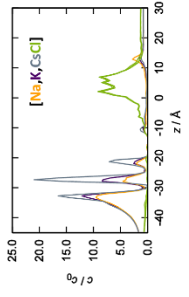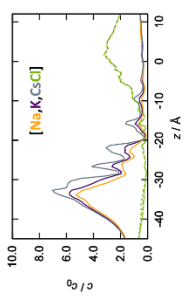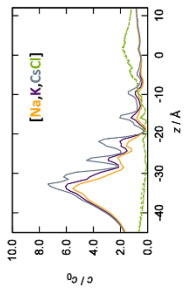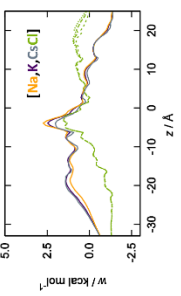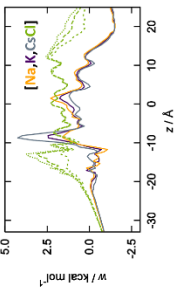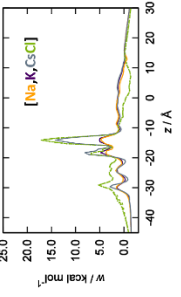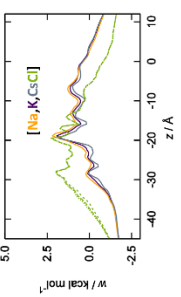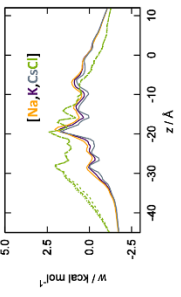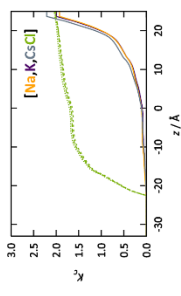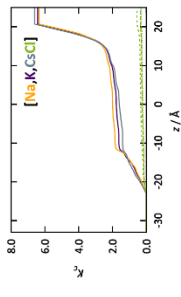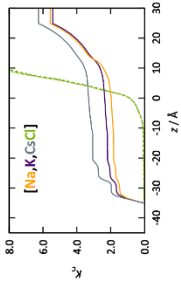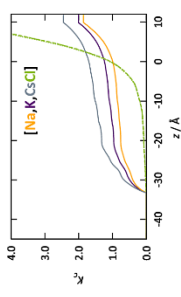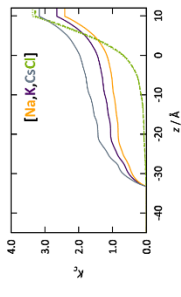
**Figure 6.4:** Charged structure profiles. Cartoon representation of the tertiary structure for the deletions mutants $1ZLL_{\Delta 27}$ and $1ZLL_{\Delta 23}$, GluCl, 5-HT$_3$R and the closed PLN structure 1XNU in **a** (accessible volume blue). Corresponding radius profiles are given in subfigure **b**. The $c(z)$, $w(z)$ and $K_C$ profiles for all channels are shown in **c**, **d** and **e**. Data for the cations Na$^+$ (orange), K$^+$ (purple), and Cs$^+$ (gray) are depicted. Their corresponding Cl$^-$ results are shown as dotted (CsCl), long dashed (NaCl) and short dashed lines (KCl). The CHARMM parameter set was used for all calculations.

## 6.3.4 Effect of net charges

The structure of 1ZLL is characterized by a strong dipole moment due to the accumulated charges at cytosolic N-terminus. For this reason, calculations without charges were carried out and analyzed alike to their charged variants. By artificially neglecting charges, the channel could be assumed to be completely hydrophobic. The derived $c(z)$ profiles for 1ZLL(CHA,uncharged) and 1ZLL(JC,uncharged) (dig. 6.5) are clearly distinguished by alternations of increasing and decreasing concentrations over the whole channel. Artifacts due to the chosen parameter set could be excluded, as the revealed changes were the same in 1ZLL(JC,uncharged) as in 1ZLL(CHA,uncharged). Nevertheless the increasing and decreasing alternations were more intense in calculations with the parameters of Joung and Cheatham. Despite the changes in the $c(z)$ profile, the corresponding $K_c$ values preserved the same inter-cationic selectivity order and anion discrimination as in the wildtype 1ZLL (table 6.2, fig. 6.3).
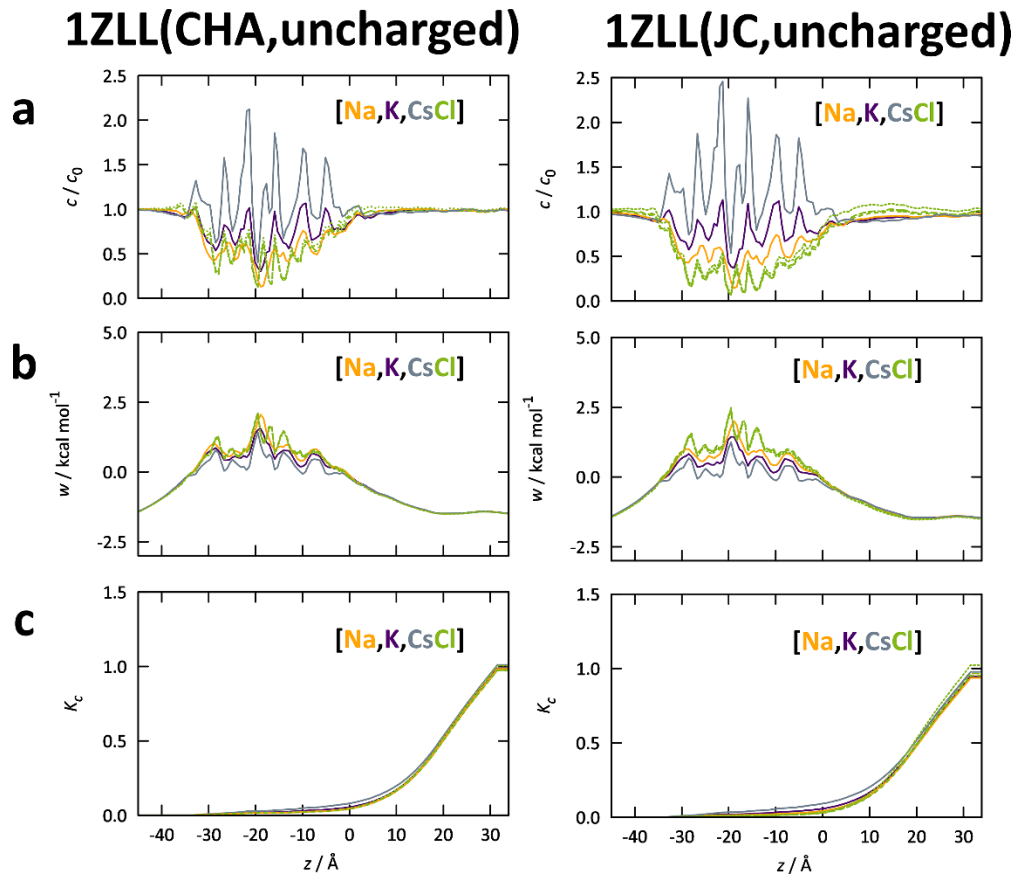


**Figure 6.5:** Variation of charge in 1ZLL(CHA,uncharged) and 1ZLL(JC,uncharged). **a** Depiction of the $c(z)$, $w(z)$ and $K_c$ profiles for 1ZLL(CHA,uncharged). Analogue results using the parameter set JC are given in **b**, **c**. Colors follow and line types follow fig. 6.3.
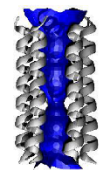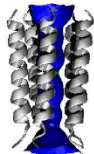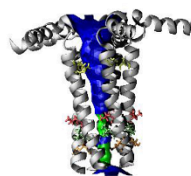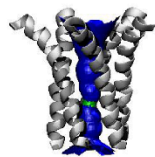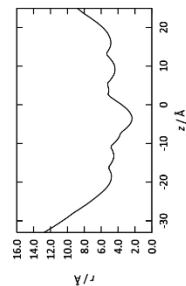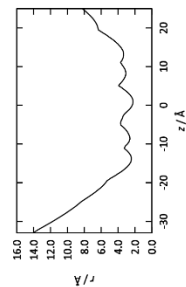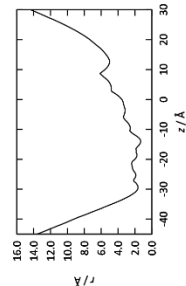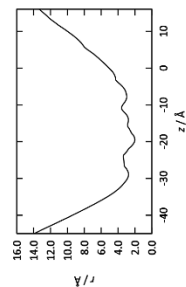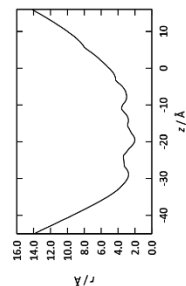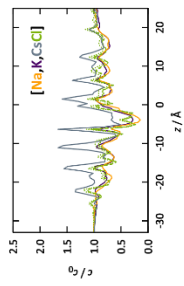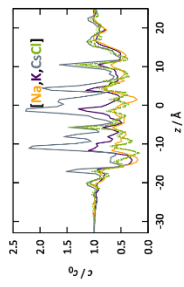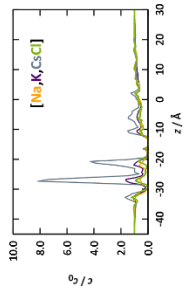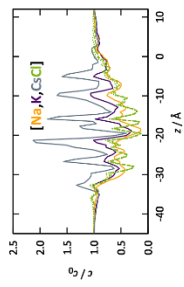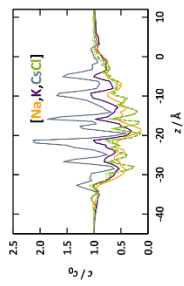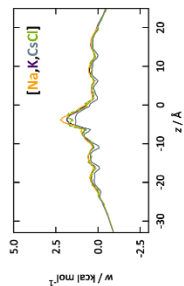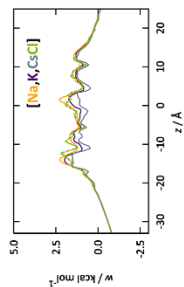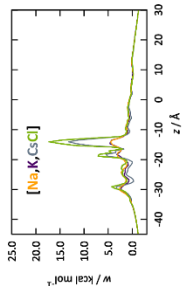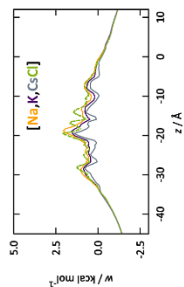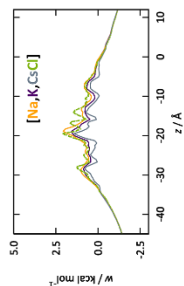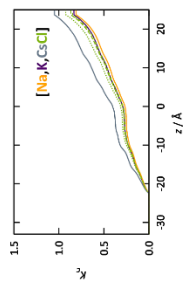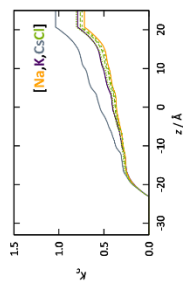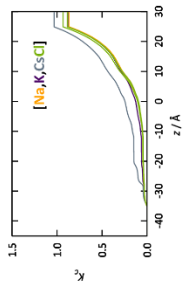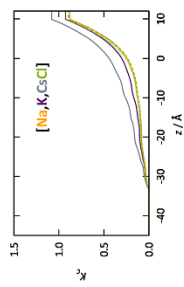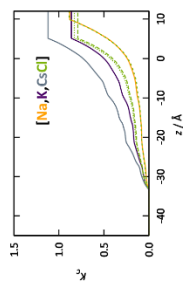
**Figure 6.6:** Uncharged structure profiles. Cartoon representation of the tertiary structure for the *in silico* uncharged deletion mutants 1ZLL$_{\Delta27}$ and 1ZLL$_{\Delta23}$, GluCl, 5-HT$_3$R and the closed PLN structure 1XNU in **a** (accessible volume blue). Corresponding radius profiles are given in subfigure **b**. The $c(z)$, $w(z)$ and $K_C$ profiles for all channels are shown in **c**, **d** and **e**. Results for the cations Na$^+$ (orange), K$^+$ (purple), and Cs$^+$ (gray) are depicted. Their corresponding Cl$^-$ data are shown as dotted (CsCl), long dashed (NaCl) and short dashed lines (KCl). The CHARMM parameter set was used for all calculations.

101

## 6.3.5 Kinetic selectivity: Conductances

In analogy to the investigations of the synthetic pore in chapter 5, the here obtained one dimensional pmfs were used for the calculation of the theoretical conductance $\gamma_{theo}$ by application of equation 3.3.20. An overview of all data is provided in table 6.2. In accordance to the identified surmountable barriers in the $w(z)$ profiles of 1ZLL, 1ZLL$_{\Delta23}$ and 1ZLL$_{\Delta27}$ (fig. 6.3, fig. 6.4) a cation selectivity order $Cs^+ > K^+ > Na^+$ is reflected in the calculated conductances. This is supported by the observed surmountable barriers of 4 kcal mol$^{-1}$ in 1ZLL and 1ZLL(JC). While a significant discrimination of the anion $Cl^-$ occurs in comparison to $K^+$ and $Cs^+$, it competes with the conductance of $Na^+$ in the case of 1ZLLand 1ZLL$_{\Delta23}$. This result is confirmed by both applied parameter sets. The difference between the calculated $Cl^-$ conductances and the measured experimental values might be related to artifacts in 3D RISM, as presented for the ion solutions at graphene sheets by Urban which overestimates the $Cl^-$ concentration in comparison to MD simulations,.[255] An elevated conductance for all ions, except for $K^+$ and $Na^+$ in the case of 1ZLL$_{\Delta27}$was obtained in the completely uncharged systems. Analysis of the conductance of the tighter 1XNUand 1XNU(CHA,uncharged) system revealed an impermeability for all ions in this structure. The calculated conductance $\gamma$ reproduce the experimentally measured ion selectivity significantly better in comparison with the corresponding thermodynamic $K_c$ values (table 6.2). This result argues for an importance role of the kinetic aspects in ion selectivity, while thermodynamic properties might play a lesser role. Nonetheless the calculated conductances overestimate the measured conductances by nearly 20 %, as the least square fit between the experimental and calculated conductances derives a scaling factor of 0.8.

Reguera and Rubi presented a feasible way to include local constriction effects to the diffusion coefficient, by calculating a weighting factor for $D(z)$, using the theory of Fick-Jacobs.[219] Their approach considers local constrictions by computation of the first derivation of the radius profile and weights it the bulk diffusion coefficient.[219]Application of this method to 1ZLL yielded $D(z)$ that are influenced by the local constrictions (fig. 6.7). Analysis of the $D(z)$ progressions reveals an nearly insignificant influence of the restrictions, according to fig. 6.7. Calculation of ion conductances with these local $D(z)$ values derived the same magnitude of conductance as in the wildtype (table 6.2).
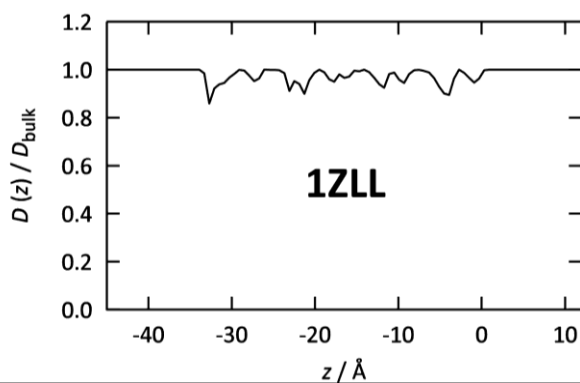
**Figure 6.7:** The radius dependent $D(z)$ profile for 1ZLL normalized to the bulk.

## 6.3.6 Pentameric ligand gated ion channels

As they share an pentameric structure as well as an ion channel functionality, two members of the pentameric LGIC family are investigated to verify the results for PLN. The anion selective GluCl and the cation selective 5-HT$_3$R channel are characterized by a extracellular receptor domain (M2) as well as five transmembrane helices lining a cylindrical pore inside the membrane, which was revealed to be essential for their ion selectivity.[1] In addition to those similarities with PLN, an hydrophobic restriction inside this M2 domain is identified in both channels. Due to these structural features the funnel forming TM parts of GluCl and 5-HT$_3$R were reasonable structure motives for a comparative analysis with PLN.

Calculations for the anion selective channel GluClreveal an strong conductance for Cl$^-$ (table 6.2). Conductances of the cations follow the order of $Cs^+ > K^+ > Na^+$ with a lower conductance in relation to the high values for Cl$^-$ (table 6.2). This result is in agreement with the obtained $K_c$ profiles (fig. 6.4, table 6.2) for GluCl. A cation over anion selectivity was confirmed for 5-HT$_3$R, in accordance to the obtained $K_c$ (fig. 6.4) values and the established cation selectivity of $K^+ > Na^+ > Cs^+$ (table 6.2).

An inversion of the anion over cation selectivity occurs in the fully hydrophobic GluCl(CHA,uncharged), reflected by a cation conductance exceeding those of Cl$^-$. Notably the Cl$^-$ conductances remained uninfluenced in GluCl(CHA,uncharged) in comparison with the charged GluCl situations (table 6.2). In contrast to the selectivity inversion in GluCl(CHA,uncharged), investigations of the uncharged 5-HT$_3$R(CHA,uncharged) revealed a different behavior (table 6.2). A cation over anion selectivity is observed for $K^+$ and $Cs^+$, due to a change of the inter-cationic selectivity order to $Cs^+ > K^+ > Na^+$ (table 6.2).

## 6.3.7 Conclusion

The presented approach demonstrates a feasible way to investigate the thermodynamic and kinetic aspects of pore systems in combination with 3D RISM. The performed investigations support the cation selectivity and channel functionality of the hydrophobic pentamer PLN in its *bellflower* conformation, while the spatial structure of the *pinwheel* is supposed to be ion impermeable, in accordance to the calculated $\gamma_{theo}$ values, which reproduced the provided *in vivo* conductances from Smeazzetto et al. successfully independent of the parameter set. Even so, the absolute calculated ion conductances overestimate the experimental values by 20 %. Calculations with a radius dependent $D(z)$ value suggest an insignificant effect of restraints on the conductance, as reflected by the results obtained by the Fick-Jackobs approach of Rubi and Reguera.[219] The good agreement between experimental and *in silico* conductances argues for a strong influence of kinetic aspects on the ion selectivity in 1ZLL. Investigation of the partition coefficient profiles $K_c$ identified a limited significance of this accumulative property, due to its dependency on the chosen $z$ position. Nonetheless $K_c$ predicts the ion selectivity qualitatively and allows identification of characteristic positions of the selectivity progression. Investigation of artificially uncharged systems demonstrate the possible variability of the overall approach to toy systems as well as it supports the cation selectivity to be preserved in a fully hydrophobic 1ZLL(CHA,unhcarged) channel. Scrutinized deletion mutants $1ZLL_{\Delta23}$ and $1ZLL_{\Delta27}$ suggest that the charged N-terminus plays a minor role for the establishment of the cation over anion selectivity, as the results indicated the same cation selectivity as in the full 1ZLL.

Reproduction of the correct ion selectivity for GluCl and 5-HT$_3$R supports the applicability of the thermodynamic and kinetic analysis of biological, hydrophobic pores with 3D RISM. The obtained ion selectivity inversion in GluCl(CHA,uncharged) illustrates the potential application of this approach in the field of computer aided design. The observed cation-anion selectivity inversion in 5-HT$_3$R(CHA, uncharged) is in agreement with the experimental 5-HT$_3$R mutation created by Gunthorpe et al., where an exchange of two of five charged residues per monomer at the mouth regions introduced an inversion of the ion selectivity (see chapter 2.4.2).[167] Data of Urban revealed a radius dependency of ion selectivity in a hard channel pore (HCP) system, which supports the observations in 1ZLL.[255]

# 7 Ion Selectivity in Phospholamban

## 7.1 Introduction

Despite the hydrophobic chemistry and tight geometry inside the transmembrane funnel of the pentameric PLN, a significant ion conducting property and cation selectivity were revealed in the previous chapter 6. While the focus of the last chapter was laid on the description of PLN and its context of conductance, the exhibited selectivity remained mostly unexplained. Still a hint leading to a possible explanation was provided by the study of the hydrophobic pore system of Gong et al. (chapter 5) and the results of PLN (chapter 6).[6] Both argued that the capability to separate ions could be a function of the pore radius. In addition the hydrophobic girdles known from pLGICs are importance elements for ion selectivity and areas of high restriction.[165,169,171–173] In this context narrow hydrophobic structures might hold the key to understand and establish ion selectivity.

To shed light on the selectivity in 1ZLL a thermodynamic cycle is established, describing the transfer of an ion from bulk to the restriction of PLN. Through this thermodynamic approach, information about local and global free energies are accessed for the monovalent ions $Na^+$, $K^+$, $Cs^+$ and $Cl^-$. In addition, the calculation of radial distribution functions $g(r)$ facilitate the description of hydration shells and coordination numbers, which are also discussed in their contribution to solvation.

The established thermodynamic cycle includes contributions of the pmf $w(z)$, which will be accessed by a new, approximatively approach that allows for a free energy decomposition into contributions of the entropy $-T\Delta S$, the internal energy $U$. This approximation provides values for these thermodynamic properties inside the restriction of PLN, which are experimentally inacessable.

## 7.2 Methods

The thermodynamic aspects of ion selectivity in PLN are investigated by the construction of a corresponding thermodynamic cycle (fig. 7.1), describing the transfer process of a single ion from bulk to a defined $z$ position on the central axis of the *bellflower* structure of 1ZLL. In accordance with the previous results of chapter 6, $z$ is chosen at $z = -19.5$ Å in the restriction of PLN, assuming that the ion permittivity and selectivity dependent on the narrowest part.

$$
\begin{array}{ccc}
\textbf{Pore}_g + \textbf{Ion}_g & \xrightarrow{\Delta G_{\text{vac}}^{\text{binding}}} & \textbf{(Pore-Ion)}_g \\
\Big\uparrow {-\Delta G_{\text{solv}}^{\text{ion}}} & & \Big\downarrow \Delta G_{\text{solv}}^{\text{ion+pore}} \\
\Big\uparrow {-\Delta G_{\text{solv}}^{\text{pore}}} & & \\
\textbf{Pore}_{aq} + \textbf{Ion}_{aq} & \xrightarrow{w(z)} & \textbf{(Pore-Ion)}_{aq}
\end{array}
$$
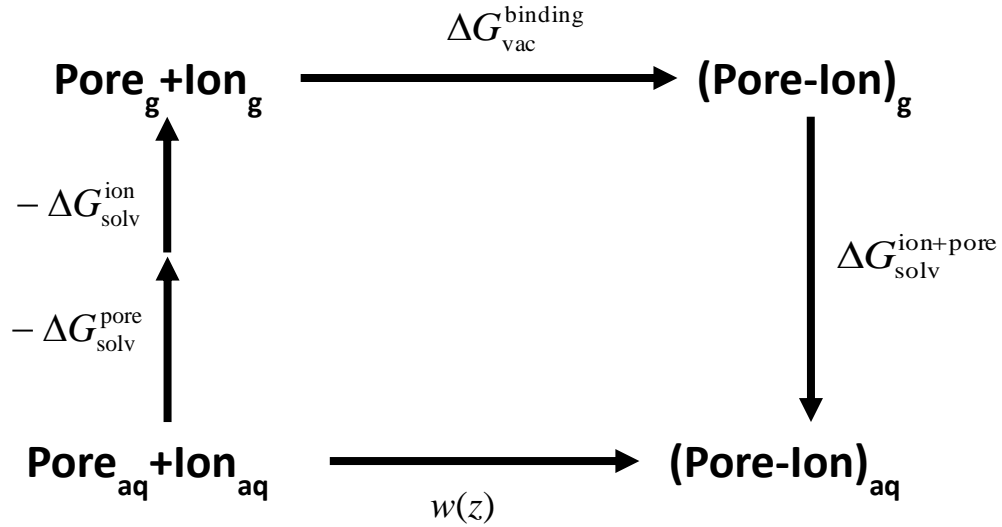
**Figure 7.1:** Illustration of the thermodynamic cycle. Depiction of the ion transfer from bulk to the restriction of the pore.

According to the transfer process in fig. 7.1, the free solvation energy difference of the ion-pore complex $\Delta G_{\text{solv}}^{\text{ion+pore}}$ can be described as

$$\Delta G_{\text{solv}}^{\text{ion+pore}} = w(z) + \underbrace{\Delta G_{\text{solv}}^{\text{ion}} + \Delta G_{\text{solv}}^{\text{pore}}}_{\text{3D RISM}} - \Delta G_{\text{vac}}^{\text{binding}}. \tag{7.1}$$

The single energies required for the calculation of $\Delta G_{\text{solv}}^{\text{ion+pore}}$ (eq. 7.1) are derived from individual approaches. The free energy of solvation for an ion $\Delta G_{\text{solv}}^{\text{ion}}$ is accessed directly by 3D RISM calculations containing a single explicit ion in ion solution. The free energy of solvation for the pore $\Delta G_{\text{solv}}^{\text{pore}}$ is obtained accordingly from 3D RISM calculations with the PLN structure 1ZLL. A different approach was chosen to derive the pmf $w(z)$. Here, we estimate $w(z)$ by the relation

$$w(z) \approx A(z)$$
$$= -RT \ln(Z(z)) \quad ,$$

[7.2]

with the free energy $A(z)$ of the regarded ion at the restriction position $z$. The partition function $Z$ can be defined as

$$Z(z) = \int\limits_{x=-\infty}^{x=\infty} \int\limits_{y=-\infty}^{y=\infty} \frac{1}{Q(z_0)} e^{-\beta w_{fit}(x,y;z)} dx dy \, ,$$

[7.3]

with the inverse temperature $\beta$ and the reference area $Q(z_0)$. Inside the restriction of the pore the distribution function $g(x,y;z)$ is approximatily assumed to follow the shape of an normal distribution. Consequently an exponential 2D harmonic oscillator in the form of

$$w_{fit}(x, y; z) = -\beta \ln(g(x, y; z)) = w_0(x_0, y_0; z) + \frac{k}{2} \cdot \left[(x - x_0)^2 + (y - y_0)^2\right],$$

[7.4]

was applied to fit the logarithmized solvent distribution function $g(x,y;z)$, which is related to an approximate pmf $w_{fit}(x,y;z)$ by definition. Further is the minimum $w_0(x_0,y_0;z)$, $k$ the force constant and $x_0$ and $y_0$ are fit parameters in close correspondence to the minimum of pmf position. For better clarity we redefine the minimum of the $w_0(x_0,y_0;z) \equiv w_0(z)$ and our overall approach as $w(z) \approx A(z) \equiv w_{fit}(z)$. A quadratic function for the pmf at position $z$ is chosen due to its analytic integrability for which

$$w_{fit}(z) = -RT \ln\left(\frac{2RT\pi}{k \cdot Q(z_0)}\right) + w_0(z) \, ,$$

[7.5]

follows for the chosen approximated pmf. The therefore calculated $w_{fit}(z)$ is an harmonic approximation to the global pmf $w(z)$ introduced in chapter 6 (see eq. 3.3.20). Our analytical approach allows for further decomposition in important thermodynamic contributions as the internal energy

$$U^v = -RT^2 \frac{\partial Z}{\partial T} \, ,$$

[7.6]

and the entropy

$$S^{v} = RT^{2}\frac{\partial Z}{\partial T} + k_{\mathrm{B}}\ln(Z),$$ [7.7]

that we address as

$$w(z) \approx \Delta U^{v}(z) - T\Delta S^{v}(z).$$ [7.8]

The superscript $v$ indicates the solvent mediated influence on $S^{v}$ and $U^{v}$. Inserting these definition in equation 7.3 leads to

$$\Delta U^{v}(z) = w_{0}(z) + RT$$ [7.9]

and

$$\Delta S^{v}(z) = RT + R\ln\left(\frac{2RT\pi}{k \cdot Q(z_{0})}\right).$$ [7.10]

It is worth mentioning that the calculated thermodynamic quantities are not estimated as absolute values. Instead the changes ($\Delta$) in the thermodynamic properties are obtained, which describes the free energy difference needed to transfer a particle from a reference state to the current position. This reference state is connected to the bulk concentration by the solute distribution function. The free energy of binding in vacuum $\Delta G_{\mathrm{vac}}^{\mathrm{binding}}$ can be defined as

$$\Delta G_{\mathrm{vac}}^{\mathrm{binding}} \equiv \Delta u^{\mathrm{binding}}(z) = u^{\mathrm{ion}}(z) + u^{\mathrm{pore}}(z) + u^{\mathrm{ion-pore}}(z) - u^{\mathrm{ion}}(z) - u^{\mathrm{pore}}(z)$$
$$= \Delta u^{\mathrm{ion-pore}}(z)$$ , [7.11]

with the interaction vacuum potentials of the ion $u^{\mathrm{ion}}(z)$, pore $u^{\mathrm{pore}}(z)$ and ion+pore complex $u^{\mathrm{ion+pore}}(z)$. In analogy to equation 7.3 $\Delta u^{\mathrm{binding}}(z)$ was obtained by

$$\Delta u^{\mathrm{binding}}(z) = -RT\ln(Z_{\mathrm{vac}}(z))$$ [7.12]

with

$$Z_{vac}(z) = \int\limits_{x=-\infty}^{x=\infty} \int\limits_{y=-\infty}^{y=\infty} \frac{1}{Q(z_0)} e^{-\beta u_{fit,vac}(x,y;z)} dxdy$$ 
, [**7.13**]

where $u_{fit,vac}(x,y;z)$ was approximated by

$$u_{fit,vac}(x,y;z) = (u_0(x_0,y_0;z)) + \frac{k}{2} \cdot \left[(x-x_0)^2 + (y-y_0)^2\right]$$ 
, [**7.14**]

with the fit minimum $u_0(x_0,y_0;z)$. The positions $x_0$ and $y_0$ were set to zero, due to convergence problems in several unrestrained anion cases. From equations 7.11 and 7.14 follows

$$\Delta G_{vac}^{binding} \approx u_{fit,vac}(x,y;z)$$ 
. [**7.15**]

For clarification, one might consider the possibility of calculating $\Delta G_{solv}^{ion+pore}$ directly by tackling an pore with an ion inside (ion+pore complex) with 3D RISM, by explicit placement of an ion in the restriction site of PLN. Whereas the here presented decomposition (eq 7.1) considers the energy contribution inside the (x,y;z) plane, this direct approach would have neglected the lateral degrees of freedom in the x,y-plane and a sophisticated sampling would be needed.

## 7.2.1 Technical details of the approximations

The restriction at $z = -19.5$ Å of the PLN structure 1ZLL was identified by the radius analysis conducted in chapter 6. All values of $g(\mathbf{r})$ in a square of $6^2$ Å$^2$ around the center of this $z$ position were considered for the exponential approximations of $w_{fit}(z)$ in accordance to equation 7.5. The information about the potential $u(\mathbf{r})$ was obtained from 3D RISM interaction potential calculations without solvent influence.

## 7.2.2 Computation of coordination numbers

As a descriptor for the amount of adjacent atoms around a central atom, coordination numbers $N_i(r)$ can be utilized for the determination of solvent molecules forming the first, second etc. solvent shell. They are connected to the radial pair distribution function and can be obtained by an altered spherical integration. The radial integral of the form

$$N_i(r) = \int\limits_{\varphi=0}^{2\pi} \int\limits_{\theta=0}^{\pi} \int\limits_{r=0}^{r} g_i(r',\theta,\varphi) \cdot r'^2 \sin(\theta) \mathrm{d}r' \mathrm{d}\theta \mathrm{d}\varphi , \qquad\qquad [7.16]$$

with angles $\theta$ and $\varphi$, the distance $r$ and the solvent distribution function $g_i(r,\theta,\varphi)$, with $r = |\mathbf{r} - \mathbf{r}_{ion}|$. Integration over the angular parts gives

$$N_i(r) = 4\pi\rho_{Bulk}\int\limits_{0}^{r} g_i(r') \cdot r'^2 dr' , \qquad\qquad [7.17]$$

with the radially averaged distribution function $g_i(r)$ and the bulk density $\rho_{Bulk}$. The number of atoms as a function of $r$ is the direct result of equation 7.17. The integration is accomplished in accordance with the method of Lebedev and Laikow.[256] All coordination numbers for the ion species of $Na^+$, $K^+$, $Cs^+$ and $Cl^-$ are collected in table 7.2. The corresponding 3D RISM calculations were performed with explicit ions (see next section for technical detail).

## 7.2.3 Computational details for 3D RISM

Individual spatial distribution functions $g(\mathbf{r})$ and the potentials $u(\mathbf{r})$ were obtained from the previously conducted calculations with the pentameric structure of phospholamban (PDB code: 1ZLL) (see *chapter* 6 for details). The results originated with the parameter set of CHARMM (1ZLL$_{CHA}$) and of Joung & Cheatham (1ZLL$_{JC}$) were investigated. Additional 3D RISM calculations on a $180^3$ Å$^3$ grid, with a spacing of 0.6 Å were conducted, which were used to access the radial distribution function $g(r)$ around the pmf minimum $w_0(z)$ in 0.1 M solutions of NaCl, KCl and CsCl.[256] Regarding calculations with explicit ions for obtainment of the coordination number, the positioning of the ions occurred according to their approximated minimum pmf positions $w_0(-19.5$ Å$)$. Other parameters were kept intentionally at their values according to the descriptions in the methods section of *chapter* 6.

## 7.3 Results

### 7.3.1 Thermodynamic investigation of the hydrophobic restriction in PLN

Evaluation of the exponential fit permitted access to structure related thermodynamic quantities. The results of the fit are visualized in Figure 7.1. Due to their relation, high values of $g(\mathbf{r})$ correspond to low values of the pmf, which are identified by low barriers. Thus the minimum position $w_0$ describes the lowest barrier in the chosen $x,y$-plane. The point of the lowest energy $w_0$ is also a meaningful indicator in the context of ion permeation, as high barriers are supposed to inhibit the transfer and thereby influence the conduction process. The entropy is reflected by the width of the fit result. In this context, smaller $-T\Delta S(z)$ or $-T\Delta S^v(z)$ values (table 7.1) allow for more realizations of possible ion permeations (fig. 7.1, 7.2). The peak height is directly proportional to the concentration.

As the here presented model approach is based on an approximation, the validity needed to be assessed (table 7.1). The equivalence between the approximated pmf $w_{\text{fit}}(z)$ and its previously introduced counterpart $w(z)$ form chapter 6 is shown (table 7.1, last row), confirming the here presented approach.

Investigation of the restriction ($z = -19.5$ Å) in aqueous solutions of NaCl, KCl and CsCl reveals the selectivity order $Na^+ < K^+ < Cl^- < Cs^+$ in respect to the quantity $w_0(z)$ (table 7.1). This order is well established in both applied parameter sets, $1ZLL_{JC}$ and $1ZLL_{CHA}$ and suggests a $Cl^-$ over $Na^+$ and $K^+$ selectivity. Still the observed inter cationic order is in agreement with the experimental and the calculated conductances (see *chapter* 6). The obtained barriers are of several kcal mol$^{-1}$ suggest a possible ion permeation for all ions. However the quantity $w_0(z)$ reflects only a single point inside the chosen $x,y$-plane that characterizes the least needed energy to pass through. The information about the chemical and structural detail is in contrast better reflect by $w_{\text{fit}}(z)$ (eq 7.3). Calculation of $w(z)$ yielded ion sequence orders of $K^+ < Na^+ < Cs^+ < Cl^-$ for $1ZLL_{CHA}$ and $K^+ < Cs^+ \leq Na^+ < Cl^-$ for $1ZLL_{JC}$, revealing a preference of cations over $Cl^-$ (table 7.1), but with an inter-cationic order deviating from the experimental results (chapter 6). According to the pure entropy $-T\Delta S^v(z)$ at a temperature of 298.15 K, an ion selectivity order of $Cl^- < Cs^+ < K^+ < Na^+$ for $1ZLL_{CHA}$ and $1ZLL_{JC}$ is established, which is inverse to the cation trend of $w_{\text{fit}}(z)$. Thus the entropy shows a sensitivity in close correspondence to the radius of the ion at hydrophobic barrier. The contrary ion selectivity behavior between $-T\Delta S^v(z)$ and the $w_{\text{fit}}(z)$ excludes an entropy controlled

mechanism as a mono-causal explanation for the established inter-cationic selectivity insight the hydrophobic restriction.
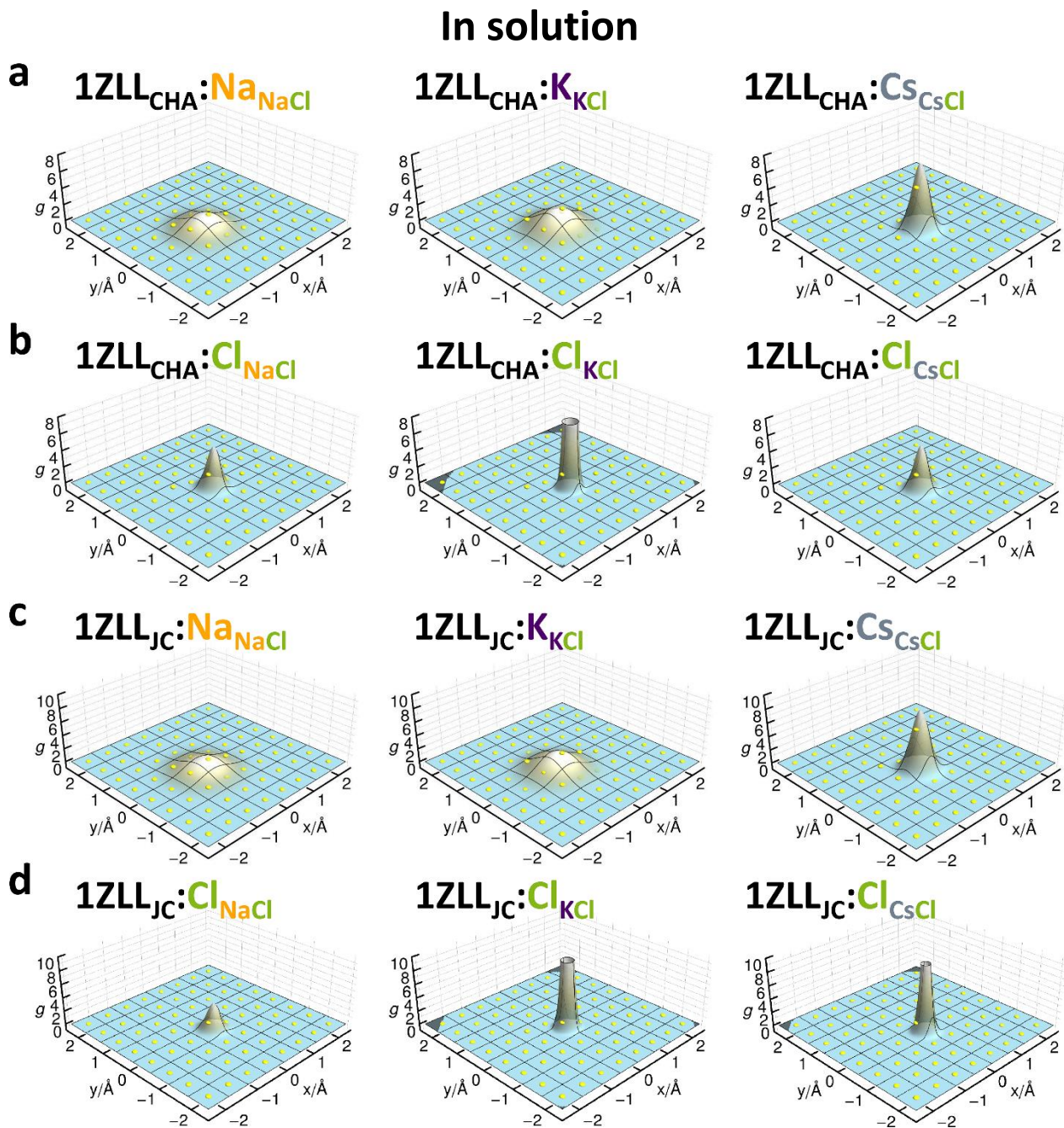


**Figure 7.1:** Visualization of the exponential fit for 1ZLL$_{JC}$ and 1ZLL$_{CHA}$ in solution. The fit result (blue) is shown in overlay with the original data points (yellow dots) in panels **a, c** for Na$^+$, K$^+$ and Cs$^+$ and in **b, d** for the corresponding Cl$^-$. The displayed fit was applied to all $g(x,y;z)$ values inside a plane at position $z = -19.5$ Å spanning a range from -2 to 2 for $x$ and $y$ borders.

**Table 7.1** Thermodynamic quantities of $1ZLL_{CHA}$/$1ZLL_{JC}$

| Property | Na$^+$ | K$^+$ | Cs$^+$ | Cl$_{NaCl}$ | Cl$_{KCl}$ | Cl$_{CsCl}$ |
|---|---|---|---|---|---|---|
| | | | $z$ = -19.5 Å in solution | | | |
| $w_0$ | -0.38/-0.33 | -0.56/-0.58 | -1.21/-1.28 | -0.96/-0.81 | -2.09/-1.94 | -0.99/-1.64 |
| $w_{fit}(z)$ | 1.87/1.87 | 1.68/1.65 | 1.96/1.81 | 2.39/2.61 | 1.77/1.89 | 2.35/2.11 |
| $\Delta U^v(z)$ | 0.22/0.26 | 0.03/0.01 | -0.61/-0.69 | -0.36/-0.21 | -1.50/-1.35 | -0.40/-1.05 |
| $-T\Delta S^v(z)$ | 1.65/1.61 | 1.66/1.64 | 2.58/2.49 | 2.75/2.83 | 3.26/3.24 | 2.75/3.16 |
| | | | $z$ = -19.5 Å in vacuum | | | |
| $u_0$ | 92.37/92.25 | 94.96/93.56 | 94.02/92.60 | -95.06/-93.92 | -95.06/-93.92 | -95.06/-93.92 |
| $u_{fit,vac}(z)$ | 95.45/95.44 | 98.56/97.20 | 97.85/96.42 | -91.00/-89.84 | -91.00/-89.84 | -91.00/-89.84 |
| | | | Free energies of the thermodynamic cycle $1ZLL_{CHA}$/$1ZLL_{JC}$ | | | |
| $\Delta G_{solv}^{ion}$ | -85.18/-81.96 | -67.27/-66.71 | -54.39/-56.62 | -94.15/-86.92 | -94.33/-86.80 | -94.25/-86.67 |
| $\Delta G_{solv}^{pore}$ | -3454.70/ -3464.28 | -3456.21/-3443.58 | -3427.76/-3422.11 | -3454.70/-3464.28 | -3456.21/-3443.58 | -3427.76/-3422.11 |
| $\Delta G_{solv}^{ion+pore}$ | -3633.49/-3639.81 | -3620.34/-3605.82 | -3578.18/-3573.48 | -3455.58/-3458.83 | -3457.28/-3438.02 | -3428.78/-3416.47 |
| $\Delta G_{vac}^{binding}$ | 95.45/95.44 | 98.56/97.20 | 97.85/96.42 | -91.00/-89.84 | -91.00/-89.84 | -91.00/-89.84 |
| | | | $z$ = -19.5 Å in solvation | | | |
| $w(z)$ | 1.85/1.87 | 1.70/1.67 | 1.83/1.66 | 2.26/2.53 | 2.25/2.52 | 2.22/2.46 |

All values are provided in units of kcal mol$^{-1}$.

$w_{fit}(z)$ represent the full pmf in solvation, with the fit minimum $w_0$.

$u_{fit,vac}(z)$ represent the vacuum potential, with the fit minimum $u_0(z)$.

$w(z)$ designates the pmf obtained in chapter 6.

$-T\Delta S^v(z)$ describes the entropy of the free energy in solvation.

$\Delta U^v(z)$ denotes the internal energy.

$\Delta G_{solv}^{ion}$, $\Delta G_{solv}^{pore}$, $\Delta G_{solv}^{ion+pore}$ and $\Delta G_{vac}^{binding}$ designate the free energies.

$1ZLL_{CHA}$ and $1ZLL_{JC}$ identify the different parameter sets of CHARMM and Joung & Cheatham.

To investigate the influence of the solvent, the participated vacuum energies were estimated inside the restriction, by approximation in analogy to Ansatz (eq. 7.13, 7.14). Analysis of $u_{fit,vac}(z)$ inside the restriction reveals a difference of 100 kcal mol$^{-1}$, demonstrating an strong influence of the solvents. Regarding to $u_{fit,vac}(z)$, anions are revealed to be energetically favored, while the cations face an unsurmountable barrier. The opposing anion and cation selectivity in $w_{fit}(z)$ and $u_{fit,vac}(z)$ (table 7.1) reflects that this selectivity is influenced by solvation effects at the restriction. According to the described differences between $w_{fit}(z)$ and $u_{fit,vac}(z)$ (table 7.1), a change from a simple size selective restriction under vacuum to an cation vs anion discrimination element in solution is performed by the solvent. Considering the limitation of the obtained data to local chemical and topological aspects at the restriction as well as the discovered influence of the solvent on the selectivity, global aspects of solvation attracted attention. Therefore further thermodynamic

analysis regarding the process of solvation were investigated in more detail and are discussed in the next subchapter.

# In vacuum

**a**    **1ZLL$_{CHA}$:Na$_{NaCl}$**      **1ZLL$_{CHA}$:K$_{KCl}$**      **1ZLL$_{CHA}$:Cs$_{CsCl}$**

**b**    **1ZLL$_{CHA}$:Cl$_{NaCl}$**      **1ZLL$_{CHA}$:Cl$_{KCl}$**      **1ZLL$_{CHA}$:Cl$_{CsCl}$**

**c**    **1ZLL$_{JC}$:Na$_{NaCl}$**      **1ZLL$_{JC}$:K$_{KCl}$**      **1ZLL$_{JC}$:Cs$_{CsCl}$**

**d**    **1ZLL$_{JC}$:Cl$_{NaCl}$**      **1ZLL$_{JC}$:Cl$_{KCl}$**      **1ZLL$_{JC}$:Cl$_{CsCl}$**
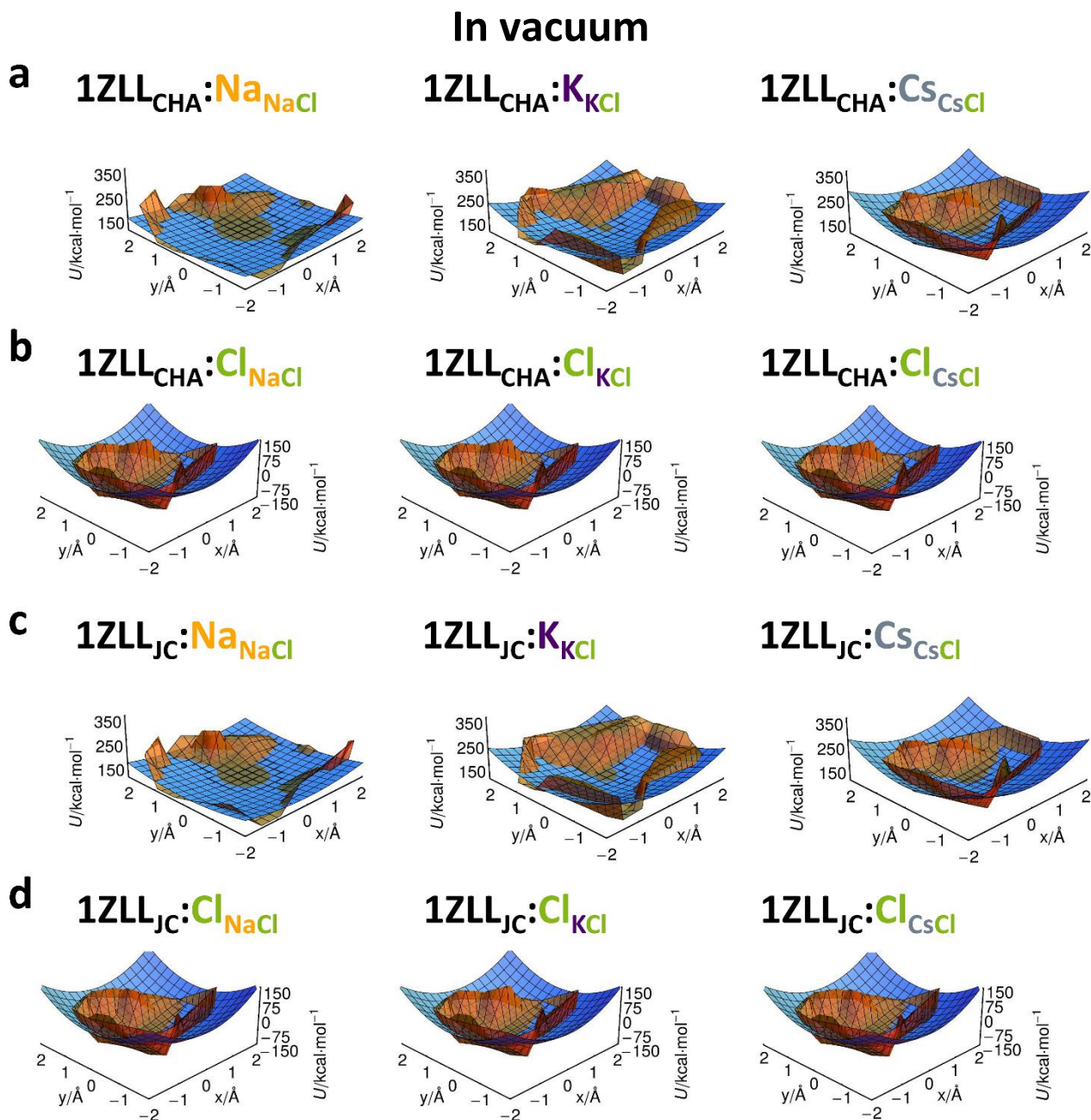


**Figure 7.2:** Interaction potential $u(\mathbf{r})$ in overly with $u_{\text{fit,vac}}(z)$ at position $z = -19.5$ Å in 1ZLL$_{JC}$ and 1ZLL$_{CHA}$. **A,C:** For the cations (Na$^+$, orange; K$^+$, purple; Cs$^+$, grey) the $u(\mathbf{r})$ (brown) and the corresponding fit (blue) are shown as surfaces. **B**, **D**: Representation of $u(\mathbf{r})$ equal result for Cl$_{NaCl}$, Cl$_{KCl}$, Cl$_{CsCl}$ (subscript denotes the associated ion solution). The fit was restrained with $x_0 = y_0 = 0$.

## 7.3.2 Thermodynamic effects of solvation

According to fig. 7.1 a thermodynamic cycle was established. Potential energetic effects of a membrane are not tackled, as their contributions vanish by cancelation in the here defined cycle.
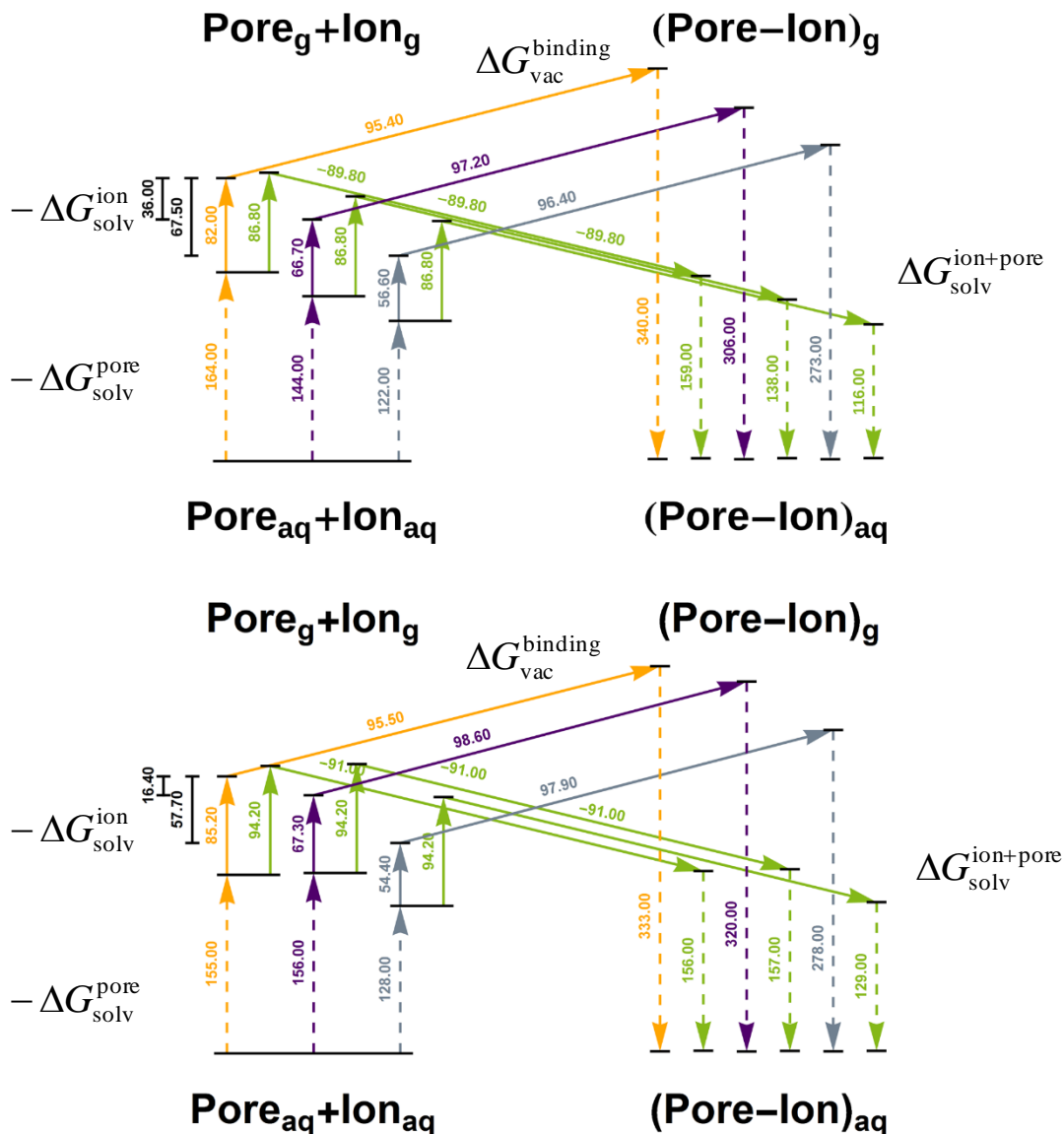


**Figurge 7.3:** Thermodynamic cycle of 1ZLL$_{JC}$ and 1ZLL$_{CHA}$ at $z = -19.5$ Å. Depiction of the contributing energies comprising the $w_{fit}(z)$ inside the restriction of 1ZLL$_{JC}$ (upper panel) and 1ZLL$_{CHA}$ (lower panel). Desolvation of the pore and ion is described by $-\Delta G_{solv}^{ion}$ (dashed arrows left) and $-\Delta G_{desolv}^{pore}$ (solid arrows left). Interaction of the pore and the ion in vacuum is denoted as $\Delta G_{vac}^{binding}$ (connecting solid arrow) and in solution $\Delta G_{solv}^{ion+pore}$ (dashed arrow right). Energies and arrows for Na$^+$, K$^+$, Cs$^+$, Cl$^-$ are color coded in orange, purple, gray and green. Energy values shown adjacent to the corresponding arrow. Arrow length for $\Delta G_{solv}^{pore}$ and $\Delta G_{solv}^{ion+pore}$ is truncated by 3300 kcal mol$^{-1}$. Particular differences are marked by black bars.

Beginning with $\Delta G_{\text{solv}}^{\text{pore}}$ as a descriptor for the transfer of 1ZLL from solution to vacuum, a strong dependence of the chosen ion solution for both parameter cases (fig.7.3) was revealed. For instance an energy difference of 20 kcal mol$^{-1}$ is provided between CsCl and KCl as well as between NaCl and KCl for 1ZLL$_{\text{JC}}$. The desolvation process of 1ZLL$_{\text{CHA}}$ is energetically equivalent in NaCl and KCl, while the desolvation from CsCl is favoured by 30 kcal mol$^{-1}$. Interpretation of this energetic difference establishes a higher solubility for the pore in NaCl than in KCl or even CsCl. A similar disparity occurs in the process of ion desolvation $-\Delta G_{\text{solv}}^{\text{ion}}$ in fig. 7.3. Again a difference of 10 to 26 kcal mol$^{-1}$ between Cs$^+$, K$^+$, and Na$^+$ occurs in the process of desolvation from their corresponding solutions in case of 1ZLL$_{\text{JC}}$. A analogue effect was obtained with the CHARMM parameter set where differences of 13 and 18 kcal mol$^{-1}$ occur between Na$^+$, K$^+$ and Cs$^+$. This result implicates that a desolvation of Cs$^+$ solved in CsCl is energetically favoured over a desolvation of K$^+$ from KCl or Na$^+$ form NaCl. This result is important for the interpretation of ion selectivity, as a lower desolvation energy supports the permeation from bulk into the hydrophobic pore. Thus Cs$^+$ is favoured over K$^+$ and Na$^+$ in accordance to their $-\Delta G_{\text{solv}}^{\text{ion}}$ values. In addition, the calculated ion desolvation energies follow the experimental inter-cationic selectivity, emphasizing the importance of $-\Delta G_{\text{solv}}^{\text{ion}}$. In contrast the desolvation process for a Cl$^-$ anion is identified to be independent of the solution and is highly unfavored in comparison to the cations. This solvent specific cooperative effects did not occur according to the nearly equal $-\Delta G_{\text{solv}}^{\text{ion}}$ values of the anions. The constantly higher $-\Delta G_{\text{solv}}^{\text{ion}}$ values for Cl$^-$ in comparison to the cations imply a penalization for the anion desolvation process. Together $\Delta G_{\text{desolv}}^{\text{pore}}$ and $\Delta G_{\text{desolv}}^{\text{ion}}$ exhibit an energetic difference of 67.50 kcal mol$^{-1}$ between Cs$^+$ and Na$^+$ and 36 kcal mol$^{-1}$ for Cs$^+$ and K$^+$ in 1ZLL$_{\text{JC}}$ and a difference of 57.70 kcal mol$^{-1}$ and 16.40 kcal mol$^{-1}$ in 1ZLL$_{\text{CHA}}$. Calculation of the coordination number (CN) for cations and anions in bulk and inside 1ZLL (*see following result section*) confirmt this result, as Cs$^+$ strips off 2.73/2.69 water molecules in dependence of the parameter sets of CHARMM/JC, where Na$^+$ and K$^+$ lose only 1.05/0.90 and 1.83/1.67 water molecules (table 7.2). The identified energetic inequalities amongst the cations are responsible for the finally obtained inter-cationic order. Due to the overall positive charge of the protein, the transfer of an anion to the restriction is favoured in comparison to a positive cation. A difference of 180 to 190 kcal mol$^{-1}$ in $\Delta G_{\text{vac}}^{\text{binding}}$ was obtained between cations and anions in dependency of the chosen parameter set (table 7.2). Insignificant deviations in $\Delta G_{\text{vac}}^{\text{binding}}$ were quantified focusing on the comparison amongst the

individual cation species, leading to basically equal values. With those results for $\Delta G_{\text{vac}}^{\text{binding}}$, the previously stated desolvation advantages and penalties reasoned by $\Delta G_{\text{solv}}^{\text{ion}}$ and $\Delta G_{\text{solv}}^{\text{pore}}$ are nearly completely compensated, but do not fully vanish. Thus the observed penalization of the cation-pore complexation in vacuum is overcompensated by the previously introduced energies of solvation, in particular $\Delta G_{\text{solv}}^{\text{ion+pore}}$. In consequence of the gained results an inter-cationic selectivity inside the pore of $\text{Na}^+ < \text{K}^+ < \text{Cs}^+$ is established by a combination of the local solvent effects, namely $-\Delta G_{\text{solv}}^{\text{ion}}$ and $-\Delta G_{\text{solv}}^{\text{pore}}$. The presented results argue that inter-cation selectivity is established by a combination of huge contributing energies, finally cancelling to distinct small differences. In this regard, the inter-cationic ion selectivity is of course sensitive to the applied force field, as revealed by here presented approach with CHARMM and Joung and Cheatham.

The final resolution process of the ion-complex is described by the property of $\Delta G_{\text{solv}}^{\text{ion+pore}}$. Independent of the chosen cation, $\Delta G_{\text{solv}}^{\text{ion+pore}}$ has an compensating effect, reducing the huge vacuum energies to the low energetic barriers of $w(z)$. An equivalent compensation occurrs also in the anion case. For clarification the global property of $\Delta G_{\text{solv}}^{\text{ion+pore}}$ reduces the accumulated vacuum energies accurately to small, distinct energies, which in consequence revealed $\Delta G_{\text{solv}}^{\text{ion+pore}}$ as the driving reason for the determination of the cation versus anion selectivity. According to these remarkable results the energy connected to the process of resolution of the ion+pore complex $\Delta G_{\text{solv}}^{\text{ion+pore}}$ is supposed to be the key modulator of anion versus cation selectivity. A possible explanation might be deduced by using the formula of Born, which can be used to approximate the change in the free energy of solvation $\Delta G_{\text{solv}}$.[257] The Born equation

$$\Delta G_{\text{solv}} = -\frac{Z^2 e^2 N_{\text{A}}}{8\pi\varepsilon_0\alpha}\left(1 - \frac{1}{\varepsilon}\right), \qquad\qquad \textbf{[7.16]}$$

describes the energy difference between the process of charging a single spherical particle with radius $\alpha$ up to a total change of $Z$ in solvent. In equation 7.16 $\varepsilon$ and $\varepsilon_0$ are the permittivity of the solvent and vacuum, while $N_{\text{A}}$ describes the Avogadro constant and $e$ is the elementary charge. Assuming the protein 1ZLL and an incorporated ion to be a macro particle, the model of Born is applicable. For a correct model approach the ion was assumed to be buried inside the protein and therefore screened from the solvent, omitting any interaction with it. In the picture of

117

the thermodynamic cycle, the calculated $\Delta G_{\text{solv}}$ (eq. 7.16) is connected to the solvation energy of the ion-pore complex $\Delta G_{\text{solv}}^{\text{ion+pore}}$. As the charge is squared in equation 7.16, the Born approximation can provide information about the cation-anion selectivity difference. In dependency on the chosen ion charge (+1 for cations; -1 for anions) the total charge of a constructed 1ZLL-ion macro particle elevates from +20 to a total of +21 (cation+channel) or diminishes to +19 (anion+channel). Evaluation of equation 7.16 with the described macro ion charges of +19 (anion+channel) and +21 (cation+channel) would gain a lower $\Delta G_{\text{solv}}$ for the cation case, due to the higher total charge of the ion-pore complex (fig. 7.4), assuming all other parameters to be equal. Thus solving 1ZLL with an additional buried cation is favoured over the corresponding process with an anion. In accordance to this argument the discrimination between anions and cations could be related to global solvation effects regarding $\Delta G_{\text{solv}}^{\text{ion+pore}}$ in the thermodynamic cycle.

## 7.3.3 Coordination numbers

To investigate hydration effects in greater detail, coordination numbers (CN) were obtain from by spherical integration of the spatial distribution functions $g(\mathbf{r})$.

**Table 7.2** Coordination of $1\text{ZLL}_{\text{JC}}/1\text{ZLL}_{\text{CHA}}$

|  | Ion | Na$^+$ | K$^+$ | Cs$^+$ | Cl$_{\text{NaCl}}$ | Cl$_{\text{KCl}}$ | Cl$_{\text{CsCl}}$ |
|---|---|---|---|---|---|---|---|
| CN in ionic solutions | O$_{\text{water}}$ | 4.27/4.15 | 5.18/4.99 | 6.41/6.30 | 10.08/10.01 | 10.02/9.95 | 10.04/9.95 |
|  | H$_{\text{water}}$ | 7.15/6.81 | 9.53/9.23 | 12.26/12.27 | 2.18/2.19 | 2.22/2.22 | 2.24/2.23 |
|  | $r_{\text{oxy}}$ | 3.14/3.08 | 3.50/3.44 | 3.82/3.83 | 4.32/4.28 | 4.32/4.28 | 4.32/4.28 |
|  | $r_{\text{hyd}}$ | 3.96/3.89 | 4.36/3.44 | 4.73/4.75 | 2.66/2.59 | 2.66/2.59 | 2.66/2.59 |
| CN inside 1ZLL$_{\text{JC}}$ /1ZLL$_{\text{CHA}}$ | O$_{\text{water}}$ | 3.22/3.25 | 3.35/3.32 | 3.68/3.61 | 4.61/4.60 | 4.59/4.58 | 4.58/4.56 |
|  | H$_{\text{water}}$ | 4.04/3.81 | 4.80/4.72 | 5.85/5.74 | 1.82/1.84 | 1.83/1.85 | 1.84/1.85 |
|  | $r_{\text{oxy}}$ | 3.17/3.12 | 3.48/3.43 | 3.83/3.83 | 4.28/4.23 | 4.28/4.23 | 4.28/4.23 |
|  | $r_{\text{hyd}}$ | 4.09/3.96 | 4.51/4.48 | 5.00/5.00 | 2.70/2.64 | 2.70/2.64 | 2.70/2.64 |
| change | $\Delta$O$_{\text{water}}$ | 1.05/0.90 | 1.83/1.67 | 2.73/2.69 | 5.47/5.41 | 5.43/5.37 | 5.46/5.39 |
|  | $\Delta$H$_{\text{water}}$ | 3.11/3.00 | 4.73/4.51 | 6.41/6.53 | 0.36/0.35 | 0.39/0.37 | 0.40/0.38 |

O$_{\text{water}}$ and H$_{\text{water}}$ designate the CN of water oxygen and hydrogen atoms around the corresponding ion species.
$r_{\text{oxy}}$ and $r_{\text{hyd}}$ identifies the minimum position after the first solvation shell in $g(r)$
CN in ionic solutions: analogous CN of the ion species in 0.1 M ion solutions.
CN inside 1ZLL$_{\text{CHA}}$: CN inside the restriction of 1ZLL$_{\text{JC}}$/1ZLL$_{\text{CHA}}$.
The change in CN between solution and the inside is given in the last two rows

A focus was laid on changes in the first solvation shell occurring due to transition of an ion from bulk phase (fig. 7.5) to the hydrophobic restriction (fig. 7.6). Using solutions of 0.1 M NaCl, KCl and CsCl, CN values for ions in bulk phase and correspondingly positioned at the restriction $w_0$ of 1ZLL ($z = -19.5$ Å) were calculated. As a descriptor for the solvation and interaction of the ions with the water oxygen (O$_{\text{water}}$) and hydrogen (H$_{\text{water}}$) CNs were estimated (table 7.2), where (O$_{\text{water}}$)

was used as a substitutional for the complete water molecule. Based on these calculations, the first solvation shell in the bulk phase for Cl⁻ is comprised of 10 to 9 water molecules in dependency of the chosen parameter set, where $Na^+$, $K^+$ and $Cs^+$ have 6, 5 and 4 water molecules in their first solvation shell in the mean. Mimicking the transition into the most restricted position of the hydrophobic funnel in 1ZLL resulted in $O_{water}$ CNs of 3.25, 3.32 and 3.61 for the cations $Na^+$, $K^+$ and $Cs^+$, implicating a loss of 1 to 3 water molecules in the first shell. For the same transition, Cl⁻ needs to strip off 5 to 6 water molecules to a total CN for $O_{water}$ of 4 to 5.
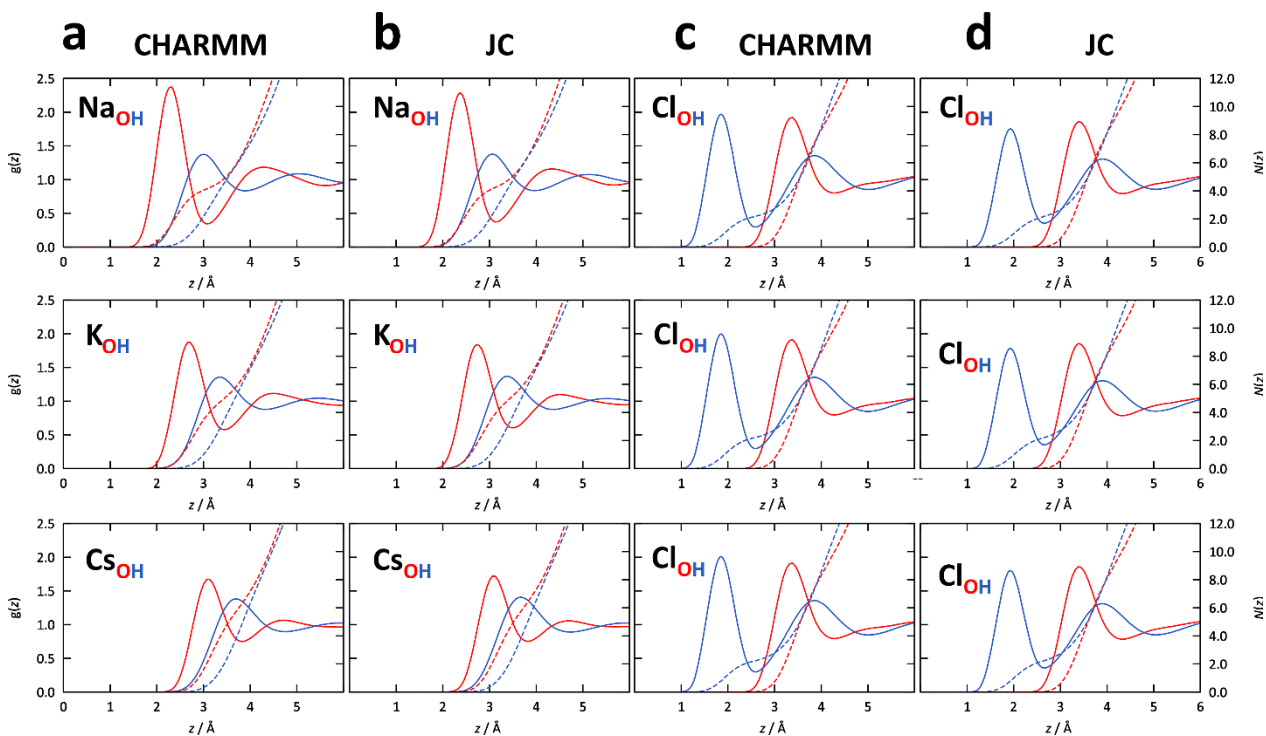


**Figure 7.5**: Distribution function $g(\mathbf{r})$ in ionic bulk solution for the parameter sets of Cheatham and CHARMM. **a, b**: Representation of the radial distribution function for oxygen (red) and hydrogen (blue) with $Na^+$, $K^+$, $Cs^+$ in bulk solutions of 0.1 M concentration. The cumulative integration over $g(\mathbf{r})$ is shown for oxygen and hydrogen in dashed lines. **c, d**: Depiction of the spherical distribution function between Cl⁻ and oxygen (red) or hydrogen (blue) in solutions of 0.1 M NaCl, KCl and CsCl. Dashed lines indicate the integration of the distribution function resulting in $N(r)$.
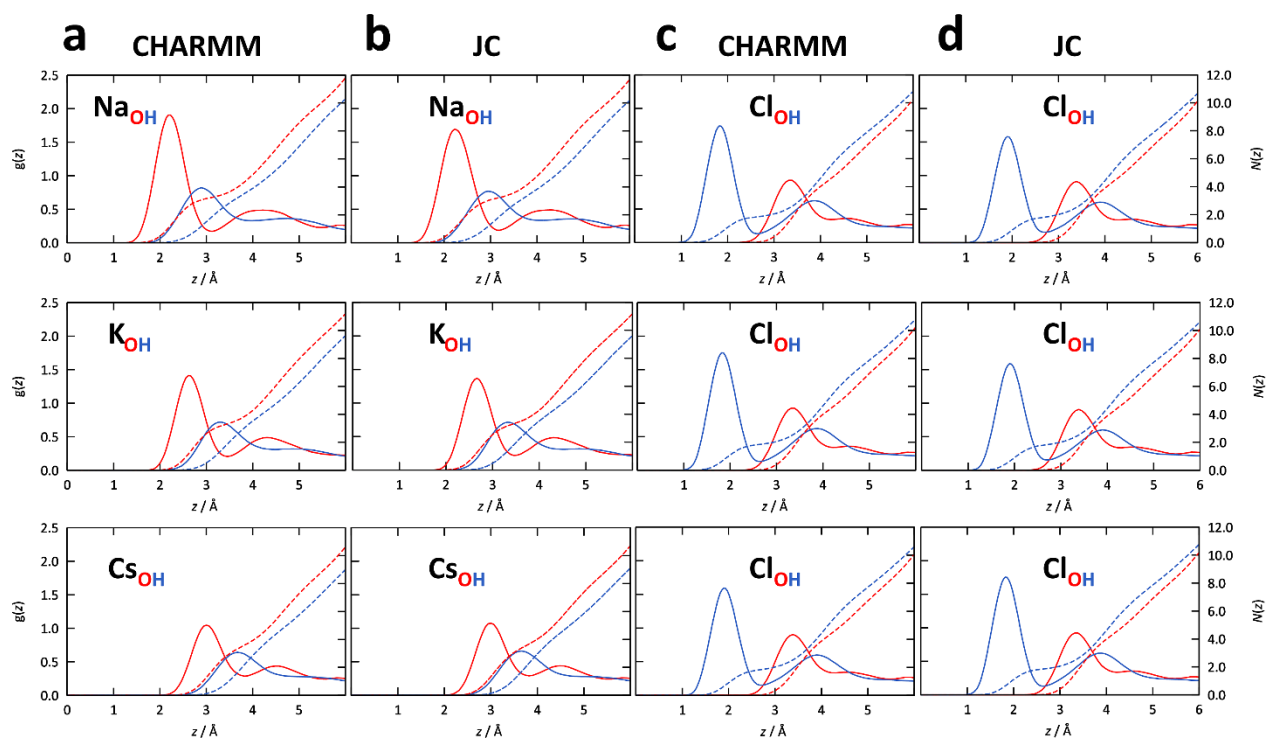
**Figure 7.6**: Distribution function inside the restriction of 1ZLL$_{JC}$ and 1ZLL$_{CHA}$. **a**, **b**: Depiction of the radial pair distribution function $g(\mathbf{r})$ for the cations (Na$^+$, K$^+$, Cs$^+$) localized inside the restriction ($z$ =-19.5 Å) and hydrogen (blue) or oxygen (red). **c**, **d**: Distribution function of hydrogen and oxygen with the anions of NaCl, KCl and CsCl. The dashed lines indicate the increasing integration over the distribution function $N(r)$

## 7.4  Conclusion

Due to a novel combination of 3D RISM results and approximations for the pmf, solvation effects are revealed to be of importance in the establishment of the inter-cationic order as well as for the general cation-anion selectivity in the hydrophobic pentamer PLN. Local investigations of the hydrophobic constriction revealed the influence of solvent effects on the cation-anion selectivity, considering the compensation of the opposing anion selectivity in vacuum, described by $u_{\text{fit,vac}}(z)$ (table 7.1). According to the inter-cation changes in the pmf between vacuum ($u_{\text{fit,vac}}(z)$) and solution ($w_{\text{fit}}(z)$), solvent effects are also involved in the inter-cation selectivity.

Investigation of the free energies contributing to the thermodynamic cycle, that describes the ion-to-restriction transfer in PLN, permitted a further detailed explanation for the established inter-cationic order and provide a possible reason for the anion discrimination. In particular the process of ion solvation ($\Delta G_{\text{solv}}^{\text{ion}}$) was pointed out to be the driving force behind the inter-cationic selectivity, while the discrimination of anions was identified to be dependent on the solvation

process of the ion+pore complex ($\Delta G_{\text{solv}}^{\text{ion+pore}}$). According to these results the inter-cationic selectivity order is predominantly controlled by the local property of ion and pore solvation ($\Delta G_{\text{solv}}^{\text{ion}}, \Delta G_{\text{solv}}^{\text{pore}}$) as supported by the corresponding coordination numbers, while the anion over cation selectivity depends on global solvation effects ($\Delta G_{\text{solv}}^{\text{ion+pore}}$). Contributions of a membrane would cancel in consequence of the established thermodynamic cycle (fig. 7.1).

Besides explaining the selectivity of PLN, the information derived from the established thermodynamic cycle emphasizes the pmf to be the result of drastic energy cancellation that in the end leads to surmountable barriers. This circumstance emphasizes the obtained sensitivity of ion selectivity on the parameter set. As the pmf is the determining quantity for ion permeation, the conductivity is affected by the revealed cancelation of the solvent free energy with the vacuum contributions.

A sensitivity of the ion conduction on the different force field parameters is also emphasized by deviations in $w_{\text{fit}}(z)$ between 1ZLL$_{\text{CHA}}$ and 1ZLL$_{\text{JC}}$ (table 7.1).

The experimentally stated cation selectivity of the hydrophobic pentamer PLN is supported by the here presented results, gained from a novel combination of *in silico* experiments. Finally we shed light on the solvation mechanism for ion transport and the selectivity in hydrophobic channels without a specialized filter and cavity structure, by revealing the small pmf barriers to be the result of huge energy cancellations, which controls the conductivity and ion selectivity of the channel.

# 8 Conclusion

The subject of this work was the thermodynamic and kinetic characterization of the ion selectivity of three different nanopore systems and the associated establishment of the required analysis tools, using a computational multiscale approach. A brief summary of the most important results shall be given in the following paragraphs.

In a first approach the small ion channel $Kcv_{ATCV-1}$ from the *Acanthocystis turfacea* virus was investigated on an atomistic scale by MD simulations. Due to the absence of any spatial structural information, a homology model was successfully created on the basis of the closed structure of KirBac1.1. The calculated model was shown to be stable over several 100 ns of unrestrained MD simulations in which it kept its secondary structure and coordinated cations in its filter region. An average structural model of the minimalistic $Kcv_{ATCV-1}$ channel was generated from these simulations which forms the basis for further mutant models that are currently examined experimentally. It was not possible at this point to characterize this structure as open or closed, although the stability and the ion distribution features hint at a possible open form. Calculation of the solvent distribution by 3D RISM for this structure and evaluation of the accessible inner volume allowed for the determination of characteristic profiles of local concentrations, partition coefficients and potentials of mean force, all relevant for understanding solvation effects on permeation pathways, which is experimentally difficult or impossible to access. Cooperative effects of the solvent were considered in all studies, which is a remarkable advantage of the 3D RISM implicit solvent model in contrast to simpler continuum electrostatics approaches. Applied to the $Kcv_{ATCV-1}$ channel, the results support the cation selectivity of this structure. In particular, the potential of mean force near the filter and the mouth region properly reveal the ion coordination by the protein and a possible aromatic gate.

In contrast to the polar tetrameric channels with a highly conserved protein architecture, the recently synthesized hydrophobic nanopore of Gong et al. attracted further attention as a model system to apply 3D RISM theory, as it presumably inherits a strong ion selectivity even in biological membranes with an also stated gating activitiy.[6] By investigations with the established thermodynamic tool chain for the analysis of 3D RISM results, this pore was revealed to be predominantly anion-selective, independent of the applied concentrations, and in contrast to

experimentally claimed behavior. As a novel development, ion conductance was computed from a mean-field theory[5] based on 3D RISM pmfs, which is possible in this case due to the low overall occupancy. The results support the anion selectivity of this pore in agreement with MD simulations also conducted in order to examine the validity of the RISM-based conductance estimation approach. This promising evidence together with earlier data obtained for Kcv$_{ATCV-1}$ allowed for further application of the 3D RISM methodology to the hydrophobic phospholamban channel.

Investigation of this pore confirmed theoretically the experimentally observed cation channel conductance with a selectivity order of $Na^+ < K^+ < Cs^+$ in the conducting state. Truncation mutations showed the insignificance of the cytosolic domain in the context of ion conductance while a supposedly closed form was indeed found to be impermeable to ions. Clear evidence was found for an intrinsic dependence of the ionic selectivity of hydrophobic channels on their internal radius, validated by comparison with ligand gated ion channels with known discrimination capabilities. Detailed thermodynamic analysis of the hydrophobic constriction of phospholamban allowed for a decomposition of the total pmf into local energetic and entropic contributions and a thermodynamic cycle containing individual solvation free energies of the pore and the ions. The results uncovered a size selectivity of the restriction under vacuum conditions which is inverted by overcompensating solvation effects. In particular, the differences in the solvation free energies of the ions are decisive for the inter-cation order. In contrast, the cation-over-anion selectivity is exhibited by global aspects, specifically by the reduced solubility of the ion-pore complex for anions in comparison with cations.

In summary, this work showed that ionic selectivity is a complex feature which depends on subtle individual structural, energetic and dynamical properties of the nanopore under investigation. The combination of various computational methods on varying scales and theoretical levels is essential to understand experimental features.

# 9 Appendix
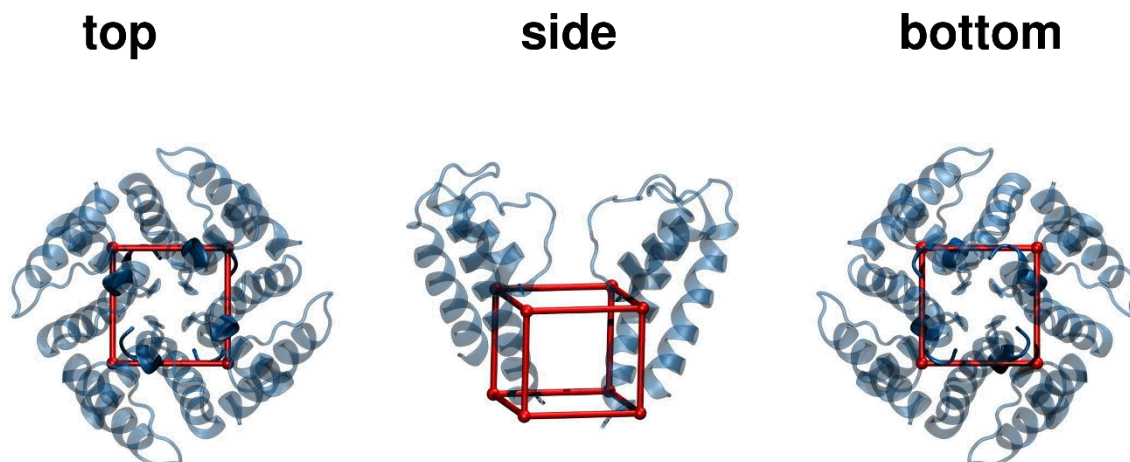
**top**        **side**        **bottom**



**Figure A9.1**: Water selection volume. Representation of the defined volume (red box) inside the ATCV-1 (blue) cavity. The overlay is shown for the top, side and bottom view. Only two monomers are shown for clarification in the side view. The protein is represented as a transparent cartoon.

## Results of the Blastp local alignment

Blastp was used to estimate the homology between the closed KirBac1.1 and ATCV-1$_{hom}$ structure. The local alignment of the Kirbac1.1 with Kcv$_{ATCV-1}$ amino acid sequence follows:

```
KirBac 29   LFALLYQLGDAPIANQSPPGFVGAFFFSVETLATVGYGDMHPQTVYAHAIATLEIFV 85
            +F  +Y++     + + + P +V   +FS  T  TVGYGD+ P++  A   AT  + +
ATCV-1 13   VFTAIYKMLPGGMFSNTDPTWVDCLYFSASTHTTVGYGDLTPKSPVAKLTATAHMLI 69
```

Thereby a Score of 37.0 bits (84) by an identity of 30 % was stated. Also 31 of the 57 (54%) residues are positive. *Blastp* was used in version 2.2.31.[234,258]

# Alignment for Modeller

Initial input alignment for the creation of the ATCV-1$_{hom}$ homology model

```
>P1;kirbac1_1_only.pdb
structure:kirbac1_1_only.pdb:1:A:94:D::::
MDLYYWALKVSWPVFFASLAALFVVNNTLFALLYQLGDAPIANQSPP
GFVGAFFFSVETLATVGYGDMHPQTVYAHAIATLEIFVGMSGIALST
----/
MDLYYWALKVSWPVFFASLAALFVVNNTLFALLYQLGDAPIANQSPP
GFVGAFFFSVETLATVGYGDMHPQTVYAHAIATLEIFVGMSGIALST
----/
MDLYYWALKVSWPVFFASLAALFVVNNTLFALLYQLGDAPIANQSPP
GFVGAFFFSVETLATVGYGDMHPQTVYAHAIATLEIFVGMSGIALST
----/
MDLYYWALKVSWPVFFASLAALFVVNNTLFALLYQLGDAPIANQSPP
GFVGAFFFSVETLATVGYGDMHPQTVYAHAIATLEIFVGMSGIALST
----/*


>P1;atcv1
sequence:atcv1::::::::0.00:0.00
-------------MLLLIIHIIILI---VFTAIYKMLPGGMFSNTDP
TWVDCLYFSASTHTTVGYGDLTPKSPVAKLTATAHMLIVFAIVISGF
TFPW/
-------------MLLLIIHIIILI---VFTAIYKMLPGGMFSNTDP
TWVDCLYFSASTHTTVGYGDLTPKSPVAKLTATAHMLIVFAIVISGF
TFPW/
-------------MLLLIIHIIILI---VFTAIYKMLPGGMFSNTDP
TWVDCLYFSASTHTTVGYGDLTPKSPVAKLTATAHMLIVFAIVISGF
TFPW/
-------------MLLLIIHIIILI---VFTAIYKMLPGGMFSNTDP
TWVDCLYFSASTHTTVGYGDLTPKSPVAKLTATAHMLIVFAIVISGF
TFPW/*
```

# 1D RISM and 3D RISM parameters

**Table A9.1**: 1D RISM parameters overview in dependency on the chapter

| Solution | chapter 4 | | chapter 5,6 and 7 | |
| --- | --- | --- | --- | --- |
| | $\rho$ / Å | $\varepsilon_r$ | $\rho$ / Å | $\varepsilon_r$ |
| NaCl | 55.246 | 78.4 | 55.246 | 78.4 |
| KCl | 55.189 | 78.4 | 55.189 | 78.4 |
| CsCl | 55.189 | 75.8 | 55.189 | 78.4 |

$\varepsilon_r$ describes the permittivity

$\rho$ denotes the solvent density

**Table A9.2**: 3D RISM: CHARMM[186,190] and JC[250] force fields parameter

| Element | CHARMM | | | Joung and Cheatham | | |
| --- | --- | --- | --- | --- | --- | --- |
| | $\sigma$ / Å | $\varepsilon$ / kcal mol$^{-1}$ | charge | $\sigma$ / Å | $\varepsilon$ / kcal mol$^{-1}$ | charge |
| O | 3.151 | 0.152 | -0.834 | 3.151 | 0.152 | -0.834 |
| H | 0.400 | 0.046 | 0.417 | 0.400 | 0.046 | 0.417 |
| Na$^+$ | 2.430 | 0.047 | 1.000 | 2.439 | 0.087 | 1.000 |
| K$^+$ | 3.143 | 0.087 | 1.000 | 3.038 | 0.194 | 1.000 |
| Cs$^+$ | 3.742 | 0.190 | 1.000 | 3.530 | 0.407 | 1.000 |
| Cl$^-$ | 4.045 | 0.150 | -1.000 | 4.478 | 0.036 | -1.000 |

$\sigma$ and $\varepsilon$ parameters and charges from CHARMM or JC (Joung and Cheatham) force fields used in 3D RISM.

# Pore monomer partial charges

Partial charges of a single monomor for the pore of Gong et al.[6] are provided in table A9.3

**Table A9.3:** Monormer structure

| Index | atom | type | $q$ | Index | atom | type | $q$ | Index | atom | type | $q$ |
|---|---|---|---|---|---|---|---|---|---|---|---|
| 1 | C01 | CA | -0.067035 | 39 | O02 | O | -0.5978 | 77 | H22 | H | 0.15713 |
| 2 | H01 | H | 0.15096 | 40 | O51 | O | -0.5978 | 78 | C30 | CA | -0.062035 |
| 3 | C07 | C | -0.096535 | 41 | O52 | O | -0.5978 | 79 | H3 | H | 0.15713 |
| 4 | C09 | CA | 0.016465 | 42 | O53 | O | -0.5978 | 80 | C38 | CA | -0.067035 |
| 5 | C15 | C | -0.096535 | 43 | O54 | O | -0.5978 | 81 | H38 | H | 0.15096 |
| 6 | C17 | CA | 0.016465 | 44 | O56 | O | -0.5978 | 82 | C46 | CA | -0.067035 |
| 7 | C23 | C | -0.096535 | 45 | C03 | CA | -0.062035 | 83 | H46 | H | 0.15096 |
| 8 | C25 | CA | 0.016465 | 46 | H03 | H | 0.15713 | 84 | N06 | N | -0.57194 |
| 9 | C31 | C | -0.096535 | 47 | C11 | CA | -0.14364 | 85 | C54 | C | 0.077932 |
| 10 | C33 | CA | 0.016465 | 48 | C19 | CA | 0.016465 | 86 | H541 | HA | 0.046773 |
| 11 | C39 | C | -0.096535 | 49 | C27 | CA | 0.016465 | 87 | H542 | HA | 0.046665 |
| 12 | C41 | CA | 0.016465 | 50 | C35 | CA | -0.14364 | 88 | H543 | HA | 0.046665 |
| 13 | C47 | C | -0.096535 | 51 | C43 | CA | -0.14364 | 89 | C57 | C | 0.077932 |
| 14 | C49 | CD | 0.66933 | 52 | N03 | N | -0.57194 | 90 | H571 | HA | 0.046665 |
| 15 | C50 | CD | 0.66933 | 53 | C04 | CA | -0.14364 | 91 | H572 | HA | 0.046665 |
| 16 | C51 | CD | 0.66933 | 54 | C12 | CA | -0.062035 | 92 | H573 | HA | 0.046665 |
| 17 | C52 | CD | 0.66933 | 55 | H1 | H | 0.15713 | 93 | C59 | C | 0.077932 |
| 18 | C53 | CD | 0.66933 | 56 | C20 | CA | -0.062035 | 94 | H591 | HA | 0.046665 |
| 19 | C55 | CD | 0.66933 | 57 | H20 | H | 0.15713 | 95 | H592 | HA | 0.046665 |
| 20 | N01 | N | -0.57194 | 58 | C28 | CA | -0.062035 | 96 | H593 | HA | 0.046665 |
| 21 | C02 | CA | 0.016465 | 59 | H28 | H | 0.15713 | 97 | C61 | C | 0.077932 |
| 22 | C08 | C | -0.096535 | 60 | C36 | CA | -0.062035 | 98 | H611 | HA | 0.046665 |
| 23 | C10 | CA | -0.062035 | 61 | H36 | H | 0.15713 | 99 | H612 | HA | 0.046665 |
| 24 | H10 | H | 0.15713 | 62 | C44 | CA | -0.062035 | 100 | H613 | HA | 0.046665 |
| 25 | C16 | C | -0.096535 | 63 | H44 | H | 0.15713 | 101 | C63 | C | 0.077932 |
| 26 | C18 | CA | -0.067035 | 64 | N04 | N | -0.57194 | 102 | H631 | HA | 0.046665 |
| 27 | H18 | H | 0.15096 | 65 | C05 | CA | -0.062035 | 103 | H632 | HA | 0.046665 |
| 28 | C24 | C | -0.096535 | 66 | H2 | H | 0.15713 | 104 | H633 | HA | 0.046665 |
| 29 | C26 | CA | -0.067035 | 67 | C13 | CA | 0.016465 | 105 | C65 | C | 0.077932 |
| 30 | H26 | H | 0.15096 | 68 | C21 | CA | -0.14364 | 106 | H651 | HA | 0.046665 |
| 31 | C32 | C | -0.096535 | 69 | C29 | CA | -0.14364 | 107 | H652 | HA | 0.046665 |
| 32 | C34 | CA | -0.062035 | 70 | C37 | CA | 0.016465 | 108 | H653 | HA | 0.046665 |
| 33 | H34 | H | 0.15713 | 71 | C45 | CA | 0.016465 | 109 | H05 | H | 0.31213 |
| 34 | C40 | C | -0.096535 | 72 | N05 | N | -0.57194 | 110 | H07 | H | 0.31213 |
| 35 | C42 | CA | -0.062035 | 73 | C06 | CA | 0.016465 | 111 | H09 | H | 0.31213 |
| 36 | H42 | H | 0.15713 | 74 | C14 | CA | -0.067035 | 112 | H11 | H | 0.31213 |
| 37 | C48 | C | -0.096535 | 75 | H3 | H | 0.15096 | 113 | H12 | H | 0.31213 |
| 38 | N02 | N | -0.57194 | 76 | C22 | CA | -0.062035 | 114 | H14 | H | 0.31213 |

$q$ denotes the partial charger in elementary units.
Type defines the CHARMM like "atomtype" name.

# Grid size dependency

The influence of the applied grid size in and the point spacing in chapter 5 was also evaluated. A grid size of 120³ Å³ was chosen with a grid spacing of 0.6 Å. Control calculations were conducted varying the grid size and spacing parameters (table A9.4). The restrained hydrophobic pore used in $MD_{fix}$ was chosen as the test case, treated with 1 M concentrations of KCl. Smaller grid sizes have a slight effect on the absolute value (table A9.4). Still several 3D RISM calculations failed to converge for smaller grid spacing. The similar $\gamma_{RISM}$ between the smaller 100³ Å³ and the slightly bigger 120³ Å³ grid confirm the size of the core box to be suitable.

**Table A9.4** Grid size variation in 1 M KCl with restrained pore geometry

|  | grid size / spacing | $K^+$ | $Cl^-$ |
|---|---|---|---|
|  | 150³ Å³ / 0.4 Å | 180.90 | 461.60 |
| $\gamma_{RISM}$ / pS | 100³ Å³ / 0.6 Å | 171.82 | 440.17 |
|  | **120³ Å³ / 0.6 Å** | 171.92 | 440.07 |

$\gamma_{RISM}$ denotes the calculated conductance value.
Bold font indicates the standard used in this work.

# Benchmark studies for chapter 6

The influence of the closure was evaluated by calculations for 1ZLL(CHA) and 1ZLL(CHA,uncharged), which is in focus of this work (fig. A9.2). The systems 1ZLL(CHA) and 1ZLL(CHA,uncharged) were applied in 3D RISM $uv$ calculations using the HNC, PSE-4 and PSE-3 closure. While results obtained with a PSE-3 closure overestimate the influence of the cation (fig. A9.2a, left) in charged systems, the PSE-4 closure underestimates the same in uncharged systems (fig. A9.2a, right).
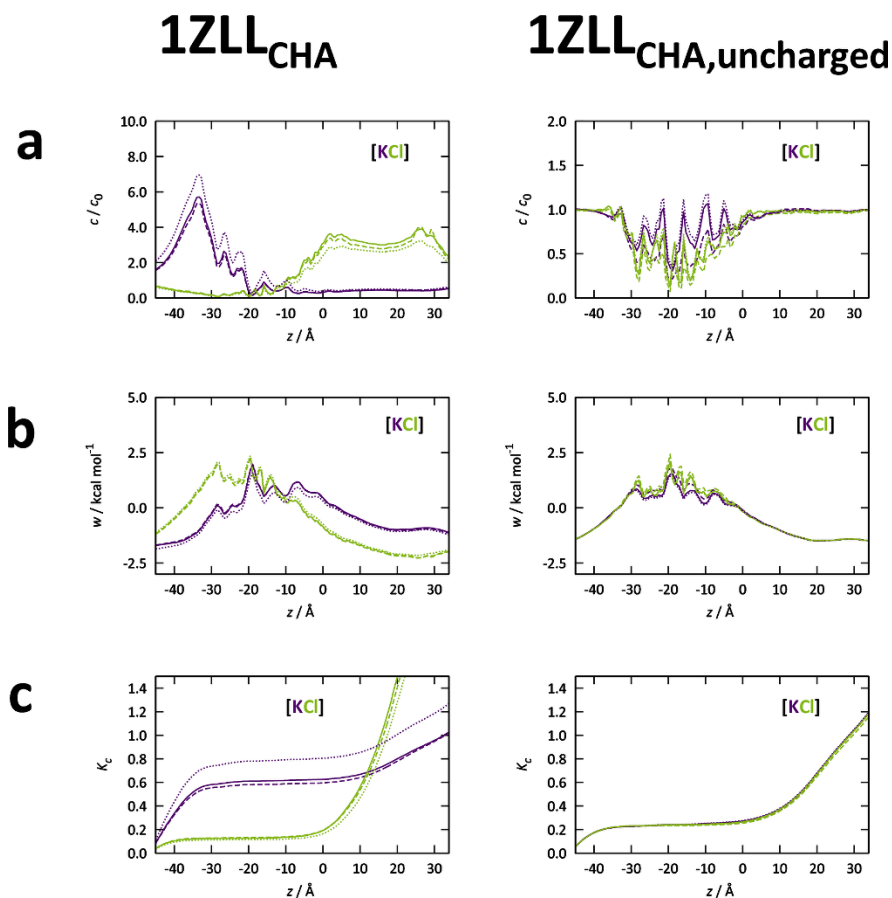


**Figure A9.2**: Closure validation. Results for only the KCl $c(z)$ (**a**), $w(z)$ (**b**), $K_C$ (**c**) and profiles for 1ZLL(CHA) and 1ZLL(CHA,uncharged) applying the closures PSE-3 (dotted), PSE-4 (solid line) and HNC (dashed). A salt concentration of 0.1 M was chosen for $K^+$ (purple) and $Cl^-$ (green). The parameter set of CHARMM was applied.

For 3D RISM *uv* calculations with the pentameric ion channel 5-HT$_3$R, PSE-3 was the only feasible closure relation. A corresponding benchmark study is provided in fig. A9.3.
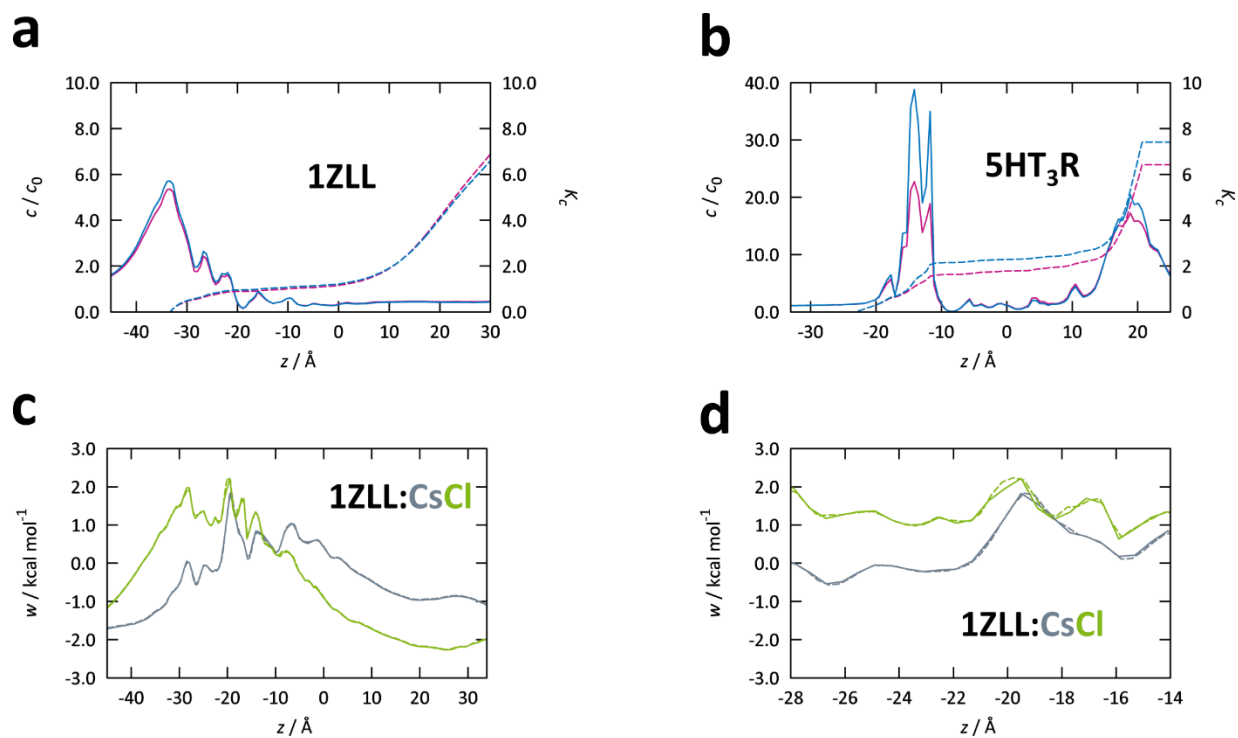


**Figure A9.3**: Benchmark studies of 1ZLL and Comparison of 3D RISM *uv* calculation results using a PSE-4 and a HNC closure for 0.1 M solutions of 1ZLL(CHA) (**a**). Depicted are the concentration profiles (solid lines) and partition constants (dashed lines) obtained by 3D RISM *uv* calculations with PSE-4 (light blue) and HNC (light red) for 0.1 M solutions of KCl (only K$^+$ is shown) in 1ZLL. Compare of order PSE-4 (light blue) and PSE-3 (light red) closures applied to 5HT$_3$R depicted for 0.1 M KCl solutions (only K is shown, Line style follows **a**) (**b**). Influence of grid size (**c-d**). Computation of the CsCl (Cs$^+$: gray; Cl$^-$: green) pmf with a grid size of 0.4 Å (dashed) for 1ZLL **c** in overlay with results from 0.6 Å (solid). Excerpts are shown for clarification **d**.

Full panel of all approximated thermodynamic values in chapter 7

## Part I: cations

| Property | position | Na$^+$ | K$^+$ | Cs$^+$ | parameter set |
|---|---|---|---|---|---|
| $w_0(z)$ [kcal/mol] | $z$=-19.5 | -0.38/-0.33 | -0.56/-0.58 | -1.21/-1.28 | (1ZLL$_{CHA}$/1ZLL$_{JC}$) |
| $Z(z)$ | $z$=-19.5 | 0.04/0.04 | 0.06/0.06 | 0.04/0.05 | (1ZLL$_{CHA}$/1ZLL$_{JC}$) |
| $w_{fit}(z)$ [kcal/mol] | $z$=-19.5 | 1.87/1.87 | 1.68/1.65 | 1.96/1.81 | (1ZLL$_{CHA}$/1ZLL$_{JC}$) |
| $U^v(z)$ [kcal/mol] | $z$=-19.5 | 0.22/0.26 | 0.03/0.01 | -0.61/-0.69 | (1ZLL$_{CHA}$/1ZLL$_{JC}$) |
| $S^v(z)$ [cal/mol K] | $z$=-19.5 | -0.01/-5.40 | -0.01/-5.51 | -0.01/-8.36 | (1ZLL$_{CHA}$/1ZLL$_{JC}$) |
| $-T\Delta S^v(z)$ [kcal/mol] | $z$=-19.5 | 1.65/1.61 | 1.66/1.64 | 2.58/2.49 | (1ZLL$_{CHA}$/1ZLL$_{JC}$) |
| $k$ [kcal/mol Å²] | $z$=-19.5 | 2.98/2.79 | 3.01/2.95 | 14.26/12.35 | (1ZLL$_{CHA}$/1ZLL$_{JC}$) |
| $u_0$ [kcal/mol] | $z$=-19.5 | 92.37/92.25 | 94.96/93.56 | 94.02/92.60 | (1ZLL$_{CHA}$/1ZLL$_{JC}$) |
| $Z(z)_{vac}$ | $z$=-19.5 | 399.38/0.00 | 412.38/0.00 | 409.41/0.00 | (1ZLL$_{CHA}$/1ZLL$_{JC}$) |
| $u(z)_{fit,vac}$ [kcal/mol] | $z$=-19.5 | 95.45/95.44 | 98.56/97.20 | 97.85/96.42 | (1ZLL$_{CHA}$/1ZLL$_{JC}$) |
| $U(z)_{vac}$ [kcal/mol] | $z$=-19.5 | 92.97/92.84 | 95.55/94.15 | 94.61/93.19 | (1ZLL$_{CHA}$/1ZLL$_{JC}$) |
| $S(z)_{vac}$[cal/mol K] | $z$=-19.5 | -8.34/-8.74 | -10.08/-10.24 | -10.86/-10.82 | (1ZLL$_{CHA}$/1ZLL$_{JC}$) |
| $-T\Delta S(z)_{vac}$ [kcal/mol] | $z$=-19.5 | 2.49/2.61 | 3.01/3.05 | 3.24/3.23 | (1ZLL$_{CHA}$/1ZLL$_{JC}$) |
| $k_{vac}$ [kcal/mol Å²] | $z$=-19.5 | 12.25/14.98 | 29.46/31.91 | 43.51/42.60 | (1ZLL$_{CHA}$/1ZLL$_{JC}$) |
| $w_0(z)$ [kcal/mol] | $z$=-18.9 | -0.32/0.01 | -0.68/-0.48 | -4.50/-3.25 | (1ZLL$_{CHA}$/1ZLL$_{JC}$) |
| $Z(z)$ | $z$=-18.9 | 0.04/0.02 | 0.06/0.04 | 1.76/0.03 | (1ZLL$_{CHA}$/1ZLL$_{JC}$) |
| $w_{fit}(z)$ [kcal/mol] | $z$=-18.9 | 1.97/2.23 | 1.70/1.92 | 0.33/0.63 | (1ZLL$_{CHA}$/1ZLL$_{JC}$) |
| $U^v(z)$ [kcal/mol] | $z$=-18.9 | 0.27/0.59 | -0.09/0.11 | -3.91/-2.66 | (1ZLL$_{CHA}$/1ZLL$_{JC}$) |
| $S^v(z)$ [cal/mol K] | $z$=-18.9 | -5.72/-5.52 | 5.99/-6.07 | -12.00/11.04 | (1ZLL$_{CHA}$/1ZLL$_{JC}$) |
| $-T\Delta S^v(z)$ [kcal/mol] | $z$=-18.9 | 1.71/1.65 | 1.79/1.81 | 3.58/3.29 | (1ZLL$_{CHA}$/1ZLL$_{JC}$) |
| $k$ [kcal/mol Å²] | $z$=-18.9 | 3.28/2.97 | 3.75/3.90 | 77.30/47.78 | (1ZLL$_{CHA}$/1ZLL$_{JC}$) |
| $u_0$ [kcal/mol] | $z$=-18.9 | 93.15/93.27 | 95.68/95.57 | 98.52/97.03 | (1ZLL$_{CHA}$/1ZLL$_{JC}$) |
| $Z(z)_{vac}$ | $z$=-18.9 | 0.00/0.00 | 0.00/0.00 | 0.00/0.00 | (1ZLL$_{CHA}$/1ZLL$_{JC}$) |
| $u(z)_{fit,vac}$ [kcal/mol] | $z$=-18.9 | 96.59/96.74 | 99.43/99.36 | 102.59/101.08 | (1ZLL$_{CHA}$/1ZLL$_{JC}$) |
| $U(z)_{vac}$ [kcal/mol] | $z$=-18.9 | 93.75/93.86 | 96.27/96.17 | 99.12/97.62 | (1ZLL$_{CHA}$/1ZLL$_{JC}$) |
| $S(z)_{vac}$[cal/mol K] | $z$=-18.9 | 9.53/-9.68 | -10.60/-10.72 | -11.64/-11.59 | (1ZLL$_{CHA}$/1ZLL$_{JC}$) |
| $-T\Delta S(z)_{vac}$ [kcal/mol] | $z$=-18.9 | 2.84/2.88 | 3.16/3.20 | 3.47/3.46 | (1ZLL$_{CHA}$/1ZLL$_{JC}$) |
| $k_{vac}$ [kcal/mol Å²] | $z$=-18.9 | 22.26/23.99 | 38.12/40.52 | 64.47/63.00 | (1ZLL$_{CHA}$/1ZLL$_{JC}$) |
| $\Delta G_{solv}^{ion}$ | $z$=-19.5 | -85.18/-81.96 | -67.27/-66.71 | -54.39/-56.62 | (1ZLL$_{CHA}$/1ZLL$_{JC}$) |
| $\Delta G_{solv}^{pore}$ | $z$=-19.5 | -3,454.70/-3,464.28 | -3,456.21/-3,443.58 | -3,427.76/-3,422.11 | (1ZLL$_{CHA}$/1ZLL$_{JC}$) |
| $\Delta G_{solv}^{ion+pore}$ | $z$=-19.5 | -3,633.49/-3,639.81 | -3,620.34/-3,605.82 | -3,578.18/-3,573.48 | (1ZLL$_{CHA}$/1ZLL$_{JC}$) |
| $\Delta G_{vac}^{binding}$ | $z$=-19.5 | 95.45/95.44 | 98.56/97.20 | 97.85/96.42 | (1ZLL$_{CHA}$/1ZLL$_{JC}$) |

Subscript *vac* designates vacuum energies.

$w_{fit}(z)$ represent the full pmf in solvation, with the fit minimum $w_0$.

$u_{fit,vac}(z)$ represent the vacuum potential, with the fit minimum $u_0(z)$.

$w(z)$ designates the pmf obtained in chapter 6.

$-T\Delta S^v(z)$ describes the entropy of the free energy in solvation.

$U^v(z)$ and denotes the internal energy.

The partition sum is denoted as $Z(z)$.

$\Delta G_{solv}^{ion}$, $\Delta G_{solv}^{pore}$, $\Delta G_{solv}^{ion+pore}$ and $\Delta G_{vac}^{binding}$ designate the free energies.

$k$ is the calculated force constant.

# Part II: anions

| Property | Position | Cl$_{NaCl}$ | Cl$_{KCl}$ | Cl$_{CsCl}$ | parameter set |
|---|---|---|---|---|---|
| $w_0(z)$ [kcal/mol] | $z$=-19.5 | -0.96/-0.81 | -2.09/-1.94 | -0.99/-1.64 | (1ZLL$_{CHA}$/1ZLL$_{JC}$) |
| $Z(z)$ | $z$=-19.5 | 0.02/0.01 | 0.05/0.04 | 0.02/0.03 | (1ZLL$_{CHA}$/1ZLL$_{JC}$) |
| $w_{fit}(z)$ [kcal/mol] | $z$=-19.5 | 2.39/2.61 | 1.77/1.89 | 2.35/2.11 | (1ZLL$_{CHA}$/1ZLL$_{JC}$) |
| $U^v(z)$ [kcal/mol] | $z$=-19.5 | -0.36/-0.21 | -1.50/-1.35 | -0.40/-1.05 | (1ZLL$_{CHA}$/1ZLL$_{JC}$) |
| $S^v(z)$ [cal/mol K] | $z$=-19.5 | -0.01/-9.48 | -0.01/-10.88 | -0.01/-10.60 | (1ZLL$_{CHA}$/1ZLL$_{JC}$) |
| $-T\Delta S^v(z)$ [kcal/mol] | $z$=-19.5 | 2.75/2.83 | 3.26/3.24 | 2.75/3.16 | (1ZLL$_{CHA}$/1ZLL$_{JC}$) |
| $k$ [kcal/mol Å$^2$] | $z$=-19.5 | 19.19/21.77 | 45.51/43.95 | 19.10/38.20 | (1ZLL$_{CHA}$/1ZLL$_{JC}$) |
| $u_0$ [kcal/mol] | $z$=-19.5 | -95.06/-93.92 | -95.06/-93.92 | -95.06/-93.92 | (1ZLL$_{CHA}$/1ZLL$_{JC}$) |
| $Z(z)_{vac}$ | $z$=-19.5 | -380.76/7.22704E+65 | -380.76/7.22704E+65 | -380.76/7.22704E+65 | (1ZLL$_{CHA}$/1ZLL$_{JC}$) |
| $u(z)_{fit,vac}$ [kcal/mol] | $z$=-19.5 | -91.00/-89.84 | -91.00/-89.84 | -91.00/-89.84 | (1ZLL$_{CHA}$/1ZLL$_{JC}$) |
| $U(z)_{vac}$ [kcal/mol] | $z$=-19.5 | -94.47/-93.33 | -94.47/-93.33 | -94.47/-93.33 | (1ZLL$_{CHA}$/1ZLL$_{JC}$) |
| $S(z)_{vac}$[cal/mol K] | $z$=-19.5 | -11.61/-11.69 | -11.61/-11.69 | -11.61/-11.69 | (1ZLL$_{CHA}$/1ZLL$_{JC}$) |
| $-T\Delta S(z)_{vac}$ [kcal/mol] | $z$=-19.5 | 3.46/3.49 | 3.46/3.49 | 3.46/3.49 | (1ZLL$_{CHA}$/1ZLL$_{JC}$) |
| $k_{vac}$ [kcal/mol Å$^2$] | $z$=-19.5 | 63.45/66.06 | 63.45/66.06 | 63.45/66.06 | (1ZLL$_{CHA}$/1ZLL$_{JC}$) |
| $w_0(z)$ [kcal/mol] | $z$=-18.9 | -7.18/-1.53 | -1.75/-1.37 | -1.96/-1.74 | (1ZLL$_{CHA}$/1ZLL$_{JC}$) |
| $Z(z)$ | $z$=-18.9 | 94.97/0.06 | 0.08/0.06 | 0.12/0.08 | (1ZLL$_{CHA}$/1ZLL$_{JC}$) |
| $w_{fit}(z)$ [kcal/mol] | $z$=-18.9 | -2.70/1.66 | 1.48/1.71 | 1.27/1.51 | (1ZLL$_{CHA}$/1ZLL$_{JC}$) |
| $U^v(z)$ [kcal/mol] | $z$=-18.9 | -6.65/-0.94 | -1.16/-0.78 | -1.37/-1.15 | (1ZLL$_{CHA}$/1ZLL$_{JC}$) |
| $S^v(z)$ [cal/mol K] | $z$=-18.9 | 13.27/-8.71 | -8.88/-8.34 | -8.79/-8.92 | (1ZLL$_{CHA}$/1ZLL$_{JC}$) |
| $-T\Delta S^v(z)$ [kcal/mol] | $z$=-18.9 | 3.96/2.60 | 2.65/2.49 | 2.64/2.66 | (1ZLL$_{CHA}$/1ZLL$_{JC}$) |
| $k$ [kcal/mol Å$^2$] | $z$=-18.9 | 146.37/14.74 | 16.06/12.27 | 15.74/16.40 | (1ZLL$_{CHA}$/1ZLL$_{JC}$) |
| $u_0$ [kcal/mol] | $z$=-18.9 | -107.04/-104.91 | -107.04/-104.91 | -107.04/-104.91 | (1ZLL$_{CHA}$/1ZLL$_{JC}$) |
| $Z(z)_{vac}$ | $z$=-18.9 | 1.89191E+75/0.00 | 1.89191E+75/0.00 | 1.89191E+75/0.00 | (1ZLL$_{CHA}$/1ZLL$_{JC}$) |
| $u(z)_{fit,vac}$ [kcal/mol] | $z$=-18.9 | -102.69/-100.55 | -102.69/-100.55 | -102.69/-100.55 | (1ZLL$_{CHA}$/1ZLL$_{JC}$) |
| $U(z)_{vac}$ [kcal/mol] | $z$=-18.9 | -106.44/-104.31 | -106.44/-104.31 | -106.44/-104.31 | (1ZLL$_{CHA}$/1ZLL$_{JC}$) |
| $S(z)_{vac}$[cal/mol K] | $z$=-18.9 | -12.59/-12.63 | -12.59/-12.63 | -12.59/-12.63 | (1ZLL$_{CHA}$/1ZLL$_{JC}$) |
| $-T\Delta S(z)_{vac}$ [kcal/mol] | $z$=-18.9 | 3.75/3.76 | 3.75/3.76 | 3.75/3.76 | (1ZLL$_{CHA}$/1ZLL$_{JC}$) |
| $k_{vac}$ [kcal/mol Å$^2$] | $z$=-18.9 | 103.96/105.87 | 103.96/105.87 | 103.96/105.87 | (1ZLL$_{CHA}$/1ZLL$_{JC}$) |
| $\Delta G_{solv}^{ion}$ | $z$=-19.5 | -94.47/-93.33 | -94.47/-93.33 | -94.47/-93.33 | (1ZLL$_{CHA}$/1ZLL$_{JC}$) |
| $\Delta G_{solv}^{pore}$ | $z$=-19.5 | -11.61/-11.69 | -11.61/-11.69 | -11.61/-11.69 | (1ZLL$_{CHA}$/1ZLL$_{JC}$) |
| $\Delta G_{solv}^{ion+pore}$ | $z$=-19.5 | 3.46/3.49 | 3.46/3.49 | 3.46/3.49 | (1ZLL$_{CHA}$/1ZLL$_{JC}$) |
| $\Delta G_{vac}^{binding}$ | $z$=-19.5 | 63.45/66.06 | 63.45/66.06 | 63.45/66.06 | (1ZLL$_{CHA}$/1ZLL$_{JC}$) |

Subscript *vac* designates vacuum energies.

$w_{fit}(z)$ represent the full pmf in solvation, with the fit minimum $w_0$.

$u_{fit,vac}(z)$ represent the vacuum potential, with the fit minimum $u_0(z)$.

$w(z)$ designates the pmf obtained in chapter 6.

$-T\Delta S^v(z)$ describes the entropy of the free energy in solvation.

$U^v(z)$ and denotes the internal energy.

The partition sum is denoted as $Z(z)$.

$\Delta G_{solv}^{ion}$, $\Delta G_{solv}^{pore}$, $\Delta G_{solv}^{ion+pore}$ and $\Delta G_{vac}^{binding}$designate the free energies.

$k$ is the calculated force constant.

# 10 References

1. Thiel, G., Greiner, T., Dunigan, D. D., Moroni, A. & Van Etten, J. L. Large dsDNA chloroviruses encode diverse membrane transport proteins. *Virology* **479,** 38–45 (2015).

2. Hille, B. *Ion Channels of Excitable Membranes*. (Sinauer, 2001).

3. Kuo, A. *et al.* Crystal Structure of the Potassium Channel KirBac1. 1 in the Closed State. *Science* **300,** 1922–1926 (2003).

4. Fitzgerald, L. A. *et al.* Sequence and annotation of the 288-kb ATCV-1 virus that infects an endosymbiotic chlorella strain of the heliozoon Acanthocystis turfacea. *Virology* **362,** 350–361 (2007).

5. Zhu, F. & Hummer, G. Theory and simulation of ion conduction in the pentameric GLIC channel. *J. Chem. Theory Comput.* **8,** 3759–3768 (2012).

6. Zhou, X. *et al.* Self-assembling subnanometer pores with unusual mass-transport properties. *Nat. Commun.* **3,** 949 (2012).

7. Li, H., Francisco, J. S. & Zeng, X. C. Unraveling the mechanism of selective ion transport in hydrophobic subnanometer channels. *Proc. Natl. Acad. Sci.* **112,** 10851–10856 (2015).

8. Choe, S. Potassium channel structures. *Nat. Rev. Neurosci.* **3,** 115–121 (2002).

9. MacKinnon, R. Potassium channels. *FEBS Lett.* **555,** 62–65 (2003).

10. Ashcroft, F. M. From molecule to malady. *Nature* **440,** 440–447 (2006).

11. Johns, D. C., Marban, E. & Nuss, H. B. Virus-Mediated Modification of of Cellular Excitability. *Ann. N. Y. Acad. Sci.* **868,** 418–422 (1999).

12. Sanguinetti, M. C. Dysfunction of delayed rectifier potassium channels in an inherited cardiac arrhythmia. *Ann. N. Y. Acad. Sci.* **868,** 406–413 (1999).

13. Sakmann, B. & Neher, E. Patch clamp techniques for studying ionic channels in excitable membranes. *Annu. Rev. Physiol.* **46,** 455–472 (1984).

14. Neher, E. & Sakmann, B. Single-channel currents recorded from membrane of denervated frog muscle fibres. *Nature* **260,** 799–802 (1976).

15. Hodgkin, A. L. & Huxley, A. F. A Quantitative Description of Membrane Current and its Application to Conduction and Excitation in Nerves. *J. Physiol.* **117,** 500–544 (1952).

16. Hille, B. Ionic channels in nerve membranes. *Prog. Biophys. Mol. Biol.* **21,** 1–32 (1970).

17. Hodgkin, A. L. & Keynes, R. D. The potassium permeability of a giant nerve fibre. *J. Physiol.* **128,** 61–88 (1955).

18. Hille, B. The permeability of the sodium channel to organic cations in myelinated nerve. *J. Gen. Physiol.* **58,** 599–619 (1971).

19. Hille, B. Potassium channels in myelinated nerve. Selective permeability to small cations. *J. Gen. Physiol.* **61,** 669–686 (1973).

20. Hille, B. & Schwarz, W. Potassium channels as multi-ion single-file pores. *J. Gen. Physiol.* **72,** 409–442 (1978).

21. Hille, B. The Receptor for Tetrodotoxin and Saxitoxin. *Biophys. J.* **15,** 615–619 (1975).

22. Armstrong, C. M. Time course of TEA(+)-induced anomalous rectification in squid giant axons. *J. Gen. Physiol.* **50,** 491–503 (1966).

23. Armstrong, C. M. Interaction of tetraethylammonium ion derivatives with the potassium channels of giant

axons. *J. Gen. Physiol.* **58,** 413–437 (1971).

24. Armstrong, C. M. & Taylor, S. R. Interaction of barium ions with potassium channels in squid giant axons. *Biophys. J.* **30,** 473–88 (1980).

25. Halstead, B. W. *Poisonous and venomous marine animals of the world*. (Darwin Press, 1978).

26. Bezanilla, F. & Armstrong, C. M. Inactivation of the sodium channel. I. Sodium current experiments. *J. Gen. Physiol.* **70,** 549–566 (1977).

27. Jan, Y. N., Jan, L. Y. & Dennis, M. J. Two mutations of synaptic transmission in Drosophila. *Proc. R. Soc. Lond. B. Biol. Sci.* **198,** 87–108 (1977).

28. Gazzarrini, S. *et al.* Chlorella virus ATCV-1 encodes a functional potassium channel of 82 amino acids. *Biochem. J.* **420,** 295–303 (2009).

29. Plugge, B. *et al.* A Potassium Channel Protein Encoded by Chlorella Virus PBCV-1. *Science* **287,** 1641–1644 (2000).

30. Tempel, B. L., Papazian, D. M., Schwarz, T. L., Jan, Y. N. & Jan, L. Y. Sequence of a probable potassium channel component encoded at Shaker locus of Drosophila. *Science* **237,** 770–775 (1987).

31. Zagotta, W. N., Hoshi, T. & Aldrich, R. W. Shaker Potassium Channel Gating III: Evaluation of Kinetic Models for Activation. *J. Gen. Physiol.* **103,** 321–362 (1994).

32. Zagotta, W. N., Hoshi, T., Dittman, J. & Aldrich, R. W. Shaker potassium channel gating. II: Transitions in the activation pathway. *J. Gen. Physiol.* **103,** 279–319 (1994).

33. Hurst, R. S., Latorre, R., Toro, L. & Stefani, E. External barium block of Shaker potassium channels: evidence for two binding sites. *J. Gen. Physiol.* **106,** 1069–87 (1995).

34. Heginbotham, L., Lu, Z., Abramson, T. & MacKinnon, R. Mutations in the K+ channel signature sequence. *Biophys. J.* **66,** 1061–7 (1994).

35. Doyle, D. A. *et al.* The structure of the potassium channel: molecular basis of K+ conduction and selectivity. *Science* **280,** 69–77 (1998).

36. Kaufman, A., Mackinnon, R. & Zhou, Y. Chemistry of ion coordination and hydration revealed by a K+ channel-Fab complex at 2.0 Å resolution. *Nature* **414,** 43–48 (2001).

37. Morais-Cabral, J. H., Zhou, Y. & MacKinnon, R. Energetic optimization of ion conduction rate by the K+ selectivity filter. *Nature* **414,** 37–42 (2001).

38. Noskov, S. Y., Bernèche, S. & Roux, B. Control of ion selectivity in potassium channels by electrostatic and dynamic properties of carbonyl ligands. *Nature* **431,** 830–834 (2004).

39. Roux, B. *et al.* Ion selectivity in channels and transporters. *J. Gen. Physiol.* **137,** 415–426 (2011).

40. Kandt, C., Ash, W. L. & Tieleman, D. P. Setting up and running molecular dynamics simulations of membrane proteins. *Methods* **41,** 475–475 (2007).

41. van Gunsteren, W. F., Dolenc, J. & Mark, A. E. Molecular simulation as an aid to experimentalists. *Curr. Opin. Struct. Biol.* **18,** 149–153 (2008).

42. Hansson, T., Oostenbrink, C. & van Gunsteren, W. F. Molecular dynamics simulations. *Curr. Opin. Struct. Biol.* **12,** 190–196 (2002).

43. Roux, B. *et al.* Ion selectivity in channels and transporters. *J. Gen. Physiol.* **137,** 415–426 (2011).

44. Gumbart, J., Aksimentiev, A., Tajkhorshid, E., Wang, Y. & Schulten, K. Molecular dynamics simulations of proteins in lipid bilayers. *Curr. Opin. Struct. Biol.* **15,** 423–431 (2005).

45. Khalili-Araghi, F. *et al.* Molecular dynamics simulations of membrane channels and transporters. *Curr. Opin. Struct. Biol.* **19,** 128–137 (2009).

46. Gumbart, J., Aksimentiev, A., Tajkhorshid, E., Wang, Y. & Schulten, K. Molecular dynamics simulations of

proteins in lipid bilayers. *J. Comput. Chem.* **15,** 80–90 (2007).

47.  Capener, C. E. *et al.* Homology modeling and molecular dynamics simulation studies of an inward rectifier potassium channel. *Biophys. J.* **78,** 2929–2942 (2000).

48.  Bernèche, S. & Roux, B. A microscopic view of ion conduction through the K+ channel. *Proc. Natl. Acad. Sci. U. S. A.* **100,** 8644–8 (2003).

49.  Egwolf, B. & Roux, B. Ion Selectivity of the KcsA Channel: A Perspective from Multi-Ion Free Energy Landscapes. *J. Mol. Biol.* **401,** 831–842 (2010).

50.  Dixit, P. D., Merchant, S. & Asthagiri, D. Ion Selectivity in the KcsA Potassium Channel from the Perspective of the Ion Binding Site. *Biophys. J.* **96,** 2138–2145 (2009).

51.  Dixit, P. D. & Asthagiri, D. Perspectives on: Ion selectivity: Thermodynamics of ion selectivity in the KcsA K+ channel. *J. Gen. Physiol.* **137,** 427–433 (2011).

52.  Dixit, P. D. & Asthagiri, D. Thermodynamics of ion selectivity in the KcsA K+ channel. *J. Gen. Physiol.* **137,** 427–33 (2011).

53.  Kast, S. M., Kloss, T., Tayefeh, S. & Thiel, G. A minimalist model for ion partitioning and competition in a K+ channel selectivity filter. *J. Gen. Physiol.* **138,** 371–373 (2011).

54.  Varma, S., Sabo, D. & Rempe, S. B. K+/Na+ Selectivity in K Channels and Valinomycin: Over-coordination Versus Cavity-size constraints. *J. Mol. Biol.* **376,** 13–22 (2008).

55.  Roux, B. B. *et al.* Theoretical and computational models of biological ion channels. *Q. Rev. Biophys.* **37,** 182–189 (2004).

56.  Bernèche, S. & Roux, B. Energetics of ion conduction through the K+ channel. *Nature* **414,** 73–77 (2001).

57.  Kim, I. & Allen, T. W. On the selective ion binding hypothesis for potassium channels. *Proc. Natl. Acad. Sci. U. S. A.* **108,** 17963–17978 (2011).

58.  Jensen, M. O. *et al.* Principles of conduction and hydrophobic gating in K+ channels. *Proc. Natl. Acad. Sci.* **107,** 5833–5838 (2010).

59.  Tayefeh, S. *et al.* Model development for the viral Kcv potassium channel. *Biophys. J.* **96,** 485–498 (2009).

60.  Aqvist, J. & Luzhkov, V. Ion permeation mechanism of the potassium channel. *Nature* **404,** 881–884 (2000).

61.  Kopfer, D. A. *et al.* Ion permeation in K+ channels occurs by direct Coulomb knock-on. *Science* **346,** 352–355 (2014).

62.  Hummer, G. Potassium ions line up. *Science* **346,** 303–303 (2014).

63.  Nimigean, C. M. & Allen, T. W. Perspectives on: Ion selectivity: Origins of ion selectivity in potassium channels from the perspective of channel block. *J. Gen. Physiol.* **137,** 405–413 (2011).

64.  Thompson, A. N. *et al.* Mechanism of potassium-channel selectivity revealed by Na+ and Li+ binding sites within the KcsA pore. *Nat. Struct. &#38; Mol. Biol.* **16,** 1317–1324 (2009).

65.  Roux, B. Ion Conduction and Selectivity in K $^+$ Channels. *Annu. Rev. Biophys. Biomol. Struct.* **34,** 153–171 (2005).

66.  Gokel, G. W. & Negin, S. Synthetic ion channels: From pores to biological applications. *Acc. Chem. Res.* **46,** 2824–2833 (2013).

67.  Sakai, N. & Matile, S. Synthetic ion channels. *Langmuir* **29,** 9031–9040 (2013).

68.  Song, C. & Corry, B. Intrinsic ion selectivity of narrow hydrophobic pores. *J. Phys. Chem. B* **113,** 7642–7649 (2009).

69.  Apel, P. Y., Blonskaya, I. V., Dmitriev, S. N., Orelovich, O. L. & Sartowska, B. a. Ion track symmetric and asymmetric nanopores in polyethylene terephthalate foils for versatile applications. *Nucl. Instruments Methods Phys. Res. Sect. B Beam Interact. with Mater. Atoms* 6–10 (2015). doi:10.1016/j.nimb.2015.07.016

70.     Gong, B. Gong suplimental. *Nat. Commun.* **1,** (2011).

71.     Beckstein, O. & Sansom, M. S. P. A hydrophobic gate in an ion channel: the closed state of the nicotinic acetylcholine receptor. *Phys. Biol.* **3,** 147–159 (2006).

72.     Aryal, P., Sansom, M. S. P. & Tucker, S. J. Hydrophobic Gating in Ion Channels. *J. Mol. Biol.* **427,** 1–10 (2014).

73.     Beckstein, O., Biggin, P. C. & Sansom, M. S. P. A Hydrophobic Gating Mechanism for Nanopores. *J. Phys. Chem. B* **105,** 12902–12905 (2001).

74.     Domene, C., Grottesi, A. & Sansom, M. S. P. Filter Flexibility and Distortion in a Bacterial Inward Rectifier K+ Channel: Simulation Studies of KirBac1.1. *Biophys. J.* **87,** 256–267 (2004).

75.     Swartz, K. J. Towards a structural view of gating in potassium channels. *Nat. Rev. Neurosci.* **5,** 905–916 (2004).

76.     Yellen, G. The moving parts of voltage-gated ion channels. *Q. Rev. Biophys.* **31,** 239–295 (1998).

77.     Siotto, F. *et al.* Viruses infecting marine picoplancton encode functional potassium ion channels. *Virology* **466-467,** 103–111 (2014).

78.     Abenavoli, A. *et al.* Fast and slow gating are inherent properties of the pore module of the K+ channel Kcv. *J. Gen. Physiol.* **134,** 219–29 (2009).

79.     Gazzarrini, S. *et al.* Long distance interactions within the potassium channel pore are revealed by molecular diversity of viral proteins. *J. Biol. Chem.* **279,** 28443–28449 (2004).

80.     Thiel, G. *et al.* Minimal art: or why small viral K+ channels are good tools for understanding basic structure and function relations. *Biochim. Biophys. Acta* **1808,** 580–588 (2011).

81.     Gebhardt, M. *et al.* Relevance of Lysine Snorkeling in the Outer Transmembrane Domain of Small Viral Potassium Ion Channels. *Biochemistry* **51,** 5571–5579 (2012).

82.     Lee, A. G. Ion channels: paddle in oil. *Nature* **444,** 697 (2006).

83.     Bavro, V. N. *et al.* Structure of a KirBac potassium channel with an open bundle crossing indicates a mechanism of channel gating. *Nat. Struct. Mol. Biol.* **19,** 158–163 (2012).

84.     Jiang, Y. *et al.* The open pore conformation of potassium channels. *Nature* **417,** 523–526 (2002).

85.     García-Fandiño, R. & Sansom, M. S. P. Designing biomimetic pores based on carbon nanotubes. *Proc. Natl. Acad. Sci. U. S. A.* **109,** 6939–6944 (2012).

86.     Trick, J. L., Wallace, E. J., Bayley, H. & Sansom, M. S. P. Designing a Hydrophobic Barrier within Biomimetic Nanopores. *ACS Nano* **8,** 1–29 (2014).

87.     Hilder, T. A., Gordon, D. & Chung, S.-H. Computational modeling of transport in synthetic nanotubes. *Nanomedicine* **7,** 702–709 (2011).

88.     Hilder, T. A. & Chung, S.-H. Carbon nanotube as a gramicidin analogue. *Chem. Phys. Lett.* **501,** 423–426 (2011).

89.     Hilder, T. A., Gordon, D. & Chung, S.-H. Synthetic chloride-selective carbon nanotubes examined by using molecular and stochastic dynamics. *Biophys. J.* **99,** 1734–1742 (2010).

90.     Park, J. H., Sinnott, S. B. & Aluru, N. R. Ion separation using a Y-junction carbon nanotube. *Nanotechnology* **17,** 895–900 (2006).

91.     Joseph, S., Mashl, R. J., Jakobsson, E. & Aluru, N. R. Electrolytic Transport in Modified Carbon Nanotubes. *Nano Lett.* **3,** 1399–1403 (2003).

92.     Keramidas, A., Moorhouse, A. J., Schofield, P. R. & Barry, P. H. Ligand-gated ion channels: Mechanisms underlying ion selectivity. *Prog. Biophys. Mol. Biol.* **86,** 161–204 (2004).

93.     Jensen, M. L., Schousboe, A. & Ahring, P. K. Charge selectivity of the Cys-loop family of ligand-gated ion

channels. *J. Neurochem.* **92,** 217–225 (2005).

94. Bass, R. B., Strop, P., Barclay, M. & Rees, D. C. Crystal structure of Escherichia coli MscS, a voltage-modulated and mechanosensitive channel. *Science* **298,** 1582–1587 (2002).

95. Trudeau, M. C., Warmke, J. W., Ganetzky, B. & Robertson, G. A. HERG, a human inward rectifier in the voltage-gated potassium channel family. *Science* **269,** 92–95 (1995).

96. Sands, Z., Grottesi, A. & Sansom, M. S. P. Voltage-gated ion channels. *Curr. Biol.* **15,** R44–R47 (2005).

97. Gulbis, J. M. & Doyle, D. A. Potassium channel structures: do they conform? *Curr. Opin. Struct. Biol.* **14,** 440–446 (2004).

98. Hoshi, T., Zagotta, W. N. & Aldrich, R. W. Shaker potassium channel gating. I: Transitions near the open state. *J. Gen. Physiol.* **103,** 249–278 (1994).

99. Yellen, G. The voltage-gated potassium channels and their relatives. *Nature* **419,** 35–42 (2002).

100. Catterall, W. A. Structure and function of voltage-gated ion channels. *Annu. Rev. Biochem.* 493–531 (1995).

101. Hamacher, K. *et al.* Phycodnavirus potassium ion channel proteins question the virus molecular piracy hypothesis. *PLoS One* **7,** e38826 (2012).

102. Hertel, B. *et al.* Salt bridges in the miniature viral channel Kcv are important for function. *Eur. Biophys. J.* **39,** 1057–1068 (2010).

103. Tayefeh, S. *et al.* Molecular dynamics simulation of the cytosolic mouth in Kcv-type potassium channels. *Biochemistry* **46,** 4826–4839 (2007).

104. Frohns, F. *et al.* Potassium ion channels of Chlorella viruses cause rapid depolarization of host cells during infection. *J. Virol.* **80,** 2437–2444 (2006).

105. Braha, O. *et al.* Designed protein pores as components for biosensors. *Chem. Biol.* **4,** 497–505 (1997).

106. Steller, L., Kreir, M. & Salzer, R. Natural and artificial ion channels for biosensing platforms. *Anal. Bioanal. Chem.* **402,** 209–230 (2012).

107. Choi, Y., Baker, L. A., Hillebrenner, H. & Martin, C. R. Biosensing with conically shaped nanopores and nanotubes. *Phys. Chem. Chem. Phys.* **8,** 4976–4988 (2006).

108. Krishnamurthy, V. & Cornell, B. Engineering aspects of biological ion channels--from biosensors to computational models for permeation. *Protoplasma* **249,** S3–S9 (2012).

109. Stoloff, D. H. & Wanunu, M. Recent trends in nanopores for biotechnology. *Curr. Opin. Biotechnol.* **24,** 699–704 (2013).

110. Kowalczyk, S. W., Blosser, T. R. & Dekker, C. Biomimetic nanopores: learning from and about nature. *Trends Biotechnol.* **29,** 607–614 (2011).

111. Gyurcsányi, R. E. Chemically-modified nanopores for sensing. *TrAC - Trends Anal. Chem.* **27,** 627–639 (2008).

112. Shim, J. W. *et al.* Detection and Quantification of Methylation in DNA using Solid-State Nanopores. *Sci. Rep.* **3,** 1–8 (2013).

113. Siwy, Z. & Fuliński, A. Fabrication of a synthetic nanopore ion pump. *Phys. Rev. Lett.* **89,** 198103 (2002).

114. Wen, L. & Jiang, L. Construction of biomimetic smart nanochannels for confined water. *Natl. Sci. Rev.* **1,** 144–156 (2013).

115. Holt, J. K. *et al.* Fast mass Transport Trough Sub-2-Nanometer Carbon Nanotubes. *Science* **312,** 1034–1038 (2006).

116. Siwy, Z. *et al.* Voltage-gated nanopores analogous to biochannels. 100 (2001).

117. Siwy, Z. & Fuliński, A. A nanodevice for rectification and pumping ions. *Am. J. Phys.* **72,** 567 (2004).

118. R., E. C.-C., Ritz, T., Siwy, Z. S. & Schulten, K. Molecular control of ionic conduction in polymer nanoporesccess. *Faraday Discuss.* 47–93 (2010).

119. DiFrancesco, M. *et al.* Engineering a Ca++-Sensitive (Bio)Sensor from the Pore-Module of a Potassium Channel. *Sensors* **15,** 4913–4924 (2015).

120. Sumikama, T., Saito, S. & Ohmine, I. Mechanism of ion permeation through a model channel: roles of energetic and entropic contributions. *J. Chem. Phys.* **139,** 165106 (2013).

121. Beckstein, O., Tai, K. & Sansom, M. S. P. Not ions alone: barriers to ion permeation in nanopores and channels. *J. Am. Chem. Soc.* **126,** 14694–14695 (2004).

122. Beu, T. A. Molecular dynamics simulations of ion transport through carbon nanotubes. I. Influence of geometry, ion specificity, and many-body interactions. *J. Chem. Phys.* **132,** 164513 (2010).

123. Beu, T. A. Molecular dynamics simulations of ion transport through carbon nanotubes. II. Structural effects of the nanotube radius, solute concentration, and applied electric fields. *J. Chem. Phys.* **135,** 044515 (2011).

124. Hummer, G., Rasaiah, J. C. & Noworyta, J. P. Water conduction through the hydrophobic channel of a carbon nanotube. *Nature* **414,** 188–190 (2001).

125. Harrison, B. S. & Atala, A. Carbon nanotube applications for tissue engineering. *Biomaterials* **28,** 344–353 (2007).

126. Kalluri, R. K., Ho, T. A. & Biener, J. Partition and structure of aqueous NaCl and CaCl2 electrolytes in carbon-slit electrodes. *J. Phys. Chem. C* **117,** 13609–13619 (2013).

127. Lu, D. *et al.* The role of molecular modeling in bionanotechnology. *Phys. Biol.* **3,** S40–53 (2006).

128. Bordin, J., Diehl, A., Barbosa, M. & Levin, Y. Ion fluxes through nanopores and transmembrane channels. *Phys. Rev. E* **85,** 031914 (2012).

129. Corry, B., Kuyucak, S. & Chung, S. H. Invalidity of continuum theories of electrolytes in nanopores. *Chem. Phys. Lett.* **320,** 35–41 (2000).

130. Apel, P. Y., Blonskaya, I. V, Orelovitch, O. L., Ramirez, P. & Sartowska, B. a. Effect of nanopore geometry on ion current rectification. *Nanotechnology* **22,** 175302 (2011).

131. Corry, B. & Chung, S. H. Mechanisms of valence selectivity in biological ion channels. *Cell. Mol. Life Sci.* **63,** 301–315 (2006).

132. Liu, J., LeVan, M. D. & Do, D. D. Accessible Volumes for Adsorption in Carbon Nanopores of Different Geometries and Wall Thicknesses. *J. Phys. Chem. C* **115,** 12077–12081 (2011).

133. González, A., White, J. A., Román, F. L. & Velasco, S. Entropic selectivity of binary mixtures in cylindrical pores. *J. Chem. Phys.* **135,** 154704 (2011).

134. Peterson, B. K., Walton, J. P. R. B. & Gubbins, K. E. Fluid behaviour in narrow pores. *Journal of the Chemical Society, Faraday Transactions 2* **82,** 1789 (1986).

135. Peterson, B. K., Gubbins, K. E., Heffelfinger, G. S., Marconi, M. B. U. & van Swol, F. Lennard-Jones fluids in cylindrical pores: Nonlocal theory and computer simulation. *J. Chem. Phys.* **88,** 6487 (1988).

136. Roth, R. & Gillespie, D. Physics of Size Selectivity. *Phys. Rev. Lett.* **95,** 247801 (2005).

137. Roth, R., Rauscher, M. & Archer, A. Selectivity in binary fluid mixtures: Static and dynamical properties. *Phys. Rev. E* **80,** 021409 (2009).

138. Carrillo-Tripp, M., Saint-Martin, H. & Ortega-Blake, I. Minimalist Molecular Model for Nanopore Selectivity. *Phys. Rev. Lett.* **93,** 168104 (2004).

139. Vitarelli, M. J. & Talaga, D. S. Theoretical models for electrochemical impedance spectroscopy and local $\zeta$-potential of unfolded proteins in nanopores. *J. Chem. Phys.* **139,** 105101 (2013).

140. Peng, B. & Yu, Y.-X. Ion distributions, exclusion coefficients, and separation factors of electrolytes in a

charged cylindrical nanopore: a partially perturbative density functional theory study. *J. Chem. Phys.* **131,** 134703 (2009).

141. Yang, L. & Garde, S. Modeling the selective partitioning of cations into negatively charged nanopores in water. *J. Chem. Phys.* **126,** 084706 (2007).

142. Beckstein, O. & Sansom, M. S. P. The influence of geometry, surface character, and flexibility on the permeation of ions and water through biological pores. *Phys. Biol.* **1,** 42–52 (2004).

143. Shrivastava, I. H., Tieleman, D. P., Biggin, P. C. & Sansom, M. S. P. K+ versus Na+ ions in a K channel selectivity filter: a simulation study. *Biophys. J.* **83,** 633–645 (2002).

144. Frank, K. & Kranias, E. G. Phospholamban and cardiac contractility. *Ann. Med.* **32,** 572–578 (2000).

145. Cornea, R. L., Jones, L. R., Autry, J. M. & Thomas, D. D. Mutation and phosphorylation change the oligomeric structure of phospholamban in lipid bilayers. *Biochemistry* **36,** 2960–2967 (1997).

146. Robia, S. L., Flohr, N. C. & Thomas, D. D. Phospholamban Pentamer Quaternary Conformation Determined by In-Gel. *Biochemistry* **44,** 4302–4311 (2005).

147. Oxenoid, K. & Chou, J. J. The structure of phospholamban pentamer reveals a channel-like architecture in membranes. *Proc. Natl. Acad. Sci. U. S. A.* **102,** 10870–10875 (2005).

148. Kobayashi, Y. M. A Leucine Zipper Stabilizes the Pentameric Membrane Domain of Phospholamban and Forms a Coiled-coil Pore Structure. *J. Biol. Chem.* **271,** 5941–5946 (1996).

149. Kimura, Y., Kurzydlowski, K., Tada, M. & MacLennan, D. H. Phospholamban Inhibitory Function Is Activated by Depolymerization. *J. Biol. Chem.* **272,** 15061–15064 (1997).

150. Smeazzetto, S., Schröder, I., Thiel, G. & Moncelli, M. R. Phospholamban generates cation selective ion channels. *Phys. Chem. Chem. Phys.* **13,** 12935–12939 (2011).

151. Smeazzetto, S., Saponaro, A., Young, H. S., Moncelli, M. R. & Thiel, G. Structure-function relation of phospholamban: modulation of channel activity as a potential regulator of SERCA activity. *PLoS One* **8,** e52744 (2013).

152. Kovacs, R. J., Nelson, M. T., Simmerman, H. K. & Jones, L. R. Phospholamban forms Ca2+-selective channels in lipid bilayers. *J. Biol. Chem.* **263,** 18364–18368 (1988).

153. Decrouy, A., Juteau, M. & Rousseau, E. Examination of the role of phosphorylation and phospholamban in the regulation of the cardiac sarcoplasmic reticulum Cl− channel. *J. Membr. Biol.* **326,** 315–326 (1995).

154. Decrouy, A., Juteau, M., Proteau, S., Teijiera, J. & Rousseau, E. Biochemical regulation of sarcoplasmic reticulum Cl- channel from human atrial myocytes: involvement of phospholamban. *J. Mol. Cell. Cardiol.* **28,** 767–80 (1996).

155. Arkin, I. T., Adams, P. D., Brünger, A. T., Smith, S. O. & Engelman, D. M. Structural perspectives of phospholamban, a helical transmembrane pentamer. *Annu. Rev. Biophys. Biomol. Struct.* **26,** 157–179 (1997).

156. Becucci, L. *et al.* On the function of pentameric phospholamban: ion channel or storage form? *Biophys. J.* **96,** L60–L62 (2009).

157. Vostrikov, V. V, Mote, K. R., Verardi, R. & Veglia, G. Structural dynamics and topology of phosphorylated phospholamban homopentamer reveal its role in the regulation of calcium transport. *Structure* **21,** 2119–30 (2013).

158. Becucci, L., Papini, M., Verardi, R., Veglia, G. & Guidelli, R. Phospholamban and its phosphorylated form require non-physiological transmembrane potentials to translocate ions. *Soft Matter* **8,** 3881–3888 (2012).

159. Lian, P., Wei, D.-Q., Wang, J.-F. & Chou, K.-C. An allosteric mechanism inferred from molecular dynamics simulations on phospholamban pentamer in lipid membranes. *PLoS One* **6,** 2–7 (2011).

160. Kim, T., Lee, J. & Im, W. Molecular dynamics studies on structure and dynamics of phospholamban monomer and pentamer in membranes. *Proteins* **76,** 86–98 (2009).

161.    Hassaine, G. *et al.* X-ray structure of the mouse serotonin 5-HT3 receptor. *Nature* **512,** 276–281 (2014).

162.    Hibbs, R. E. & Gouaux, E. Principles of activation and permeation in an anion-selective Cys-loop receptor. *Nature* **474,** 54–60 (2011).

163.    Miller, P. S. & Aricescu, a R. Crystal structure of a human GABAA receptor. *Nature* **512,** 270–275 (2014).

164.    Althoff, T., Hibbs, R. E., Banerjee, S. & Gouaux, E. X-ray structures of GluCl in apo states reveal a gating mechanism of Cys-loop receptors. *Nature* **512,** 333–337 (2014).

165.    Hilf, R. J. C. & Dutzler, R. Structure of a potentially open state of a proton-activated pentameric ligand-gated ion channel. *Nature* **457,** 115–118 (2009).

166.    Imoto, K. *et al.* Rings of negatively charged amino acids determine the acetylcholine receptor channel conductance. *Nature* **335,** 645–648 (1988).

167.    Gunthorpe, M. J. & Lummis, S. C. Conversion of the ion selectivity of the 5-HT(3a) receptor from cationic to anionic reveals a conserved feature of the ligand-gated ion channel superfamily. *J. Biol. Chem.* **276,** 10977–10983 (2001).

168.    Keramidas, A., Moorhouse, A. J., Pierce, K. D., Schofield, P. R. & Barry, P. H. Cation-selective mutations in the M2 domain of the inhibitory glycine receptor channel reveal determinants of ion-charge selectivity. *J. Gen. Physiol.* **119,** 393–410 (2002).

169.    White, B. H. & Cohen, J. B. Agonist-induced changes in the structure of the acetylcholine receptor M2 regions revealed by photoincorporation of an uncharged nicotinic noncompetitive antagonist. *J. Biol. Chem.* **267,** 15770–15783 (1992).

170.    Song, C. & Corry, B. Ion conduction in ligand-gated ion channels- Brownian dynamics studies of four recent crystal structures. *Biophys. J.* **98,** 404–411 (2010).

171.    O'Mara, M., Barry, P. H. & Chung, S.-H. A model of the glycine receptor deduced from Brownian dynamics studies. *Proc. Natl. Acad. Sci. U. S. A.* **100,** 4310–4315 (2003).

172.    Corry, B. An energy-efficient gating mechanism in the acetylcholine receptor channel suggested by molecular and Brownian dynamics. *Biophys. J.* **90,** 799–810 (2006).

173.    Nury, H. *et al.* One-microsecond molecular dynamics simulation of channel gating in a nicotinic receptor homologue. *Proc. Natl. Acad. Sci. U. S. A.* **107,** 6275–6280 (2010).

174.    Song, C. & Corry, B. Role of acetylcholine receptor domains in ion selectivity. *Biochim. Biophys. Acta - Biomembr.* **1788,** 1466–1473 (2009).

175.    Song, C. & Corry, B. Computational study of the transmembrane domain of the acetylcholine receptor. *Eur. Biophys. J.* **38,** 961–970 (2009).

176.    Sunesen, M. *et al.* Mechanism of Cl- selection by a glutamate-gated chloride (GluCl) receptor revealed through mutations in the selectivity filter. *J. Biol. Chem.* **281,** 14875–14881 (2006).

177.    Allen, M. P. & Tildesley, D. J. *Computer Simulation of Liquids*. (Oxford University Press, 1987).

178.    Alder, B. J. & Wainwright, T. E. Studies in Molecular Dynamics. I. General Method. *J. Chem. Phys.* **31,** 459–466 (1959).

179.    Born, M. & Oppenheimer, R. Zur Quantentheorie der Molekeln. *Ann. Phys.* **20,** 457–484 (1927).

180.    Adcock, S. A. & McCammon, J. A. Molecular dynamics: survey of methods for simulating the activity of proteins. *Chem. Rev.* **106,** 1589–1615 (2006).

181.    Essmann, U. *et al.* A smooth particle mesh Ewald method. *J Chem Phys* **103,** 8577–8593 (1995).

182.    Ewald, P. P. Die Berechnung optische und elektrostatischer Gitterpotentiale. *Ann. Phys.* **64,** 253–287 (1920).

183.    Phillips, J. C. & Braun, R. Scalable molecular dynamics with NAMD. *J. Comput. Chem.* **26,** 1781–1802 (2005).

184. Jorgensen, W. L. & Tirado-Rives, J. Potential energy functions for atomic-level simulations of water and organic and biomolecular systems. *Proc. Natl. Acad. Sci. U. S. A.* **102,** 6665–6670 (2005).

185. Baştuğ, T. & Kuyucak, S. Importance of the peptide backbone description in modeling the selectivity filter in potassium channels. *Biophys. J.* **96,** 4006–12 (2009).

186. Buck, M., Bouguet-Bonnet, S., Pastor, R. W. & MacKerell, A. D. Importance of the CMAP correction to the CHARMM22 protein force field: dynamics of hen lysozyme. *Biophys. J.* **90,** L36–L38 (2006).

187. Jorgensen, W. L., Chandrasekhar, J., Madura, J. D., Impey, R. W. & Klein, M. L. Comparison of simple potential functions for simulating liquid water. *J. Chem. Phys.* **79,** 926 (1983).

188. Berendsen, H. J. C., Grigera, J. R. & Straatsma, T. P. The Missing Term in Effective Pair Potentials. *J. Phys. Chem.* **91,** 6269–6271 (1987).

189. Jorgensen, W. L., Blake, F. & Buckner, J. K. Free energy of TIP4P water and the free energies of hydration of CH4 and Cl- from statistical perturbation theory. *Chem. Phys.* **20,** 193–200 (1988).

190. MacKerell, A. D. *et al.* All-atom empirical potential for molecular modeling and dynamics studies of proteins. *J. Phys. Chem. B* **102,** 3586–616 (1998).

191. Beglov, D., Roux, B. & Hc, C. Finite representation of an infinite for computer simulations bulk system : Solvent boundary potential. *J. Med. Phys.* **100,** 9050–9063 (1994).

192. Bahar, I., Lezon, T. R., Bakan, A. & Shrivastava, I. H. Normal Mode Analysis of Biomolecular Structures: Functional Mech Membrane Proteins. *Chem. Rev.* **110,** 1463–1497 (2010).

193. Doruker, P., Jernigan, R. L. & Bahar, I. Dynamics of large proteins through hierarchical levels of coarse-grained structures. *J. Comput. Chem.* **23,** 119–127 (2002).

194. Bahar, I., Atilgan, A. R. & Erman, B. Direct evaluation of thermal fluctuations in proteins using a single-parameter harmonic potential. *Fold. Des.* **2,** 173–181 (1997).

195. William C. Swope Hans C. Andersen, P. H. B. & Wilson, K. R. A computer simulation method for the calculation of equilibrium constants for the formation of physical clusters of molecules: Application to small water clusters. *J. Chem. Phys.* **76,** 637–649 (1982).

196. Keskin, O., Bahar, I., Flatow, D., Covell, D. G. & Jernigan, R. L. Molecular mechanisms of chaperonin GroEL-GroES function. *Biochemistry* **41,** 491–501 (2002).

197. Bahar, I., Atilgan, A. R. & Erman, B. Direct evaluation of thermal fluctuations in proteins using a single-parameter harmonic potential. *Fold. Des.* **2,** 173–181 (1997).

198. Haliloglu, T., Bahar, I. & Erman, B. Gaussian Dynamics of Folded Proteins. *Phys. Rev. Lett.* **79,** 3090–3093 (1997).

199. Shrivastava, I. H. & Bahar, I. Common mechanism of pore opening shared by five different potassium channels. *Biophys. J.* **90,** 3929–3940 (2006).

200. Lezon, T. R., Shrivastava, I. H., Yang, Z. & Bahar, I. Elastic Network Models For Biomolecular Dynamics: Theory and Application to Membrane Proteins and Viruses. *Handb. Biol. Networks* 129–158 (2009). at <papers2://publication/uuid/9B230FBB-A40F-4630-9421-7FF883030646>

201. Liu, X. & Karimi, H. A. High-throughput modeling and analysis of protein structural dynamics. *Brief. Bioinform.* **8,** 432–445 (2007).

202. Kloczkowski, A., Mark, J. E. & Erman, B. Chain dimensions and fluctuations in random elastomeric networks. 1. Phantom Gaussian networks in the undeformed state. *Macromolecules* **22,** 1423–1432 (1989).

203. Flory, P. J. Statistical thermodynamics of random networks. *Proc. R. Soc. Lond. B. Biol. Sci.* **351,** 351–380 (1976).

204. Tirion, M. M. Large Amplitude Elastic Motions in Proteins from a Single-Parameter, Atomic Analysis. *Phys. Rev. Lett.* **77,** 1905–1908 (1996).

205. Tama, F. & Brooks, C. L. Symmetry, form, and shape: guiding principles for robustness in macromolecular machines. *Annu. Rev. Biophys. Biomol. Struct.* **35,** 115–133 (2006).

206. Hoffgaard, F., Kast, S. M., Moroni, A., Thiel, G. & Hamacher, K. Biochimica et Biophysica Acta Tectonics of a K + channel : The importance of the N-terminus for channel gating. *BBA - Biomembr.* **1848,** 3197–3204 (2015).

207. Kast, S. M. & Kloss, T. Closed-form expressions of the chemical potential for integral equation closures with certain bridge functions. *J. Chem. Phys.* **129,** 14–17 (2008).

208. Chandler, D. *Introduction to Modern Statistical Mechanics*. (Oxford University Press, 1987).

209. Kirkwood, J. G. Statistical mechanics of fluid mixtures. *J. Chem. Phys.* **3,** 300–313 (1935).

210. Andersen, H. C. & Chandler, D. Optimized Cluster Expansions for Classical Fluids. I. General Theory and Variational Formulation of the Mean Spherical Model and Hard Sphere Percus-Yevick Equations. *J. Chem. Phys.* **57,** 1918–1929 (1972).

211. Perkyns, J. S. & Pettitt, B. M. A site-site theory for finite concentration saline solutions. *J. Chem. Phys.* **97,** 7656–7666 (1992).

212. Phongphanphanee, S., Yoshida, N. & Hirata, F. Molecular selectivity in aquaporin channels studied by the 3D-RISM theory. *J. Phys. Chem. B* **114,** 7967–7973 (2010).

213. Phongphanphanee, S., Yoshida, N., Oiki, S. & Hirata, F. Probing 'ambivalent' snug-fit sites in the KcsA potassium channel using three-dimensional reference interaction site model (3D-RISM) theory. *Pure Appl. Chem.* **86,** 1–8 (2014).

214. Kloss, T. Quantitative Berechnung thermodynamischer Observablen mittels dreidimensionaler Integralgleichungsthe orien. (Technische Universität Darmstadt, 2007).

215. Smart, O. S., Breed, J., Smith, G. R. & Sansom, M. S. P. A novel method for structure-based prediction of ion channel conductance properties. *Biophys. J.* **72,** 1109–1126 (1997).

216. Zhu, F. & Hummer, G. Drying transition in the hydrophobic gate of the GLIC channel blocks ion conduction. *Biophys. J.* **103,** 219–227 (2012).

217. Phongphanphanee, S., Yoshida, N. & Hirata, F. Reply to 'Comment on 'Molecular Selectivity in Aquaporin Channels Studied by the 3D- RISM Theory''. *J. Phys. Chem. B* 3–5 (2011).

218. Atkins, P. W. & De Paula, J. *Physical Chemistry*. (Oxford University Press, 2006).

219. Reguera, D. & Rubí, J. Kinetic equations for diffusion in the presence of entropic barriers. *Phys. Rev. E* **64,** 061106 (2001).

220. Humphrey, W., Dalke, A. & Schulten, K. VMD: visual molecular dynamics. *J. Molec. Graph.* **14,** 33–38 (1996).

221. Gur, M., Madura, J. D. & Bahar, I. Global Transitions of Proteins Explored by a Multiscale Hybrid Methodology: Application to Adenylate Kinase. *Biophys. J.* **105,** 1643–1652 (2013).

222. Beglov, D. & Roux, B. An integral equation to describe the solvation of polar molecules in liquid water. *J. Phys. Chem. B* **5647,** 7821–7826 (1997).

223. Larkin, M. A. *et al.* Clustal W and Clustal X version 2.0. *Bioinformatics* **23,** 2947–2948 (2007).

224. Fiser, A. & Šali, A. *Comparative protein structure modeling*. *Protein Structure Determination, Analysis, and Applications for Drug Discovery* (CRC Press, 2003).

225. Shen, M.-Y. & Sali, A. Statistical potential for assessment and prediction of protein structures. *Protein Sci.* **15,** 2507–2524 (2006).

226. Laskowski, R. A., MacArthur, M. W., Moss, D. S. & Thornton, J. M. PROCHECK: a program to check the stereochemical quality of protein structures. *J. Appl. Crystallogr.* **26,** 283–291 (1993).

227. Jo, S., Kim, T., Iyer, V. G. & Im, W. CHARMM-GUI: A web-based graphical user interface for CHARMM. *J. Comput. Chem.* **29,** 1859–1865 (2008).

228. Posch, H. A. & Hoover, W. G. Nonequilibrium molecular dynamics of classical fluids. *Mol. Liq. New Perspect. Phys. Chem.* **379,** 527–547 (1992).

229. Martyna, G., Klein, M. L. & Tuckerman, M. E. Nose-Hoover chains - the canonical ensemble via continuous dynamics. *J Chem Phys* **97,** 2635–2643 (1992).

230. Kubo, R., Toda, M. & Hashitsume, N. *Nonequilibrium Statistical Mechanics. FewBody Systems* **31,** (Springer-Verlag, 1985).

231. Eyal, E., Lum, G. & Bahar, I. The Anisotropic Network Model web server at 2015 ( ANM 2 . 0 ). *Struct. Bioinforma.* **2015,** 1–3 (2015).

232. Yang, L. W. *et al.* oGNM: Online computation of structural dynamics using the Gaussian Network Model. *Nucleic Acids Res.* **34,** 24–31 (2006).

233. Shi, N., Ye, S., Alam, A., Chen, L. & Jiang, Y. Atomic structure of a Na+ - and K+ -conducting channel. *Nature* **440,** 570–574 (2006).

234. Altschul, S. F. *et al.* Gapped BLAST and PSI- BLAST: a new generation of protein database search programs. *Nucleic acids Res* **25,** 3389–3402 (1997).

235. Möller, S., Croning, M. D. & Apweiler, R. Evaluation of methods for the prediction of membrane spanning regions. *Bioinformatics* **17,** 646–53 (2001).

236. Jo, S., Lim, J. B., Klauda, J. B. & Im, W. CHARMM-GUI membrane builder for mixed bilayers and its application to yeast membranes. *Biophys. J.* **97,** 50–58 (2009).

237. Marrink, S. J., de Vries, A. H. & Tieleman, D. P. Lipids on the move: simulations of membrane pores, domains, stalks and curves. *Biochim. Biophys. Acta* **1788,** 149–68 (2009).

238. Sansom, M. S. P. *et al.* Potassium channels: structures, models, simulations. *Biochim. Biophys. Acta* **1565,** 294–307 (2002).

239. Biggin, P. C. & Sansom, M. S. P. Open-state models of a potassium channel. *Biophys. J.* **83,** 1867–1876 (2002).

240. Anishkin, A., Milac, A. A. L. & Guy, H. R. Symmetry- • restrained molecular dynamics simulations improve homology models of potassium channels. *Proteins Struct. Funct. Bioinforma.* **78,** 932–949 (2010).

241. Grottesi, A., Domene, C., Hall, B. & Sansom, M. S. P. Conformational dynamics of M2 helices in KirBac channels: helix flexibility in relation to gating via molecular dynamics simulations. *Biochemistry* **44,** 14586–14594 (2005).

242. Amiry-Moghaddam, M. & Ottersen, O. P. The molecular basis of water transport in the brain. *Nat. Rev. Neurosci.* **4,** 991–1001 (2003).

243. Storm, a J., Chen, J. H., Ling, X. S., Zandbergen, H. W. & Dekker, C. Fabrication of solid-state nanopores with single-nanometre precision. *Nat. Mater.* **2,** 537–540 (2003).

244. Matile, S., Som, A. & Sordé, N. Recent synthetic ion channels and pores. *Tetrahedron* **60,** 6405–6435 (2004).

245. Pradeep, H. & Rajanikant, G. K. Nanochannels: biological channel analogues. *IET Nanobiotechnol.* **6,** 63–70 (2012).

246. Vanommeslaeghe, K. *et al.* CHARMM general force field: A force field for drug-like molecules compatible with the CHARMM all-atom additive biological force fields. *J. Comput. Chem.* **31,** 671–690 (2010).

247. Laliberté, M. & Cooper, W. E. Model for Calculating the Density of Aqueous Electrolyte Solutions. *J. Chem. Eng. Data* **49,** 1141–1151 (2004).

248. Hasted, H. B., Ritson, D. M. & Collie, C. H. Dielectric Properties of Aqueous Ionic Solutions. Parts I and II. *J. Chem. Phys.* **16,** 1 (1948).

249.  Elmore, D. E. & Dougherty, D. a. Molecular dynamics simulations of wild-type and mutant forms of the Mycobacterium tuberculosis MscL channel. *Biophys. J.* **81,** 1345–1359 (2001).

250.  Joung, I. S. & Cheatham, T. E. Determination of alkali and halide monovalent ion parameters for use in explicitly solvated biomolecular simulations. *J. Phys. Chem. B* **112,** 9020–41 (2008).

251.  Kovalenko, A., Ten-no, S. & Hirata, F. Solution of three-dimensional reference interaction site model and hypernetted chain equations for simple point charge water by modified method of direct inversion in iterative subspace. *J. Comput. Chem.* **20,** 928–936 (1999).

252.  Wagner, W. & Pruß, a. The IAPWS formulation 1995 for the thermodynamic properties of ordinary water substance for general and scientific use. *J. Phys. Chem. Ref. Data* **31,** 387–535 (2002).

253.  Kloss, T. & Kast, S. M. Treatment of charged solutes in three-dimensional integral equation theory. *J. Chem. Phys.* **128,** 134505 (2008).

254.  Montal, M. Reconstitution of Channel Proteins from Excitable Cells in Planar Lipid Bilayer Membranes Mauricio. *J. Membr. Biol.* **98,** 101–115 (1987).

255.  Urban, M. Ionenselektivität von Nanoporen. (TU Dortmund, 2014).

256.  Lebedev, I. V & Laikov, D. N. A quadrature formula for the sphere of the 131st algebraic order of accuracy. *Dokl. Math.* **59,** 477–481 (1999).

257.  Atkins, P. W. & MacDermott, J. The Born equation and ionic solvation. *J. Chem. Educ.* **59,** 359 (1982).

258.  Altschul, S. F. *et al.* Protein database searches using compositionally adjusted substitution matrices. *FEBS J.* **272,** 5101–5109 (2005).